Spectroscopic Studies On Structure, Function And Dynamics Of Biological Macromolecules In Physiologically Relevant And Engineered Environments

THESIS

SUBMITTED FOR THE DEGREE OF

DOCTOR OF PHILOSOPHY (SCIENCE)

BY

PRIYA SINGH

DEPARTMENT OF CHEMISTRY

UNIVERSITY OF CALCUTTA

2019

To My Family

Acknowledgements

Completion of this doctoral dissertation would never have been possible without the support and guidance of several people. Though it will not be enough to express my gratitude in words still I would like to give my many, many thanks to all these people.

First of all I would like to express my heartfelt gratitude to my supervisor Professor Samir Kumar Pal, whom I am extremely grateful for being an exceptional mentor for me. This work would not have been possible without his guidance, unconditional support, motivation, patience, constant availability and myriad helpful discussions. I am extremely fortunate to get opportunity to do my research under his guidance and to learn from his instrumental expertise, vast knowledge in multidisciplinary field and insight into various experimental problems. He did never mind making sacrifices of all his leisure for our accomplishment and always available to clarify my doubts. Despite coming from different region, his impartial comportment toward me and his firm conviction and motivation towards his female students makes him a most superlative supervisor. I thank him for providing me with the opportunity to work with a talented team of researchers and an excellent research environment.

I would also like to thank Prof. Kyo-Han Ahn of Pohang University of Science and Technology, Republic of Korea, Prof. Saleh A. Ahmed of Umm Al-Qura University, KSA, Prof. Peter Lemmens of TU Braunschweig, Germany, Prof. Ramaprosad Mukhopadhyay of BARC, India, Dr. Veerendra Kumar Sharma of BARC, India, Dr. Indranil Banerjee, National Institute of Technology Rourkela, India, Prof. Thalappil Pradeep, of Department of Chemistry, IIT Madras, India, Prof. Ranjan Das of Department of Chemistry, West Bengal State University, India and Prof. Debasish Pal of Uluberia College. Special mention is given to Prof. Das for his valuable advices and for reviewing my works.

I must acknowledge all the teaching and non-teaching staff of S. N. Bose National Centre for Basic Sciences for their kind helps at various phases of this research. I acknowledge S. N. Bose National Centre for Basic Sciences for providing the research fellowship and Department of Biotechnology (DBT), India for projects.

I also appreciate the beautiful work culture and environment in the lab maintained by my seniors and colleagues. I am especially thankful to Dr. Susobhan Choudhury for mentoring me at the initial stage of my research work. I am grateful to Dr. Prasanna kumar Mondal and Dr. Gautam Chandra for helping me in microfluidic experiment. I also want to thanks Dr. Shreyasi Dutta for helping me in biology. My sincere appreciation goes to all my seniors: Dr. Samim Sardar, Dr. Nabarun Polley, Dr. Prasenjit Kar, Dr. Tanushree Datta and earlier lab-member Mr. Ramesh Nandi. I acknowledge Damayanti for working with me in certain portion of my thesis. I would like to acknowledge all the present group members: Damayanti, Jayita, Probir, Aniruddha, Tuhin, Animesh da, Dipanjan, Arko, Arpan, Susmita, Nur, Dr. Gulmi Chakraborty, Dr. Tatini Rakshit, Dr. Soumendra Darbar, Soumendra da, Lopamudra, Deep Shikha, Amrita, Pritam, Ria, Sumana di, Oiendrila for providing a homely and a cheerful environment, and also for assisting me during research work. I am, especially, thankful to Damayanti who shared glorious moments over a long period of time, supported my work annoyances, and also for the good moments of fun! My close friends especially Sonal, Anshuman, Sonam and Abhishek also need to be mentioned for being a great source of strength; they always lent an ear to the hassles in my life and encouraged me to pursue research.

Last but not the least, I express my gratitude to my parents and my siblings (elder brother and younger brother). A career in science would not have been possible without the great support from my parents, who have always encouraged me to chart my own path in life. Without their sacrifices, moral supports and blessings the thesis would not have taken its shape. I also like to acknowledge my sister-in-law and brother from Howrah for caring me and for being my local guardian. I must thank all my other extended family members for being extremely supportive and providing me with an environment which enabled me to do research.

Dated:
Department of Chemical, Biological and Macromolecular Sciences,
S. N. Bose National Centre for Basic Sciences,
Salt Lake, Kolkata 700106, India *(Priya singh)*

CONTENTS

Chapter 1

Introduction

1.1. Background

A large number of clinically important drugs/ligands and antibiotics are believed to exert their primary biological action by means of interactions with biological macromolecules (lipid, protein, DNA etc) [1]. These recognition is usually driven by many weak interactions like van der Waals, hydrophobic, electrostatic and hydrogen bonding etc. leading to macromolecules-ligand complexation [2]. The drugs/ligands interact at the active site of biomolecules and efficient biological activity demands good geometric fit as suggested by Emil Fischer in the "lock and key"[3]. However, during last decades, it appeared that these concepts were insufficient to understand completely the mechanism of biomolecular recognitions [4, 5]. Indeed, the outcomes of these interactions were found to be depends on other factors and that are not currently accounted for, such as solvent polarity, temperature, effector, molecular crowding, and so on. Biomolecular recognition is also strongly influenced by the conformation and dynamics of the biological macromolecules and the environment in which the biomolecules are embedded. These dynamical behaviors is characterized by the thermodynamics (lifetimes of the conformational states, the relative populations and probabilities) and the kinetics (transition that leads to the population redistribution between these conformational states) of the macromolecules [6, 7]. Elucidating the role of conformation and dynamics of biological macromolecules and the time scales involved provide insights into the mechanism of molecular recognition [8]. A thorough knowledge of the structure and dynamics of macromolecules that command such molecular interactions can find immense use in the modulations of

the ligand-macromolecular recognition process which may have enormous application in medicine [9].

1.2. Dynamical Modulation of Macromolecules in Physiologically Relevant and Engineered Environments:

The essential dynamics of any macromolecules is chemically implicit in its structure and is very well linked to its function [10]. The correlation between structure and dynamics allows the biological macromolecules to adapt and alternate its conformation as a response to environmental stimuli leading to differential molecular recognition at different times scale. The most striking conformational changes are often triggered by environmental changes (e.g., change in pH, temperature, ligand binding and external milieu). In recent study, enzyme-ligand interaction following two different pathways namely, conformational selection and induced-fit mechanisms were recognized at two different pH [11]. Similarly, the ultrafast dynamics (cis-trans isomerization) of small ligands dihydroindolizine (DHI) encapsulated in protein is found to be responsible for altered enzymatic activity [12]. However, several computational and experimental studies have revealed that hydration water also play a significant role in macromolecular dynamics and activity [13]. Beece et al. [14] and Frauenfelder et al. [15] anticipated that the water ''slaves'' the biological molecule, in the sense that the biomolecule dynamics and activity are related to the solvent dynamics. Indeed, several results validated a strong coupling between structure of macromolecules and solvent dynamics [16, 17]. Recent studies of hydration dynamics suggest that interfacial water (hydration layer) molecules are constantly in exchange with outside bulk water and this dynamical exchange is extremely sensitive to the external environment such as molecular crowding, temperature, pressure, external stimuli, "etc." [18, 19]. A thorough knowledge of the water dynamics, reactivity, and energetics of biological macromolecules e.g., protein,

DNA, lipids, reverse micelle (RM) etc. can find immense use in modulation of the biomolecular recognition. Moreover, water in protein interior, lipid bilayers, micropores of minerals exists mainly as isolated water molecules or small clusters and their dynamics and reactivity remains poorly understood in spite of their profound biological implications. This emphasizes investigation of ultrafast hydration dynamics, regulate by molecular crowding, interfacial charge, temperature, pH, etc. to understand the differential functionality of biological macromolecules.

1.3. Scope of Spectroscopic Investigation on Structure, Function and Dynamics of Biological Macromolecules:

It is well accepted that the dynamics of biological macromolecules (proteins, DNA, lipids etc.) plays a key role in their function. Yet, understanding the ultrafast dynamics of biological macromolecules remains a great challenge. The local flexibility and dynamical motion of macromolecules (protein, DNA, lipid, etc.) varies from femtosecond to several microseconds. Like, bond vibrations takes place in femtoseconds (10^{-15} s), side-chain rotations and loop motions occurs on picosecond (10^{-12} s), nanosecond (10^{-9} s), and microsecond (10^{-6} s) timescales. The larger conformational dynamics of macromolecules take place from several tens to hundreds of nanoseconds whereas allosteric regulation occurs on the microsecond timescale. The valuation of alteration in conformational dynamics due to a biomolecular recognition from molecular dynamics simulations remains a considerable challenge [20]. Experimental measurement of the conformational dynamics of biomolecules in their free and complexed states is therefore required. While, X-ray crystallography provides high-resolution structural information, however, it is usually unfavourable for understanding the dynamical properties of macromolecules. NMR spectroscopy proved to be a better source for studying the dynamics and flexibility of biomolecules, nevertheless, is only proficient to

monitored the relatively slow dynamical motions (millisecond to microsecond) rather fast dynamics (subpicosecond-nanosecond) of biomolecules [21]. Hence, ultrafast dynamics (femtosecond to nanosecond) of biomolecules is less explored and understood [20]. Fluorescence spectroscopic techniques including picosecond resolved fluorescence anisotropy, Förster resonance energy transfer (FRET) and time dependent stokes shift (TDSS), proved to be useful for exploring biomolecular dynamics over a broad time scale [22, 23].

The key focus of this thesis is to understand the role of structure and ultrafast dynamics leading to differential biomolecular interactions. The structure and dynamics of the individual biomolecules play very crucial role in the biomolecular recognition processes. Several X-ray crystallography and NMR studies have been reported for the structural properties of the interface of some biologically active complexes [24, 25]. Very few studies on the interfacial dynamics of the biologically relevant complexes are reported with picosecond to nanosecond resolution. In this regard, to explore the coupling between ultrafast dynamics and functionality of lipids, we have performed the photo physical studies of coumarin 500 and ANS in the lipid bilayer (DODAB) at different phases. While ANS corroborates hydration dynamics of head group region of lipids, C500 located deeper in the lipid follows dynamics of lipids bilayer. At low temperature, plants and cyanobacteria maintained their membrane fluidity by introducing unsaturation to the lipids. Hence, subsequently we have explored the role of unsaturated lipid (monoolein) in modulation of dynamics and membrane fluidity of DODAB at different phases. The encapsulation of unsaturated lipid monoolein to a cationic lipid DODAB not only alters the structural organization of the vesicles between multilamellar and inverted non-lamellar structures, but, also modulates its cell transfection efficiency [26]. Further to correlate the dynamics of structural relaxation of the DODAB:MO mixed vesicles with the transfection efficiency, the associated hydration dynamics was monitored at different

compositions of mixed vesicles. We have also tried to monitor the dynamical modulation of liposome by photoresponsive ligand dihydroindolizine for potential drug delivery application. Relaxation dynamics at the surface of biologically important macromolecules is important taking into account their functionality in molecular recognition. In this regard, we have used synthesized dye ACYMAN to study solvation dynamics of a model protein–surfactant interface. Similarly, the functionality of gene delivery vehicles i.e. the condensation of DNA with CTAB was monitored by labelling DNA with ethidium bromide and CTAB with nonyl acridine orange. Lastly, we have explored the role of hydration dynamics leading to its altered enzymatic activity. As the dilute solution experiments differ significantly from *in vivo* conditions as 40% volume of cytosol is occupied by a wide variety of macromolecules. In this regard, we have studies the hydrolysis of DNA by DNase I enzyme in presence of PEG 3350 as a molecular crowder. Finally we have studied the effect of differential hydration dynamics due to different charge reverse micelle leading to altered enzymatic activity of α-chymotrysin using a model microfluidics system equipped with a microscopic and spectroscopic attachment.

1.4. Objective:

Molecular recognition of biological macromolecules is crucial for almost every physiological process including mediation of cell motility, catalysis, cellular transport and for drug designing and for the discovery of new medicines to benefit human health. Recognition required flexibility of biomolecules as it aids conformational rearrangements and differential interaction leading to an altered activity [27, 28]. The objective of this thesis is to study the dynamical driven molecular recognition of various macromolecules (lipid, DNA, protein etc) in presence of external milieu.

In this regard, firstly, we have studied the dynamical flexibility and molecular recognition of the lipid bilayer of dioctadecyldimethylammonium bromide (DODAB) at different phases by using picosecond resolved fluorescence spectroscopy. While, hydrophobic dye coumarin 500 (C500) followed the dynamics of lipid bilayer, 8-anilino-1-naphthalenesulfonic acid ammonium salt (ANS) corroborates the hydration dynamics of lipid head group. Förster resonance energy transfer (FRET) between an anti-tuberculosis drug rifampicin and ANS depicts the differential molecular recognition of lipid bilayer at various temperatures. The objective is to rationalize the coupling between structural fluctuation and the dynamics of associated water molecules of DODAB lipids and their effect on molecular recognition. As membrane fluidity is crucial for various cellular functions, at lower temperature plants and cyanobacteria maintained its membrane fluidity by introducing unsaturation to the lipids. In this regard, to understand the effect of unsaturation on membrane fluidity, a unsaturated lipid monoolein has been used. The alteration of structural dynamics and phase behaviour of DODAB due to incorporation of unsaturated lipid monoolein (MO) has been observed by quasi-elastic neutron scattering (QENS) and picosecond resolved fluorescence spectroscopy. Lipid vesicles constituted of cationic lipid DODAB and neutral lipid monoolein are also found to be promising non-viral carriers of nucleic acids. Hence in this regard, we have correlated the structural dynamics of mixed DODAB- MO system with transfection efficiency at different concentration of MO. In another study, we have examined the role of photochromic ligand dihydroindolizine (DHI) on the dynamical modulation of liposome for controlled drug delivery application. Here we have validate that the structural conversion of DHI from closed to open isomer can fluctuate or defect the liposomal membrane by mechanical stress and leads to photoresponsive destabilization of liposome.

The investigation of the surface and interface of a biological macromolecule using a non-covalently bound fluorophore is quite challenging as they found to be displaced to bulk water upon complexation of the biological macromolecules. Hence for this purpose we have synthesized a fluorescent probe (derivative of acedan) namely 6-acetyl-(2-((4-hydroxycyclohexyl)(methyl)amino)naphthalene) (ACYMAN), for the investigation of a biological interface. We have used the noncovalent novel fluorescent dye ACYMAN to probe the H1–SDS interface, especially the structurally ordered water (SOW) and associated environmental dynamics upon structural transition from random coil to α-helix. Subsequently, we have also extended our studies to molecular recognition of the genomic DNA in the condensate with CTAB for potential gene delivery application. Time resolved fluorescence spectroscopy of EB intercalated to DNA clearly indicates some degree of perturbation to the intercalative binding of the genomic DNA in the condensate compared to that in aqueous solution.

The ultrafast hydration dynamics in the close vicinity of biological macromolecules also play a crucial role in the functionalities of the macromolecules. In this regard, we have monitored the role of hydration dynamics on the enzymatic activity of DNase I using polyethylene glycol (PEG) as a crowding agent. The alteration in activity and binding of DNase I towards DNA in presence of molecular crowding was monitored by using time-resolved fluorescence spectroscopic techniques. While the fluorescence transients of EB intercalated to DNA indicates the extent of DNA hydrolysis by enzyme in presence and absence of PEG, FRET from ANS labelled DNase I to EB intercalated to DNA corroborates effective binding between enzyme and DNA in presence of molecular crowding. Finally we have studied molecular recognition and enzyme kinetics of α-chymotrypsin inside reverse micelle using a model microfluidics system equipped with a microscopic and spectroscopic attachment. While, enzyme kinetics of α-chymotrypsin follows conformational selection pathways

inside positive charge reverse micelles, whereas, molecular recognition inside negative charge reverse micelle dictates induced fit mechanisms. The alteration of interaction and dynamics of water molecules inside two oppositely charged reverse micelles as depicted by FTIR and time-resolved fluorescence measurements is found to be responsible for two different pathways of molecular recognition.

1.5. Summary of the Work Done:

1.5.1. Spectroscopic Studies on Dynamics-Driven Molecular Recognition of Biomimetic Systems:

1.5.1.1. Modulation of Solvation and Molecular Recognition of a Lipid Bilayer under Dynamical Phase Transition [29]: The dynamic organization of lipid molecules both across the lipid bilayer and in the lateral dimension are known to be crucial for cellular transport and molecular recognition by important biological macromolecules. Here we study dilute (20 mM) Dioctadecyldimethylammonium bromide (DODAB) vesicles at different temperatures in aqueous dispersion with well-defined phases namely liquid crystalline, gel and subgel. The spectroscopic studies on two fluorescent probes 8-anilino-1-naphthalenesulfonic acid ammonium salt (ANS) and Coumarin 500 (C500), former in the head group region of the lipid-water interface and later located deeper in the lipid bilayer follow dynamics (solvation and fluidity) of their local environments in the vesicles. Binding of an anti-tuberculosis drug rifampicin has also been studied employing Förster resonance energy transfer (FRET) technique. The molecular insight concerning the effect of dynamical organization of the lipid molecules on the local dynamics of aqueous environments in different phases leading to molecular recognition becomes evident in our study.

1.5.1.2. Unravelling the Role of Monoolein in Fluidity and Dynamical Response of a Mixed Cationic Lipid Bilayer [30]: The maintenance of cell membrane fluidity is of critical importance for various cellular functions. At lower temperature when membrane fluidity decreases, plants and cyanobacteria react by introducing unsaturation to the lipids so that the membranes return to a more fluidic state. To probe how introduction of unsaturation leads to reduced membrane fluidity a model cationic lipid Dioctadecyldimethylammonium bromide (DODAB) has been chosen, and the effects of an unsaturated lipid monoolein (MO) on the structural dynamics and phase behaviour of DODAB has been monitored by quasi-elastic neutron scattering (QENS) and time-resolved fluorescence measurements. In the coagel phase fluidity of the lipid bilayer increases significantly in presence of MO relative to pure DODAB vesicles and becomes manifest in significantly enhanced dynamics of the constituent lipids along with faster hydration and orientational relaxation dynamics of a fluorophore. On the contrary, MO restricts both lateral and internal motions of the lipid molecules in the fluid phase (>330K), which is consistent with relatively slow hydration and orientational relaxation dynamics of the fluorophore embedded in mixed lipid bilayer. The present study illustrates how incorporation of an unsaturated lipid at lower temperature (below phase transition) assists the model lipid (DODAB) in regulating fluidity via enhancement of dynamics of the constituent lipids.

1.5.2. Spectroscopic Studies on Photosensitization of a Biomimetic System and its Interaction with Biological Cell Lines:

1.5.2.1. Photo-triggered Destabilization of Nanoscopic Vehicles by Dihydroindolizine for Enhanced Anticancer Drug Delivery in Cervical Carcinoma [31]: The efficacy and toxicity of drugs depend not only on their potency but also on their ability to reach the target sites in preference to non-target sites. In this regards destabilization of delivery vehicles induced by light can be an

effective strategy for enhancing drug delivery with spatial and temporal control. Herein we demonstrate that the photoinduced isomerization from closed (hydrophobic) to open isomeric form (hydrophilic) of a novel DHI encapsulated in liposome leads to potential light-controlled drug delivery vehicles. We have used steady state and picosecond resolved dynamics of a drug 8-anilino-1-naphthalenesulfonic acid ammonium salt (ANS) incorporated in liposome to monitor the efficacy of destabilization of liposome in absence and presence UVA irradiation. Steady state and picosecond resolved polarization gated spectroscopy including the well-known strategy of solvation dynamics and Förster resonance energy transfer; reveal the possible mechanism out of various phenomena involved in destabilization of liposome. We have also investigated the therapeutic efficacy of doxorubicin (DOX) delivery from liposome to cervical cancer cell line HeLa. The FACS, confocal fluorescence microscopic and MTT assay studies reveal an enhanced cellular uptake of DOX leading to significant reduction in cell viability (~40%) of HeLa followed by photoresponsive destabilization of liposome. Our studies successfully demonstrate that these DHI encapsulated liposomes have potential application as a smart photosensitive drug delivery system.

1.5.3. Spectroscopic Studies on a Novel Fluorescence Probe for Interfacial Biomolecular Recognition:

1.5.3.1. A Sensitive Fluorescence Probe for the Polar Solvation Dynamics at Protein- Surfactant Interface [32]: Relaxation dynamics at the surface of biologically important macromolecules is important taking into account of their functionality in molecular recognition. Over the years it has been shown that solvation dynamics of a fluorescence probe at biomolecular sufaces and interfaces account for the relaxation dynamics of polar residues and associated water molecules. However, the sensitivity of the dynamics depends largely on the localization and exposure of the probe. For noncovalent fluorescence probes,

localization at the region of interest in addition to the surface exposure, is an added challenge compared to the covalently attached probes at the biological interfaces. Here we have used a synthesized donor-acceptor type dipolar fluorophore, 6-acetyl-(2-((4-hydroxycyclohexyl) (methyl) amino) naphthalene (ACYMAN) for the investigation of solvation dynamics of a model protein-surfactant interface. A significant structural rearrangement of a model Histone protein (H1) upon interaction with anionic surfactant sodium dodecyl sulphate (SDS) as revealed from the circular dichroism (CD) studies is nicely corroborated in the solvation dynamics of the probe at the interface. The polarization gated fluorescence anisotropy of the probe compared to that at the SDS micellar surface clearly reveals the localization of the probe at the protein-surfactant interface. We have also compared the sensitivity of ACYMAN with other solvation probes including Coumarin 500 (C500) and 4-(dicyanomethylene)-2-methyl-6-(p-dimethylamino-styryl) 4H-pyran (DCM). In comparison to ACYMAN, both C500 and DCM fail to probe the interfacial solvation dynamics of a model protein-surfactant interface. While C500 is found to be delocalized from the protein-surfactant interface, DCM becomes destabilized upon the formation of the interface (protein-surfactant complex).

1.5.4. Spectroscopic Studies on DNA-Surfactant Interaction for a Specific Biological Function:

1.5.4.1. Molecular Recognition of Genomic DNA in a Condensate with a Model Surfactant for Potential Gene-delivery Applications [33]: The functionality of a gene carrying nucleic acid in an artificial gene-delivery system is important for the overall efficiency of the vehicle *in vivo*. Here, we have studied a well-known artificial gene-delivery system, which is a condensate of calf thymus DNA (CT-DNA) with a model cationic surfactant cetyltrimethylammonium bromide (CTAB) to investigate the molecular recognition of the genomic DNA in the condensate.

While dynamic light scattering (DLS) and circular dichroism reveal structural aspects of the condensate and the constituting DNA respectively, picosecond resolved polarization gated spectroscopy and Förster resonance energy transfer (FRET) reveal molecular recognition of the genomic DNA in the condensate. We have considered ethidium bromide (EB) and crystal violet (CV), which are well known DNA-binding agents through intercalative (specific) and electrostatic (non-specific) interactions, respectively, as model ligands for the molecular recognition studies. A fluorescent cationic surfactant, Nonyl Acridine Orange (NAO) is considered to be a mimic of CTAB in the condensate. The excellent spectral overlap of NAO emission and the absorption spectra of both EB and CV allow us to investigate FRET-distances of the ligands with respect to NAO in the condensate at various temperatures and thermal stability of ligand-binding of the genomic DNA. The thermodynamic properties of the molecular recognition have also been explored using Van't Hoff equation. We have also extended our studies to molecular recognition of the genomic DNA in the condensate as dried thin films. This has important implications for its application in bioelectronics.

1.5.5. Spectroscopic Studies on Protein-DNA Interaction in a Physiologically Relevant Environment:

1.5.5.1. Ultrafast Spectroscopy on DNA-Cleavage by Endonuclease in Molecular Crowding [34]: The jam-packed intracellular environments differ the activity of a biological macromolecule from that in laboratory environments (in vitro) through a number of mechanisms called molecular crowding related to structure, function and dynamics of the macromolecule. Here, we have explored the structure, function and dynamics of a model enzyme protein DNase I in molecular crowing of polyethylene glycol (PEG; MW 3350). We have used steady state and picosecond resolved dynamics of a well-known intercalator ethidium bromide (EB) in a 20-mer double-stranded DNA (dsDNA) to monitor the DNA-cleavage by

the enzyme in absence and presence PEG. We have also labelled the enzyme by a well-known fluorescent probe 8-anilino-1-naphthalenesulfonic acid ammonium salt (ANS) to study the molecular mechanism of the protein-DNA association through exited state relaxation of the probe in absence (dictated by polarity) and presence of EB in the DNA (dictated by Förster resonance energy transfer (FRET)). The overall and local structures of the protein in presence of PEG have been followed by circular dichroism and time resolved polarization gated spectroscopy respectively. The enhanced dynamical flexibility of protein in presence of PEG as revealed from excited state lifetime and polarization gated anisotropy of ANS has been correlated with the stronger DNA-binding for the higher nuclease activity. We have also used conventional experimental strategy of agarose gel electrophoresis to monitor DNA-cleavage and found consistent results of enhanced nuclease activities both on synthetic 20-mer oligonucleotide and long genomic DNA from calf thymus.

1.5.6. Spectroscopic Studies on Biomolecular Recognition of an Enzyme in a Model Engineered Environment:

1.5.6.1. Modulation of Kinetic Pathways of Enzyme-Substrate Interaction in a Microfluidic Channel: Nanoscopic Water Dynamics as a Switch [35]: Enzyme mediated catalysis is attributed to enzyme-substrate interactions, with models such as induced fit and conformational selection emphasizing the role of protein conformational transitions. The dynamic nature of the protein structure, thus, plays a crucial role in molecular recognition and substrate binding. As large-scale protein motions are coupled to water motions, hydration dynamics plays a key role in protein dynamics, and hence, enzyme catalysis. Here, we have employed microfluidic techniques and time-dependent fluorescence Stokes shift (TDFSS) measurements to elucidate the role of nanoscopic water dynamics in the interaction of an enzyme, α-Chymotrypsin (CHT) with a substrate, Ala-Ala-Phe-7-

amido-4-methylcoumarin (AMC) in the cationic reverse micelles of benzylhexadecyldimethylammonium chloride (BHDC/benzene) and anionic reverse micelles of sodium bis(2-ethylhexyl)sulfosuccinate (AOT/benzene). While the kinetic pathways unravelled from the microfluidic set-up is consistent with the 'conformational selection' fit for the interaction of CHT with AMC in the cationic reverse micelles, an 'induced fit' mechanism is indicated for the anionic reverse micelles. In the cationic reverse micelles of BHDC, faster hydration dynamics (~550 ps) aids the pathway of 'conformational selection' whereas, in the anionic reverse micelles of AOT significantly slower dynamics of hydration (~1600 ps) facilitates an 'induced fit mechanism for the formation of the final enzyme-substrate complex. The role of water dynamics in dictating the mechanism of enzyme-substrate interaction becomes further manifest in neutral reverse micelles of Brij-30 and Triton X-100. In the former, faster water dynamics aids the 'conformational selection' pathway, whereas significantly slower dynamics of water molecules in the latter becomes conducive to 'induced fit' mechanism in the enzyme-substrate interaction. Thus, nanoscopic water dynamics acts as a switch in modulating the pathway of recognition of an enzyme (CHT) by the substrate (AMC) in reverse micelles.

1.6. Plan of Thesis:

The plan of the thesis is as follows:

Chapter 1: This chapter gives a brief introduction to the scope and motivation behind the thesis work. A brief summary of the work done is also included in this chapter.

Chapter 2: This chapter provides a brief overview of the steady-state and dynamical tools, the structural aspects of biologically important systems (biomimetic, proteins, DNA etc.) and fluorescent probes used in the experiments.

Chapter 3: Details of instrumentation, data analysis and experimental procedures have been discussed in this chapter.

Chapter 4: In this chapter, the coupling between ultrafast dynamics and functionality of DODAB lipids at different phases has been investigated. The effect of monoolein (unsaturated lipid) in modulation of fluidity and dynamics of DODAB lipids have also been elaborated in this chapter.

Chapter 5: Spectroscopic studies on photo-triggered destabilization of nanoscopic vehicles and its interaction with biological cell lines have been addressed in this chapter.

Chapter 6: In this chapter, spectroscopic studies on a novel fluorescence probe for interfacial biomolecular recognition has been investigated.

Chapter 7: Spectroscopic studies on DNA-Surfactant interaction for a specific biological function is elaborated in this chapter.

Chapter 8: In this chapter, the role of hydration dynamics on the enzymatic activity of DNase I in presence of molecular crowding as a physiologically relevant environment has been investigated.

Chapter 9: Spectroscopic studies on biomolecular recognition of an enzyme in a model engineered environment have been addressed in this chapter.

References

[1] M.R. Lockett, H. Lange, B. Breiten, A. Heroux, W. Sherman, D. Rappoport, P.O. Yau, P.W. Snyder, G.M. Whitesides, The binding of benzoarylsulfonamide ligands to human carbonic anhydrase is insensitive to formal fluorination of the ligand, *Angew. Chem. Int. Ed.,* 52 (2013) 7714-7717.

[2] C.G. Kalodimos, N. Biris, A.M. Bonvin, M.M. Levandoski, M. Guennuegues, R. Boelens, R. Kaptein, Structure and flexibility adaptation in nonspecific and specific protein-DNA complexes, *Science,* 305 (2004) 386-389.

[3] A.L. Lehninger, D.L. Nelson, M.M. Cox, M.M. Cox, Lehninger principles of biochemistry, *Macmillan*, 2005.

[4] K. Wollschläger, K. Gaus, A. Körnig, R. Eckel, S.D. Wilking, M. McIntosh, Z. Majer, A. Becker, R. Ros, D. Anselmetti, Single-molecule experiments to elucidate the minimal requirement for DNA recognition by transcription factor epitopes, *Small,* 5 (2009) 484-495.

[5] R. Eckel, S.D. Wilking, A. Becker, N. Sewald, R. Ros, D. Anselmetti, Single-molecule experiments in synthetic biology: An approach to the affinity ranking of DNA-binding peptides, *Angew. Chem. Int. Ed.,* 44 (2005) 3921-3924.

[6] K. Henzler-Wildman, D. Kern, Dynamic personalities of proteins, *Nature,* 450 (2007) 964-972.

[7] S. Dong, J.-M. Liu, Recent progress of multiferroic perovskite manganites, *Mod. Phys. Lett. B,* 26 (2012) 1-26.

[8] K.K. Frederick, M.S. Marlow, K.G. Valentine, A.J. Wand, Conformational entropy in molecular recognition by proteins, *Nature,* 448 (2007) 325-329.

[9] L. Skjærven, N. Reuter, A. Martinez, Dynamics, flexibility and ligand-induced conformational changes in biological macromolecules: a computational approach, *Future Med. Chem.,* 3 (2011) 2079-2100.

[10] Ø. Halskau, R. Perez-Jimenez, B. Ibarra-Molero, J. Underhaug, V. Muñoz, A. Martinez, J.M. Sanchez-Ruiz, Large-scale modulation of thermodynamic protein

folding barriers linked to electrostatics, *Proc. Natl. Acad. Sci. U.S.A.,* 105 (2008) 8625-8630.

[11] S. Choudhury, S. Batabyal, P.K. Mondal, P. Singh, P. Lemmens, S.K. Pal, Direct observation of kinetic pathways of biomolecular recognition, *Chem. Eur. J.,* 21 (2015) 16172-16177.

[12] D. Bagchi, A. Ghosh, P. Singh, S. Dutta, N. Polley, I.I. Althagafi, R.S. Jassas, S.A. Ahmed, S.K. Pal, Allosteric inhibitory molecular recognition of a photochromic dye by a digestive enzyme: Dihydroindolizine makes α-chymotrypsin photo-responsive, *Sci. Rep.,* 6 (2016) 34399.

[13] K. Luby-Phelps, F. Lanni, D. Taylor, The submicroscopic properties of cytoplasm as a determinant of cellular function, *Annu. Rev. Biophys. Biophys. Chem.,* 17 (1988) 369-396.

[14] D. Beece, L. Eisenstein, H. Frauenfelder, D. Good, M. Marden, L. Reinisch, A. Reynolds, L. Sorensen, K. Yue, Solvent viscosity and protein dynamics, *Biochemistry,* 19 (1980) 5147-5157.

[15] H. Frauenfelder, P. Fenimore, B. McMahon, Hydration, slaving and protein function, *Biophys. Chem.,* 98 (2002) 35-48.

[16] G. Caliskan, D. Mechtani, J. Roh, A. Kisliuk, A. Sokolov, S. Azzam, M. Cicerone, S. Lin-Gibson, I. Peral, Protein and solvent dynamics: How strongly are they coupled?, *J. Chem. Phys.,* 121 (2004) 1978-1983.

[17] M. Tarek, D. Tobias, Role of protein-water hydrogen bond dynamics in the protein dynamical transition, *Phys. Rev. Lett.,* 88 (2002) 1-4.

[18] J. Peon, S.K. Pal, A.H. Zewail, Hydration at the surface of the protein Monellin: dynamics with femtosecond resolution, *Proc. Natl. Acad. Sci. U.S.A.,* 99 (2002) 10964-10969.

[19] N. Nandi, B. Bagchi, Dielectric relaxation of biological water, *J. Phys. Chem. B,* 101 (1997) 10954-10961.

[20] D. Andreatta, J.L. Pérez Lustres, S.A. Kovalenko, N.P. Ernsting, C.J. Murphy, R.S. Coleman, M.A. Berg, Power-law solvation dynamics in DNA over six decades in time, *J. Am. Chem. Soc.,* 127 (2005) 7270-7271.

[21] R. Grünberg, M. Nilges, J. Leckner, Flexibility and conformational entropy in protein-protein binding, *Structure,* 14 (2006) 683-693.

[22] E.B. Brauns, M.L. Madaras, R.S. Coleman, C.J. Murphy, M.A. Berg, Complex local dynamics in DNA on the picosecond and nanosecond time scales, *Phys. Rev. Lett.,* 88 (2002) 1-4.

[23] E.B. Brauns, M.L. Madaras, R.S. Coleman, C.J. Murphy, M.A. Berg, Measurement of local DNA reorganization on the picosecond and nanosecond time scales, *J. Am. Chem. Soc.,* 121 (1999) 11644-11649.

[24] M. Akke, NMR methods for characterizing microsecond to millisecond dynamics in recognition and catalysis, *Curr. Opin. Struct. Biol.,* 12 (2002) 642-647.

[25] N. Tjandra, A. Bax, Direct measurement of distances and angles in biomolecules by NMR in a dilute liquid crystalline medium, *Science,* 278 (1997) 1111-1114.

[26] J.N. Silva, A. Oliveira, M. Casal, A. Gomes, P.J. Coutinho, O. Coutinho, M.R. Oliveira, DODAB: Monoolein-based lipoplexes as non-viral vectors for transfection of mammalian cells, *Biochim. Biophys. Acta, Biomembr.,* 1808 (2011) 2440-2449.

[27] J. Lee, M. Natarajan, V.C. Nashine, M. Socolich, T. Vo, W.P. Russ, S.J. Benkovic, R. Ranganathan, Surface sites for engineering allosteric control in proteins, *Science,* 322 (2008) 438-442.

[28] J.-P. Changeux, S.J. Edelstein, Allosteric mechanisms of signal transduction, *Science,* 308 (2005) 1424-1428.

[29] P. Singh, S. Choudhury, V. Sharma, S. Mitra, R. Mukhopadhyay, R. Das, S.K. Pal, Modulation of solvation and molecular recognition of a lipid bilayer under dynamical phase transition, *ChemPhysChem,* 19 (2018) 2709-2716.

[30] P. Singh, V.K. Sharma, S. Singha, V. García-Sakai, R. Mukhopadhyay, R. Das, S.K. Pal, Unravelling the role of monoolein in fluidity and dynamical response of a mixed cationic lipid bilayer, *Langmuir,* 35 (2019) 4682-4692.

[31] P. Singh, S. Choudhury, S. Kulanthaivel, D. Bagchi, I. Banerjee, S.A. Ahmed, S.K. Pal, Photo-triggered destabilization of nanoscopic vehicles by dihydroindolizine for enhanced anticancer drug delivery in cervical carcinoma, *Colloids Surf. B,* 162 (2018) 202-211.

[32] P. Singh, S. Choudhury, S. Singha, Y. Jun, S. Chakraborty, J. Sengupta, R. Das, K.-H. Ahn, S.K. Pal, A sensitive fluorescent probe for the polar solvation dynamics at protein–surfactant interfaces, *Phys. Chem. Chem. Phys.,* 19 (2017) 12237-12245.

[33] P. Singh, S. Choudhury, G.K. Chandra, P. Lemmens, S.K. Pal, Molecular recognition of genomic DNA in a condensate with a model surfactant for potential gene-delivery applications, *J. Photochem. Photobiol. B,* 157 (2016) 105-112.

[34] P. Singh, S. Choudhury, S. Dutta, A. Adhikari, S. Bhattacharya, D. Pal, S.K. Pal, Ultrafast spectroscopy on DNA-cleavage by endonuclease in molecular crowding, *Int. J. Biol. Macromol.,* 103 (2017) 395-402.

[35] P. Singh, D. Mukherjee, S. Singha, R. Das, S.K. Pal, Modulation of kinetic pathways of enzyme-substrate interaction in a microfluidic channel: Nanoscopic water dynamics as a switch, *Chem. Eur. J.,* (2019) doi: 10.1002/chem.201901751.

Chapter 2

An Overview of Experimental Techniques and Systems

In order to investigate the ultrafast processes involved in the course of study on structure, function and dynamics of biomolecules, different steady-state and dynamical tools have been employed. These include solvation dynamics, fluorescence anisotropy, Förster resonance energy transfer (FRET), determination of activation energy barrier using Arrhenius theory, diffusion studies, and circular dichroism (CD). In this chapter, brief discussions about these tools and an overview of various systems used in our studies have been provided.

2.1. Steady-State and Dynamical Tools:

2.1.1. Solvation Dynamics:

2.1.1.1. Theory: Solvation dynamics refer to the process of reorganization of solvent dipoles around a dipole created instantaneously or an electron/proton injected suddenly in a polar liquid. In order to understand the meaning and scope of solvation dynamics, let us first visualize the physical essence of the dynamical process involved for a solute molecule in a polar solvent [1]. A change in the probe (solute) is made at time t=0, by an excitation pulse, which leads to the creation of a dipole. This dipole gives rise to an instantaneous electric field on the solvent molecules. The interaction of permanent dipoles of the solvent with the instantaneously created electric field, shifts the free energy minimum of the solvent to a non-zero value of the polarization. The solvent motion is crucial (Figure 2.1). Since the probe is excited instantaneously (a Franck-Condon transition as far as the nuclear degrees of freedom are concerned), the solvent

molecules at t=0 find themselves in a relatively high-energy configuration. Subsequently, the solvent molecules begin to move and rearrange themselves to reach their new equilibrium positions (Figure 2.2). The nuclear motion involved can be broadly classified into rotational and translational motions.

When the solvent is bulk water, rotational motion would also include hindered rotation and libration, while translation would include the intermolecular vibration due to the extensive hydrogen bonding. The two specific motions, libration and intermolecular vibration, are relatively high in frequency and are expected to play a dominant role in the initial part of solvation [2]. The molecular motions involved are shown schematically in

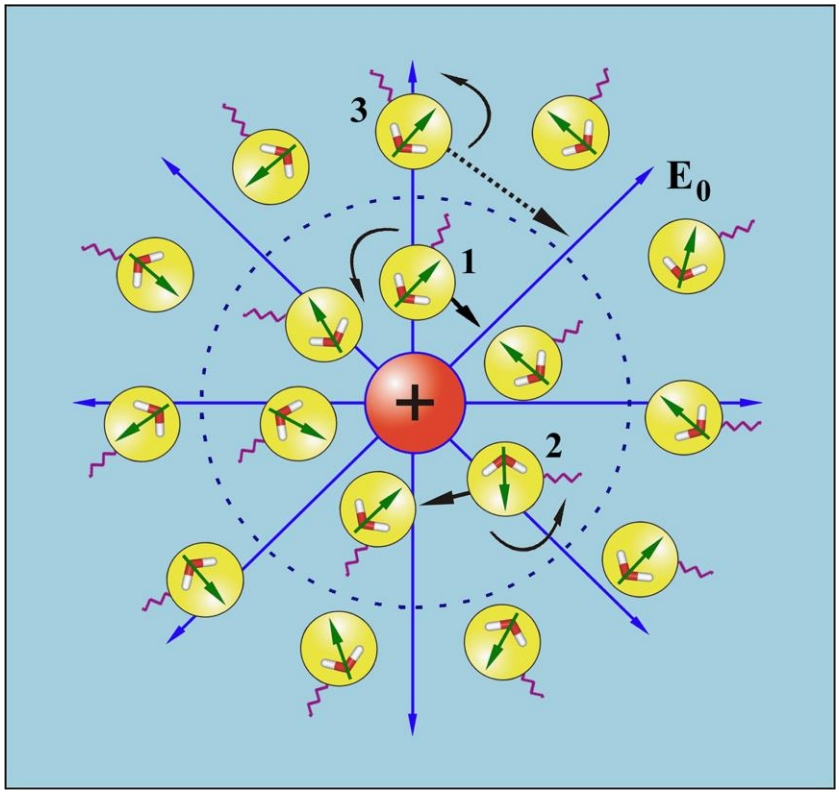

Figure 2.1. *Schematic illustration of solvation of an ion (or dipole) by water. The neighboring molecules (numbered 1 and 2) can either rotate or translate to attain the minimum energy configuration. On the other hand, distant water molecule 3 can only rotate to attain minimum energy configuration. The field is shown as* E_0*. The springs connected to the molecules are meant to denote hydrogen bonding.*

Figure 2.1, and in Figure 2.3 a typical solvation time correlation function is depicted. For clarity, we approximate the motions responsible for the decay in different regions.

A simple way to address the dynamics of polar solvation is to start with the following expression for the solvation energy, $E_{solv}(t)$ [3],

$$E_{solv}(t) = -\frac{1}{2}\int dr\, E_0(r)\cdot P(r,t) \tag{2.1}$$

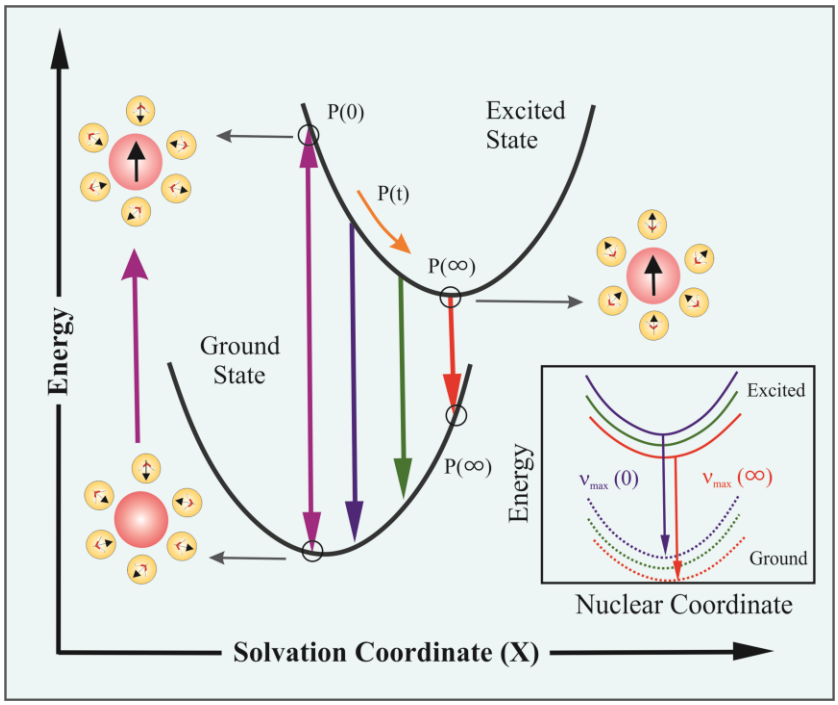

Figure 2.2. *Schematic representation of the potential energy surfaces involved in solvation dynamics showing the water orientational motions along the solvation coordinate together with instantaneous polarization P. In the inset we show the change in the potential energy along the intramolecular nuclear coordinate. As solvation proceeds the energy of the solute comes down giving rise to a red shift in the fluorescence spectrum. Note the instantaneous P, e.g., P(∞), on the two connected potentials.*

where $E_0(r)$ is the instantaneously created, position-dependent electric field from the ion or the dipole of the solute and $P(r,t)$ is the position and time-dependent polarization.

The latter is defined by the following expression,

$$P(r,t) = \int d\Omega\ \mu(\Omega)\ \rho\ (r,\Omega,t) \tag{2.2}$$

where $\mu(\Omega)$ is the dipole moment vector of a molecule at position r, and $\rho\ (r,\Omega,t)$ is the position, orientation and time-dependent density. Therefore, the time dependence of the solvation energy is determined by the time dependence of polarization that is in turn determined by the time dependence of the density. If the perturbation due to the probe on dynamics of bulk water is negligible, then the time dependence of polarization is dictated by the natural dynamics of the liquid. The theoretical analysis of the time-dependent density is usually carried out using a molecular hydrodynamic approach that is based on the basic conservation (density, momentum and energy) laws and includes the effects of intermolecular (both spatial and orientational) correlations. The latter provides the free energy surface on which solvation proceeds. The equation of motion of the density involves both orientational and translational motions of the solvent molecules.

The details of the theoretical development are reported in literature [1], here we shall present a simple physical picture of the observed biphasic solvation dynamics. Within linear response theory, the solvation correlation function is directly related to the solvation energy as,

$$C(t) = \frac{\langle \delta E(0) \cdot \delta E(t) \rangle}{\langle \delta E^2 \rangle} = \frac{\langle E(t) \rangle - \langle E(\infty) \rangle}{\langle E(0) \rangle - \langle E(\infty) \rangle} \tag{2.3}$$

where δE is the fluctuation of solvation energy from the average, equilibrium value. Note that the equality in equation (2.3) indicates the direct relation for the average of the fluctuations over the equilibrium distribution (left) and the non-equilibrium function (right) which relates to observables; without $\langle E(\infty) \rangle$ the correspondence is clear, and $\langle E(\infty) \rangle$ is rigorously the result of the equilibrium term in the numerator and for normalization in the denominator.

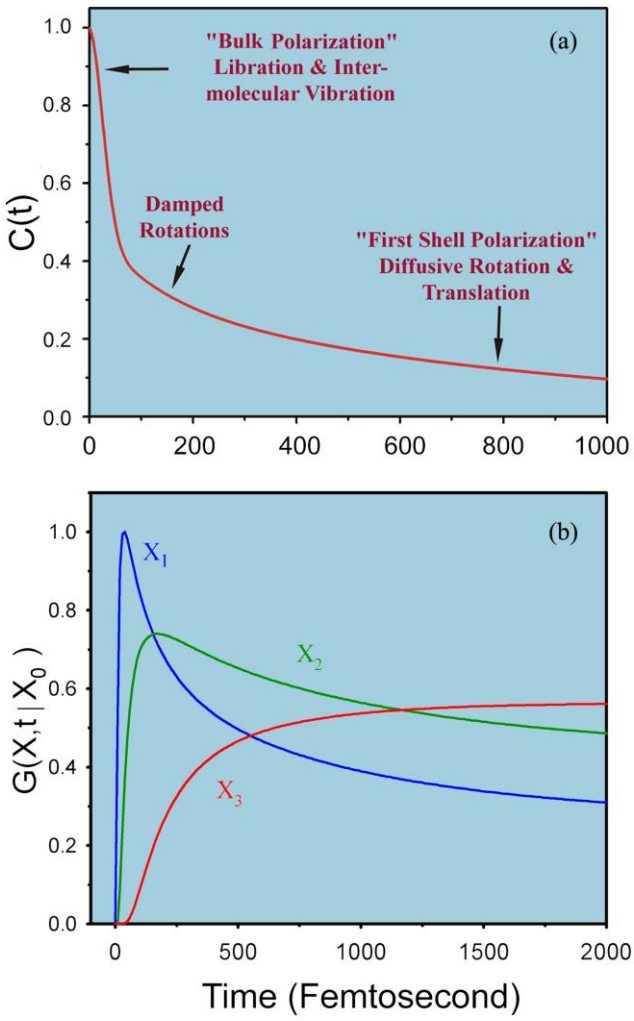

Figure 2.3. *(a) A typical solvation time correlation function for water is shown here. The time correlation function exhibits three distinct regions: The initial ultrafast decay, an intermediate decay of about 200 fs and the last slow decay with time constant of 1 ps. The physical origin of each region is indicated on the plot itself; see text. (b) Green's function G(X, t | X₀) for population relaxation along the solvation coordinate (X) is plotted against time in femtosecond. In G, X₀ is the initial position at t = 0. This Figure shows the position and time dependence of the population fluorescence intensity. At early times (when the population is at X₁) there is ultrafast rise followed by an ultrafast decay. At intermediate times (when the population is at X₂) there is a rise followed by a slow decay as shown by the green line. At long times when the population is nearly relaxed (position X₃, red line) we see only a rise.*

The ultrafast component in the solvation time correlation function (see Figure 2.3.a), originates from the initial relaxation in the steep collective solvation potential. The collective potential is steep because it involves the total polarization of the system [1, 4]. This initial relaxation couples mainly to the hindered rotation (i.e., libration) and the hindered translation (i.e., the intermolecular vibration),

which are the available high frequency modes of the solvent; neither long amplitude rotation nor molecular translation are relevant here. The last part in the decay of the solvation correlation function involves larger amplitude rotational and translational motions of the nearest neighbor molecules in the first solvation shell. In the intermediate time, one gets contributions from the moderately damped rotational motions of water molecules. In a sense, with the above description one recovers the famous Onsager's "inverse snow-ball" picture of solvation [5]. The slowest time constant is ~1 ps, which is determined by the individual rotational and translational motions of the molecules in the "first solvation shell" nearly close to the probe. The femtosecond component is dominated by the high frequency hindered rotational and translational (vibration) polarization [6].

Figure 2.2 shows a schematic of the solvation potential and the orientational motions for the water molecules involved. From the shape of the potential, it can be seen that the transient behavior for the population during solvation should be a decay function on the blue edge of the spectrum and a rise function on the red edge. These wavelength-dependent features can be explained nicely within a generalized model of relaxation in which a Gaussian wave packet relaxes on a harmonic surface. The relaxation is non-exponential and a Green's function can describe the approach of the wave packet along the solvation coordinate, X, to its equilibrium value. For the general non-Markovian case it is given by [7],

$$G(X,t|X_0) = \frac{1}{\sqrt{2\pi\langle X^2\rangle[1-C^2(t)]}} \exp\left[-\frac{[X - X_0C(t)]^2}{2\langle X^2\rangle[1-C^2(t)]}\right] \qquad (2.4)$$

where $\langle X^2\rangle$ is the equilibrium mean square fluctuation of the polarization coordinate in the excited state surface, *C(t)* is the solvation correlation function described in equation (2.3) and X_0 is the initial value of the packet on the solvation coordinate. Equation (2.4) describes the motion of the wave packet (polarization density) beginning at $t = 0$ (X_0) as a delta function and according to the solvation

time correlation function. As $t \rightarrow \infty$, $C(t) \rightarrow 0$ and we recover the standard Gaussian distribution. Initially, ($t \rightarrow 0$), the exponential is large, so the decay is ultrafast, but at long times, the relaxation slows down, ultimately to appear as a rise. In Figure 2.3.b, we present calculations of $G(X, t \mid X_0)$ at different positions along the solvation coordinate giving decays at X_1 and X_2, but with different time constants, and a rise at X_3, as demonstrated experimentally.

2.1.1.2. Experimental Methods: In order to study solvation stabilization of a probe in an environment, a number of fluorescence transients are taken at different wavelengths across the emission spectrum of the probe. As described earlier, blue and red ends of the emission spectrum are expected to show decay and rise, respectively in the transients. The observed fluorescence transients are fitted by using a nonlinear least square fitting procedure to a function,

$$\left(X(t) = \int_0^t E(t')R(t-t')dt' \right) \tag{2.5}$$

comprising of convolution of the instrument response function (IRF) ($E(t)$) with a sum of exponentials,

$$\left(R(t) = A + \sum_{i=1}^{N} B_i \exp\left(-t/\tau_i\right) \right) \tag{2.6}$$

with pre-exponential factors (B_i), characteristic lifetimes (τ_i) and a background (A). Relative concentration in a multiexponential decay is finally expressed as;

$$\alpha_n = \frac{B_n}{\sum_{i=1}^{N} B_i} \tag{2.7}$$

The relative contribution of a particular decay component (f_n) in the total fluorescence is defined as,

$$f_n = \frac{\tau_n B_n}{\sum_{i=1}^{N} B_i \tau_i} \times 100. \tag{2.8}$$

The quality of the curve fitting is evaluated by reduced chi-square (0.9-1.1) and residual data. The purpose of the fitting is to obtain the decays in an analytical form suitable for further data analysis.

To construct time resolved emission spectra (TRES) we follow the technique described in references [8]. As described above, the emission intensity decays are analyzed in terms of the multiexponential model,

$$I(\lambda,t) = \sum_{i=1}^{N} \alpha_i(\lambda) \exp\left(-t/\tau_i(\lambda)\right) \tag{2.9}$$

where $\alpha_i(\lambda)$ are the pre-exponential factors, with $\Sigma\alpha_i(\lambda)$ = 1.0. In this analysis we compute a new set of intensity decays, which are normalized so that the time-integrated intensity at each wavelength is equal to the steady-state intensity at that wavelength. Considering $F(\lambda)$ to be the steady-state emission spectrum, we calculate a set of $H(\lambda)$ values using,

$$H(\lambda) = \frac{F(\lambda)}{\int_0^\infty I(\lambda,t)dt} \tag{2.10}$$

which for multiexponential analysis becomes,

$$\mathrm{H}(\lambda) = \frac{\mathrm{F}(\lambda)}{\sum_i \alpha_i(\lambda)\tau_i(\lambda)} \tag{2.11}$$

Then, the appropriately normalized intensity decay functions are given by,

$$I'(\lambda,t) = H(\lambda)I(\lambda,t) = \sum_{i=1}^{N} \alpha_i'(\lambda) \exp\left(-t/\tau_i(\lambda)\right) \tag{2.12}$$

where $\alpha'_i(\lambda) = H(\lambda)\alpha_i(\lambda)$. The values of $I'(\lambda,t)$ are used to calculate the intensity at any wavelength and time, and thus the TRES. The values of the emission maxima and spectral width are determined by nonlinear least-square fitting of the spectral shape of the TRES. The spectral shape is assumed to follow a lognormal line shape [8, 9],

$$I(\bar{\nu}) = I_0 \exp\left\{-\left[\ln 2\left(\frac{\ln(\alpha+1)}{b}\right)^2\right]\right\} \quad (2.13)$$

with α = [2b($\bar{\nu}$- $\bar{\nu}_{max}$)]/Δ, where I_0 is amplitude, $\bar{\nu}_{max}$ is the wavenumber of the emission maximum and spectral width is given by, Γ=Δ(sinh(b)/b). The terms *b* and *Δ* are asymmetry and width parameters, respectively and equation (2.9) reduces to a Gaussian function for *b*=0.

The time-dependent fluorescence Stokes shifts, as estimated from TRES are used to construct the normalized spectral shift correlation function or the solvent correlation function *C(t)* and is defined as,

$$C(t) = \frac{\bar{\nu}(t) - \bar{\nu}(\infty)}{\bar{\nu}(0) - \bar{\nu}(\infty)} \quad (2.14)$$

where, $\bar{\nu}(0)$, $\bar{\nu}(t)$ and $\bar{\nu}(\infty)$ are the emission maxima (in cm^{-1}) of the TRES at time zero, *t* and infinity, respectively. The $\bar{\nu}(\infty)$ value is considered to be the emission frequency beyond which insignificant or no spectral shift is observed. The *C(t)* function represents the temporal response of the solvent relaxation process, as occurs around the probe following its photoexcitation and the associated change in the dipole moment.

In order to further investigate possible heterogeneity in the positional distribution of fluoroprobes at the interfaces of biomimicking self-assemblies we follow time-resolved area normalized emission spectroscopy (TRANES), which is a well-established technique [10] and is a modified version of TRES. TRANES were constructed by normalizing the area of each spectrum in TRES such that the area of the spectrum at time *t* is equal to the area of the spectrum at *t* = 0. A useful feature of this method is the presence of an isoemissive point in the spectra involves emission from two species, which are kinetically coupled either irreversibly or reversibly or not coupled at all.

2.1.2. Fluorescence Anisotropy: Anisotropy is defined as the extent of polarization of the emission from a fluorophore. Anisotropy measurements are commonly used in biochemical applications of fluorescence. It provides information about the size and shape of proteins or the rigidity of various molecular environments. Anisotropy measurements have also been used to measure protein-protein associations, fluidity of membranes and for immunoassays of numerous substances. These measurements are based on the principle of photoselective excitation of those fluorophore molecules whose absorption transition dipoles are parallel to the electric vector of polarized excitation light. In an isotropic solution, fluorophores are oriented randomly. However, upon selective excitation, partially oriented population of fluorophores with polarized fluorescence emission results. The relative angle between the absorption and emission transition dipole moments determines the maximum measured anisotropy (r_0). The fluorescence anisotropy (r) and polarization (P) are defined by,

$$r = \frac{I_{II} - I_{\perp}}{I_{II} + 2I_{\perp}} \tag{2.15}$$

$$P = \frac{I_{II} - I_{\perp}}{I_{II} + I_{\perp}} \tag{2.16}$$

where the fluorescence intensities of vertically and horizontally polarized emission when the fluorophore is excited with vertically polarized light. Polarization and anisotropy are interrelated as,

$$r = \frac{2P}{3 - P} \tag{2.17}$$

$$P = \frac{3r}{2 + r} \tag{2.18}$$

Although polarization and anisotropy provides the same information, anisotropy is preferred since the latter is normalized by total fluorescence intensity ($I_T = I_{II} + 2I_{\perp}$) and in case of multiple emissive species anisotropy is additive while polarization is not. Several phenomena, including rotational diffusion and energy transfer, can decrease the measured anisotropy to values lower than

maximum theoretical values. Following a pulsed excitation the fluorescence anisotropy, *r(t)* of a sphere is given by,

$$r(t) = r_0 \exp(-t/\tau_{rot}) \tag{2.19}$$

where r_0 is the anisotropy at time $t = 0$ and τ_{rot} is the rotational correlation time of the sphere.

2.1.2.1. Theory: For a radiating dipole the intensity of light emitted is proportional to the square of the projection of the electric field of the radiating dipole onto the transmission axis of the polarizer. The intensity of parallel and perpendicular projections are given by,

$$I_{II}(\theta,\psi) = \cos^2\theta \tag{2.20}$$

$$I_{\perp}(\theta,\psi) = \sin^2\theta \sin^2\psi \tag{2.21}$$

where θ and ψ are the orientational angles of a single fluorophore relative to the z and y-axis, respectively (Figure 2.4.a). In solution, fluorophores remain in random distribution and the anisotropy is calculated by excitation photoselection. Upon photoexcitation by polarized light, the molecules having absorption transition moments aligned parallel to the electric vector of the polarized light have the highest probability of absorption. For the excitation polarization along z-axis, all molecules having an angle ψ with respect to the y-axis will be excited. The population will be symmetrically distributed about the z-axis. For experimentally accessible molecules, the value of ψ will be in the range from 0 to 2π with equal probability. Thus, the ψ dependency can be eliminated.

$$\left\langle \sin^2\psi \right\rangle = \frac{\int_0^{2\pi} \sin^2\psi \, d\psi}{\int_0^{2\pi} d\psi} = \frac{1}{2} \tag{2.22}$$

$$\text{and } I_{II}(\theta) = \cos^2\theta \tag{2.23}$$

$$I_{\perp}(\theta) = \frac{1}{2}\sin^2\theta \tag{2.24}$$

Consider a collection of molecules oriented relative to the z-axis with probability *f(θ)*. Then, measured fluorescence intensities for this collection after photoexcitation are,

$$I_{II} = \int_0^{\pi/2} f(\theta)\cos^2\theta d\theta = k\left\langle \cos^2\theta \right\rangle \tag{2.25}$$

$$\mathrm{I}_{\perp} = \frac{1}{2}\int_0^{\pi/2} f(\theta)\ \sin^2\theta d\theta = \frac{k}{2}\left\langle \sin^2\theta \right\rangle \tag{2.26}$$

where $f(\theta)d\theta$ is the probability that a fluorophore is oriented between θ and $\theta + d\theta$ and is given by,

$$f(\theta)d\theta = \cos^2\theta \sin\theta d\theta \tag{2.27}$$

k is the instrumental constant. Thus, the anisotropy (*r*) is defined as,

$$r = \frac{3\left\langle \cos^2\theta \right\rangle - 1}{2} \tag{2.28}$$

when $\theta = 54.7^0$ i.e. when $cos^2\theta = 1/3$, the complete loss of anisotropy occurs. Thus, the fluorescence taken at $\theta = 54.7^0$ with respect to the excitation polarization is expected to be free from the effect of anisotropy and is known as magic angle emission. For collinear absorption and emission dipoles, the value of $\langle cos^2\theta \rangle$ is given by the following equation,

$$\left\langle \cos^2\theta \right\rangle = \frac{\int_0^{\pi/2} \cos^2\theta f(\theta) d\theta}{\int_0^{\pi/2} f(\theta) d\theta} \tag{2.29}$$

Substituting equation (2.27) in equation (2.29) one can get the value of $\langle cos^2\theta \rangle$ = 3/5 and anisotropy value to be 0.4 (from equation (2.28)). This is the maximum value of anisotropy obtained when the absorption and emission dipoles are collinear and when no other depolarization process takes place. However, for most fluorophore, the value of anisotropy is less than 0.4 and it is dependent on the excitation wavelength. It is demonstrated that as the displacement of the

absorption and emission dipole occurs by an angle γ relative to each other, it causes further loss of anisotropy (reduction by a factor 2/5) [11] from the value obtained from equation (2.28). Thus, the value of fundamental anisotropy, r_0 is given by,

$$r_0 = \frac{2}{5}\left(\frac{3\cos^2\gamma - 1}{2}\right) \tag{2.30}$$

For any fluorophore randomly distributed in solution, with one-photon excitation, the value of r_0 varies from -0.20 to 0.40 for γ values varying from 90^0 to 0^0.

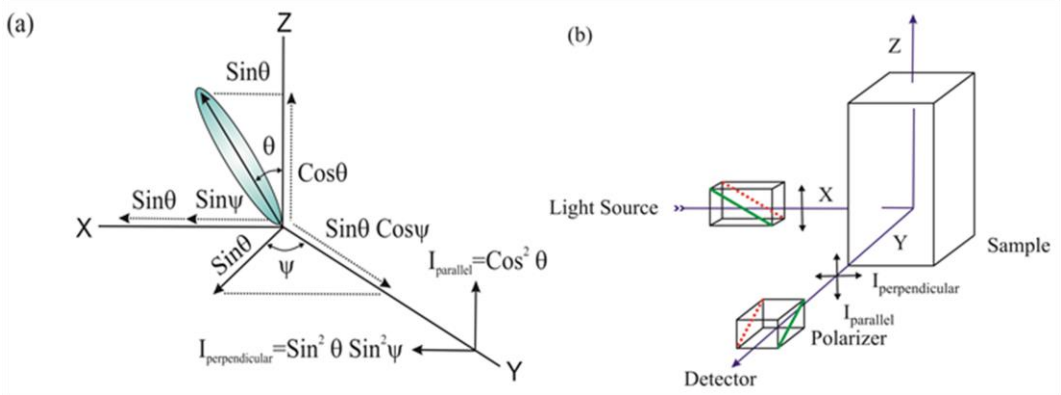

Figure 2.4. *(a) Emission intensity of a single fluorophore (blue ellipsoid) in a coordinate system. (b) Schematic representation of the measurement of fluorescence anisotropy.*

2.1.2.2. Experimental Methods: For time resolved anisotropy (*r(t)*) measurements (Figure 2.4.b), emission polarization is adjusted to be parallel and perpendicular to that of the excitation polarization. Spencer and Weber [12] have derived the relevant equations for the time dependence of $I_{II}(t)$ (equation (2.31)) and $I_{\perp}(t)$ (equation (2.32)) for single rotational and fluorescence relaxation times, τ_{rot} and τ_f, respectively,

$$I_{II}(t) = \exp\left(-t/\tau_f\right)\left(1 + 2r_0\exp\left(-t/\tau_{rot}\right)\right) \tag{2.31}$$

$$I_{\perp}(t) = \exp\left(-t/\tau_f\right)\left(1 - r_0\exp\left(-t/\tau_{rot}\right)\right) \tag{2.32}$$

The total fluorescence is given by,

$$F(t) = I_{II}(t) + 2I_{\perp}(t) = 3\exp\left(-t/\tau_f\right) = F_0\exp\left(-t/\tau_f\right) \tag{2.33}$$

The time dependent anisotropy, *r(t)* is given by,

$$r(t) = \frac{I_{II}(t) - I_{\perp}(t)}{I_{II}(t) + 2I_{\perp}(t)} = r_0 \exp(-t/\tau_{rot}) \tag{2.34}$$

F(t) depends upon τ_f and *r(t)* depends upon τ_{rot} so that these two lifetimes can be separated. This separation is not possible in steady-state measurements. It should be noted that the degree of polarization (*P*) is not independent of τ_f and is therefore not as useful quantity as *r*. For reliable measurement of *r(t)*, three limiting cases can be considered.

(a) If $\tau_f < \tau_{rot}$, the fluorescence decays before the anisotropy decays, and hence only r_0 can be measured.

(b) If $\tau_{rot} < \tau_f$, in contrast to steady-state measurements, τ_{rot} can be measured in principle. The equations (2.31) and (2.32) show that the decay of the parallel and perpendicular components depends only upon τ_{rot}. The only experimental disadvantage of this case is that those photons emitted after the period of a few times τ_{rot} cannot contribute to the determination of τ_{rot}, but provided the signal-to-noise ratio is favorable, this need not be of great concern.

(c) If $\tau_{rot} \approx \tau_f$, then it becomes the ideal situation since almost all photons are counted within the time (equal to several rotational relaxation times) in which *r(t)* shows measurable changes.

For systems with multiple rotational correlation times, *r(t)* is given by,

$$r(t) = r_0 \sum_i \beta_i e^{-t/\tau_i} \tag{2.35}$$

where $\sum_i \beta_i = 1$ It should be noted that the instrument monitoring the fluorescence, particularly the spectral dispersion element, responds differently to different polarizations of light, thus emerging the need for a correction factor. For example, the use of diffraction gratings can yield intensities of emission, which depend strongly upon orientation with respect to the plane of the grating. It is

inevitably necessary when using such instruments to correct for the anisotropy in response. This instrumental anisotropy is usually termed as G-factor (grating factor) and is defined as the ratio of the transmission efficiency for vertically polarized light to that for horizontally polarized light ($G = I_{II} + I_{\perp}$). Hence, values of fluorescence anisotropy, *r(t)* corrected for instrumental response, would be given by [13],

$$r(t) = \frac{I_{II}(t) - GI_{\perp}(t)}{I_{II}(t) + 2GI_{\perp}(t)} \tag{2.36}$$

The G-factor at a given wavelength can be determined by exciting the sample with horizontally polarized excitation beam and collecting the two polarized fluorescence decays, one parallel and other perpendicular to the horizontally polarized excitation beam. G-factor can also be determined following longtime tail matching technique [14]. If $\tau_{rot} < \tau_f$, it can be seen that the curves for $I_{II}(t)$ and $I_{\perp}(t)$ should become identical. If in any experiment they are not, it can usually be assumed that this is due to a nonunitary G-factor. Hence normalizing the two decay curves on the tail of the decay eliminates the G-factor in the anisotropy measurement.

2.1.3. Estimation of Microviscosity from Stokes-Einstein-Debye Equation: The interfacial microviscosity, η_m as experienced by probe molecule in the biological/biomimicking systems like protein cavities, reverse micelle/micelle, can be estimated from the time-resolved fluorescence anisotropy using the modified Stokes-Einstein-Debye equation (SED) [13, 14],

$$\tau_r = \frac{\eta_m V_h}{k_B T} \tag{2.37}$$

where k_B is the Boltzmann constant, T is the absolute temperature. Hydrodynamic volume of the probe (V_h) can be calculated as:

$$V_h = V_m fC \tag{2.38}$$

where f is the shape factor (f = 1 for a spherical probe) and C represents solute-solvent coupling constant (C = 1 for "stick" condition and C < 1 for "slip" condition) and V_m is the molecular volume of the probe [15]. In case of f = C = 1, equation (2.37) reduces to the original simple SED equation,

$$\tau_r = \frac{\eta_m V_m}{k_B T} \tag{2.39}$$

For probe molecules with prolate ellipsoid shape, the value of f is calculated using the equation [13, 14],

$$f = \frac{2}{3} \frac{1-p^4}{[(2-p^2)p^2(1-p^2)^{-1/2} \ln \frac{1+(1-p^2)^{1/2}}{p}] - p^2} \tag{2.40}$$

where p is the axial ratio (ratio of minor axis to major axis) of the prolate ellipsoid. The energy barrier, E_η for the viscous flow is estimated according to the relation [16],

$$\eta_m = \eta_0 \exp(\frac{E_\eta}{RT}) \tag{2.41}$$

2.1.4. Arrhenius Theory of Activation Energy: The dynamics of solvation at a biomolecular interface can be exploited to give information about the energetics of the participating water molecules [3]. Water present at the surface of biomolecules or biomimetic can broadly be distinguished as bound type (water hydrogen bonded to the interface, BW) and free type water (FW). In the water layer around the surface, the interaction with water involves hydrogen bonding to the polar and charged groups of the surface. When strongly bonded to the biomacromolecules or biomimicking surfaces, the water molecules cannot contribute to solvation dynamics because they can neither rotate nor translate. However, hydrogen bonding is transient and there exists a dynamic equilibrium between the free and the bound water molecules. The potential of the interaction can be represented by a double-well structure to symbolize the processes of bond breaking and bond forming. In general, the bonded water molecules become free by translational and

rotational motions. The equilibrium between bound and free water can be written as [16],

$$(\text{water})_{\text{free state}} \leftrightarrow (\text{water})_{\text{bound state}} \tag{2.42}$$

Using the dynamic exchange model, an expression for this equilibrium can be derived. In a coupled diffusion-reaction equation the rate constant $k_{\pm}$ can be written as,

$$k_{\pm} = 0.5[-B \pm (B^2 - 4D_R k_{bf})^{1/2}] \tag{2.43}$$

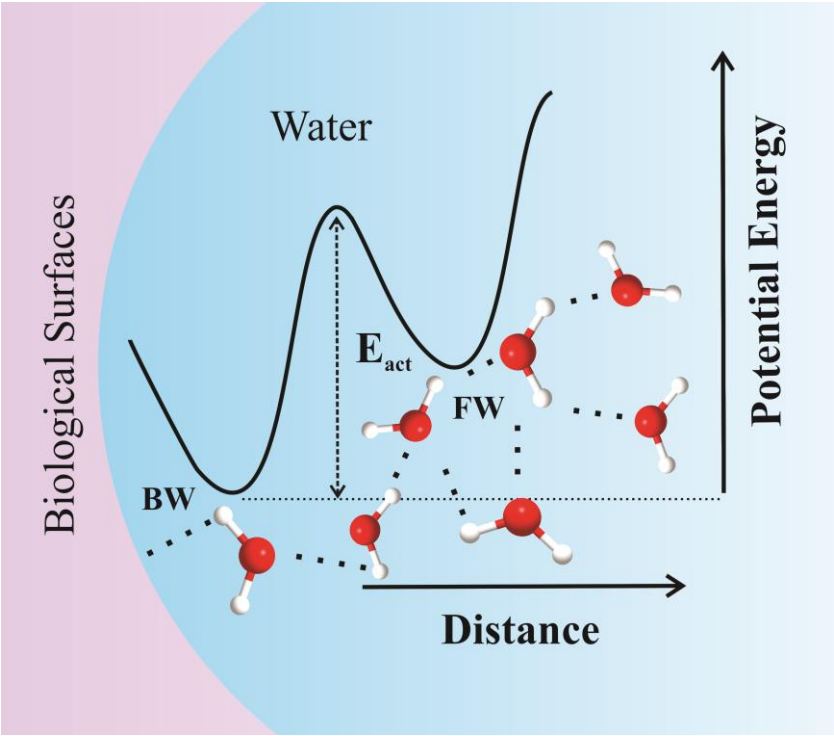

***Figure* 2.5.** *Schematic representation of different types of water molecules (BW and FW) present at various bimolecular interfaces and the corresponding activation energy barrier.*

where $B = 2D_R + k_{bf} + k_{fb}$ and D_R is the rotational diffusion constant, k_{bf} is the rate constant of the bound to free transition and k_{fb} is that of the reverse process. Typically, the rate constant of free to bound reaction, is larger than that for the reverse process. It can be shown that, when the rates of interconversion between "bound" and "free" water molecules are small as compared to $2D_R$, then,

$$\tau_{slow} \approx k_{bf}^{-1} \tag{2.44}$$

and from the activated complex theory one can have,

$$k_{bf} = (k_B T / h) \exp(-\Delta G^0 / RT) \tag{2.45}$$

If the transition process (equation (2.42)) follows a typical Arrhenius type of energy barrier crossing model, one can write,

$$\tau_{slow}^{-1} \approx k_{bf} = A \exp(-E_{act} / RT) \tag{2.46}$$

where 'E_{act}' is the activation energy for the transition process and 'A' is the pre-exponential factor. A plot of $ln(1/\tau_{slow})$ against $1/T$ produces a straight line and from the slope of the line E_{act} can be calculated. The temperature dependence of the solvation follows the Arrhenius equation and yields the activation energy needed for the conversion of bound and free forms [17].

2.1.5. Förster Resonance Energy Transfer (FRET): FRET is an electrodynamic phenomenon involving the nonradiative transfer of the excited state energy from the donor dipole (D) to an acceptor dipole (A) in the ground state (Figure 2.6.a). FRET has got wide applications in all fluorescence applications including medical diagnostics, DNA analysis and optical imaging. Since FRET can measure the size of a protein molecule or the thickness of a membrane, it is also known as 'spectroscopic ruler' [18]. FRET is very often used to measure the distance between two sites on a macromolecule [19]. Basically, FRET is of two types: (i) homo-molecular FRET and (ii) hetero-molecular FRET. In the former case the same fluorophore acts both as energy donor and acceptor, while in the latter case two different molecules act as donor and acceptor.

Each donor-acceptor (D-A) pair participating in FRET is characterized by a distance known as Förster distance (R_0) i.e., the D-A separation at which energy transfer is 50% efficient. The R_0 value ranges from 20 to 60 Å. The rate of resonance energy transfer (k_T) from donor to an acceptor is given by [20],

$$k_T = \frac{1}{\tau_D}\left(\frac{R_0}{r}\right)^6 \tag{2.47}$$

where τ_D is the lifetime of the donor in the absence of acceptor and r is the donor to acceptor (D-A) distance. The rate of transfer of donor energy depends upon the

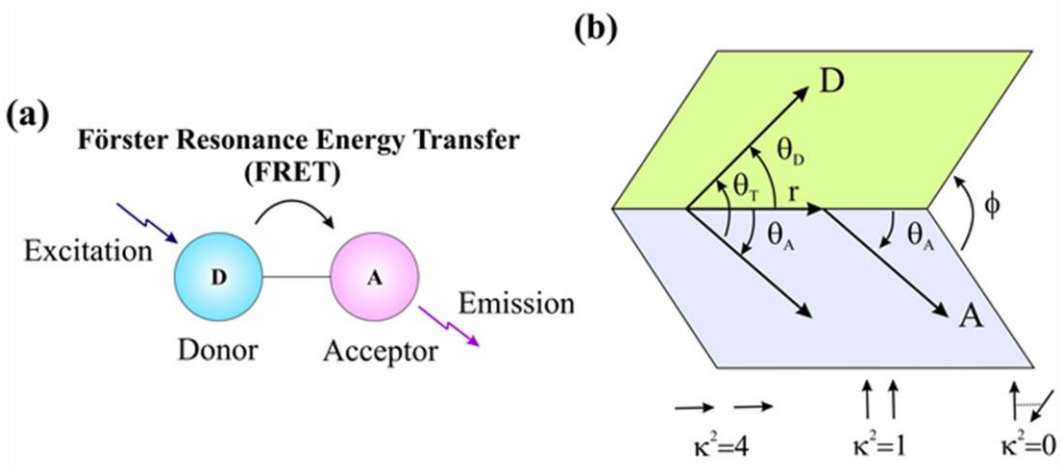

Figure 2.6. *(a) Schematic illustration of the FRET process. (b) Dependence of the orientation factor κ^2 on the directions of the emission and absorption dipoles of the donor and acceptor, respectively.*

extent of overlap of the emission spectrum of the donor with the absorption spectrum of the acceptor ($J(\lambda)$), the quantum yield of the donor (Q_D), the relative orientation of the donor and acceptor transition dipoles (κ^2) and the distance between the donor and acceptor molecules (r) (Figure 2.6.b). In order to estimate FRET efficiency of the donor and hence to determine distances between donor-acceptor pairs, the methodology described below is followed [21]. R_0 is given by,

$$R_0 = 0.211\left[\kappa^2 n^{-4} Q_D J(\lambda)\right]^{1/6} \text{ (in Å)} \tag{2.48}$$

where n is the refractive index of the medium, Q_D is the quantum yield of the donor and $J(\lambda)$ is the overlap integral. κ^2 is defined as,

$$\kappa^2 = \left(\cos\theta_T - 3\cos\theta_D \cos\theta_A\right)^2 = \left(\sin\theta_D \sin\theta_A \cos\varphi - 2\cos\theta_D \cos\theta_A\right)^2 \tag{2.49}$$

where θ_T is the angle between the emission transition dipole of the donor and the absorption transition dipole of the acceptor, θ_D and θ_A are the angles between these dipoles and the vector joining the donor and acceptor and φ is angle between the planes of the donor and acceptor (Figure 2.6.b). κ^2 value can vary from 0 to 4. For collinear and parallel transition dipoles, $\kappa^2 = 4$; for parallel dipoles, $\kappa^2 = 1$; and

for perpendicularly oriented dipoles, $\kappa^2 = 0$. For donor and acceptors that randomize by rotational diffusion prior to energy transfer, the magnitude of κ^2 is assumed to be 2/3. However, in systems where there is a definite site of attachment of the donor and acceptor molecules, to get physically relevant results, the value of κ^2 has to be estimated from the angle between the donor emission and acceptor absorption dipoles [20]. $J(\lambda)$, the overlap integral, which expresses the degree of spectral overlap between the donor emission and the acceptor absorption, is given by,

$$J(\lambda) = \frac{\int_0^\infty F_D(\lambda)\varepsilon_A(\lambda)\lambda^4 d\lambda}{\int_0^\infty F_D(\lambda)d\lambda} \tag{2.50}$$

where $F_D(\lambda)$ is the fluorescence intensity of the donor in the wavelength range of λ to $\lambda+d\lambda$ and is dimensionless. $\varepsilon_A(\lambda)$ is the extinction coefficient (in $M^{-1}cm^{-1}$) of the acceptor at λ. If λ is in nm, then $J(\lambda)$ is in units of $M^{-1}\,cm^{-1}\,nm^4$.

Once the value of R_0 is known, the efficiency of energy transfer can be calculated. The efficiency of energy transfer (E) is the fraction of photons absorbed by the donor which are transferred to the acceptor and is defined as,

$$E = \frac{k_T(r)}{\tau_D^{-1} + k_T(r)} \tag{2.51}$$

$$\text{Or, } E = \frac{R_0^6}{r^6 + R_0^6} \tag{2.52}$$

For D-A systems decaying with multiexponential lifetimes, E is calculated from the amplitude weighted lifetimes $\langle\tau\rangle = \sum_i \alpha_i\tau_i$ of the donor in absence (τ_D) and presence (τ_{DA}) of the acceptor as,

$$E = 1 - \frac{\tau_{DA}}{\tau_D} \tag{2.53}$$

The D-A distances can be measured using equations (2.52) and (2.53).

2.1.5.1. Distance Distribution between Donor and Acceptor: Distance distribution between donor and acceptor was estimated according to the procedure described in the literature [21, 22]. The observed fluorescence transients of the donor molecules in absence of acceptor were fitted using a nonlinear least-squares fitting procedure (software SCIENTIST) to the following function,

$$I_D(t) = \int_0^t E(t')\, p(t'-t)dt' \tag{2.54}$$

which comprises the convolution of the instrument response function (IRF) ((*E(t)*) with exponential $(p(t) = \sum_i \alpha_{Di} \exp(-t/\tau_{Di}))$. The convolution of the distance distribution function *P(r)* in the fluorescence transients of donor in presence of acceptor in the system under studies is estimated using the same software (SCIENTIST) in the following way.

The intensity decay of D-A pair, spaced at a distance *r*, is given by

$$I_{DA}(r,t) = \sum_i \alpha_{Di} \exp\left[-\frac{t}{\tau_{Di}} - \frac{t}{\tau_{Di}}\left(\frac{R_0}{r}\right)^6 \right] \tag{2.55}$$

and the intensity decay of the sample considering distance distribution probablity function, *P(r)* is given by,

$$I_{DA}(t) = \int_{r=0}^{\infty} P(r) I_{DA}(r,t)dr \tag{2.56}$$

where *P(r)* consist of the folowing terms:

$$P(r) = \frac{1}{\sigma\sqrt{2\pi}} \exp\left[-\frac{1}{2}\left(\frac{\bar{r}-r}{\sigma}\right)^2 \right] \tag{2.57}$$

In this equation $\bar{r}$ is the mean of the Gaussian with a standard deviation of σ. Usually distance distributions are described by the full width at half maxima (*hw*). This half width is given by $hw = 2.354\sigma$.

2.1.6. Circular Dichroism (CD): CD is now a routine tool in many laboratories with applications to determine whether a chiral molecule has been synthesized or

resolved into pure enantiomers and probing the structures of biomolecules, in particular determining the α-helical content of proteins [22, 23].

2.1.6.1. Theory: When a plane polarized light passes through an optically active substance, not only do the left (*L*) and right (*R*) circularly polarized light rays travel at different speeds, $c_L \neq c_R$, but these two rays are absorbed to a different extent, i.e. $A_L \neq A_R$. The difference in the absorbance of the left and right circularly polarized light, i.e., $\Delta A = A_L - A_R$, is defined as circular dichroism (CD). Circular dichroism spectroscopy follows Beer-Lambert law. If I_0 is the intensity of light incident on the cell, and *I*, that of emergent light, then absorbance is given by,

$$A = \log_{10}\left(\frac{I_0}{I}\right) = \varepsilon c l \tag{2.58}$$

i.e., *A* is proportional to concentration (*c*) of optically active substance and optical path length (*l*). If '*c*' is in moles litre^{-1} and '*l*' is in cm, then ε is called the molar absorptivity or molar extinction coefficient. In an optically active medium, two absorbances, A_L and A_R are considered, where $A_L = \log_{10}\left(I_0/I_L\right)$ and $A_R = \log_{10}\left(I_0/I_R\right)$. At the time of incidence on the sample, intensity of left and right circularly polarized light are same, i.e. $I_0 = I_L = I_R$. Any dicrograph passes periodically changing light through the medium, oscillating between left and right circular polarization, and the difference in absorbances are recorded directly.

$$\Delta A = A_L - A_R = \log_{10}\left(\frac{I_0}{I_L}\right) - \log_{10}\left(\frac{I_0}{I_R}\right) = \log_{10}\left(\frac{I_R}{I_L}\right) \tag{2.59}$$

$$\Delta A = \left(\Delta\varepsilon\right) c l \tag{2.60}$$

As seen from equation (2.59), I_0 does not appear in this final equation, so there is no need for a reference beam. The instruments are, therefore, of single beam type.

After passing through an optically active substance, light is changed in two aspects. The maximal amplitude of intensity is no longer confined to a plane;

instead it traces out an ellipse. Ellipticity is defined as the arctangent of the ratio of minor axis to the major axis of the ellipse (Figure 2.7). The orientation of ellipse is another aspect. The major axis of the ellipse no longer remains parallel to the polarization of the incident light. Thus, after passing through an optically active substance, neither do the absorbance nor do the radii of the emergent left and right circularly polarized light remains same. Hence, CD is equivalent to ellipticity.

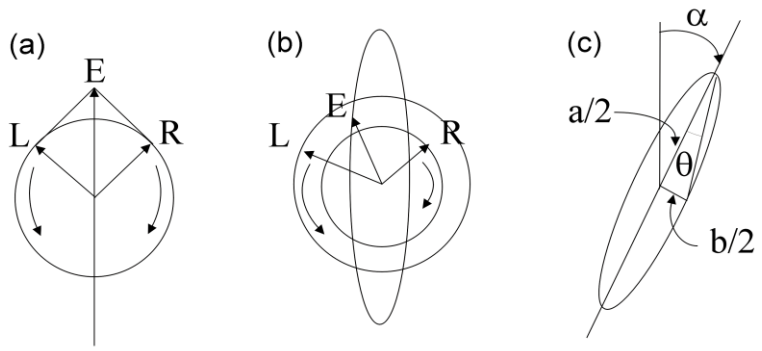

***Figure* 2.7.** *(a) Left (L) and right (R) circularly polarized light component having same intensities and phases lying in one plane and oscillating with same magnitude, (b) R component being less intense (more absorbed) than L component leading to elliptically polarized light and (c) θ, ellipticity is the angle made by semi-major and semi-minor axes of the ellipse. The major axis has rotated through angle α corresponding to optical rotation.*

Most of the CD spectropolarimeters, although they measure differential absorption, produce a CD spectrum in units of ellipticity (θ) expressed in milli-degrees versus λ, rather than ΔA versus λ. The relation between ellipticity and CD is given by,

$$\theta = \frac{2.303 \times 180 \times \left(A_L - A_R \right)}{4\pi} \text{ (in degrees)} \tag{2.61}$$

to compare the results from different samples, optical activity is computed on a molar or residue basis. Molar ellipticity, $[\theta]$ is defined as,

$$[\theta] = \frac{\theta}{cl} \tag{2.62}$$

where (θ) is in degrees, 'c' is in moles per litre and 'l' is in cm. The unit of molar ellipticity is deg. M^{-1} cm^{-1}. Sometimes, CD is reported as $\Delta\varepsilon=\Delta\varepsilon_L-\Delta\varepsilon_R$. From Beer-Lambert law and molar ellipticity relation it can be shown that,

$$[\theta] = 3300.\Delta\varepsilon \tag{2.63}$$

2.1.6.2. Experimental Methods: In biophysical studies, CD is mostly used to determine the secondary structures of proteins and nucleic acids and the changes in secondary structures upon recognition by small molecules and other biomolecules. Through CD spectropolarimeter, we obtain CD spectrograph having a plot of optical rotation in millidegrees versus wavelength in nm. In order to obtain information about the secondary structures of proteins, the graph is fitted with non-linear least square fitting method using freely available software. The percentages of different secondary structures are calculated by matching the experimental data with that of reference standard. In proteins, the secondary structural content includes α–helix, β–sheet, β–turn and random coil while for DNA, CD is used to determine the structures of different A, B, Z and condensed forms of DNA. The CD spectrum of α–helix contains two negative peaks, one at 208 nm (π–π* transition) and 222 nm (n–π* transition). β–sheet has a negative band at 216 nm and a positive band of similar magnitude at 195 nm. β–turn has weak negative peak at 225 nm (n–π* transition), a strong positive peak between 200 nm and 205 nm due to π–π* transition and a strong negative band between 180 nm and 190 nm. Random coil or unordered conformation has a strong negative band below 200 nm; a positive band at 218 nm and in some cases has a very weak negative band at 235 nm. A positive band centered at 275 nm and a negative band at 240 nm with crossover at 258 nm characterizes B-DNA.

2.1.7. Microfluidics Theory: The flow of a fluid through a microfluidic channel can be characterized by the Reynolds number, defined as,

$$R_e = \frac{LV_{avg}\rho}{\mu} \tag{2.64}$$

where L is the most relevant length scale, μ is the viscosity, ρ is the fluid density, and V_{avg} is the average velocity of the flow. For microchannels, L is equal to $4A/P$ where A is the cross sectional area of the channel and P is the wetted perimeter of the channel. Due to the small dimensions of microchannels, the R_e is usually much less than 100. In this Reynolds number regime, flow is completely laminar and no turbulence occurs. The transition to turbulent flow generally occurs in the range of Reynolds number 2000. Laminar flow provides a means by which molecules can be transported in a relatively predictable manner through microchannels.

Due to laminar flow in the microchannel, the transport of the mass of the subjected species within the microchannel follows the diffusion law. Figure 2.9 depicts the molecular diffusion of the species under study in the microchannel. The diffusion coefficient is estimated according to the procedure described by in the literature [24]. Considering the two-dimensional diffusion law, Einstein's equation of Brownian motion states that,

$$\tau = \frac{d^2}{2D} \tag{2.65}$$

where, d is the root mean square distance traversed by a molecule during the time interval for a given diffusion coefficient D.

The kinetics of molecular recognition/interaction was analyzed by measuring the fluorescence intensity of fluoroprobe along the microchannel. For a single step first order reaction, reactants will produce products as follows:

$$\text{Reactants} \xrightarrow{k} \text{Products}$$

The rate equation can be written as [25],

$$x = a(1 - e^{-kt}) \tag{2.66}$$

where, 'x' corresponds to the product concentration at time t and k is the first-order rate constant. Considering a reaction having an intermediate step, i.e. $A \xrightarrow{k_1} I \xrightarrow{k_2} P$, the product concentration at time, t would be [26],

$$x = a(1 + \frac{k_1 e^{-k_2 t} - k_2 e^{-k_1 t}}{k_2 - k_1}) \tag{2.67}$$

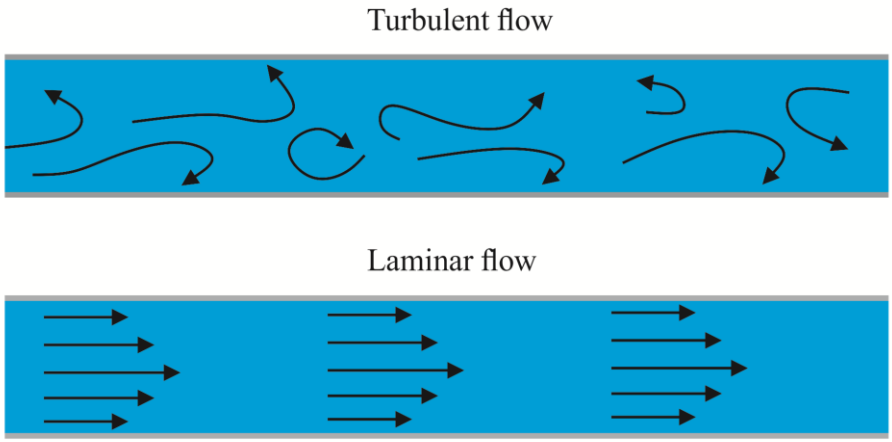

Figure 2.8. *Graphical representation of turbulent and laminar flow within a microchannel.*

Where, 'a' denotes the initial concentration at time t=0 and k_1, k_2 are the respective rate constants. The precision of the measurement of the kinetics parameter will depend on the uniformity and accuracy of the flow velocity and the signal-to-noise ratio in the fluorescence measurement.

Moreover, concentrations of the unbound substrate and the intermediate can be written in terms of the following equations,

$$[A] = ae^{-k_1 t} \tag{2.68}$$

$$[B] = \frac{ak_1}{k_2 - k_1}(e^{-k_1 t} - e^{-k_2 t}) \tag{2.69}$$

As the concentration of A decreases, its rate of transformation into B decreases as well; at the same time the rate of conversion of B to C increases as more B is

formed with progress in time, so a maximum concentration of B is reached at a time given by

$$t = \frac{\ln(k_1 / k_2)}{k_2 - k_1} \tag{2.70}$$

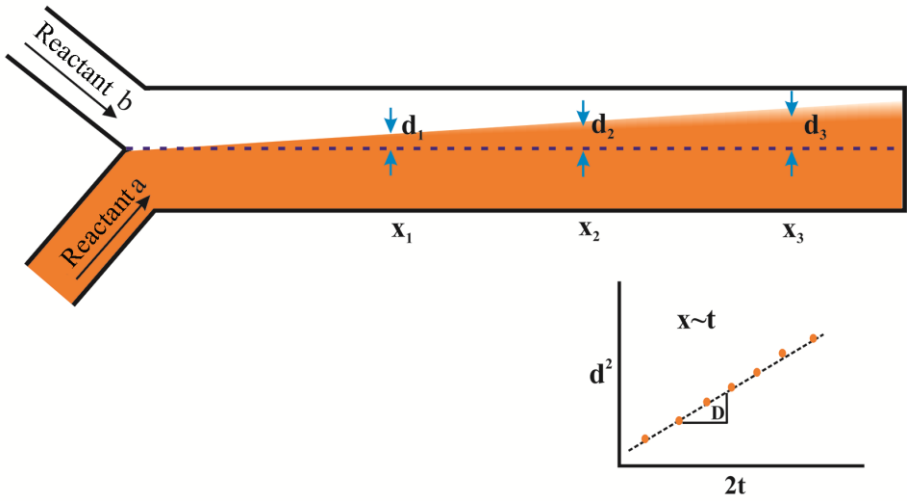

Figure 2.9. *Measurement of the diffusion of the subjected species by monitoring the spreading width at different time interval is graphically represented.*

2.2. Systems:

2.2.1. Organized Assemblies (biomimetics): Amphiphilic molecules like surfactant and lipids aggregates to form macromolecular assemblies, like micelles, reverse micelles and vesicles, which very often resemble the structural properties of biomolecules. In the following section, we will discuss about these entities.

2.2.1.1. Micelles: Micelles are spherical or nearly spherical aggregates of amphiphilic surfactant molecules formed in aqueous solution above a concentration known as critical micellar concentration (CMC). Micelles are formed above a critical temperature called "Kraft point" which is different for different surfactants. Micellar aggregates have diameter varying within 10 nm and the aggregation number, i.e., the number of surfactant molecules per micelle, ranges from 20 to 200. Israelachvili et al. [27] have proposed that surfactant molecular packing considerations are determinant in the formation of large surfactant

aggregates. In particular, it is considered that the surfactant packing parameter θ ($\theta = v/\sigma l$, where v is the surfactant molecular volume, σ is the area per polar head, and l is the length of hydrophobic part) gives a good idea of the shape of aggregates which will form spontaneously [28]. Micelles can be both neutral (triton X-100) and ionic (sodium dodecyl sulfate, SDS (anionic) and cetyl trimethyl ammonium bromide, CTAB (cationic)). The structure of a typical micelle is schematically shown in Figure 2.10. The core of a micelle is essentially "dry" and consists of the hydrocarbon chains with the polar and charged head groups

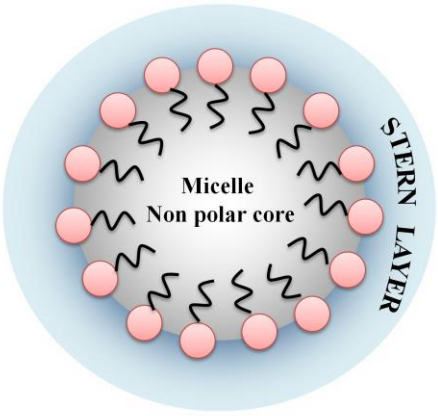

Figure 2.10. *The schematic representation of the structure of a micelle.*

projecting outward toward the bulk water. The stern layer, surrounding the core, comprises of the ionic or polar head groups, bound counter ions and water molecules. Between the stern layer and the bulk water there is a diffused Guoy-Chapman (GC) layer, which contains the free counter ions and water molecules. Small angle X-ray and neutron scattering have provided detailed information on the structure of the CTAB micelles [29, 30]. According to these studies, CMC and aggregation number of CTAB micelle are 0.8 mM and 52 respectively and the thickness of the stern layer is 6-9 Å. The overall radius of CTAB micelle is about 50 Å. For TX-100 micelle, the CMC, thickness of the palisade layer and overall radius of the hydrophobic core are reported to be 0.1 mM, 51 Å and 25-27 Å, respectively and that of SDS micelles are 8.6 mM, 33 Å and 5 Å, respectively.

2.2.1.2. Reverse Micelles: Reverse micelles (RMs) or water-in-oil microemulsions (Figure 2.11) are nanopools of polar solvent protected by a monolayer of surfactant molecules at the periphery with polar head groups pointing inward into the polar solvent, and the hydrocarbon tails directed toward the non-polar organic solvents [31]. RMs with water nanopools resemble the water pockets found in various bio-aggregates such as proteins, membranes, and mitochondria. Thus, these systems are very often considered as templates for the synthesis of nanoparticles and as excellent biomimetic for exploration of biological membranes and biologically confined water molecules. Aqueous RMs are generally characterized by the degree of hydration (w_0), which is the ratio of molar concentration of water to that of surfactant, where the radius of the water pool (r *in Å*) is empirically defined as, $r = 2 \times w_0$ [32]. Shapes and sizes of the surfactant aggregates depend strongly on the type and concentration of the surfactant, and on the nature of counterion and external solvent. In principle, reverse micelles can be formed in the presence and in the absence of solubilized water. However, it has generally been proposed that if the medium is completely water-free, there is not a well-defined CMC (critical micelle concentration), and the aggregates formed are very small and polydisperse, indicating minimum cooperativity in the surfactant association.

Fluorescence spectroscopy has been extensively used to study the RMs system. Fluorescent probes have been used to determine the viscosity, binding site, rigidity and proximity within the water pool. These studies have shown that water inside the RMs is generally of two types: i) interfacial (bound) and ii) core (free) water. One of the studies [33] has shown the existence of third type of water (trapped) molecules present between the polar head groups of the individual surfactant molecules. Thus, the interior of RMs is extremely heterogeneous. Dielectric relaxation studies indicate the presence of 7 ns component for bound water in RM, very similar to those of water molecules in the close vicinity of

biological macromolecules (biological water). In contrast to anionic, sodium bis(2-ethylhexyl) sulfosuccinate **(**AOT) and cationic, benzyl-n-hexadecyldimethyl ammonium chloride (BHDC) RM, non-ionic or neutral surfactants (TX-100) have been reported to form RMs in pure and mixed hydrocarbon solvents.

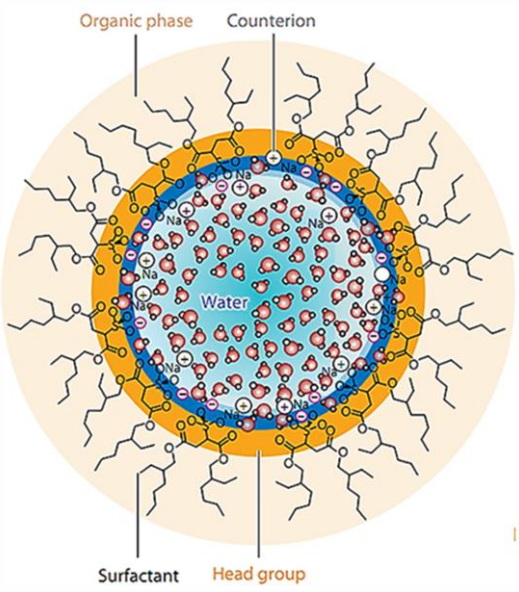

Figure 2.11. *Schematic depiction of a potential structure of a reverse micelle. Water molecules reside in the interior, sometimes interacting with head groups and counterions. Surfactant tails reside in contact with the continuous, nonpolar, organic supporting phase.*

2.2.1.3. Vesicles: Amphiphilic molecules, because of their solubility properties, aggregate into molecularly ordered structures, which often take the form of bilayers. When these bilayers curve and close, the resulting aggregates are called vesicles. The presence of a solvent inner reservoir (in most cases water) enclosed inside bilayers of amphiphiles, in turn comprised of a solvophobic (hydrophobic) middle shell and solvophilic (hydrophilic) layers on both sides, are the key morphological characteristics of a vesicular structure (Figure 2.12). This vesicle phase can consist of unilamellar vesicles (ULVs) or multi-lamellar vesicles (MLVs). When the Amphiphilic molecules in addition are phospholipids, the vesicles are known as liposomes. Formation of vesicles depends on a number of factors such as amphiphilicity, as well as generalized geometric parameters of the constituent amphiphiles [34]. It is important to keep in mind that all vesicular characteristics

like overall size, membrane mechanical stability, bilayer width, fluidity and permeability, outer and inner layer functionalities and consequently the ability to encapsulate and release hydrophobic and hydrophilic molecules of interest are determined by the chemical characteristics of the constituting amphiphile and therefore can be tuned accordingly by synthesis. Bhattacharyya et al. [35] demonstrated that the solvation dynamics in lipid vesicles is biexponential with

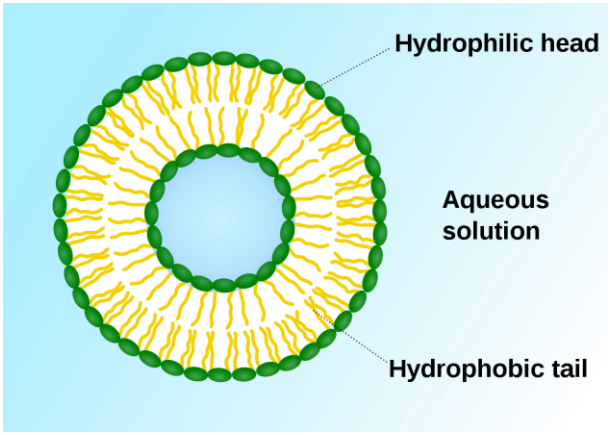

Figure 2.12. *Schematic representation of a vesicle structure.*

one component of a few hundred picoseconds and another of several thousand picoseconds. The slow solvation dynamics clearly demonstrates that the motion of the water molecules is highly constrained in the vesicles and is similar to the water molecules present in the immediate vicinity of biomolecules also called "biological water". The similarities of vesicles with cellular membranes have made them model systems for investigating phenomena and behavioral characteristics found in biological systems [36].

2.2.2. Proteins: Three types of proteins; histone from calf thymus (type III-SS), bovine pancreatic deoxyribonuclease I (DNase I) and alpha chymotrypsin (CHT), have been used in our study.

2.2.2.1. Histone-I from Calf Thymus (type III-SS): Histone H1 is one of the five main histone protein families which are components of chromatin in eukaryotic

cells. Though highly conserved, it is nevertheless the most variable histone in sequence across species. While most histone H1 in the nucleus is bound to chromatin, H1 molecules shuttle between chromatin regions at a fairly high rate. It is difficult to understand how such a dynamic protein could be a structural component of chromatin, but it has been suggested that the steady-state equilibrium within the nucleus still strongly favors association between H1 and chromatin, meaning that despite its dynamics, the vast majority of H1 at any given timepoint is chromatin bound. H1 compacts and stabilizes DNA under force and during chromatin assembly, which suggests that dynamic binding of H1 may provide protection for DNA in situations where nucleosomes need to be removed. Cytoplasmic factors appear to be necessary for the dynamic exchange of histone H1 on chromatin, but these have yet to be specifically identified. H1 dynamics may be mediated to some degree by O-glycosylation and phosphorylation. O-glycosylation of H1 may promote chromatin condensation and compaction. Phosphorylation during interphase has been shown to decrease H1 affinity for chromatin and may promote chromatin decondensation and active transcription. However, during mitosis phosphorylation has been shown to increase the affinity of H1 for chromosomes and therefore promote mitotic chromosome condensation.

2.2.2.2. Bovine Pancreatic Deoxyribonuclease I (DNase I): Deoxyribonuclease I (DNase I) (Figure 2.13) is an endonuclease isolated from bovine pancreas, digests double and single stranded DNA into oligo and mononucleotides. Bovine pancreatic DNase exists as four isozymes, having isoelectric points for A, B, C and D: 5.22, 4.96, 5.06 and 4.78.3. The predominant form is A, with smaller amounts of B and C, and only minor amount of D. DNase I is an endonuclease that acts on phosphodiester bonds adjacent to pyrimidines to produce polynucleotides with terminal 5′-phosphates. In the presence of Mg^{2+}, DNAse I cleaves each strand of DNA independently and the cleavage sites are random. Both DNA strands are cleaved at approximately the same site in the presence of Mn^{2+} [37]. Divalent

cations such as Mn^{2+}, Ca^{2+}, Co^{2+}, and Zn^{2+} are activators of the enzyme. A concentration of 5 mM Ca^{2+} stabilizes the enzyme against proteolytic digestion. The pH optimum is found to be between 7 and 8. DNAse I from bovine pancreas consists of four chromatographically distinguishable components, A, B, C, and D, with their molar ratios being 4:1:1 respectively. Only minor amounts of D are found.

Figure 2.13. *X-ray crystallographic structure of Deoxyribonuclease I (DNase I) depicting the different domains.*

2.2.2.3. α-Chymotrypsin (CHT): α-Chymotrypsin (Figure 2.14) isolated from bovine pancreas, is a member of the family serine endopeptidase (molecular weight of 25,191 Da) catalysing the hydrolysis of peptides in the small intestine [38]. The three dimensional structure of CHT was solved by David Blow [39]. The molecule is a three-dimensional ellipsoid of dimensions 51 × 40 × 40 Å. and comprises of 245 amino acid residues. CHT contains several antiparallel β-pleated sheet regions and little α-helix. Physiological activity of CHT is determined by the pH. The enzyme is not active at lower pH, but the activity increases nonmonotonically with pH, in the duodenum (low pH), it is inactive, whereas in the lower small intestinal track (high pH), it becomes active. The inactivity of the enzyme at lower pH is known to be related to the protonation of the residues of the catalytic triad. From spectroscopic studies, it was suggested that the degree of

mobility of water molecules, not hydrophobicity, may be the important factor for the change with pH.

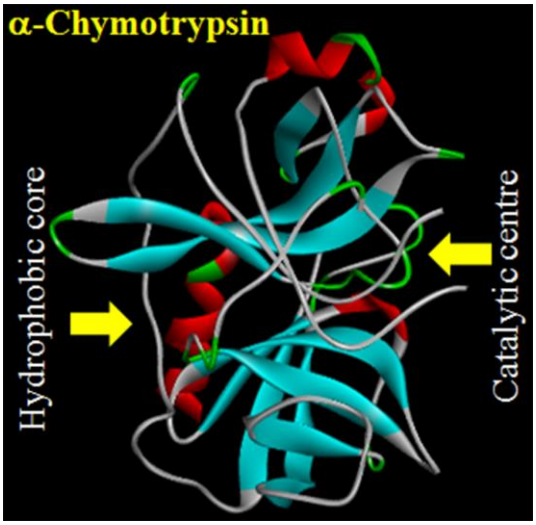

Figure 2.14. *X-ray crystallographic structure (PDB code: 2CHA) of CHT depicting the different domains.*

2.2.3. Deoxyribonucleic Acid (DNA): Deoxyribonucleic acids (DNA) are polynucleotide with each nucleotide comprising of deoxyribose sugar, purine and pyrimidine bases and phosphate groups. The main bases whose intermolecular hydrogen bonding holds the DNA strands together are adenine, guanine, thymine and cytosine. DNA serves as carrier of genetic information. The classic example of how biological function follows from biomolecular structure comes from the elucidation of double helical structure of DNA by Watson and Crick [40]. There are generally three forms of DNA-A, B and Z-form. Natural DNA, however, exists in B-form. Natural DNA is about meter long and comprises of hundreds of base pairs. The distance between two base pairs in B-DNA is 3.4 Å [40]. In about 4 M NaCl, B-form assumes Z-form. DNA structures consist of major and minor grooves and intercalation spaces through which DNA interacts with ligands. There are two modes of interaction between DNA and ligands: (i) intercalation, where the planar polycyclic hetero-aromatic ligands sit in between the base pairs of DNA and interact through π–π interaction [41] and (ii) groove binding, where

the ligands bind in the major and minor grooves of DNA [42]. The water molecules at the surface of DNA are critical for the molecular recognition and maintaining the structure. We have used calf thymus DNA for studying the DNA surfactant interaction and 20-mer sequences, 5′-GCGTGTAAACGATTCCACGC-3′ DNA in order to monitor the enzymatic activity of DNase I.

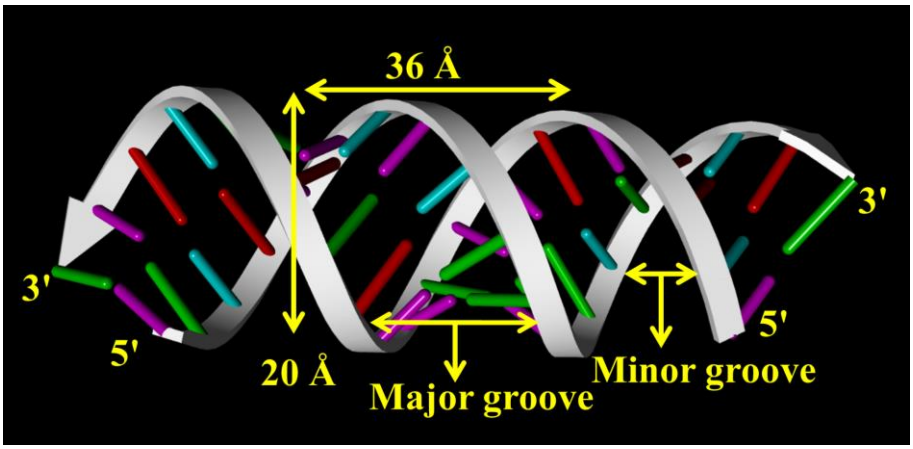

Figure 2.15. *Schematic representation of deoxyribonucleic acid (DNA).*

2.2.4. Molecular Probes: In this section we will discuss about the different probe molecules that have been used in the course of study.

2.2.4.1. Acridine Orange 10-nonyl Bromide (NAO): Nonyl acridine orange is an organic compound. It is fluorescent cationic dye having an acridine head group and a long alkyl tail useful for selective labelling of nucleic acid. Being cationic dye, it interacts with negative charge DNA by intercalation or electrostatic attractions, respectively. When bound to DNA, the absorption peak and emission peaks of NAO are at 492 and 520 nm [43].

2.2.4.2. Ethidium Bromide (EB): EtBr is a well-known fluorescent probe for DNA, which readily intercalates into the DNA double helix. Compared to bulk water, the emission intensity and lifetime of EtBr increases significantly when EtBr intercalates into the double helix of DNA [44]. This remarkable fluorescence enhancement of EtBr is utilized to study the motion of DNA segments, and the

interaction of DNA with surfactants and drug. Absorption maxima of EtBr in aqueous solution are at 285 nm and 480 nm, after excitation EtBr emits orange light with wavelength maxima at 620 nm.

2.2.4.3. Crystal Violet (CV): Crystal violet is a cationic triarylmethane dye used as a nontoxic DNA stain. When dissolved in water, the dye has a blue-violet colour with an absorbance maximum at 590 nm and an extinction coefficient of 87,000 M^{-1} cm^{-1}. The absorption spectrum of CV overlaps well with the emission spectrum of nonyl acridine orange, making it useful as an acceptor in FRET experiments [43].

2.2.4.4. 8-Anilino-1-Naphthalenesulfonic Acid Ammonium Salt (ANS): ANS is a well-known solvation probe which binds selectively to the native state of certain proteins and enzymes in their hydrophobic as well as polar sites (Figure 2.16). In aqueous solution, the emission quantum yield of ANS is very small (0.004) with emission peak at ~520 nm and a lifetime of ~0.25 ns. The steady-state emission is quenched dramatically in polar solvents. Because of its bichromophoric structure, ANS is known to undergo charge transfer (CT) from one aromatic moiety to the other ring and solvation. In nonpolar solvents, the emission is strong and is mostly from the locally excited state i.e., before charge separation. In polar solvents, the fluorescence decreases and is dominated by emission from the CT state. The solvent polarity and rigidity determine the wavelength and yield of emission and that is why ANS is a useful biological probe [44].

2.2.4.5. Doxorubicin Hydrochloride (DOX): Doxorubicin (DOX) is one of the most commonly used chemotherapeutic drugs and a popular research tool due to the inherent fluorescence of the DOX molecule. After DOX injection, fluorescence imaging of organs or cells can provide information on drug biodistribution. Therapeutic and imaging capabilities combined in a DOX molecule make it an excellent theranostic agent. The sensitivity of DOX fluorescence intensity to DOX

concentration, local microenvironment, and interaction with model cellular components is illustrated by fluorescence spectra of paired DOX complex. The photophysics of the probe with nanoscopic vehicles have also been studied in detail [45].

2.2.4.6. Dihydroindolizine (DHI): Photochromic DHI has received much attention owing to its remarkable photo-fatigue resistance and broad range of absorption. Moreover, photochromic DHI is used to tether peptides and proteins via a maleimide functional group, which corresponds to absorption in the red region of the visible spectrum and in the near-IR spectral domain, indicating the potential for future use in *in vivo* applications. The basis of the photochromic behavior of DHI is light-induced reversible pyrroline ring opening, which transforms the molecule from a light-yellow colored form (cis) to a red colored betaine form (trans). Betaines undergo a thermal back reaction to their corresponding DHI cis form by 1,5-electrocyclization [46].

2.2.4.7. Coumarin 500 (C500): The solvation probe C500 (Figure 2.16) is sparingly soluble in water and shows reasonably good solubility in isooctane. In bulk water the absorption peak (400 nm) is significantly red shifted compared to that in isooctane (360 nm). The emission peak of C500 in bulk water (500 nm) also shows a 90 nm red shift compared to that in isooctane (excitation at 350 nm). The significantly large solvochromic effect in the absorption and emission spectra of C500 makes the dye an attractive solvation probe for microenvironments. The photophysics of the probe have also been studied in detail [47].

2.2.4.8. Rifampicin (RF): Rifampicin (RF) is an antibiotic drug of the rifamycin group. RF is a first line anti-tuberculosis drug which is active against *Mycobacterium tuberculosis* as well as few other Mycobacterial species. It can be used alone or in combination with other drugs like, isoniazid and pyrazinamide for the treatment of tuberculosis. It is a potent inhibitor of DNA dependent RNA

synthesis from bacteria. Binding affinity of RF to HSA is 65 % to 75 %. RF absorbs light at 228 nm, 333 nm and 473 nm. Its solubility in water is 1.3 mg/ml at pH 4.3. The molar extinction coefficient of RF at 473 nm is 15286 M^{-1} cm^{-1}.

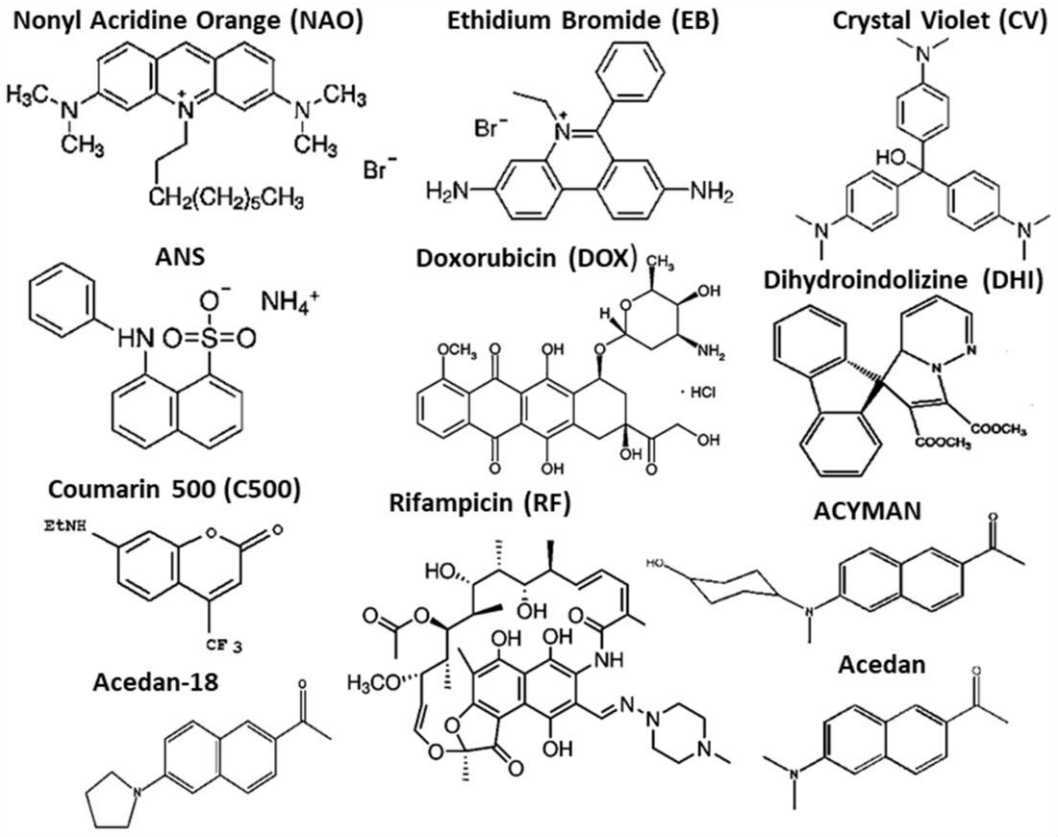

***Figure* 2.16.** *Schematic representation of the molecular probes used.*

2.2.4.9. 6-Acetyl-2-(dimethyl amino) naphthalene (Acedan): Acedan is a donor–acceptor (D–A) type dipolar fluorophores have been widely used in molecular probes and biological tags owing to their highly emissive nature. It has an electron-donating 6-dimethylamino group and an electron-accepting 2-acetyl group, allowing ICT through the p-electron delocalization. The emission of acedan is expected to come from the locally excited (LE) state, or the ICT excited states—twisted (TICT) or planarized (PICT), depending on the medium. In bulk water the absorption peak and emission peaks of Acedan are at 360 and 516 nm, respectively and it is sensitive to the polarity of the medium. The significant solvochromic

effect (solvation) in the absorption and emission spectra of Acedan makes the dye an attractive solvation probe for microenvironments [48].

2.2.4.10. 6-Acetyl-(2-((4-hydroxycyclohexyl) (methyl) amino) naphthalene (ACYMAN): ACYMAN is the derivative of Acedan form by replacing the N,Ndimethylamino by 4-hydroxycyclohexyl(methyl)amino group. A bulky amino group is expected to undergo a slower or hindered internal rotation in the excited state, which can also contribute to the fluorescence enhancement of acedan derivatives by reducing the nonradiative decay. In bulk water the absorption peak and emission peaks of ACYMAN are at 368 and 519 nm [49], respectively and it is also sensitive to the polarity of the medium.

2.2.4.11. 6-Acetyl-2-((pyrrolidine) (methyl) amino) naphthalene (Acedan 18): Like ACYMAN, Acedan 18 is also the derivative of Acedan form by replacing N,N dimethylamino by pyrrolidine)(methyl)amino group. In bulk water the absorption peak and emission peaks of ACYMAN are at 384 and 524 nm [50], respectively and it is also sensitive to the polarity of the medium. The significant solvochromic effect (solvation) in the absorption and emission spectra of Acedan 18 makes the dye an attractive solvation probe for microenvironments

References

[1] B. Bagchi, R. Biswas, Polar and nonpolar solvation dynamics, ion diffusion, and vibrational relaxation: Role of biphasic solvent response in chemical dynamics, *Adv. Chem. Phys.,* 109 (1999) 207-433.

[2] R. Jimenez, G.R. Fleming, P. Kumar, M. Maroncelli, Femtosecond solvation dynamics of water, *Nature,* 369 (1994) 471-473.

[3] S.K. Pal, J. Peon, B. Bagchi, A.H. Zewail, Biological water: Femtosecond dynamics of macromolecular hydration, in, *J. Phys. Chem. B*, 48 (2002), 12376-12395.

[4] B. Bagchi, Dynamics of solvation and charge transfer reactions in dipolar liquids, *Annu. Rev. Phys. Chem.,* 40 (1989) 115-141.

[5] J. Jortner, A. Gaathon, Effects of phase density on ionization processes and electron localization in fluids, *Can. J. Chem.,* 55 (1977) 1801-1819.

[6] R.M. Stratt, M. Maroncelli, Nonreactive dynamics in solution: The emerging molecular view of solvation dynamics and vibrational relaxation, *J. Phys. Chem.,* 100 (1996) 12981-12996.

[7] J.T. Hynes, Outer-sphere electron-transfer reactions and frequency-dependent friction, *J. Phys. Chem.,* 90 (1986) 3701-3706.

[8] M. Horng, J. Gardecki, A. Papazyan, M. Maroncelli, Subpicosecond measurements of polar solvation dynamics: Coumarin 153 revisited, *J. Phys. Chem.,* 99 (1995) 17311-17337.

[9] J. Lakowicz, Principles of fluorescence spectroscopy. , *2nd ed1999 NY, USA.,* 1999.

[10] N. Periasamy, A. Koti, Time resolved fluorescence spectroscopy: TRES and TRANES, *Proc. Indian Natn. Sci. Acad.,* 69 (2003) 41-48.

[11] A. Koti, M. Krishna, N. Periasamy, Time-resolved area-normalized emission spectroscopy (TRANES): A novel method for confirming emission from two excited states, *J. Phys. Chem. A,* 105 (2001) 1767-1771.

[12] R.D. Spencer, G. Weber, Measurements of subnanosecond fluorescence lifetimes with a cross-correlation phase fluorometer, *Ann. N. Y. Acad. Sci.,* 158 (1969) 361-376.

[13] L. A. Philips, S. P.Webb, J. H. Clark, High-pressure studies of rotational reorientation dynamics: The role of dielectric friction, *J. Chem. Phys.,* 83 (1985) 5810-5821.

[14] B. Kalman, N. Clarke, L. B. A. Johansson, Dynamics of a new fluorescent probe, 2,5,8,11-tetra-tert-butylperylene in solution, cubic lyotropic liquid crystals, and model membranes, *J. Phys. Chem.,* 93 (1989) 4608-4615.

[15] N. Ito, O. Kajimoto, K. Hara, Picosecond time-resolved fluorescence depolarization of p-terphenyl at high pressures, *Chem. Phys. Lett.,* 318 (2000) 118-124.

[16] R. Zana, Microviscosity of aqueous surfactant micelles: Effect of various parameters, *J. Phys. Chem. B,* 103 (1999) 9117-9125.

[17] N. Nandi, B. Bagchi, Dielectric relaxation of biological water, *J. Phys. Chem. B,* 101 (1997) 10954-10961.

[18] L. Stryer, Fluorescence energy transfer as a spectroscopic ruler, *Annu. Rev. Biochem.,* 47 (1978) 819-846.

[19] P. Verma, S. Pal, Ultrafast resonance energy transfer in bio-molecular systems, *Eur. Phys. J. D,* 60 (2010) 137-156.

[20] D. Banerjee, S.K. Pal, Simultaneous binding of minor groove binder and intercalator to dodecamer DNA: Importance of relative orientation of donor and acceptor in FRET, *J. Phys. Chem. B,* 111 (2007) 5047-5052.

[21] S. Batabyal, T. Mondol, S.K. Pal, Picosecond-resolved solvent reorganization and energy transfer in biological and model cavities, *Biochimie,* 95 (2013) 1127-1135.

[22] A. Rodger, B. Nordén, Circular dichroism and linear dichroism, *Oxford University Press, USA*, 1997.

[23] N. Sreerama, R. Woody, Circular dichroism: Principles and applications, *Berova N, Nakanishi K, Woody RW, editors,* 2 (2000) 601-620.

[24] R.F. Ismagilov, A.D. Stroock, P.J. Kenis, G. Whitesides, H.A. Stone, Experimental and theoretical scaling laws for transverse diffusive broadening in two-phase laminar flows in microchannels, *Appl. Phys. Lett.,* 76 (2000) 2376-2378.

[25] K.J. Laidler, A glossary of terms used in chemical kinetics, including reaction dynamics (IUPAC Recommendations 1996), *Pure Appl. Chem.,* 68 (1996) 149-192.

[26] J.N. Israelachvili, D.J. Mitchell, B.W. Ninham, Theory of self-assembly of hydrocarbon amphiphiles into micelles and bilayers, *J. Chem. Soc. Faraday Trans.,* 72 (1976) 1525-1568.

[27] D.J. Mitchell, B.W. Ninham, Micelles, vesicles and microemulsions, *J. Chem. Soc. Faraday Trans.,* 77 (1981) 601-629.

[28] H.H. Paradies, Shape and size of a nonionic surfactant micelle. Triton X-100 in aqueous solution, *J. Phys. Chem.,* 84 (1980) 599-607.

[29] S.S. Berr, Solvent isotope effects on alkytrimethylammonium bromide micelles as a function of alkyl chain length, *J. Phys. Chem.,* 91 (1987) 4760-4765.

[30] S.S. Berr, E. Caponetti, J.S. Johnson, J.R.R.M. Jones, L.J. Magid, Small-angle neutron scattering from hexadecyltrimethylammonium bromide micelles in aqueous solutions, *J. Phys. Chem.,* 90 (1986) 5766-5770.

[31] P. Luisi, M. Giomini, M.a. Pileni, B. Robinson, Reverse micelles as hosts for proteins and small molecules, *Biochim. Biophys. Acta, Rev. Biomembr.,* 947 (1988) 209-246.

[32] M.-P. Pileni, Water in oil colloidal droplets used as microreactors, *Adv. Colloid Interface Sci.,* 46 (1993) 139-163.

[33] C. Petit, P. Lixon, M. Pileni, Structural study of divalent metal bis (2-ethylhexyl) sulfosuccinate aggregates, *Langmuir,* 7 (1991) 2620-2625.

[34] K. Edwards, M. Almgren, Surfactant-induced leakage and structural change of lecithin vesicles: Effect of surfactant headgroup size, *Langmuir,* 8 (1992) 824-832.

[35] S.K. Pal, D. Sukul, D. Mandal, S. Sen, K. Bhattacharyya, Solvation dynamics of DCM in dipalmitoyl phosphatidylcholine lipid, *Tetrahedron,* 56 (2000) 6999-7002.

[36] M. Antonietti, S. Förster, Vesicles and liposomes: A self-assembly principle beyond lipids, *Adv. Mater.,* 15 (2003) 1323-1333.

[37] S. Sonawane, V. Khanolkar, A. Namavari, S. Chaudhary, S. Gandhi, S. Tibrewal, S.H. Jassim, B. Shaheen, J. Hallak, J.H. Horner, Ocular surface extracellular DNA and nuclease activity imbalance: A new paradigm for inflammation in dry eye disease, *Investig. Ophthalmol. Vis. Sci.,* 53 (2012) 8253-8263.

[38] J.D. Johnson, M.A. El-Bayoumi, L.D. Weber, A. Tulinsky, Interaction of. alpha.-Chymotrypsin with the fluorescent probe 1-anilinonaphthalene-8-sulfonate in solution, *Biochemistry,* 18 (1979) 1292-1296.

[39] J.J. Birktoft, D. Blow, Structure of crystalline α-chymotrypsin: V. The atomic structure of tosyl-α-chymotrypsin at 2 Å resolution, *J. Mol. Biol.,* 68 (1972) 187-240.

[40] J.D. Watson, F.H. Crick, Molecular structure of nucleic acids, *Nature,* 171 (1953) 737-738.

[41] L. Lerman, The structure of the DNA-acridine complex, *Proc. Natl. Acad. Sci. U.S.A.,* 49 (1963) 4–102.

[42] M.B. Lyles, I.L. Cameron, Interactions of the DNA intercalator acridine orange, with itself, with caffeine, and with double stranded DNA, *Biophys. Chem.,* 96 (2002) 53-76.

[43] P. Singh, S. Choudhury, G.K. Chandra, P. Lemmens, S.K. Pal, Molecular recognition of genomic DNA in a condensate with a model surfactant for potential gene-delivery applications, *J. Photochem. Photobiol. B,* 157 (2016) 105-112.

[44] P. Singh, S. Choudhury, S. Dutta, A. Adhikari, S. Bhattacharya, D. Pal, S.K. Pal, Ultrafast spectroscopy on DNA-cleavage by endonuclease in molecular crowding, *Int. J. Biol. Macromol.,* 103 (2017) 395-402.

[45] P. Singh, S. Choudhury, S. Kulanthaivel, D. Bagchi, I. Banerjee, S.A. Ahmed, S.K. Pal, Photo-triggered destabilization of nanoscopic vehicles by

dihydroindolizine for enhanced anticancer drug delivery in cervical carcinoma, *Colloids Surf. B,* 162 (2018) 202-211.

[46] A. Fernando, T.B. Shrestha, Y. Liu, A.P. Malalasekera, J. Yu, E.J. McLaurin, C. Turro, S.H. Bossmann, C.M. Aikens, Insights from theory and experiment on the photochromic spiro-dihydropyrrolo–pyridazine/betaine system, *J. Phys. Chem. A,* 120 (2016) 875-883.

[47] P. Singh, S. Choudhury, V. Sharma, S. Mitra, R. Mukhopadhyay, R. Das, S.K. Pal, Modulation of solvation and molecular recognition of a lipid bilayer under dynamical phase transition, *ChemPhysChem,* 19 (2018) 2709-2716.

[48] P. Singh, D. Mukherjee, S. Singha, R. Das, S.K. Pal, Modulation of kinetic pathways of enzyme-Substrate interaction in a microfluidic channel: Nanoscopic water dynamics as a switch, *Chem. Eur. J.,* (2019) doi: 10.1002/chem.201901751.

[49] P. Singh, S. Choudhury, S. Singha, Y. Jun, S. Chakraborty, J. Sengupta, R. Das, K.-H. Ahn, S.K. Pal, A sensitive fluorescent probe for the polar solvation dynamics at protein–surfactant interfaces, *Phys. Chem. Chem. Phys,* 19 (2017) 12237-12245.

[50] P. Singh, V. Sharma, S. Singha, V. García-Sakai, R. Mukhopadhyay, R. DAS, S. Pal, Unravelling the role of monoolein in fluidity and dynamical response of a mixed cationic lipid bilayer, *Langmuir,* 35 (2019) 4682-4692.

Chapter 3

Instrumentation and Sample Preparation

In this chapter the details of instrumental setup and sample preparation techniques used in our studies have been described.

3.1. Instrumental Setups:

3.1.1. Steady-State UV-Vis Absorption and Emission Measurement: Steady-state UV-Vis absorption and emission spectra of the probe molecules were measured with Shimadzu UV-2450 spectrophotometer and Jobin Yvon Fluoromax-3 fluorimeter, respectively. Schematic ray diagrams of these two instruments are shown in Figures 3.1 and 3.2.

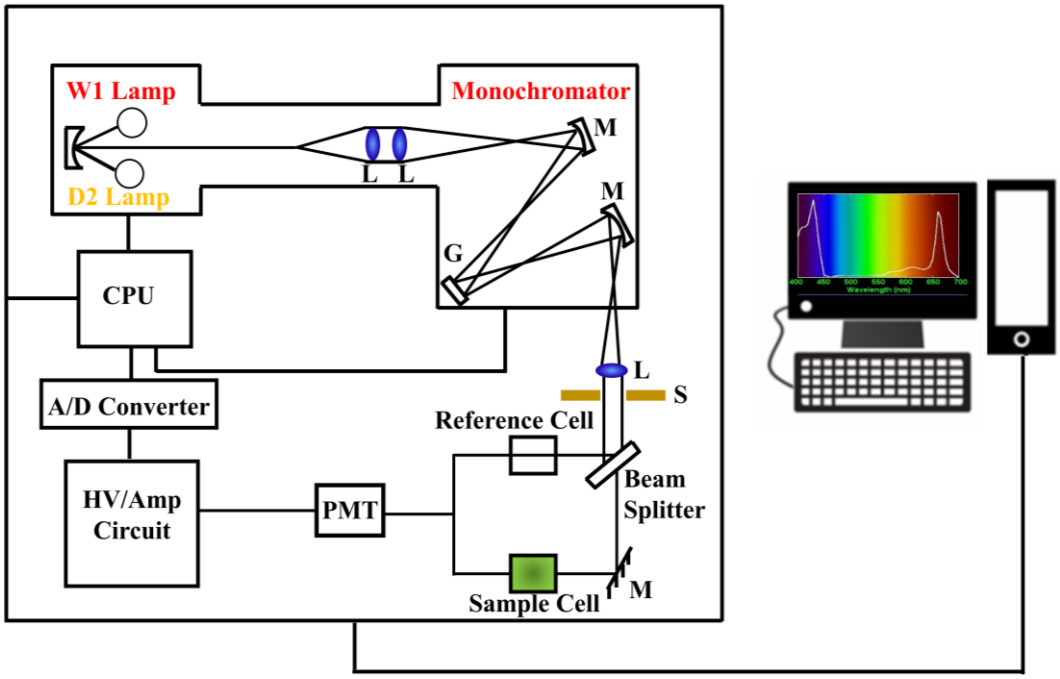

Figure 3.1. *Schematic ray diagram of an absorption spectrophotometer. Tungsten halogen (W1) and deuterium lamps (D2) are used as light sources in the visible and UV regions, respectively. M, G, L, S, PMT designate mirror, grating, lens, shutter and photomultiplier tube, respectively. CPU, A/D converter and HV/amp indicate central processing unit, analog to digital converter and high-voltage/amplifier circuit, respectively.*

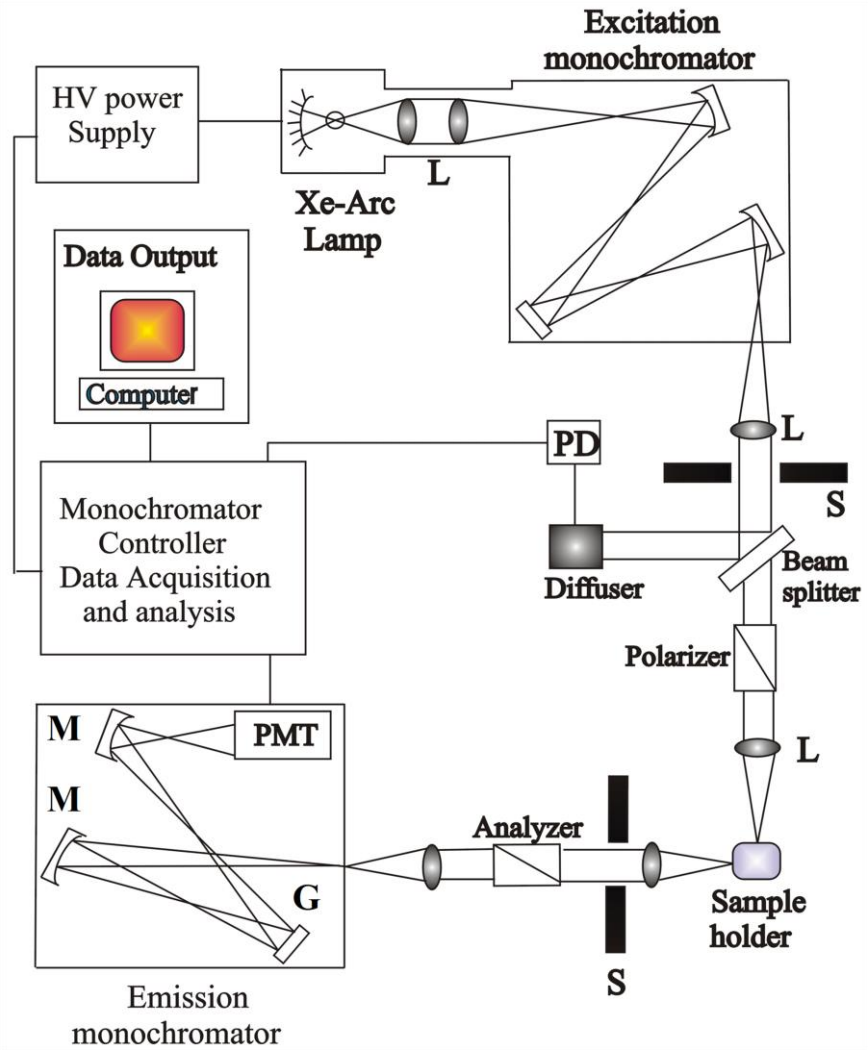

Figure 3.2. *Schematic ray diagram of an emission spectrofluorimeter. M, G, L, S, PMT and PD represent mirror, grating, lens, shutter, and photomultiplier tube and reference photodiode, respectively.*

3.1.2. Time-Correlated Single Photon Counting (TCSPC) Technique: All the picosecond-resolved fluorescence transients were recorded using TCSPC technique. The schematic block diagram of a TCSPC system is shown in Figure 3.3. TCSPC setup from Edinburgh instruments, U.K., was used during fluorescence decay acquisitions. The instrument response functions (IRFs) of the laser sources at different excitation wavelengths varied between 70 ps to 80 ps. The fluorescence from the sample was detected by a photomultiplier after dispersion through a grating monochromator [1]. For all transients, the polarizer in the emission side

was adjusted to be at 54.7^0 (magic angle) with respect to the polarization axis of excitation beam. In order to measure anisotropy, fluorescent transients were taken with emission polarizer aligned in parallel and perpendicular directions with respect to vertical polarization of excitation light. For tryptophan excitation of protein, femtosecond-coupled TCSPC setup were employed in which the sample was excited by the third harmonic laser beam (300 nm) of the 900 nm (0.5 nJ per

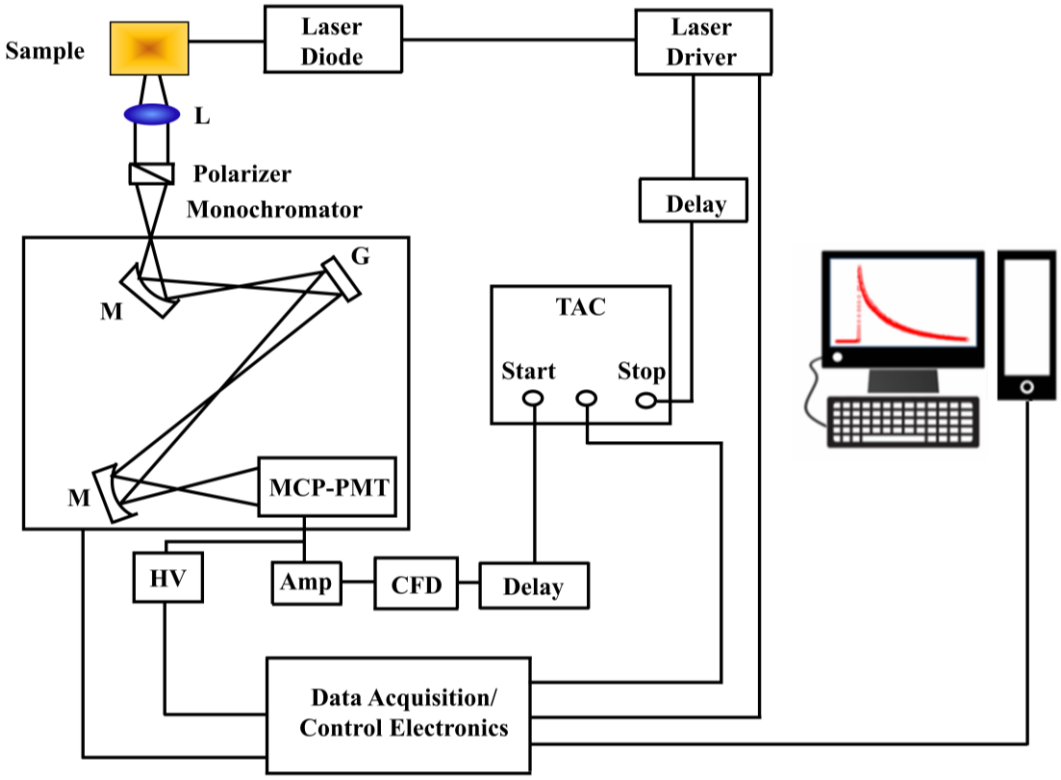

Figure 3.3. *Schematic ray diagram of a time correlated single photon counting (TCSPC) spectrophotometer. A signal from microchannel plate photomultiplier tube (MCP-PMT) is amplified (Amp) and connected to start channel of time to amplitude converter (TAC) via constant fraction discriminator (CFD) and delay. The stop channel of the TAC is connected to the laser driver via a delay line. L, M, G and HV represent lens, mirror, grating and high voltage source, respectively.*

pulse) using a mode-locked Ti-sapphire laser with an 80 MHz repetition rate (Tsunami, spectra physics), pumped by a 10 W Millennia (Spectra physics) followed by a pulse-peaker (rate 8 MHz) and a third harmonic generator (Spectra-physics, model 3980). The third harmonic beam was used for excitation of the

sample inside the TCSPC instrument (IRF = 70 ps) and the second harmonic beam was collected as for the start pulse.

3.1.3. Circular Dichroism (CD) Measurement: CD is a form of spectroscopy based on the differential absorption of left and right-handed circularly polarized light. It can be used to determine the structure of macromolecules (including the secondary structure of proteins and the handedness of DNA). The CD measurements were done in a JASCO spectropolarimeter with a temperature controller attachment (Peltier) (Figure 3.4). The CD spectra were acquired using quartz cells of 0.1 and 1.0 cm path length. For proteins and DNA the typical concentration used for CD measurements were within 10 μM.

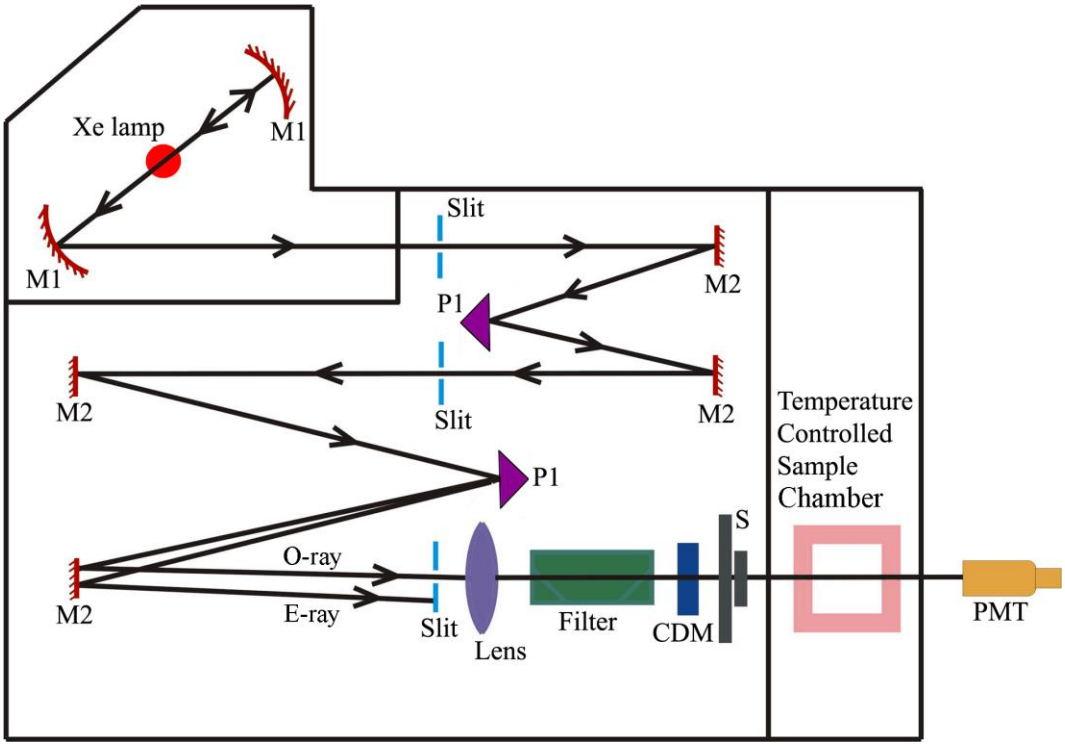

Figure 3.4. *Schematic ray diagram of a circular dichroism (CD) spectropolarimeter. M1, M2, P1, S, PMT, CDM, O-ray and E-ray represent concave mirror, plain mirror, reflecting prism, shutter, photomultiplier tube, CD-modulator, ordinary ray and extraordinary ray, respectively.*

3.1.4. Dynamic Light Scattering (DLS): Dynamic light scattering (DLS), also known as Photon Correlation Spectroscopy (PCS) or Quasi-Elastic Light Scattering (QELS), is one of the most popular techniques used to determine the

hydrodynamic size of the particle. DLS measurements were performed on a Nano S Malvern instruments, U.K. employing a 4 mW He-Ne laser (λ= 632.8 nm) and equipped with a thermostatic sample chamber. The instrument allows DLS measurements in which all the scattered photons are collected at 173˚ scattering angle (Figure 3.5). The instrument measures the time-dependent fluctuation in intensity of light scattered from the particles in solution at a fixed scattering angle. The ray diagram of the DLS setup is shown in Figure 3.5.

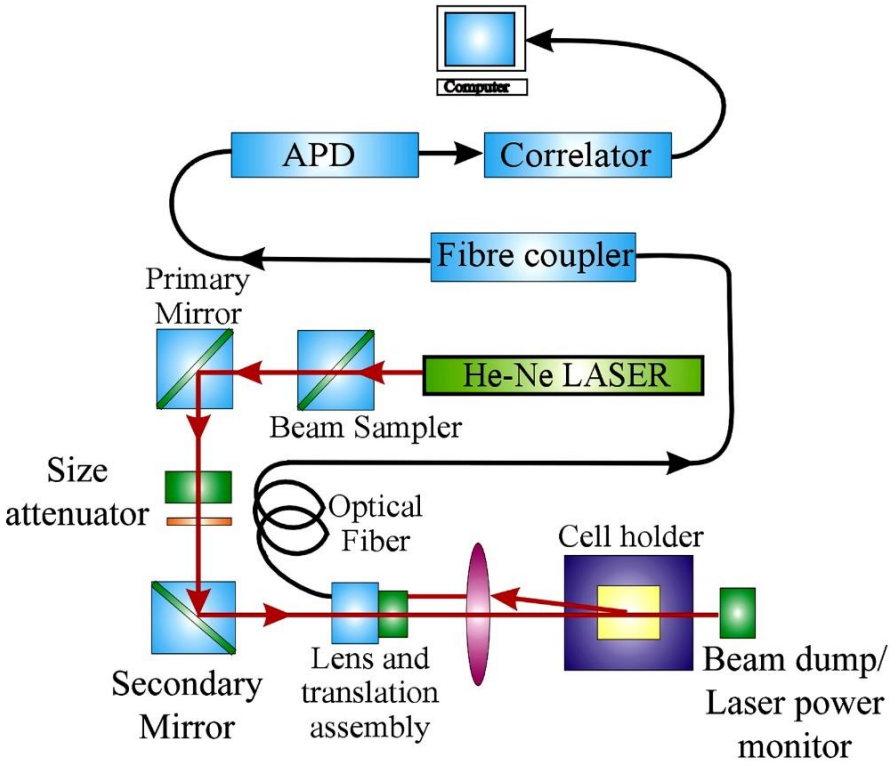

Figure 3.5. *Schematic ray diagram of dynamic light scattering (DLS) instrument. The avalanche photo diode (APD) is connected to preamplifier/amplifier assembly and finally to correlator. It has to be noted that lens and translational assembly, laser power monitor, size attenuator, laser are controlled by the computer.*

It has been seen that particles in dispersion are in a constant, random Brownian motion and this causes the intensity of scattered light to fluctuate as a function of time. The correlator used in a DLS instrument constructs the intensity autocorrelation function G(τ) of the scattered intensity,

$$G(\tau) = \langle I(t)I(t+\tau)\rangle \tag{3.1}$$

where τ is the time difference (the sample time) of the correlator. For a large number of monodisperse particles in Brownian motion, the correlation function (given the symbol G) is an exponential decay function of the correlator time delay τ,

$$G(\tau) = A[1 + B\exp(-2\Gamma\tau)] \tag{3.2}$$

where A is the baseline of the correlation function, B is the intercept of the correlation function. Γ is the first cumulant and is related to the translational diffusion coefficient as, $\Gamma = Dq^2$, where q is the scattering vector and its magnitude is defined as,

$$q = \left(\frac{4\pi n}{\lambda_0}\right)\sin\left(\frac{\theta}{2}\right) \tag{3.3}$$

where n is the refractive index of dispersant, λ_0 is the wavelength of the laser and θ, the scattering angle. For polydisperse samples, the equation can be written as,

$$G(\tau) = A\left[1 + B\left|g^{(1)}(\tau)\right|^2\right] \tag{3.4}$$

where the correlation function $g^{(1)}(\tau)$ is no longer a single exponential decay and can be written as the Laplace transform of a continuous distribution G(Γ) of decay times,

$$g^{(1)}(\tau) = \int_0^\infty G(\Gamma)\exp(-\Gamma\tau)d\Gamma \tag{3.5}$$

The scattering intensity data in DLS are processed using the instrumental software to obtain the hydrodynamic diameter (d_H) and the size distribution of the scatterer in each sample. In a typical size distribution graph from the DLS measurement, X-

axis shows a distribution of size classes in nm, while the Y-axis shows the relative intensity of the scattered light. The diffusion coefficient (D) can be calculated using the hydrodynamic diameter (d_H) of the particle by using the Stoke-Einstein relation,

$$D = \frac{k_B T}{3\pi\eta d_H} \tag{3.6}$$

where k_B, T, d_H, η are Boltzmann constant, temperature in Kelvin, hydrodynamic diameter and viscosity, respectively.

3.1.5. Scanning Electron Microscopy (SEM): Surface characterization of nanomaterials were done by scanning electron microscope FE (field emission)-SEM; JEOL. Ltd., JSM-6500F. An electron-gun is attached to SEM and the electrons from filament triggered by 0 kV to 30 kV voltages. These electrons go first through a condenser lens and then through an objective lens, then through an aperture and finally reach to the specimen. The high energy electrons go a bit

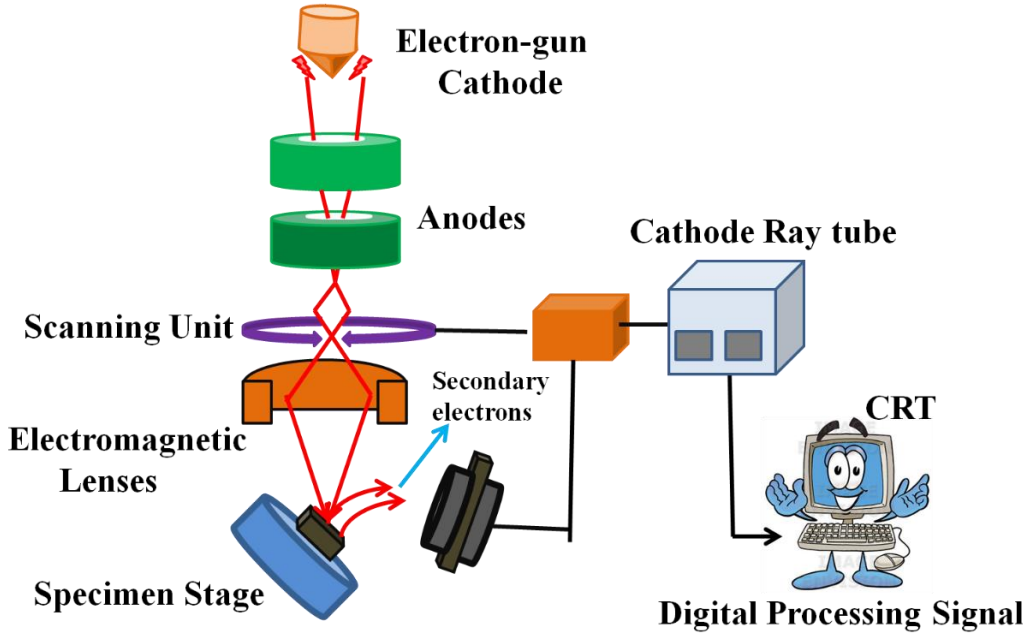

Figure 3.6. *Schematic diagram of typical scanning electron microscope (SEM).*

in the sample and back again give secondary electrons. The signal from secondary electrons are detected by detector and amplified. The ray diagram of the SEM setup is shown in Figure 3.6.

3.1.6. Quasielastic Neutron Scattering (QENS): Neutron scattering experiments were carried out using high energy resolution IRIS spectrometer at the ISIS pulsed Neutron and Muon source at the Rutherford Appleton Laboratory, UK. For neutron scattering measurements, we have used D_2O (99.9% atom D purity) as a solvent to prepare the samples. We have employed IRIS spectrometer in the offset mode with a PG (002) analyzer which provides an energy resolution (ΔE) of 17 μeV. In the used configuration of the spectrometer, energy transfer and *Q*-range were from −0.3 to +1.0 meV and 0.5-1.8 $Å^{-1}$, respectively. Two types of experiments (i) elastic fixed window scan (EFWS) and (ii) QENS were carried out. In EFWS, the elastic intensity within the ΔE of the spectrometer is measured with the temperature. EFWS experiments have been carried out in the temperature range of 285–345K in both heating and cooling cycles [2]. Quasi-elastic Neutron Scattering (QENS) measurements were carried out at 310K during the heating cycle, and at 330K during the cooling cycle. The selection of temperatures for QENS measurements were based on the elastic intensity scan results. For reference, QENS measurements were carried out on pure D_2O at the same temperatures. For instrument resolution, QENS measurement was also carried out on a standard vanadium sample. MANTID software [3] was used to perform standard data reduction. Sample was placed in an annular aluminium sample holder for the neutron scattering experiments. In order to minimize the multiple scattering effects, sample thickness was kept at 0.5 mm. We have used the DAVE software [4] for QENS data analysis. The scattering law for a lipid bilayer may be written in terms of equation 3.7

$$S(Q,E) = S_{lat}(Q,E) \otimes S_{\text{int}}(Q,E) \tag{3.7}$$

where, $S_{lat}(Q,E)$ and $S_{int}(Q,E)$ are the scattering functions associated with lateral and internal motions of the lipid molecules, respectively. The lateral motion is characterized as a continuous diffusion and the corresponding scattering law could be described by a single Lorentzian function $S_{lat}(Q,E) = L_{lat}(\Gamma_{lat},E)$, where Γ_{lat} is the half-width at half-maximum (HWHM) of the Lorentzian function corresponding to lateral motion of the lipid molecules. As for the internal motion, which is localized in character, the scattering law is written by equation. 3.8 as a linear combination of elastic and quasi-elastic components,

$$S_{\text{int}}(Q,E) = A(Q)\delta(E) + (1-A(Q))L_{\text{int}}(\Gamma_{\text{int}},E) \tag{3.8}$$

The quasi-elastic component is approximated as a single Lorentzian function with half-width at half-maximum (HWHM) Γ_{int}. The elastic fraction of the total scattering is called the elastic incoherent structure factor (EISF) and provides information about the geometry of the dynamical process. As evident from equation 3.8, $A(Q)$ is nothing but the EISF. Hence, the scattering law (equation 3.7) for the lipid bilayer becomes

$$S(Q,E) = \left[A(Q) L_{lat}(\Gamma_{lat},E) + (1-A(Q)) L_{tot}(\Gamma_{lat}+\Gamma_{\text{int}},E) \right] \tag{3.9}$$

The effective scattering law that reckons the above described model can be written as [5]

$$S(Q,E) = \frac{1}{80}\left[\begin{array}{l} \left\{ 2\left[1+2j_0(Qb)\right] + 74 p_x B_0(Qa) + 74(1-p_x) \right\} \delta(E) + \\ \frac{1}{\pi}\left\{ 4\left[1-j_0(Qb)\right] \frac{3\tau_{MG}}{9+E^2\tau_{MG}^2} + 74 p_x \sum_{l=1}^{N-1} B_l(Qa) \frac{\tau_l}{1+E^2\tau_l^2} \right\} \end{array} \right] \tag{3.10}$$

where EISF is,

$$EISF = \frac{1}{80}\left[2\left[1+2j_0(Qb)\right] + 74 p_x B_0(Qa) + 74(1-p_x) \right] \tag{3.11}$$

Here b is the distance between the H-atoms (1.8 Å) in methyl group (MG) of the quaternary ammonium headgroup of DODAB. τ_{MG} is the mean residence time, a is the radius of gyration of the alkyl chain, and τ_l is related to rotational diffusion coefficient. The effective scattering law for internal dynamics in the fluid phase is [6]

$$S_{\text{int}}(Q,E)=\frac{1}{80}\left[\begin{array}{l}\left\{2\left(1+2\,j_0(Qb)\right)+\frac{74}{N_C}\sum_{i=1}^{N_C}\left[\frac{3j_1(QR_i)}{QR_i}\right]^2\right\}\delta(E)+\\ \frac{1}{\pi}\left\{4\left(1-j_0(Qb)\right)\frac{3\tau_{MG}}{9+E^2\tau_{MG}^2}+\frac{74}{N_C}\sum_{i=1}^{N_C}\sum_{\{l,n\}\neq\{0,0\}}(2l+1)A_n^l(QR_i)\frac{\left(x_n^l\right)^2 D_i/R_i^2}{\left(\left(x_n^l\right)^2 D_i/R_i^2\right)^2+E^2}\right\}\end{array}\right] \quad (3.12)$$

where N_C = 18 is the number of the CH_2 units in the lipid tail. From equation 8 the EISF can be expressed as

$$EISF=\frac{1}{80}\left[2\left[1+2\,j_0(Qb)\right]+\frac{74}{N_C}\sum_{i=1}^{N_C}\left[\frac{3j_1(QR_i)}{QR_i}\right]^2\right] \quad (3.13)$$

where R_i and D_i are the radius and the diffusion coefficient corresponding to the i^{th} site of the lipid tail, and can be written as:

$$R_i=\frac{i-1}{N_C-1}\left[R_{\max}-R_{\min}\right]+R_{\min}$$

and

$$D_i=\frac{i-1}{N_C-1}\left[D_{\max}-D_{\min}\right]+D_{\min}$$

3.1.7. Fourier Transform Infrared (FTIR) Measurement: FTIR spectroscopy is a technique that can provide very useful information about functional groups in a sample. An infrared spectrum represents the fingerprint of a sample with absorption peaks which correspond to the frequencies of vibrations between the

bonds of the atoms making up the material. Because each different material is a unique combination of atoms, no two compounds produce the exact same infrared spectrum. Therefore, infrared spectroscopy can result in a positive identification (qualitative analysis) of every different kind of material. In addition, the size of the peaks in the spectrum is a direct indication of the amount of material present. The two-beam Michelson interferometer is the heart of FTIR spectrometer. It consists of a fixed mirror (M4), a moving mirror (M5) and a beam-splitter (BS1), as illustrated in Figure 3.7. The beam-splitter is a laminate material that reflects and transmits light equally. The collimated IR beam from the source is partially transmitted to the moving mirror and partially reflected to the fixed mirror by the beam-splitter. The two IR beams are then reflected back to the beam-splitter by the mirrors. The detector then sees the transmitted beam from the fixed mirror and reflected beam from the moving mirror, simultaneously. The two combined beams

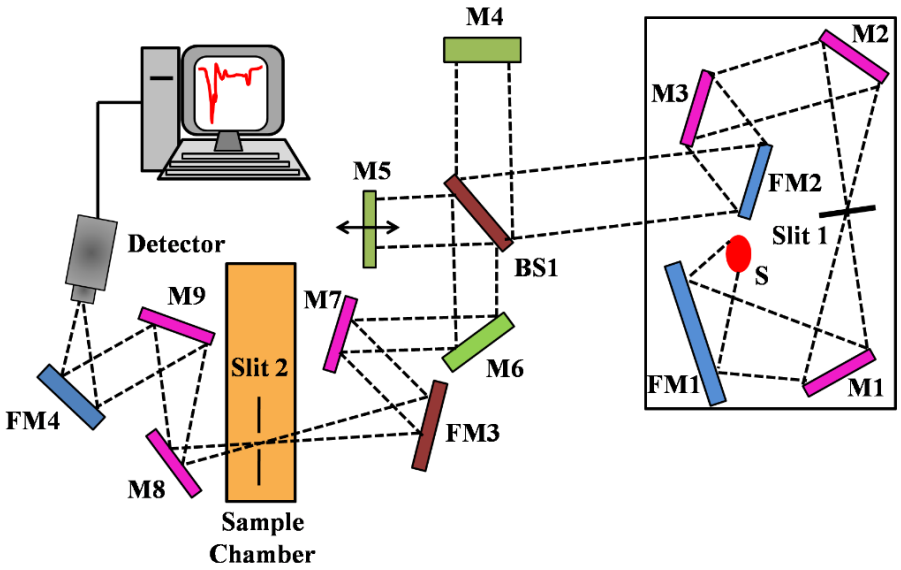

Figure 3.7. *Schematic of Fourier Transform Infrared (FTIR) spectrometer. It is basically a Michelson interferometer in which one of the two fully-reflecting mirrors is movable, allowing a variable delay (in the travel-time of the light) to be included in one of the beams. M, FM and BS1 represent the mirror, focussing mirror and beam splitter, respectively. M5 is a moving mirror.*

interfere constructively or destructively depending on the wavelength of the light (or frequency in wavenumbers) and the optical path difference introduced by the

moving mirror. The resulting signal is called an interferogram which has the unique property that every data point (a function of the moving mirror position) which makes up the signal has information about every infrared frequency which comes from the source. Because the analyst requires a frequency spectrum (a plot of the intensity at each individual frequency) in order to make identification, the measured interferogram signal cannot be interpreted directly. A means of "decoding" the individual frequencies is required. This can be accomplished via a well-known mathematical technique called the Fourier transformation. This transformation is performed by the computer which then presents the user with the desired spectral information for analysis. FTIR measurements were performed on a JASCO FTIR-6300 spectrometer (transmission mode) using CaF_2 windows with a spacer thickness of 25 μm.

3.1.8. Microfluidics Methodology: Figure 3.8 portrays the used microfluidics (MF) system, represented as the Y-shaped MF chip. The specially designed MF chip with the connectors and the syringe pumps (Atlas-ASP011) were bought from

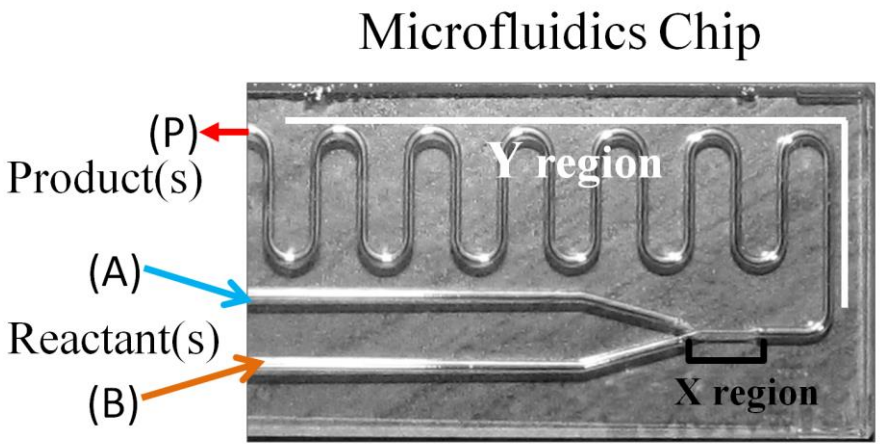

Figure 3.8. *Custom designed microfluidics chip to monitor fast reaction. Two specific regions are shown: X, for fast sub-100 ns kinetics and Y, for slower kinetics [7].*

Dolomite, UK and Syrris Ltd., UK respectively. The specially designed MF chip consists of two inlets and a common outlet. The chip was made out of optically

transparent glass, which can sustain higher temperature if required. The diameter of the microchip (440 μm) was designed to withstand high flow rates. A small special region just after the confluence (X region) with a diameter of 150 μm and a length scale around 2200 μm was deliberately added in the design, after which it expands to 440 μm (Y region). The small diameter guarantees a higher fluid front

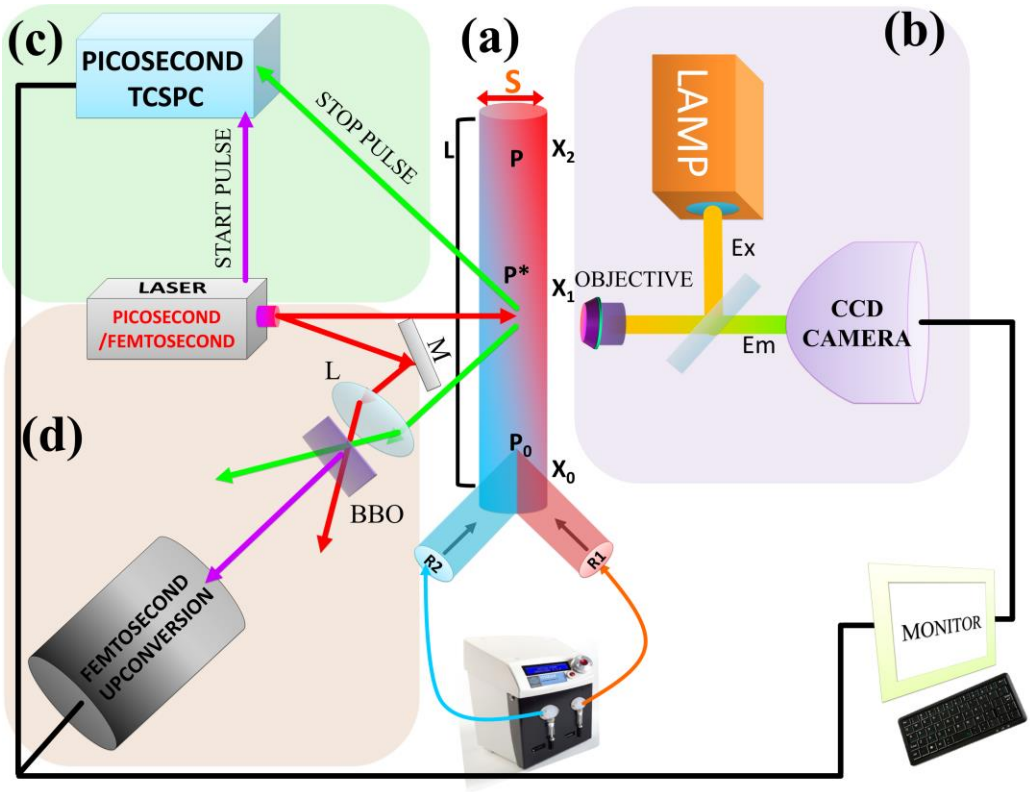

Figure 3.9. *(a) Schematic presentation of the developed microfluidics platform. L denotes the flow path length, X_i are the positions for measurements along the channel and S is the cross section of the micro-channel. (b) The fluorescence microscope coupled to the microfluidics channel. A CCD camera captures images of the ongoing reactions inside the micro-channel. (c) Picosecond resolved fluorescence technique for the collection of decay profiles along the micro-channel. (d) Femtosecond upconversion technique combined with the microfluidics platform for studying ultrafast dynamics.*

velocity with reasonably low Reynolds number. The special geometry empowers to study very fast kinetics with a time resolution in the order of nanoseconds. For the study of slow kinetics in the range of millisecond to microsecond, the other portion of the microchannel with a diameter of 440 μm is suitable. The two inlets were attached to a syringe pump by capillary tubes. The capillaries were passed

through the shaft of the holder prior to connection with the MF chip. The reagents were propelled using the syringe pump and the total volumetric flow rate was adjusted according to the requirements. The term "flow rate" refers to the combined volumetric flow rate of the reagents through the micro-channel. The schematic of the MF channel is presented as a tube with a cross section S, length L, and total volume V=SL (Figure 3.9). The streams converge and their mixing starts in the micro-channel junction, position X_0 in the Figure 3.9. The total length of the flow path of the micro-channel is around 10 cm. Fluorescence images were captured with a fluorescence microscope (BX-51, Olympus America, Inc.) equipped with a 100 W mercury arc lamp which was used as the excitation source (UV light excitation) and a DP72 CCD camera (Figure 3.9). The excitation light was cut off by using a standard filter and the fluorescence was collected through a 10× objective. The image processing and analysis were done by the 'analySIS' software provided with the microscope. A region of interest (ROI) was selected at a specific height and width. This ROI was used to obtain an intensity profile along the microchannel. Intensity profiles were acquired at a particular microchannel distance from the initial mixing confluence. The RGB analysis was performed wherever required. This channel distance was converted into the reaction time (t_n) by dividing it by the velocity of the flow (U [m/s]), obtained from the known volumetric flow rate and cross-section (S) of the micro-channel [7, 8].

3.1.9. Fluorescence Microscope: Commercially available fluorescence microscope (BX-51, Olympus America, Inc.) was used in our study. The light source is usually a mercury-vapor lamp. For bright field, Tungsten-halogen lamp was used. In particular, an inverted setup with a mercury-vapor lamp as light source is shown. The dichroic mirror, excitation and emission filter are joined together within the filter cube (Figure 3.10). Since mercury-vapor lamps emit light over the whole optical spectrum as well as in the ultraviolet range, an optical excitation filter is used to isolate one specific wavelength. Due to the Stokes shift, it is possible to separate excitation and emission light in the same light path optically via a

dichroic mirror. This way, only the emission light is collected by the objective. An emission filter helps to suppress unwanted background light.

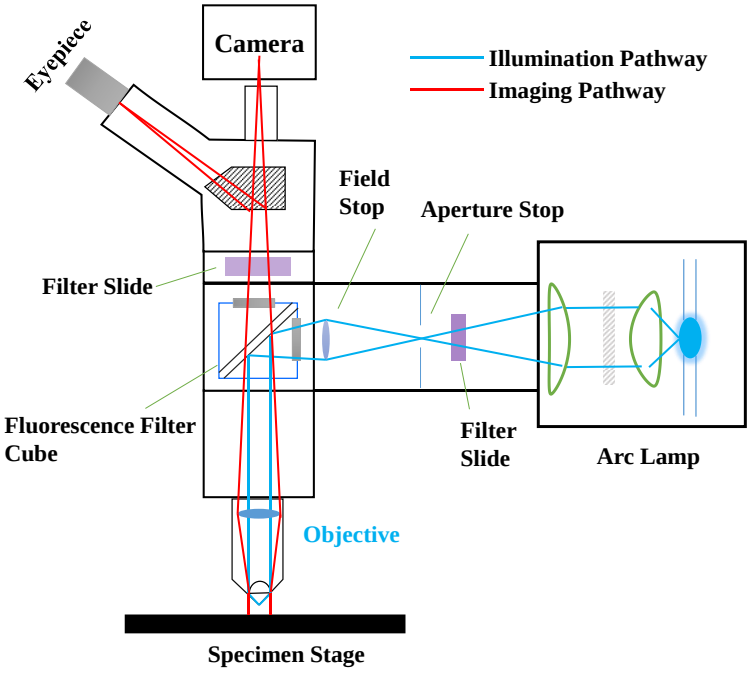

Figure 3.10. *Schematic presentation of the fluorescence microscope.*

3.1.10. Light Source Used for Irradiation: A UV light source (LED) of 400–410 nm and ~50 mW/cm² power was used to irradiate samples under UV-blue light source.

3.2. Sample Preparation: In this section the different sample preparation methods have been discussed.

3.2.1. Chemicals Used: Dimethyldioctadecylammonium bromide ≥98% (DODAB), L-α-phosphatidylcholin from soybean (PC), histone from calf thymus (type III-SS) (H1), calf thymus DNA (CT-DNA), bovine pancreatic deoxyribonuclease I (DNase I), polyethylene glycol 3350 (PEG), sodium dodecyl sulfate (SDS), sodium bis(2-ethylhexyl)sulfosuccinate (AOT), benzyl hexadecyldimethylammonium chloride (BHDC), α-chymotrypsin (CHT), Ala-Ala-Phe-7-amido-4-methylcoumarin (AMC), tetraethyleneglycolmonododecyl ether (Brij-30), triton X-100 (TX100), doxorubicin

hydrochloride (DOX), acridine orange 10-nonyl bromide (NAO) and 8-anilino-1-naphthalenesulfonic acid ammonium salt (ANS) were purchased from Sigma-Aldrich (Saint Louis, USA). 1-monooleoyl-rac-glycerol (MO) was procured from TCI Co. Ltd. The fluorescent probes rifampicin (Rf), ethidium bromide (EB) and crystal violet (CV) were purchased from Molecular probes. Coumarin 500 (C500) was from Exciton. Cetyltrimethylammonium bromide (CTAB), isooctane and benzene were purchased from Spectrochem (Mumbai, INDIA). Butanol, glycerol and calcium chloride were purchased from Merck (Mumbai, INDIA). Tris–HCl, magnesium chloride, agarose, boric acid and EDTA were from SRL (Mumbai, INDIA). HPLC-grade oligonucleotide substrates of 20-mer sequences, 5′-GCGTGTAAACGATTCCACGC-3′ and its complement were purchased from Trilink Technologies (San Diego, CA).

3.2.2. Synthesis of DODAB and DODAB-MO Vesicles: 20 mM and 70 mM DODAB vesicles were prepared by mixing the appropriate amounts of DODAB powder in H_2O. The obtained mixture was kept under magnetic stirring at 65 ^{0}C for 30–45 min, which yielded an almost transparent fluid. To prepare the aqueous dispersions of DODAB-MO (2:1), defined aliquots from the stock solutions of MO were mixed under vigorous stirring to an aqueous solution of DODAB at 70˚C [9, 10].

3.2.3. Synthesis of Photochromic DHI: The photochromic DHI was synthesized by the electrophilic addition of electron-deficient spirocyclopropenes through the nitrogen atom of the n-heterocyclic pyridazines in dry ether in the absence of light under nitrogen atmosphere for 24 h. The final photochromic DHI was obtained as pale yellow crystals after recrystallization from the proper solvent. Pure products were obtained after purification by column chromatography on silica gel using dichloromethane as eluent [11].

3.2.4. Synthesis of Liposomes: The liposomes were prepared by using the standard ethanol injection methods [12]. Typically, the phospholipids were dissolved in the ethanol solution and then injected rapidly in PBS buffer (pH 7.4) followed by vigorous stirring for half an hour. Finally, the ethanol and a part of water were removed by rotary evaporation under reduced pressure.

3.2.5. Synthesis of Liposomes-DHI Solution: Liposome-DHI solutions were prepared by adding a requisite amount of DHI (1.5 mM) to the liposome solution (20 mM) with stirring for 6 h. To ensure complete complexation of DHI with the liposome free DHI was removed by centrifuging the liposome encapsulated DHI at 5000 rpm for 2 min.

3.2.6. DOX Load and Release: The DOX solution was prepared in PBS buffer, separately. Then the DOX was dropwise added to the liposome-DHI solution and incubated (70 ^{0}C) followed by vigorous stirred for 6 h. Free DOX was removed by centrifuging the liposome encapsulated DOX at 14000 rpm for 50 min. The absorbance of encapsulated DOX ($A_{encapsulated}$) was obtained by using UV-visible spectrophotometer at 480 nm after destructing liposomes by Triton X-100. The encapsulated efficiency EE was found to be 68.5 % was calculated by following equation:

$$EE\ \% = (A_{encapsulated} / A_{total})*100 \qquad (3.14)$$

Where A_{total} was the absorbance of DOX added in solution originally.

The drug release behavior was measure by monitoring the released from dialysis tube. For this 1 mL DOX-loaded liposomes-DHI with and without UVA-irradiation for 20 min were transferred to the dialysis tube (MWCO 14 kDa), and then submerged into 250 mL PBS buffer (pH 7.4) solution under stirring condition at 37 ^{0}C. The DOX release from the liposomes-DHI was measured by Jobin Yvon Fluorolog fluorimeter. The release efficiency RE of liposomes was calculated using following equation:

$$RE\% = (A_t / A_{encapsulated})*100 \qquad (3.15)$$

Where A_t was the emission at 480nm at time t.

3.2.7. Cytotoxicity Assay: MTT assay was performed to observe the cytotoxic effect of DOX loaded liposomes and also to assess the photoinduced drug delivery. HeLa cells was grown in Dulbecco's modified eagle's medium (DMEM; HiMedia) supplemented with 10% fetal bovine serum (FBS; Gibco) and 1.0% penicillin/streptomycin (HiMedia) and cultured at 37 ^{0}C, 5.0% CO_2 , and 95% humidity. 1.0 x10^4 cells were seeded in each well of a 96 well plate and cultured in 10% FBS-supplemented DMEM for the photoresponsive treatment. Cells were incubated with PC-DHI, PC-DOX, and PC-DHI-DOX (individual concentration of PC and DOX in the complex were 2 mM and 2 µM, respectively) for 1 h and were exposed to UVA light source for 15 min. After 24h of incubation, the MTT assay was performed using a MTT assay kit (CCK003, Himedia) as per the manufacture's instruction. For in vitro studies, MTT assay was done in similar way by incubating the cell with drug obtained from dialysis of PC-DOX, and PC-DHI-DOX under dark and UVA irradiation, respectively.

3.2.8. Flow Cytometry: 5X10^5 cells were seeded in each well of a 6 well plate and cultured in 10% FBS-supplemented DMEM for 12h. After that the cells were treated with PC-DOX liposome and PC-DHI-DOX liposome both in absence and presence of UVA light. Post- treatment, cells were incubated for 4h. Then, the doxorubicin up take by the cells was checked by flow cytometry (BD accuri C6) and data was analyzed using BD accuri C6 software.

3.2.9. Fluorescence Microscopy Studies: Micrographs of HeLa cells were taken using Leica TCS SP8 confocal fluorescence microscope by staining cell using Hoechst.

3.2.10. Preparation of DNA–CTAB Complex: The stock solution of the calf thymus DNA was diluted with the potassium phosphate buffer (50 mM, pH 7) so that the final concentration of the genomic DNA in nucleotide unit was 3 mM. To

this solution, equimolar ratio of CTAB surfactant was mixed gently with continuous stirring. The resulting precipitate was separated and washed several times with the buffer solution. After that the precipitate was lyophilized to prepare condensate powder [13].

3.2.11. Assay of DNA Hydrolysis by Nucleases: DNase I was assayed in a buffer of 2.5 mM $MgCl_2$, 0.5 mM $CaCl_2$ and 10 mM Tris–HCl (pH 7.5) at 25 ^{0}C. The reactions were performed with 0.5 μM of DNase I and 10 μM dsDNA (20-mer) as a substrate. For quantitative analysis of the hydrolysis reaction of DNase I, the dsDNA was staining with ethidium bromide (EB/DNA = 1:1). DNA hydrolysis was evaluated according to the amount of residual substrate (%). The amount of the residual substrate was estimated as follows:

$$R(\%) = S_T X100/S_0 \quad (3.16)$$

where, R is residual substrate, S_T is fluorescence intensity of substrate after time T and S_0 is fluorescence intensity of substrate at zero time.

For kinetics studies, the dsDNA concentration was varied from 1 to 10 μM for DNase I. The initial rates (v) were estimated from the data for the first 30% of the reaction, where residual substrate varies linearly with time. The values of 1/v were plotted against respective 1/ [DNA] to obtain the kinetic parameters (K_m and V_{max}) from Michaelis–Menten equation,

$$1/v = (k_m/v_{max}*[S])+(1/v_{max}) \quad (3.17)$$

where [S] indicates substrate concentration.

3.2.12. Gel Electrophoresis: The electrophoretic mobility of calf thymus DNA and 20-mer dsDNA complexes upon hydrolysis by DNase I in 2.5 mM $MgCl_2$, 0.5 mM $CaCl_2$ and 10 mM Tris–HCl buffer solution (pH 7.5) was determined by gel electrophoresis using 1.5% agarose gels. Experiments were run at 100 V for 15 min in case of calf thymus DNA and 5 min for 20-mer DNA. Since the calf thymus DNA and 20-mer dsDNA were labelled with ethidium bromide, a photograph of

the gel was taken under ultraviolet illumination of gel documentation and image analysis system Syngene, UK Model:INGENIUS 3 without staining the gel with ethidium bromide.

3.2.13. Enzyme Kinetics using Microfluidic Technique: In study of the enzyme kinetics an H-shaped microfluidics channel with two inlets, one for the enzyme CHT (100 µM) in the reverse micelles BHDC/Benzene, AOT/Benzene, Brij-30/benzene, TX100/cyclohexane(50%)/benzene(50%) at w_0 = 8 and another for the substrate AMC (15 µM) in benzene solution, was used to generate the time gradient of the CHT–AMC complex along the direction of flow in the channel.

References

[1] T.-C.S.P. Counting, DV O'Connor and D. Phillips, in, Academic, London, 1984.

[2] S. Choudhury, P.K. Mondal, V. Sharma, S. Mitra, V.G. Sakai, R. Mukhopadhyay, S.K. Pal, Direct observation of coupling between structural fluctuation and ultrafast hydration dynamics of fluorescent probes in anionic micelles, *J. Phys. Chem. B,* 119 (2015) 10849-10857.

[3] O. Arnold, J.-C. Bilheux, J. Borreguero, A. Buts, S.I. Campbell, L. Chapon, M. Doucet, N. Draper, R.F. Leal, M. Gigg, Mantid—Data analysis and visualization package for neutron scattering and μ SR experiments, *Nucl. Instrum. Methods. Phys. Res. A,* 764 (2014) 156-166.

[4] R.T. Azuah, L.R. Kneller, Y. Qiu, P.L. Tregenna-Piggott, C.M. Brown, J.R. Copley, R.M. Dimeo, DAVE: A comprehensive software suite for the reduction, visualization, and analysis of low energy neutron spectroscopic data, *J. Res. Natl. Inst. Stand. Technol.,* 114 (2009) 341–358.

[5] D. Siegel, W. Green, Y. Talmon, The mechanism of lamellar-to-inverted hexagonal phase transitions: a study using temperature-jump cryo-electron microscopy, *Biophys. J.,* 66 (1994) 402-414.

[6] P. Dubey, H. Srinivasan, V. Sharma, S. Mitra, V.G. Sakai, R. Mukhopadhyay, Dynamical Transitions and Diffusion Mechanism in DODAB Bilayer, *Sci. Rep.,* 8 (2018) 1862.

[7] S. Batabyal, S. Rakshit, S. Kar, S.K. Pal, An improved microfluidics approach for monitoring real-time interaction profiles of ultrafast molecular recognition, *Rev. Sci. Instrum.,* 83 (2012) 1-6.

[8] P. Singh, D. Mukherjee, S. Singha, R. Das, S.K. Pal, Modulation of kinetic pathways of enzyme-substrate interaction in a microfluidic channel: Nanoscopic water dynamics as a switch, *Chem. Eur. J.,* (2019) doi: 10.1002/chem.201901751.

[9] P. Singh, V.K. Sharma, S. Singha, V. García-Sakai, R. Mukhopadhyay, R. Das, S.K. Pal, Unravelling the role of monoolein in fluidity and dynamical response of a mixed cationic lipid bilayer, *Langmuir,* 35 (2019) 4682-4692.

[10] P. Singh, S. Choudhury, V. Sharma, S. Mitra, R. Mukhopadhyay, R. Das, S.K. Pal, Modulation of solvation and molecular recognition of a lipid bilayer under dynamical phase transition, *ChemPhysChem,* 19 (2018) 2709-2716.

[11] S.A. Ahmed, Z.A. Hozien, A.-M.A. Abdel-Wahab, S.Y. Al-Raqa, A.A. Al-Simaree, Z. Moussa, S.N. Al-Amri, M. Messali, A.S. Soliman, H. Dürr, Photochromism of dihydroindolizines. Part 16: Tuning of the photophysical behavior of photochromic dihydroindolizines in solution and in polymeric thin film, *Tetrahedron,* 67 (2011) 7173-7184.

[12] C. Jaafar-Maalej, R. Diab, V. Andrieu, A. Elaissari, H. Fessi, Ethanol injection method for hydrophilic and lipophilic drug-loaded liposome preparation, *J. Liposome Res.,* 20 (2010) 228-243.

[13] P. Singh, S. Choudhury, G.K. Chandra, P. Lemmens, S.K. Pal, Molecular recognition of genomic DNA in a condensate with a model surfactant for potential gene-delivery applications, *J. Photochem. Photobiol. B,* 157 (2016) 105-112.

Chapter 4

Spectroscopic Studies on Dynamics-Driven Molecular Recognition of Biomimetic Systems

4.1. Introduction: In biological membranes the lipids can exist in multiple phases [1-3]. Although the bilayer lamellar states are relevant to biomembranes, non-bilayer lipid phases, such as hexagonal and cubic phases may relate to transient event in the biomembranes including fusion, fission and pore-formation [4-6]. Dioctadecyldimethylammonium bromide (DODAB) is a simple-structure double chained cationic surfactant and widely used as model system for *in vitro* studies on colloids and interfaces [7-9]. DODAB is a bilayer forming lipid, which reveals lamellar structure analogous to biological membrane [10, 11]. While the dynamics of lipid bilayers are important for various processes including cell signalling, membrane protein interaction, permittivity and endocytosis, the dynamics also plays a decisive role in molecular recognition of various drugs and their transport [12-15]. Thus *in vitro* studies on DODAB bilayers likely provides in depth understanding of the physical properties of biological membranes [16-18].

A detailed structural characterization of the neat DODAB aqueous dispersion with several concentrations of the lipid has already been investigated using various techniques [7, 16, 19, 20]. Particularly, thermotropic phase behaviours of the system reveals coagel, subgel, gel and liquid crystalline phases [16, 17, 21]. In the dilute DODAB aqueous dispersion the coagel phase is found to be most stable multilamellar crystalline phase, which transforms to liquid crystalline phase at 54 ^{0}C upon heating [22]. On the other hand, subgel phase is formed during cooling the dilute dispersion in the gel phase to a temperature below 15 ^{0}C [16, 23]. The interesting thermotropic behaviours of the DODAB lipid dispersion offer unique opportunity to study biologically relevant bilayer structures without additional new component

(physical/chemical). Although the structural aspects of almost all the phases of DODAB are explored in detail [24, 25], the hydration properties of the associated water molecules in the close vicinity of the lipid headgroups is relatively less attended in the literature and is one of the motives of the present study. In an earlier report using FTIR studies, it has been concluded that the largest difference between subgel and coagel phases lies in the hydration degree of the lipid headgroups, while the only significant difference between the gel phase and the subgel is the change of the lipid alkyl chain packing [16]. A recent report employing quasi elastic neutron scattering (QENS) and molecular dynamics (MD) simulation studies explored dynamical transition and diffusion mechanism in DODAB bilayer [7]. The study reveals slower rotational diffusion of alkyl chain ($5.3X10^{10}$ s^{-1}) and higher residence time of hydrogen (6.7 ps) in coagel phase compared to those in gel phase ($6.8X10^{10}$ s^{-1} and 5.2 ps). The observation is concluded to be due to lower hydration level and denser packing of the lipids in the coagel phase.

In the first work of this chapter, we have incorporated a well-known solvation probe Coumarin 500 (C500) in the DODAB lipid bilayer and followed the dynamics of water molecules with picosecond resolution in different phases [26]. We have also followed the solvation dynamics of an anionic dye 8-anilino-1- naphthalenesulfonic acid ammonium salt (ANS) in the lipid-water interface of DODAB multilamellar vesicles through various phases. The molecular recognition of an anti-tuberculosis drug rifampicin in the lipid bilayer at various temperatures has also been followed by using picosecond-resolved Förster resonance energy transfer (FRET) between ANS and the drug. The dynamical flexibility of the lipid bilayer at different phases has also been investigated by picosecond resolved polarization gated fluorescence spectroscopy. Special attention has been paid on the hysteresis of phases during the heating cycle, and corresponding effect on the solvation dynamics in the lipid bilayer and in close proximity of the lipid-water interface.

Biological membranes play an important role in maintaining cellular, structural and functional integrity. Usually the lipids in the membrane are often structurally heterogeneous having different acyl chain compositions [27]. The persistence of fluidity in a cell membrane is important for optimum diffusion of the vital components including lipids and proteins in the membrane. The fluidity is also important in the maintenance of dynamics and function of membrane proteins leading to essential cellular functions including division, differentiation and general adaptation to the environment [28, 29]. One of the ways to maintain the "fluidity" in the cell membrane of an organism is reported to be through regulation of double bonds in the fatty acid of the membrane lipids [30]. At a low temperature, when the membrane fluidity decreases, plants and cyanobacteria respond by insertion of unsaturation in the fatty acids of lipids so that the membranes attain a state of higher fluidity [31]. In addition to membrane "fluidity" hydration of the lipid bilayer plays a crucial role in determining the function of biomembranes by affecting their integrity and dynamics [32]. Therefore, it is of key interest to probe quantitatively how the presence of an unsaturated lipid modulates the membrane fluidity of a model bilayer forming lipid when a change in temperature is effected, and how the change in membrane fluidity is reflected on the dynamics of water molecules in the lipid-water interface. To this end, liposomes and surfactant vesicles are often regarded as adequate membrane models [33]. Although, natural lipids e.g., phospholipids are important constituents of the cell membrane the typical phospholipid structure is by no means a prerequisite for vesicle formation to model cell membranes [33], because in many respects, vesicles prepared from simple synthetic lipids mimic the properties of vesicles prepared from natural phospholipids [34]. In fact, the properties of synthetic lipids appear remarkably relevant for obtaining a better understanding of the fundamental aspects of the much more complex natural membranes [35, 36]. As for example, morphological transformations of cationic vesicles based on Dioctadecyldimethylammonium bromide (DODAB) were found to be reminiscent of endocytosis and intracellular membrane traffic [35, 36]. So, in

the present work we have chosen Dioctadecyldimethylammonium bromide (DODAB) as the model bilayer forming lipid which provides lamellar structure [10, 37] analogous to biological membranes, and monoolein (MO) as the unsaturated lipid.

This motivates the other work in this chapter where neutron scattering techniques were employed to monitor the effect of an unsaturated lipid MO on the phase behaviour and dynamical characteristics of the bilayer of a model cationic lipid DODAB. Furthermore, we have carried out measurements of TDFSS and polarization-gated anisotropy of a novel fluorophore Acedan-18 to probe the relaxation dynamics of the lipid bilayer of DODAB in the coagel phase and the fluid phase in presence and absence of an unsaturated lipid (MO). Quasielastic neutron scattering (QENS) and polarization-gated anisotropy measurements showed that MO significantly affects the dynamics of the DODAB bilayer and these effects are found to be strongly dependent on the phase of the lipid bilayer. In the coagel phase, MO acts as a plasticizer and enhances the dynamics of the cationic lipids (DODAB) in the bilayer, indicating significantly increased flexibility of the DODAB/MO lipid vesicles relative to pure DODAB. On the other hand, in the fluid phase MO acts as a stiffening agent, restricting the dynamics of the lipid bilayer. From the TDFSS measurements, incorporation of unsaturated MO is found to correspond to faster hydration dynamics due to increased structural flexibility of the lipid membrane, whereas, it causes slower dynamics of water molecules for structurally rigid lipid vesicles in the fluid phase.

4.2. Results and Discussion:

4.2.1. Modulation of Solvation and Molecular Recognition of a Lipid Bilayer under Dynamical Phase Transition [38]: Figure 4.1.a and Figure 4.1.c display fluorescence spectra of C500 and ANS incorporated in dilute aqueous dispersions of DODAB at different temperatures. On an increase in temperature from 10 ^{0}C to 40 ^{0}C (i.e. subtransition temperature from subgel to gel transition) the lipid hydrocarbon tails melt followed by increased hydration

of the head groups of lipids [22] which causes a red shift of the emission peak maximum. The observed red shift is much larger for C500 (~200 cm^{-1}) than ANS (~130 cm^{-1}) indicating more pronounced effect of increased hydration of the lipid headgroups for the former probe than the later, which may be ascribed to their different locations in the lipid bilayer. C500 being a neutral

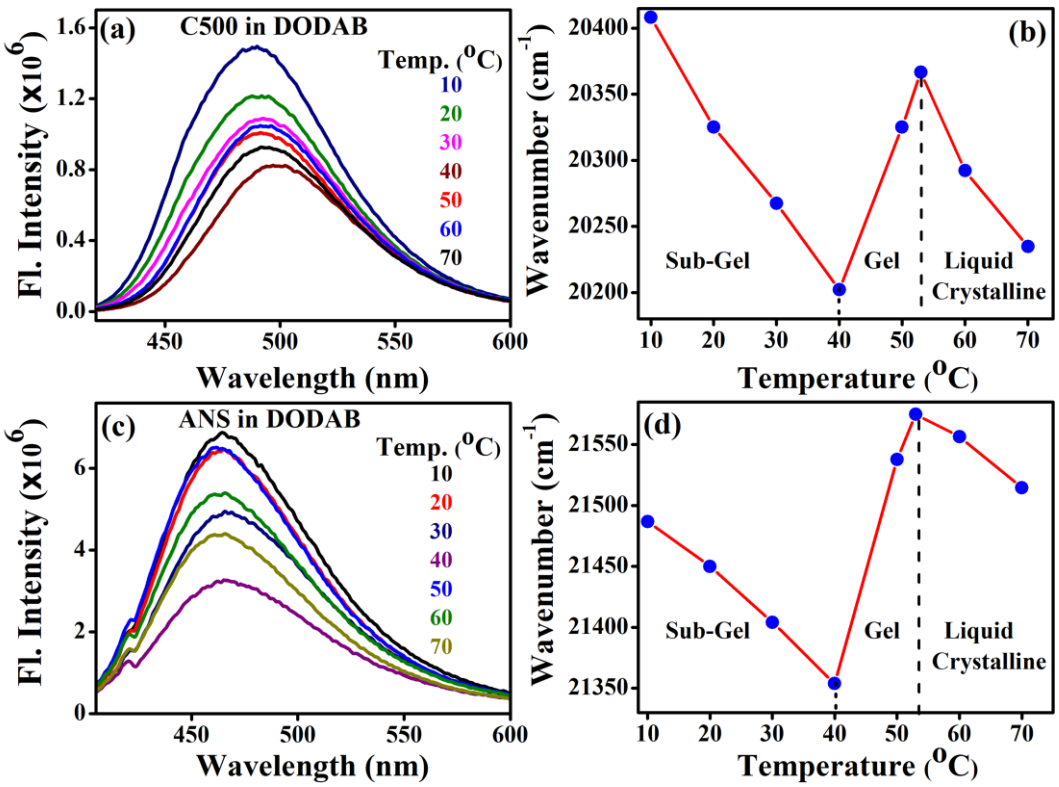

Figure 4.1. *(a) Fluorescence emission spectra of C500 in DODAB (20 mM) with variation of temperature. (b) Plot of emission maximum (λ_{max}) of C500 with temperature in aqueous DODAB. (c) Fluorescence emission spectra of ANS in DODAB (20 mM) with variation of temperature. (d) Plot of emission maximum (λ_{max}) of ANS with temperature in aqueous DODAB.*

dye is likely located deeper at the level of the lipid hydrocarbon chains, whereas ANS bearing a negatively charged sulphonate group is anchored at the lipid-water interface due to strong electrostatic interactions with the cationic head group of DODAB. In consequence, the effect of increased hydration due to melting of lipid tails following an increase in temperature (from 10 ^{0}C to 40 ^{0}C) becomes more pronounced for C500 than ANS. With a further increase in temperature, the fluorescence intensity of both ANS and C500 increases until ~53 ^{0}C, corresponding grossly to the main transition (from

gel to liquid crystalline phase) of DODAB and decreases thereafter. A moderate blue shift in the emission spectrum is also observed on an increase in temperature in the DODAB gel phase (from 40 ^{0}C until ~53 ^{0}C), hinting that both ANS and C500 senses a hydrophobic environment when temperature is raised beyond 40 ^{0}C.

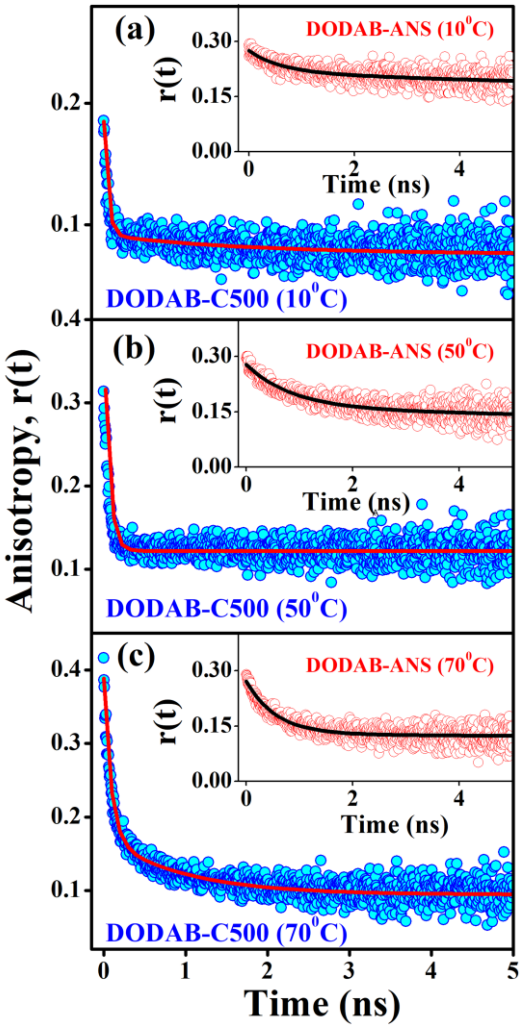

Figure 4.2. *Time-resolved anisotropy of DODAB-C500 at different temperature (a) 10 ^{0}C, (b) 50 ^{0}C and (c) 70 ^{0}C. Insets depict the time-resolved anisotropy of DODAB-ANS at corresponding temperature.*

To probe the microenvironment of the lipid bilayer in different phases (subgel, gel and liquid crystalline) time-resolved anisotropy decays (Figure 4.2) of ANS and C500 in DODAB vesicles were measured at three different temperatures. These decays were found to be bi-exponential in nature, which is attributed mainly to the occurrence of various kinds of rotational motions, rather than to different locations of the probe in the vesicles [39, 40]. The

anisotropy decays of ANS and C500 in DODAB vesicles are analyzed by the two-step wobbling in a cone model [41] where the rotational motion of the probe in the lipid bilayer is characterized by two time constants. According to the two-step wobbling in a cone model, the probe undergoes a

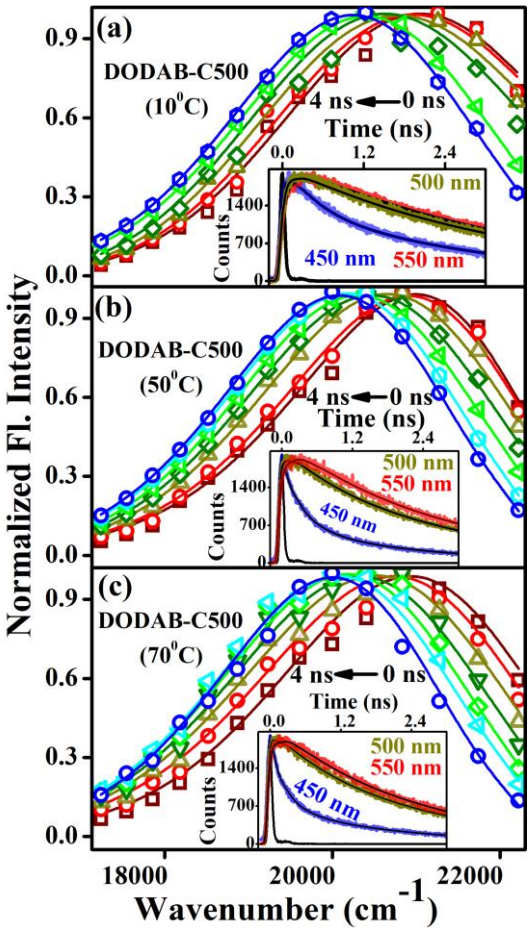

Figure 4.3. *Time-resolved emission spectra (TRES) of C500-DODAB are shown at different temperature (a) 10 ^{0}C, (b) 50 ^{0}C and (c) 70 ^{0}C. Insets depict the corresponding Picosecond-resolved transient of C500 at three different wavelengths.*

slow lateral diffusion at or near the lipid-water interface and a fast wobbling motion in the lipid bilayer, with both of these motions being coupled to the rotation of the lipid vesicles as a whole [41]. Table 4.1 lists the rotational-relaxation parameters obtained from fitting of anisotropy decay curves. The rotational-relaxation time, given by the average reorientational time of the probe is faster for C500 than ANS in all the phases (Table 4.1). Relative to the negatively charged ANS, the neutral dye C500 incorporates deeper into the

lipid bilayer exhibiting lower average rotational relaxation time (<τ_r>, Table 4.1.) which is consistent with higher degree of mobility or lower degree of rigidity of the local environment [42, 43]. Furthermore, C500 displays lower mobility (higher <τ_r>) below and above the transition temperature, but a sharp decrease of <τ_r> is noted around this temperature (50 ^{0}C). This variation in average rotational relaxation time for C500 is similar to the previously observed variation in fluorescence anisotropy [44] in DODAB vesicles, and may be ascribed to increased cooperativity of the melting process during transition from gel to liquid crystalline phase. On the other hand, the time-resolved anisotropy of ANS becomes faster upon subgel to gel and gel to liquid crystalline transition of DODAB vesicles (insets of Figure 4.2) which is reflected by decreasing average reorientational time (Table 4.1) indicating increased flexibility of the local environment of the dye. As ANS is anchored at the head group region of the lipid-water interface it senses increasing flexibility of the headgroup region due to increased hydration of the lipid headgroups associated with melting process of the lipid tails during transition from subgel to gel and gel to liquid crystalline phases.

Table 4.1. *Time-resolved anisotropy data in DODAB at different temperature.*

Systems	Probe	τ_{1r} ns (%)	τ_{2r} ns (%)	τ_{avg} ns
DODAB_10 ^{0}C	C500	0.050 (85)	2.00(15)	0.33
DODAB_50 ^{0}C	C500	0.060 (97)	1.40 (03)	0.10
DODAB_70 ^{0}C	C500	0.085 (73)	0.93 (27)	0.31
DODAB_10 ^{0}C	ANS	0.60 (55)	6.20 (45)	3.14
DODAB_50 ^{0}C	ANS	0.30 (36)	1.66 (64)	1.17
DODAB_70 ^{0}C	ANS	0.12 (30)	0.75 (70)	0.56

Inset of Figures 4.3 and Figure 4.4 display wavelength-dependent fluorescence transients of C500 and ANS in DODAB in the subgel phase (10 ^{0}C), gel phase (50 ^{0}C) and in the liquid crystalline phase (70 ^{0}C) at three characteristic wavelengths, from the blue end to the red end of the steady state fluorescence spectra. Time-resolved fluorescence at the blue and the red end

are characterized by a decay and a rise, respectively, indicating reorganization of the local environment around the excited state dipole of the fluorophore and is characterized by a time-dependent red shift of the fluorescence spectrum (Figures 4.3 and Figure 4.4). The solvation correlation function, C(t), for both

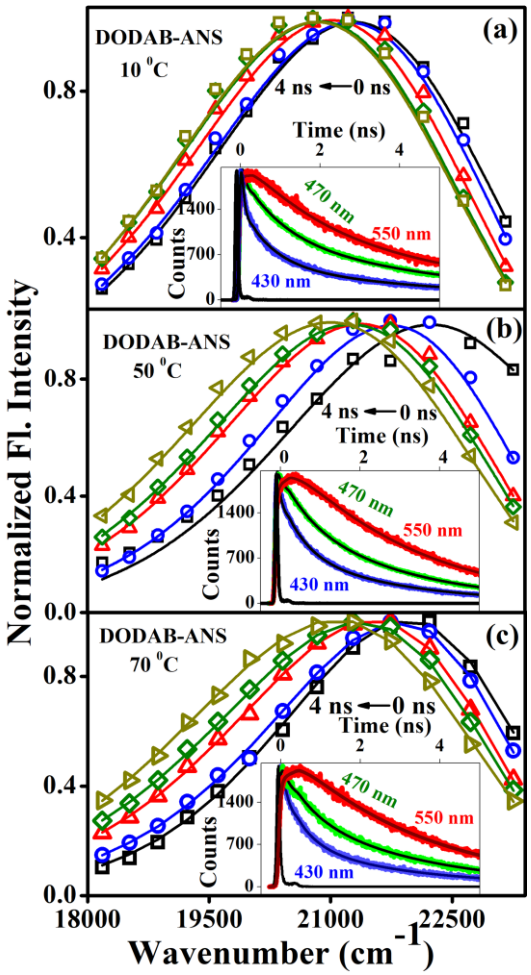

Figure 4.4. *Time-resolved emission spectra (TRES) of ANS-DODAB are shown at different temperature (a) 10 °C, (b) 50 °C and (c) 70 °C. Insets depict the corresponding Picosecond-resolved transient of C500 at three different wavelengths.*

C500 and ANS decays (Figure 4.5 and Table 4.2) with two time constants indicating mediation of two types of water trajectories in the solvent relaxation. The faster component (τ_1) may be ascribed to loosely bound water [22] (intermediate interlamellar water) coupled with the lateral motion of the DODAB monomers, whereas, the longer relaxation component likely originates from water molecules strongly bound [45] to the polar head groups of the lipid.

In the subgel phase the contribution of the longer nanosecond relaxation component is significantly large (95%) compared to the shorter relaxation component in the solvation of ANS. On the contrary, the shorter component becomes predominant (58%) in the relaxation of the local dye environment for C500. This may be ascribed to location of ANS in the head group region of the lipid-water interface relative to location of the C500 dye deeper in the bilayer. The location of ANS in the lipid-water interface makes it susceptible to sense stronger effect of hydration of the lipid headgroups. C500, on the other hand, due to its location deeper in the bilayer at the level of first few methylene groups within the densely packed lipid hydrocarbon chains in proximity of lipid-water interface seems to be a better sensor of the relaxation of water molecules coupled with the lateral motion of the lipid chains. For both ANS

Table 4.2. *Solvation time constant in different phases of DODAB vesicles.*

Systems	Probe	τ_1 ns (%)	τ_2 ns (%)	τ_{avg} ns
DODAB_10 ^{0}C	C500	0.05 (58)	1.00 (42)	0.45
DODAB_50 ^{0}C	C500	0.14 (66)	0.77 (34)	0.35
DODAB_70 ^{0}C	C500	0.12 (72)	0.64 (28)	0.27
DODAB_10 ^{0}C	ANS	0.06 (05)	1.00 (95)	0.98
DODAB_50 ^{0}C	ANS	0.04 (47)	1.12 (53)	0.61
DODAB_70 ^{0}C	ANS	0.25 (30)	1.00 (70)	0.78

and C500, the contribution of the faster relaxation component is less (5-58%) relative to the longer component in the subgel phase due to restricted motion of the alkyl chains. The contribution of the faster relaxation component increases around the transition temperature (~50 ^{0}C) from gel to liquid crystalline phase when the lipid hydrocarbon tails melt, and the overall solvation response becomes faster for both ANS and C500. In the liquid crystalline phase, at a much higher temperature (70 ^{0}C), the head groups become more strongly hydrated, and conformational disorder of the alkyl chains predominates via their translational and flip-flop motions [23]. As a

consequence the slower relaxation component due to water molecules strongly bound to lipid head groups predominates (70%) in the relaxation of the local environment for ANS, and the overall solvation response becomes slower in the liquid crystalline phase than that at the phase transition temperature (50 ^{0}C). In contrary, due to enhanced conformational disorder of the alkyl chains,

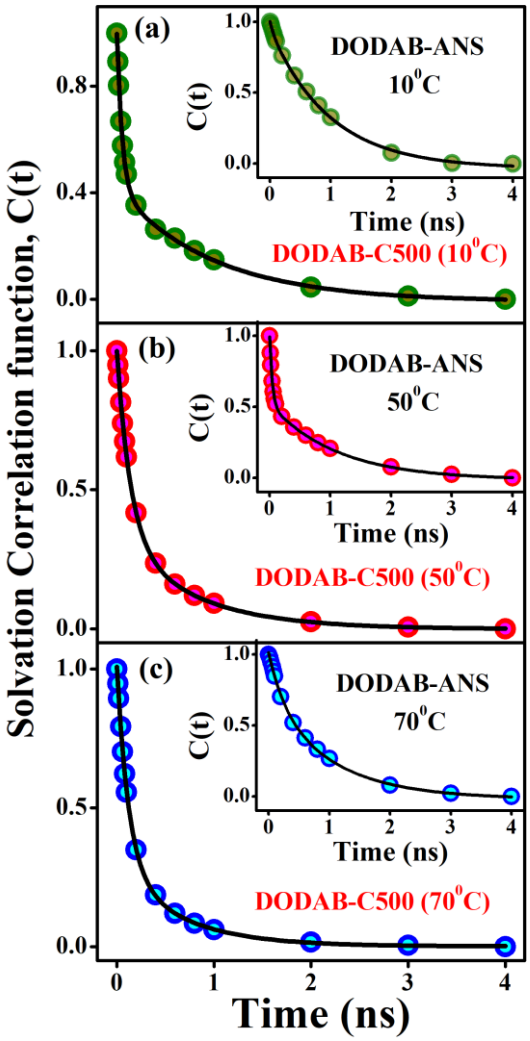

Figure 4.5. *Solvation correlation function of C500-DODAB at different temperature (a) 10 ^{0}C, (b) 50 ^{0}C and (c) 70 ^{0}C. Insets depict the solvation correlation function of ANS-DODAB at corresponding temperature.*

the faster relaxation component becomes predominant (72%) in the overall solvation response for C500, and the solvation becomes faster than those at the subgel phase (10 ^{0}C) or at the gel phase (50 ^{0}C).

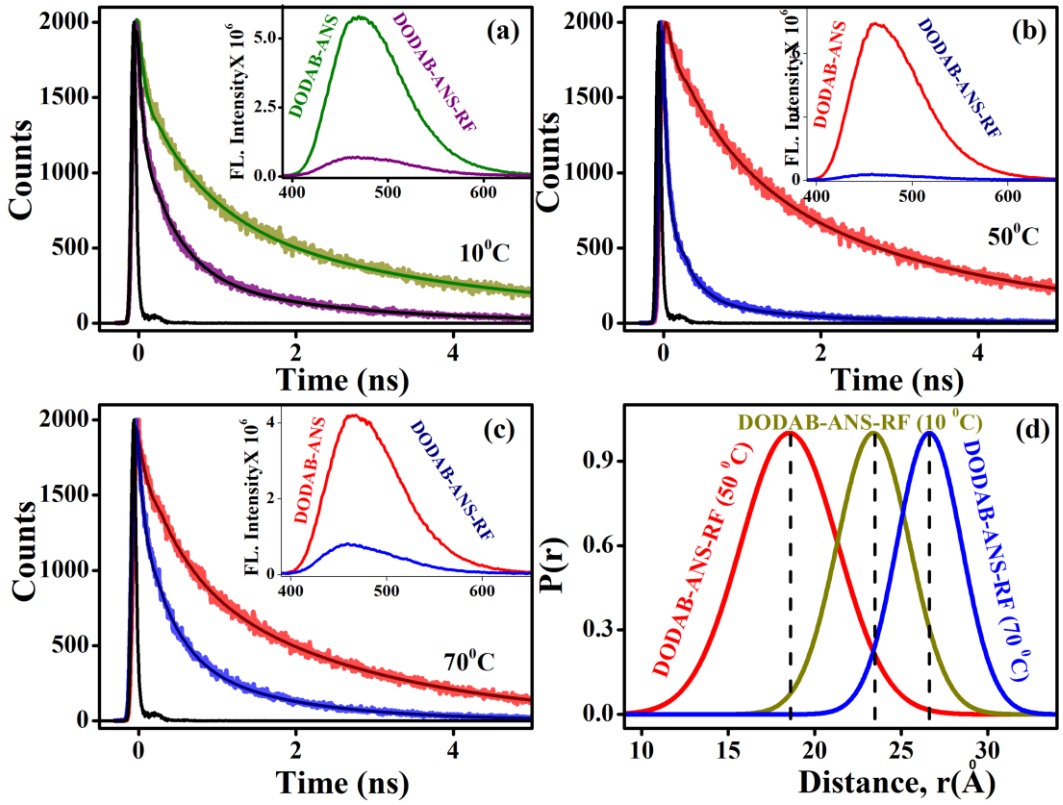

Figure 4.6. *The fluorescence transients of ANS-DODAB (excitation at 375nm) in the absence and in the presence of RF are shown at different temperature (a) 10 ^{0}C, (b) 50 ^{0}C and (c) 70 ^{0}C. Inset depicts corresponding steady state emission of ANS-DODAB in absence and presence of RF. (d) Distribution of donor-acceptor distances between ANS-DODAB and the RF are shown at different temperature.*

Water is known to actively participate in molecular recognition by mediating interactions between binding partners and contributes to either enthalpic or entropic stabilization [46]. To study the interplay between solvation dynamics and molecular recognition of an anti-tuberculosis drug rifampicin (RF) by DODAB based vesicles, we have monitored energy transfer from ANS bound to the positively charged lipid head groups to RF which is known to be efficiently entrapped by these vesicles [47]. ANS is chosen as a donor in the donor-acceptor pair with RF because its fluorescence spectrum overlaps reasonably well (overlap integral value, $2.77X10^{14}$ $M^{-1}cm^{-1}nm^4$) with the absorption spectrum of RF, and because it is located in the lipid-water interface due to strong binding interactions with the positively charged head groups of DODAB [48]. Figures 4.6.a-c display steady state and time-resolved decay profiles of ANS in lipid vesicles in absence and presence of RF in

different phases. From both the time-resolved decay profiles and the steady state fluorescence spectra (inset of Figure 4.6.a-c) of ANS in absence and presence of RF it is clearly evident that the energy transfer becomes more efficient at the gel phase (50 ^{0}C) than either in the subgel or in the liquid crystalline phase. The energy transfer from ANS to RF becomes most efficient (~93%, Table 4.3) and the distance of separation between the donor (ANS) and the acceptor (RF) becomes minimum (~23.3 Å, Table 4.3) during the onset of transition from gel to liquid crystalline phase. In the liquid crystalline phase (70 ^{0}C) or in the subgel phase (10 ^{0}C) energy transfer becomes much less efficient (63-79%) and the donor-acceptor distance significantly increases (30-50%) compared to that of gel phase. Thus recognition of RF by the DODAB based vesicles is most efficient in the gel phase (50 ^{0}C) when its distance with ANS anchored to the lipid head groups becomes minimum (~18.5 Å), whereas the efficiency of this molecular recognition becomes significantly perturbed in the subgel or in the liquid crystalline phase due to significant increase in the distance between RF and ANS. A calculation of the distribution of donor–acceptor distances in rifampicin-bound DODAB-labelled ANS (Figure 4.6.d) revealed less broadening in the case of subgel (HW= 4.9 Å) and liquid crystalline phase (HW= 4.4 Å) compared to gel phase (HW= 6.5 Å). The variation in the efficiency of molecular recognition and distribution of donor-acceptor between ANS-RF in DODAB vesicles seems to be nicely correlated with the speed of solvation of ANS in the lipid-water interface. When the solvation is slower in the subgel or in the liquid crystalline phase the molecular recognition of RF by DODAB is much less efficient than during phase transition from gel to liquid crystalline phase where solvation of ANS is fastest (~0.6 ns). In the subgel or in the liquid crystalline phase the solvation of ANS is slower because of preponderance of the slower relaxation component (70-95%, Table 4.2) due to strongly bound water molecules relative to the faster relaxation component associated with conformational fluctuation of the lipid alkyl tails. During the transition from the gel to the liquid crystalline phase the dynamic rearrangement of the lipid hydrocarbon tails occur cooperatively with

the solvation of the polar lipid headgroups [22] and a significant increase in the contribution of the faster relaxation component (47%) relative to the subgel or liquid crystalline phase (5-30%) is observed.

Table 4.3. *Picosecond-resolved fluorescence transient lifetime of ANS in different phases of DODAB vesicles.*

	Systems	τ_1 ns (%)	τ_2 ns (%)	τ_3 ns (%)	τ_{avg} ns
Fluorescence Transient Lifetime	ANS-DODAB (10 ^{0}C)	0.07 (35)	0.930 (32)	4.02 (33)	1.66
	ANS-DODAB-RF (10 ^{0}C)	0.06 (66)	0.52 (27)	2.36 (7)	0.35
	ANS-DODAB (50 ^{0}C)	0.08 (32)	0.74 (28)	3.06 (40)	1.47
	ANS-DODAB-RF (50 ^{0}C)	0.03 (83)	0.24 (14)	1.34 (3)	0.09
	ANS-DODAB (70 ^{0}C)	0.04 (38)	0.45 (27)	2.38 (35)	0.97
	ANS-DODAB-RF (70 ^{0}C)	0.6 (56)	0.39 (31)	1.50 (13)	0.35
FRET parameters		J(λ)	R_0 (Å)	Efficieny	τ_{DA}(Å)
	ANS-DODAB-RF (10 ^{0}C)	$2.77X10^{14}$	29.22	79.1	23.3
	ANS-DODAB-RF (50 ^{0}C)	$2.73X10^{14}$	29.14	93.6	18.5
	ANS-DODAB-RF (70 ^{0}C)	$2.8X10^{14}$	29.27	64.8	26.6

This significant increase in the dynamic rearrangement of the lipid hydrocarbon tails during phase transition is indicative of an enhanced intrinsic flexibility of the DODAB monomers compared to that in the subgel or in the liquid crystalline phase. The dynamic reorganization of the intrinsically flexible lipid hydrocarbon tails aids in incorporation of the drug RF in the lipid bilayers of DODAB. This is quite reasonable given that RF remains deeply buried inside the lipid bilayers [49, 50] of anionic and zwitterionic phospholipids owing to an interplay of electrostatic interaction and hydrophobic effect. As a consequence of enhanced intrinsic flexibility of the lipid alkyl tails during phase transition dynamic reorganization of the lipid tails aids in significant insertion of the drug RF and its closer positioning relative to the ANS dye in the lipid bilayers of DODAB. This leads to optimal molecular recognition of RF by the DODAB vesicles near the onset of phase transition (50 ^{0}C) compared to that in subgel or

liquid crystalline phase. Similar observations were noted in other studies [51-53] involving proteins where flexibility of the participating proteins were found to be crucial for optimal protein-based molecular recognition. In addition to the dynamic reorganization of the lipid alkyl tails, water molecules strongly bound to the lipid head groups optimize the complementarity of electrostatic interactions of the competitive binding partners ANS and RF with the cationic lipids as well as those between them in the lipid-water interface similar to proteins [54, 55]. Thus an optimum balance between the intrinsic flexibility of the lipid alkyl tails and interfacial hydration plays a key role in optimal molecular recognition of the anti-tuberculosis drug by the DODAB based vesicles, which is likely achieved near the onset of the phase transition temperature than that at the subgel (10 ^{0}C) or the liquid crystalline phase (70 ^{0}C) (Scheme 4.1).

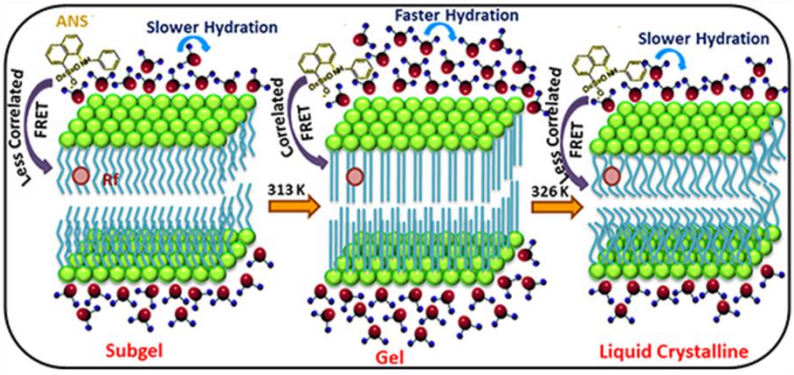

Scheme 4.1. *Schematic representation of the differential dynamical organization of the lipid molecules in different phases leading to its altered molecular recognition.*

4.2.2. Unravelling the Role of Monoolein in Fluidity and Dynamical Response of a Mixed Cationic Lipid Bilayer [56]: Elastic intensity scan satisfactorily investigates phase transitions associated with changes in microscopic dynamics and mobility of a sample with variation in temperature [57]. Any microscopic mobility in the sample shifts the scattering signal intensity away from zero energy transfer, hence, a discontinuous loss or gain of intensity in an elastic scan measurement is the signature of a phase transition, which is associated with a change in the microscopic dynamics of the system. Normalised *Q*-averaged elastic intensities for DODAB in presence and absence

of MO are shown for heating as well as cooling cycles in Figure 4.7.a. In case of pristine DODAB, upon heating, a sudden fall in the elastic intensity is observed

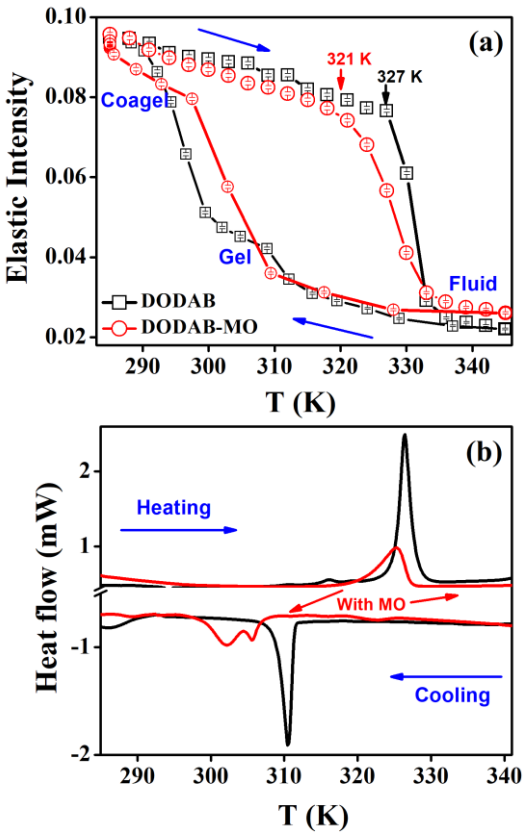

Figure 4.7. *(a) Elastic intensity scans. (b) Differential scanning calorimetry (DSC) thermograms for 70 mM DODAB bilayer with and without 33 mol% MO in the heating and the cooling cycles.*

at 327K corresponding to the coagel to fluid phase transition [58]. Upon cooling, pristine DODAB experiences transition from fluid to gel phase at 311K, and on further cooling it is converted to the coagel phase at ~299K. The formation of an intermediate 'gel' phase can be attributed to the loss of synchronicity between the change in the structure of the lipid headgroup and its alkyl chain. The headgroup of the DODAB lipid is positively charged, which interacts with the neighbouring headgroups via strong electrostatic interaction (mostly repulsive) whereas the alkyl chain of the lipid, being neutral, interact via weak van der Waals interaction with the neighbouring alkyl chains. The incongruity between the interactions among the lipid headgroups and those among the lipid alkyl chains lead to the formation of an intermediate gel phase.

Since, the interaction among the alkyl chains is relatively weaker, the chain ordering happens independently and at distinct temperature leading to the formation of gel phase where the alkyl chains in the lipid bilayer are ordered while the headgroup is still disordered.

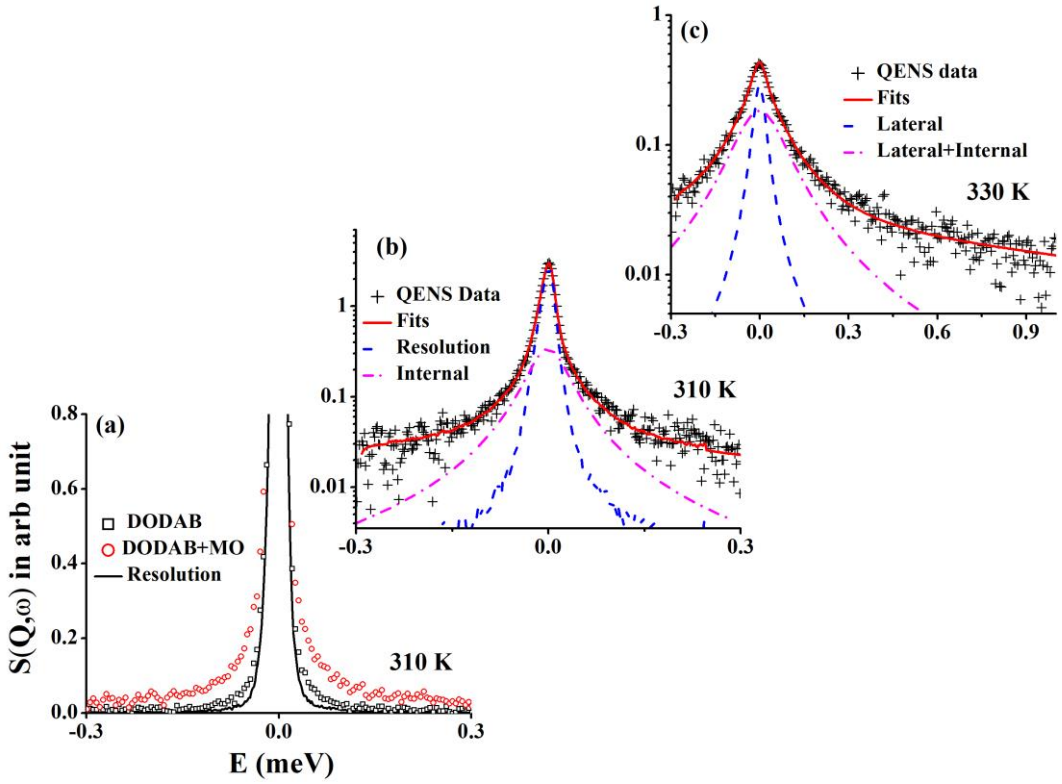

Figure 4.8. *(a) Typical observed QENS spectra for DODAB bilayer with and without MO at 310K at Q = 1.4 Å^{-1}. The contribution of the solvent (D_2O) has been subtracted, and the resultant spectra are normalized to the peak intensities. The instrumental resolution measured from standard vanadium sample is shown by solid line, (b) Typical fitted QENS spectra for DODAB in presence of MO at Q =1.4 Å^{-1} in coagel phase (310 K) and in (c) fluid phase (330 K).*

Upon incorporation of MO the phase behaviour of the DODAB bilayer is significantly affected during the heating as well as the cooling cycle. In case of heating, the coagel to fluid phase transition gets broadened, and the phase transition temperature shifts to a lower temperature (~321K) which is indicative of increased disorder in the lipid vesicles consistent with enhanced fluidity of the lipid bilayer. On the other hand, formation of the gel phase is inhibited during cooling and DODAB transforms directly from fluid phase to coagel phase indicating synchronous ordering of the lipid headgroups and the alkyl tails, which likely originates from screening of the electrostatic repulsion

between the cationic headgroups of DODAB by MO promoting in turn the van der Waals attraction between the cationic lipid molecules.

Table 4.4. *The dynamical parameters of DODAB with and without MO in the coagel phase (310 K).*

Coagel phase	p_x(%)	a (Å)	τ_{MG} (ps)	D_r (μeV)
DODAB	13 ± 3	1.7 ± 0.2	6.7 ± 0.3	14 ± 2
DODAB-MO	41 ± 4	2.3 ± 0.2	4.7 ± 0.3	21 ± 2

Differential scanning calorimetry (DSC) thermograms of DODAB vesicles, with and without MO, are shown in Figure 4.7.b. In the heating cycle, pure DODAB vesicles show a main phase transition (coagel to fluid) at 327K. On incorporation of MO the main phase transition (coagel to fluid) is shifted to a lower temperature by about ~6K. The transition enthalpy, ΔH_m, was calculated from the area under the peak and were found to be 75 kJ and 77 kJ per mol of DODAB for pure DODAB and mixed DODAB/MO vesicles, respectively. The shape of the thermogram provides additional information concerning phase transition and the peak width at half-height ($\Delta T_{1/2}$) is related to cooperativity of the transition. Upon incorporation of MO, the peak width increases from 2K to 4K suggesting that the phase transition becomes less cooperative in presence of the unsaturated lipid. The results from DSC thermograms are found to be consistent with the elastic intensity scan data (Figure 4.7.a) and indicate to a significant effect of MO on the phase behaviour of the lipid bilayer. From elastic intensity scan measurements, phase transitions of the DODAB bilayer are found to be affected upon incorporation of MO, which is associated with a change in the microscopic dynamics of the lipid bilayer.

To get insight into the effects of MO on the dynamical processes in the lipid bilayer, QENS measurements were carried out for DODAB vesicles with and without MO at 310K and 330K, respectively. Typical QENS spectra for DODAB bilayer with and without MO at Q = 1.4Å^{-1} are shown in Figure 4.8.a at 310K. The significant broadening of the QENS spectra in the coagel phase

relative to instrumental resolution indicates to the presence of stochastic motion of the lipid molecules of DODAB. In presence of MO, this broadening is found to increase relative to pure DODAB, indicating an enhancement in the dynamics of the lipid molecules. On the length and time scales of QENS, lipid molecules can undergo (i) lateral motion in which the whole lipid molecule

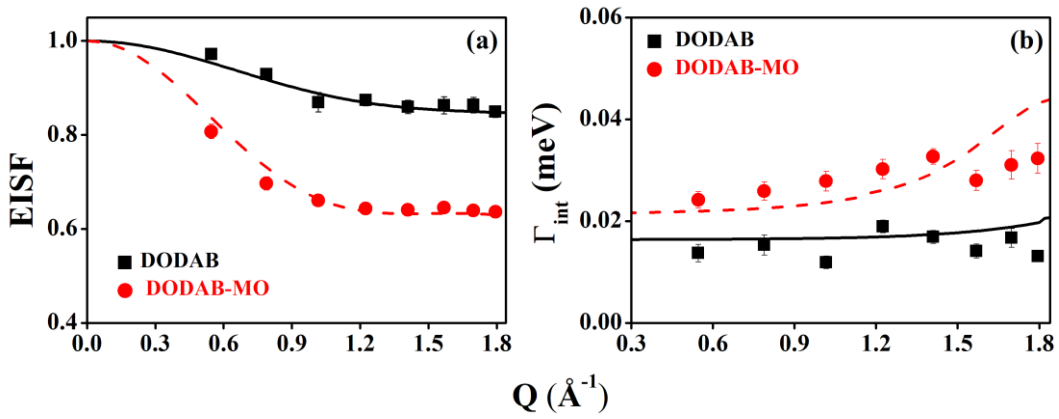

Figure 4.9. *(a) Elastic incoherent structure factor (EISF) and (b) Γ_{int} for DODAB in presence and absence of MO in the coagel phase (310 K). The solid lines represent fits assuming the fractional uniaxial rotational model.*

diffuses within the monolayer and (ii) a relatively faster internal motion [57-62]. Equation 3.10 is found to describe the QENS data quite well for the DODAB bilayer in presence and absence of MO in the coagel phase, at 310K, indicating that only internal motion of the lipid molecules are active which is consistent with rigid or tight packing of the lipid molecules in the coagel phase giving rise to a very slow lateral motion to be observed within the time scale of the IRIS spectrometer. Typical fitted QENS spectra for DODAB bilayer with MO in the coagel phase at 1.4Å^{-1} are shown in Figure 4.8.b. Components corresponding to lateral (dashed blue lines) and lateral + internal motions (dashed dotted magenta lines) of DODAB are also shown in the Figure 4.8.b-c. The variations of the different parameters (e.g. EISF and HWHMs) correspond to the underlying dynamics involved in different phases are discussed in the later sections. The obtained fitting parameters, EISF ($A(Q)$) and HWHM (Γ_{int})

for DODAB in absence and presence of MO are shown in Figure 4.9.a and Figure 4.9.b respectively.

Table 4.5. *The dynamical parameters of DODAB with and without the MO in the fluid phase (330 K).*

Fluid	Lateral motion	Internal motion		
	D_{lat} ($X10^{-6}$ cm^2/s)	R_{max}(Å)	D_{max}($X10^{-6}$ cm^2/s)	τ_{MG} (ps)
DODAB	2.2±0.1	4.2±0.2	17.3±0.4	4.5±0.2
DODAB-MO	1.7±0.1	4.5±0.2	14.3±0.4	4.9±0.2

The lower EISF and the broader QENS signal relative to pure DODAB are indicative of increased flexibility of the lipid bilayer upon incorporation of MO. In the coagel phase, lipid molecules are more ordered and tightly packed but incorporation of MO induces disorder in the DODAB/MO (2:1) vesicles enhancing its flexibility. In order to investigate the dynamical behaviour in more details we have attempted to model the observed data. Based on the structure of the DODAB molecule, containing two methyl units in the head group and two octadecyl alkyl chains, the internal dynamics should consist of

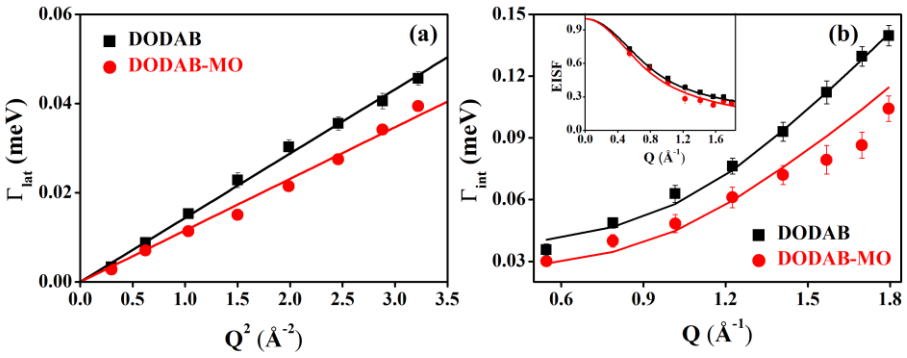

Figure 4.10. *(a) Variation of HWHM (Γ_{lat}) with Q^2 corresponding to lateral motion of DODAB with and without MO at 330 K. The solid lines correspond to the Fickian description. (b) The Q dependence of HWHM, Γ_{int}, corresponding to internal motion of DODAB bilayer in presence and absence of MO at 330 K. EISF's for DODAB bilayer with and without MO are shown in inset. The solid line represents the fit obtained from localised translational diffusion model as described in text.*

motion of the methyl units (3-fold rotation) and that of the alkyl chains. The ordering and arrangement of the lipids in the bilayer manifest itself in the

model of internal dynamics of the lipids. In the coagel phase, the alkyl chain of the lipid has an almost all-*trans* conformation with almost no *gauche* defects. This feature translates into a uniaxial rotational model for internal dynamics wherein alkyl chains rotate uniaxially along their axes. It can be pictured as hydrogen atoms of CH_2 units moving on the surface of a cylinder with a given radius, which corresponds to the radius of gyration in uniaxial rotational

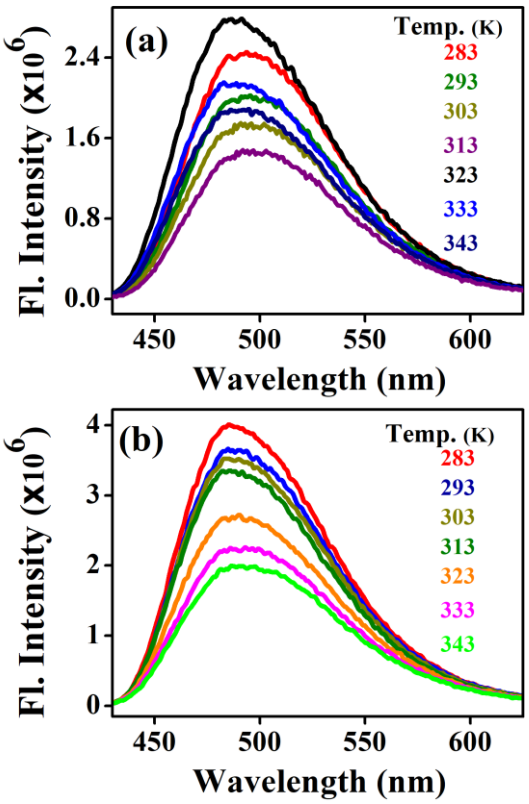

Figure 4.11. *Fluorescence emission spectra of Acedan-18 in (a) DODAB (70 mM) and (b) DODAB (70 mM) in presence of 33 mol% MO at different temperatures.*

diffusion. Given the high ordering and close packing of lipids in the coagel phase, only a fraction of hydrogen atoms (p_x) was observed to be participating in the dynamical motion. Equation 3.13 is found to describe the observed EISF (Figure 4.9.a) very well for DODAB both in absence and presence of MO. The parameters, radius of gyration, *a,* and the mobile fraction of the dynamic lipid tail, p_x, have been obtained from least squares fitting of the EISF and are given in Table 4.4. It is found that for pure DODAB bilayer, only 13% of the lipid tails are undergoing uni-axial rotation in a circle of radius 1.7 Å. However, in

presence of MO, the fluidity of the membrane is significantly enhanced and the fraction of the mobile lipid tails increases to 41%. In addition, the radius of gyration (a) increases from 1.7Å to 2.3Å indicating enhancement in flexibility of the lipid tails. The rotational diffusion coefficient D_r and τ_{MG} are obtained from least-squares fitting of equation 3.12 to the HWHM (Γ_{int}). The values of D_r for the lipid tails in DODAB in absence and presence of MO are 14(±2) μeV and 21(±2) μeV, respectively, whereas, the mean residence time (τ_{MG}) for the hydrogen atom in the methyl group in absence and presence of MO, are 6.7 ± 0.3 ps and 4.7 ± 0.3 ps, respectively. These results in the coagel phase clearly show the role of MO as a plasticizer in enhancing the dynamics of cationic lipids in mixed vesicles. In the fluid phase, lipids are more loosely packed with a large area per lipid molecules making them more mobile. There is a notable increase in the gauche defects in the alkyl chains of the lipids compared to the coagel phase. These changes in the structural feature of the lipids necessitate a more dynamically rich model involving both internal and lateral motion of the lipids. The variations in HWHM (Γ_{lat}) with Q^2 associated with the lateral diffusion of the DODAB lipids in presence and absence of MO are shown in Figure 4.10.a. In the fluid phase, MO acts oppositely to that in the coagel phase. Γ_{lat} is found to decrease on the addition of MO. For pure DODAB as well as mixed cationic (DODAB/MO) vesicles, Γ_{lat} varies linearly with Q^2 suggesting a continuous diffusion model $\Gamma_{lat} = D_{lat}Q^2$ following Fick's law. The values of the diffusion coefficients, D_{lat}, of DODAB with and without MO are shown in Table 4.5. In the fluid phase, MO is found to act as a stiffening agent restricting lateral diffusion of the lipid molecules. As for example, D_{lat} decreases from 2.2 (±0.1)X10^{-6} cm^2/s in pure DODAB to 1.7 (±0.1)X10^{-6} cm^2/s in presence of 33 mol% of MO. The addition of MO reduces the available free area per lipid and hence hinders the lateral diffusion of the lipid molecules. The HWHM (Γ_{int}) is a Lorentzian function that describes internal motions of the lipid molecules with and without MO and are displayed in Figure 4.10.b with corresponding EISFs (in the inset). EISF does not change much (Figure 4.10.b) upon the addition of MO indicating a mild effect on the nature of the internal motion of the DODAB

lipid molecules. However, Γ_{int} is reduced on addition of MO indicating retardation of the internal dynamics of the lipid molecules.

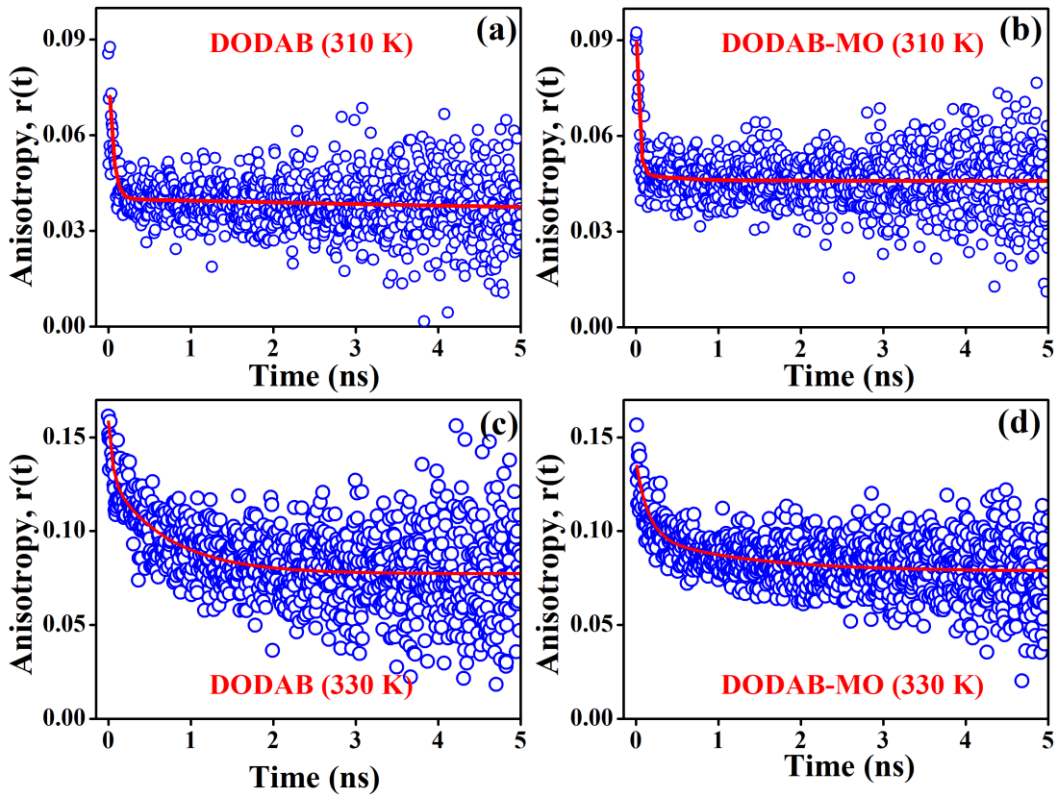

Figure 4.12. *Time-resolved anisotropy of Acedan-18 in DODAB in absence (a and c) and in presence (b and d) of 33 mol% MO in the coagel phase (310K) and liquid crystalline phase (330K).*

In the fluid phase, besides reorientational motion, lipid molecules can undergo various other internal motions (e.g. bending, stretching, etc.). The combination of these dynamical components can be approximated by a model in which the hydrogen atoms of a CH_2 unit perform translational diffusion confined within a spherical domain. As the lipid tails have large *gauche* defects, that imposes restricted homogeneity in the dynamics along the alkyl chain. Hence, a linear distribution of radii and diffusivities along the alkyl chain is assumed. In this model, the CH_2 units closest to the headgroup experience the highest restriction and therefore have the minimum radius (R_{min}) and diffusivity (D_{min}) within the linear distribution. Likewise, the radius and diffusivity would increase linearly along the alkyl chain as we move away from the head of the alkyl chain attaining maximum value of radius (R_{max}) and

diffusivity (D_{max}) for the last (CH_3) unit of the chain. A 3-fold jump motion of the headgroup methyl units are treated in the same way as in the case of coagel phase. Least square fitting has been used to describe the EISF and Γ_{int}, assuming localized translational diffusion (LTD) model and are shown by the solid lines in Figure 4.10.b. This model is found to describe the experimental *EISF* and HWHM for both DODAB systems quite satisfactorily and the resulting fitting parameters are displayed in Table 4.5. The values of R_{min} and D_{min} are found to be unrealistically small for both the systems indicating negligible movement of the H-atoms in the first CH_2 unit held by the headgroup. On addition of MO, the diffusivity corresponding to internal motion is reduced indicating that MO affects the internal motion of the lipid molecules.

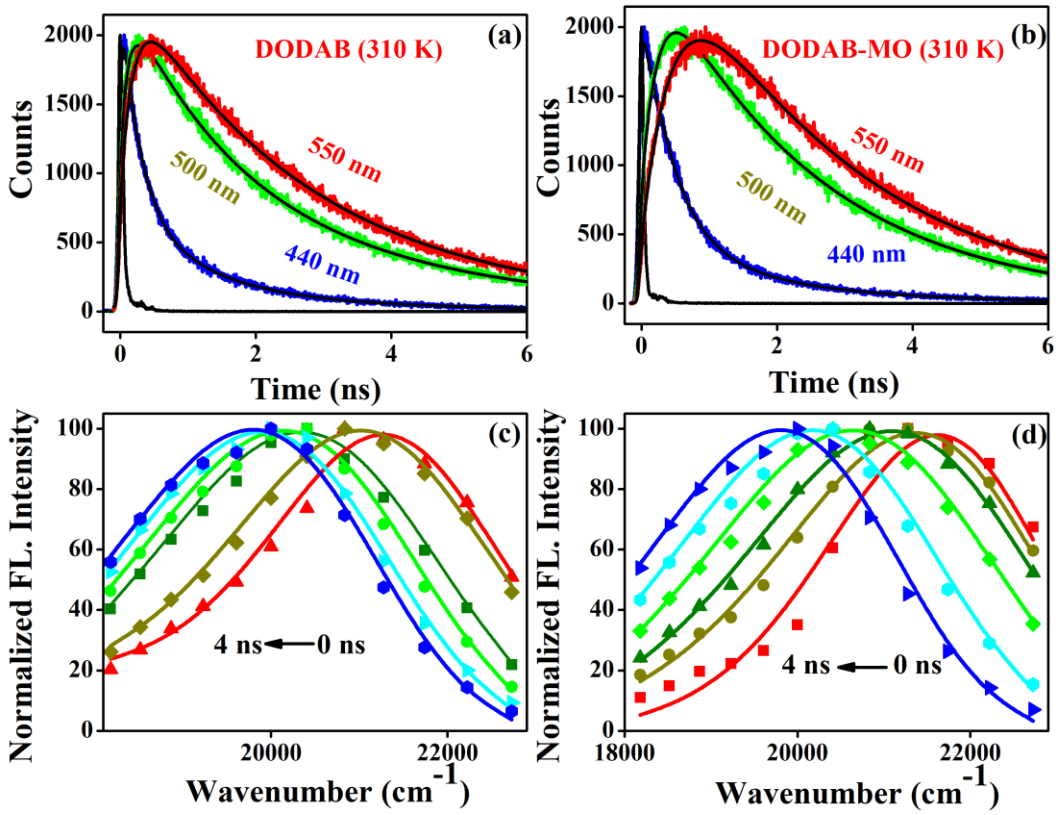

Figure 4.13. *Picosecond-resolved emission transients of Acedan-18 in DODAB in absence (a) and in presence (b) of MO in the coagel phase (310K). Time-resolved emission spectra (TRES) in DODAB in absence (c) and in presence of MO in the coagel phase.*

The steady state fluorescence spectra of Acedan-18 are sensitive to solvent polarity. For example, its emission peak maximum is significantly red

shifted from 461 nm in dimethylformamide (DMF) to 522 nm in water, which is attributed to a highly polar excited state originating from an intramolecular charge transfer (ICT) process [63]. Figure 4.11.a shows temperature dependent fluorescence spectra of Acedan-18 in pure DODAB vesicles. The emission peak maximum is significantly red shifted (~30-35 nm) relative to DMF, but is moderately blue shifted (~20 nm) in comparison to aqueous buffer which is

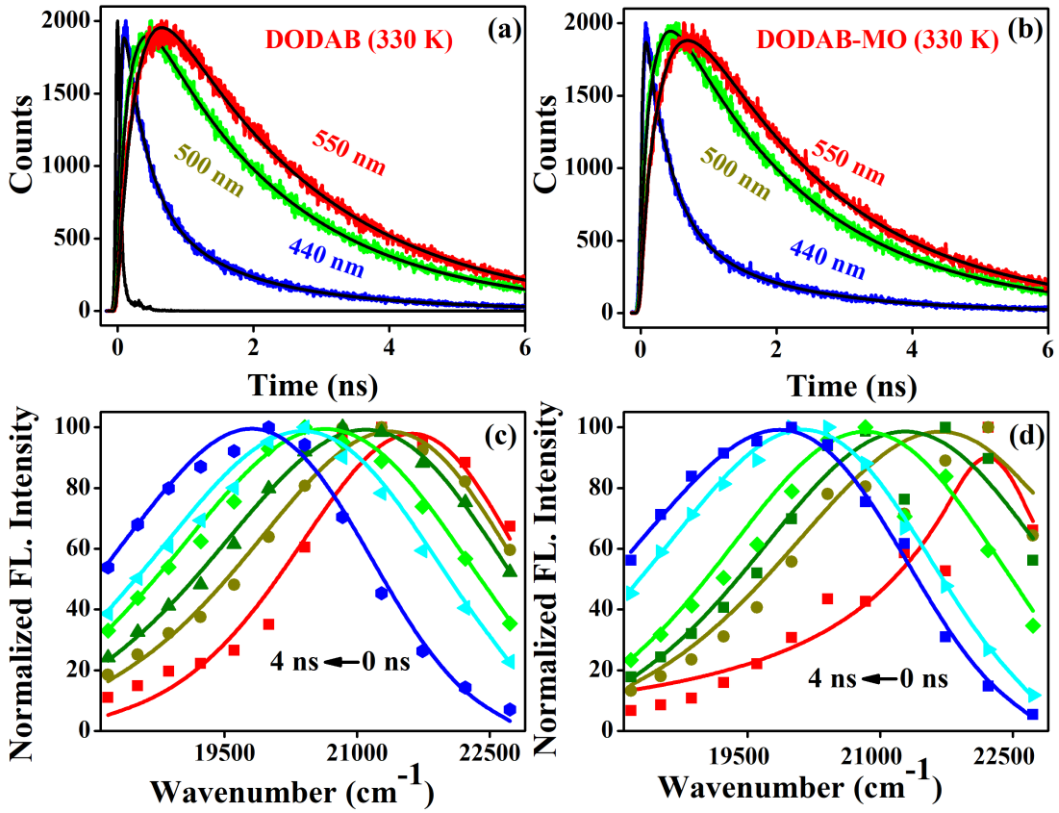

Figure 4.14. *Picosecond-resolved emission transients of Acedan-18 in DODAB in absence (a) and in presence of MO (b) in the fluid phase (330K). Time-resolved emission spectra (TRES) of Acedan-18 in DODAB in absence (c) and in presence of MO (d) in the fluid phase.*

consistent with location of the dye in the interfacial region of the membrane. The fluorescence intensity is found to decrease with increase in temperature until up to 313K followed by a dramatic increase at 323K which corresponds closely to the melting temperature (327K) for transition from coagel to fluid phase. This may be attributed to increased disorder of the cationic lipid organizations due to increase of temperature which makes packing of the lipids in the membranes looser and enhances hydration of the bilayer interface region

at 313K relative to 283K. As result water induced non-radiative relaxation process becomes enhanced leading to a decrease in fluorescence intensity. This is consistent with slightly red shifted (~ 4-5 nm) emission spectra of Acdean-18 at 313K relative to that at 283K. On further increase of temperature to 323K, near the phase transition, the dye likely relocates deeper in the lipid bilayer due to increased flexibility of the lipid chains, and becomes screened from perturbation of water molecules causing a significant increase of the fluorescence intensity relative to that at 313K along with a moderate blue shift (~10 nm). Incorporation of MO in DODAB gives rise to stronger fluorescence of Acedan-18 in the coagel phase (up to 313K) compared to that in pure DODAB (Figure 4.11.a and Figure 4.11.b) due to more efficient screening of the dye from perturbation of water molecules which is consistent with moderately blue shifted (~7-8 nm) fluorescence spectra in DODAB/MO systems relative to pure DODAB. When MO molecules incorporate in the DODAB vesicles, Acedan-18 likely penetrates deeper in the lipid bilayer thus being less exposed to water. This is likely caused by increasing fluidity or flexibility of the lipid membrane in presence of the unsaturated lipid (MO) and this effect is found to be similar to the effect of phase transition in pure DODAB. Moreover, compared to pure DODAB, fluorescence intensity in the DODAB/MO mixed vesicles decreases continuously with a mild red shift in the peak maximum on an increase of temperature. This may be ascribed to increased non-radiative deactivation due to increasing temperature along with slightly increased exposure of the dye to water. It is also noteworthy that the effect of phase transition from coagel to fluid phase is not reflected in the fluorescence spectra of AC-18 in presence of MO unlike pure DODAB vesicles. This may be ascribed to weakening and broadening of the transition peak in DSC thermograms (Figure 4.7.b) in accordance with Oliveira et al. They also failed to detect the effect of phase transition on the fluorescence spectra of pyrene in DODAB/MO system with 70 mol% of DODAB and attributed it to weakening and broadening of the transition peak in DSC thermograms. The steady state fluorescence spectra provide information on polarity of the lipid-water interface as well as its

change following phase transition in the absence and presence of MO. In order to probe the dynamics of the DODAB bilayer in presence of MO, we have carried out time resolved fluorescence measurements. Time-resolved anisotropy decays (Figure 4.12) of Acedan-18 were measured in the coagel and the fluid phase to probe the effect of MO on the fluidity or rigidity of the DODAB bilayer. The anisotropy decays, r(t), were analysed by the two-step wobbling in a cone model [41]. The anisotropy decay of Acedan-18 is

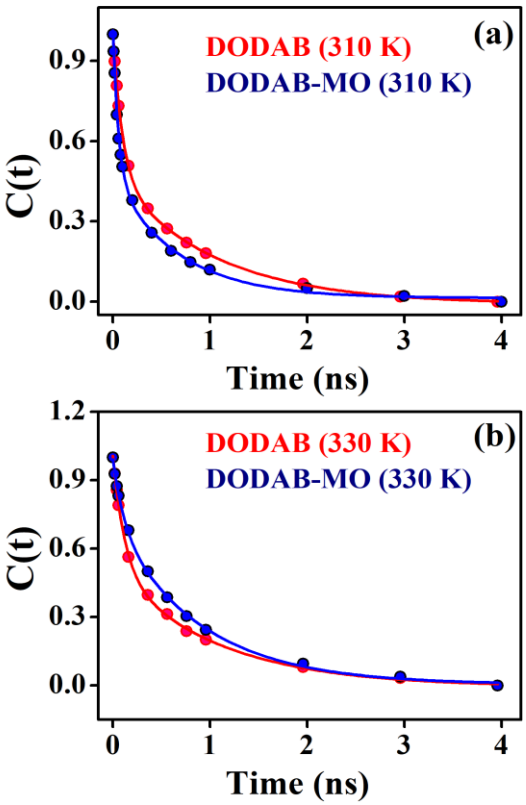

Figure 4.15. *Decay of the Solvation correlation function, C(t), for Acedan-18 in DODAB in absence and presence of 33 mol% of MO in the coagel phase (a) and in the fluid phase (b).*

characterized by two time constants with a much longer average rotational relaxation time (ϕ) of 1330 ps for pure DODAB in the coagel phase (310K, Table 4.6) relative to buffer (~180 ps), which is consistent with significantly hindered orientational motion of the probe in the highly rigid lipid vesicles compared to bulk water. Upon the incorporation of MO, the average rotational time constant decreases significantly to 510 ps in the coagel phase relative to pure DODAB, indicating much faster orientational relaxation of the dye in the

former than the latter. This is consistent with remarkably increased flexibility of the dye environment in presence of the unsaturated lipid (MO). The average rotational time constant for pure DODAB in the fluid phase (~470 ps) is comparable to that of DODAB in presence of MO in the coagel phase, which clearly manifests the effect of the unsaturated lipid in enhancement of the membrane fluidity. In the fluid phase (330K), the average rotational relaxation time of Acedan-18 increases slightly (~6%) in presence of MO relative to pure DODAB indicating a mild increase in rigidity of the lipid bilayer. From the polarization-gated fluorescence anisotropy measurements, incorporation of MO is found to significantly increase fluidity of the DODAB bilayer in the coagel phase (310K) which becomes manifest in the faster orientational relaxation dynamics of the dye relative to that in pure DODAB. On the other hand, presence of MO in the fluid phase (330K) slightly increases rigidity of the lipid bilayer slowing down the orientational relaxation of Acedan-18.

Table 4.6. *Rotational time constants of Acedan-18 in different systems.*

System	Φ_1 ns (β_1)	Φ_2 ns (β_2)	ϕ/ns
DODAB (310 K)	0.05 (87)	10 (13)	1.33
DODAB-MO (310 K)	0.03 (95)	10 (5)	0.51
DODAB (330 K)	0.05 (37)	0.71 (63)	0.47
DODAB-MO (310 K)	0.14 (67)	1.21 (33)	0.50

ϕ_1, ϕ_2 are rotational correlation times, respectively and β_1 and β_2 are associated amplitudes represented in % within parentheses. ϕ is average rotational relaxation time = $\beta_1\phi_1 + \beta_2\phi_2$

Figures 4.13 and Figure 4.14 display wavelength dependent fluorescence transients of Acedan-18 at three characteristic wavelengths. The decay and rise observed in the blue end (440 nm) and the red end (550 nm) of the emission spectra are characteristic of solvent relaxation [64, 65] around the excited state dipole of the fluorophore and is manifested by a time-dependent Stokes shift of the fluorescence spectrum. The kinetics of solvent relaxation in the lipid membrane is often interpreted in terms of the freedom of movement of water hydrating the membrane and is described by the solvation correlation function (C(t)). C(t), for the lipid vesicles decays (Figure 4.15) with two time constants

(τ_1, τ_2) indicating mediation of two types of water dynamics in relaxation of the local environment of the probe (Table 4.7). The faster component (τ_1) may be ascribed to loosely bound water (intermediate interlamellar water), whereas, the longer relaxation component (τ_2) likely originates from water molecules strongly bound to the polar head groups of the lipid molecules [38, 45].

Table 4.7. *Solvation time constants of Acedan-18 in different systems.*

System	τ_1/ns (a_1)	τ_2/ns (a_2)	$<\tau>$/ns
DODAB (310 K)	0.10 (52%)	1.04 (48%)	0.55
DODAB-MO (310 K)	0.06 (55%)	0.66 (45%)	0.33
DODAB (330 K)	0.12 (50%)	1.08 (50%)	0.60
DODAB-MO (330 K)	0.11 (28%)	0.90 (72%)	0.68

τ_1,τ_2 are solvation correlation time; a_1,a_2 are corresponding amplitudes shown in % within parentheses ; $<\tau> = a_1\tau_1 + a_2\tau_2$ is average solvation time

However, the dynamics of the overall solvation response is a better descriptor of environmental relaxation rather than the dynamics of the individual water molecules due to the coupled nature of surfactant/protein and water motions in micelles, proteins etc. [64-67]. In consequence, the overall solvation response described in terms of average or integrated relaxation time ($<\tau>$) serves as an efficient parameter to indicate flexibility/rigidity of the lipid bilayer. The decay of C(t) for DODAB (coagel phase, 310K) is characterized by two time constants of 100 ps (52%) and 1040 ps (48%), respectively, with an average solvation time ($<\tau>$) of 550 ps (Table 4.7). Upon incorporation of MO the average relaxation time decreases significantly (330 ps) indicating faster relaxation dynamics of the probe environment in the coagel phase in presence of MO compared to pure DODAB. This may be ascribed to increased flexibility of lipid molecules in the bilayer of DODAB/MO vesicles compared to pure DODAB, which gives rise to much faster hydration (solvation) response in the former than the latter due to coupled nature of the dynamics of lipid/surfactant and associated water molecules. On the other hand, the average solvation time in the lipid bilayer of DODAB becomes moderately slower (~13%) in the fluid phase in presence of MO indicating the role of MO

as a stiffening agent for lipid vesicles in the fluid phase. In the fluid phase, incorporation of MO slightly increases rigidity of the lipid bilayers resulting in slower relaxation dynamics of the associated water molecules, which becomes manifested in the longer average solvation time (680 ps) than that of pure DODAB (~600 ps, Table 4.7). The decrease of the average solvation time (<τ>) in the coagel phase or its increase in the fluid phase on incorporation of MO is also consistent with the decrease or increase of the average orientational relaxation time (ϕ) (Table 4.6) confirming the effect of MO in increasing the fluidity or rigidity of the DODAB bilayer below and above the phase transition temperature, respectively.

4.3. Conclusion: In summary, we have investigated solvation dynamics of DODAB based lipid vesicles in different phases using a neutral (C500) and an anionic dye (ANS) and the role of solvation in molecular recognition of an anti-tuberculosis drug RF by the cationic vesicles. In comparison to C500 which mainly probes the solvation near the region of the methylene groups of the lipid hydrocarbon chains, ANS is anchored to the positively charged lipid headgroups and therefore probes the lipid-water interface. The reported solvation was bimodal with a faster relaxation component due to water molecules dynamically coupled with the conformational fluctuation of the lipid hydrocarbon chains, and a slower component arising from relaxation of water molecules strongly bound to the lipid head groups. In the subgel phase (10 ^{0}C) the overall solvation is slowest due to the predominance of the slower relaxation component, whereas near the gel phase (50 ^{0}C) solvation becomes faster due to enhanced intrinsic flexibility of the lipid alkyl tails relative to the subgel phase. With further increase in temperature, the solvation of C500 becomes faster whereas that of ANS becomes slower in the liquid crystalline phase (70 ^{0}C) compared to that at 50 ^{0}C. This is because ANS being located in the lipid-water interface senses the effect of increased hydration of the polar head groups in the liquid crystalline phase compared to that at 50 ^{0}C, whereas C500 is likely located deeper in the lipid bilayer and mostly senses increased

flexibility of the lipid alkyl tails. As for the recognition of an anti-tuberculosis drug RF in the lipid bilayer intrinsic flexibility of the DODAB monomers plays a key role as dynamic reorganization of the lipid alkyl tails helps in incorporation of the drug by the lipid vesicles. ANS reveals a significant enhancement of intrinsic flexibility of the lipid alkyl tails near the gel phase (50 ^{0}C) compared to the subgel phase or the liquid crystalline phase. The enhanced intrinsic flexibility of the lipid alkyl tails at 50 ^{0}C aids in significant incorporation of RF in the lipid bilayer in close proximity of ANS leading to optimal molecular recognition relative to that in the subgel (10 ^{0}C) or the liquid crystalline phase (70 ^{0}C). In addition to the dynamic reorganization of the lipid alkyl chains, water molecules strongly bound to the lipid head groups optimize the electrostatic interactions of the competitive binding partners ANS and RF with the cationic lipids as well as those between them in the lipid-water interface. Together the intrinsic flexibility of the lipid alkyl tails and interfacial hydration contribute to optimal molecular recognition of the anti-tuberculosis drug by the DODAB based vesicles, which is achieved in the gel phase (50 ^{0}C) than that at the subgel (10 ^{0}C) or the liquid crystalline phase (70 ^{0}C).

Additionally we have highlighted the role of an unsaturated lipid MO on the dynamical and the phase behaviour of a lipid (DODAB) bilayer. Elastic intensity scan measurements and DSC thermograms show that in the heating cycle, in presence of MO, coagel to fluid phase transition is found to take place at a lower temperature and the transition gets broadened. In the cooling cycle, in case of DODAB with MO, no intermediate gel phase is observed like pristine DODAB indicating that MO induces synchronous ordering between the polar headgroups and the non-polar tails of the cationic lipids. Quasi-elastic neutron scattering (QENS) studies and polarization-gated anisotropy measurements have revealed that in the coagel phase (310K), MO acts as a plasticizer enhancing significantly the dynamics of the lipid molecules and hence membrane fluidity of the DODAB bilayer. On the contrary, in the fluid phase, MO acts as a stiffening agent where it restricts lateral and internal motions of the lipid molecules and hinders orientational relaxation of the probe compared

to the coagel phase. The dynamics of solvation response of the lipid bilayer is significantly faster for the structurally more flexible DODAB-MO vesicles relative to pure DODAB in the coagel phase (310K), whereas, it becomes moderately slower in the fluid phase (330K) indicating increased rigidity of the DODAB bilayer in presence of MO. Our present work reflects how a specific (cationic) model lipid membrane (DODAB) restores fluidity in the coagel (ordered) phase at 310K upon incorporation of unsaturation (in the form of MO) and thus provides a coherent picture between the structure and the dynamics of biomimetic membranes.

References

[1] G. Van Meer, D.R. Voelker, G.W. Feigenson, Membrane lipids: Where they are and how they behave, *Nat. Rev. Mol. Cell Biol.*, 9 (2008) 112–124.

[2] P.V. Escribá, J.M. González-Ros, F.M. Goñi, P.K. Kinnunen, L. Vigh, L. Sánchez-Magraner, A.M. Fernández, X. Busquets, I. Horváth, G. Barceló-Coblijn, Membranes: A meeting point for lipids, proteins and therapies, *J. Cell. Mol. Med.*, 12 (2008) 829-875.

[3] V. Luzzati, Biological significance of lipid polymorphism: The cubic phases, *Curr. Opin. Struct. Biol.*, 7 (1997) 661-668.

[4] S.-J. Marrink, D.P. Tieleman, Molecular dynamics simulation of spontaneous membrane fusion during a cubic-hexagonal phase transition, *Biophys. J.*, 83 (2002) 2386-2392.

[5] D. Siegel, W. Green, Y. Talmon, The mechanism of lamellar-to-inverted hexagonal phase transitions: A study using temperature-jump cryo-electron microscopy, *Biophys. J.*, 66 (1994) 402-414.

[6] D. Siegel, R. Epand, The mechanism of lamellar-to-inverted hexagonal phase transitions in phosphatidylethanolamine: Implications for membrane fusion mechanisms, *Biophys. J.*, 73 (1997) 3089-3111.

[7] P. Dubey, H. Srinivasan, V. Sharma, S. Mitra, V.G. Sakai, R. Mukhopadhyay, Dynamical transitions and diffusion mechanism in DODAB bilayer, *Sci Rep.*, 8 (2018) 1862.

[8] A.C.N. Oliveira, T.F. Martens, K. Raemdonck, R.D. Adati, E. Feitosa, C.u. Botelho, A.C. Gomes, K. Braeckmans, M.E.C.D. Real Oliveira, Dioctadecyldimethylammonium: monoolein nanocarriers for efficient in vitro gene silencing, *ACS Appl. Mater. Interfaces,* 6 (2014) 6977-6989.

[9] J.P.N. Silva, A.C. Oliveira, M. Lúcio, A.C. Gomes, P.J. Coutinho, M.E.C.R. Oliveira, Tunable pDNA/DODAB: MO lipoplexes: the effect of incubation temperature on pDNA/DODAB: MO lipoplexes structure and transfection efficiency, *Colloids Surf. B*, 121 (2014) 371-379.

[10] M. Kepczynski, J. Lewandowska, K. Witkowska, S. Kędracka-Krok, V. Mistrikova, J. Bednar, P. Wydro, M. Nowakowska, Bilayer structures in dioctadecyldimethylammonium bromide/oleic acid dispersions, *Chem. Phys. Lipids,* 164 (2011) 359-367.

[11] P. Li, D. Li, L. Zhang, G. Li, E. Wang, Cationic lipid bilayer coated gold nanoparticles-mediated transfection of mammalian cells, *Biomaterials,* 29 (2008) 3617-3624.

[12] A.Z. Fernandis, M.R. Wenk, Membrane lipids as signaling molecules, *Curr. Opin. Lipidol.,* 18 (2007) 121-128.

[13] T.J. McIntosh, S.A. Simon, Roles of bilayer material properties in function and distribution of membrane proteins, *Annu. Rev. Biophys. Biomol. Struct.,* 35 (2006) 177-198.

[14] J. Voskuhl, B.J. Ravoo, Molecular recognition of bilayer vesicles, *Chem. Soc. Rev.,* 38 (2009) 495-505.

[15] K. Simons, D. Toomre, Lipid rafts and signal transduction, *Nat. Rev. Mol. Cell Biol.,* 1 (2000) 31-39.

[16] F.-G. Wu, Z.-W. Yu, G. Ji, Formation and transformation of the subgel phase in dioctadecyldimethylammonium bromide aqueous dispersions, *Langmuir,* 27 (2011) 2349-2356.

[17] R. Brito, E. Marques, Neat DODAB vesicles: Effect of sonication time on the phase transition thermodynamic parameters and its relation with incomplete chain freezing, *Chem. Phys. Lipids,* 137 (2005) 18-28.

[18] J. Cocquyt, U. Olsson, G. Olofsson, P. Van der Meeren, Temperature quenched DODAB dispersions: Fluid and solid state coexistence and complex formation with oppositely charged surfactant, *Langmuir,* 20 (2004) 3906-3912.

[19] E. Feitosa, F.R. Alves, A. Niemiec, M.E.C. Real Oliveira, E.M. Castanheira, A.L. Baptista, Cationic liposomes in mixed didodecyldimethylammonium bromide and dioctadecyldimethylammonium bromide aqueous dispersions studied by differential scanning calorimetry, nile red fluorescence, and turbidity, *Langmuir,* 22 (2006) 3579-3585.

[20] R.S. Sarpal, G. Durocher, Temperature-induced structural and permeability changes in dioctadecyldimethylammonium bromide (DODAB) vesicles: a fluorescence investigation using 2-[(p-methylamino) phenyl]-3, 3-dimethyl-5-carboethoxy-3H-indole as a probe, *J. Photochem. Photobiol A,* 80 (1994) 307-314.

[21] E. Feitosa, P. Barreleiro, G. Olofsson, Phase transition in dioctadecyldimethylammonium bromide and chloride vesicles prepared by different methods, *Chem. Phys. Lipids,* 105 (2000) 201-213.

[22] F.-G. Wu, N.-N. Wang, Z.-W. Yu, Nonsynchronous change in the head and tail of dioctadecyldimethylammonium bromide molecules during the liquid crystalline to coagel phase transformation process, *Langmuir,* 25 (2009) 13394-13401.

[23] P. Saveyn, P. Van der Meeren, M. Zackrisson, T. Narayanan, U. Olsson, Subgel transition in diluted vesicular DODAB dispersions, *Soft Matter,* 5 (2009) 1735-1742.

[24] E.M. Pereira, D.F. Petri, A.M. Carmona-Ribeiro, Synthetic vesicles at hydrophobic surfaces, *J. Phys. Chem. B,* 106 (2002) 8762-8767.

[25] E.M. Pereira, D.B. Vieira, A.M. Carmona-Ribeiro, Cationic bilayers on polymeric particles: Effect of low NaCl concentration on surface coverage, *J. Phys. Chem. B,* 108 (2004) 11490-11495.

[26] T. Gustavsson, L. Cassara, S. Marguet, G. Gurzadyan, P. Van der Meulen, S. Pommeret, J.-C. Mialocq, Rotational diffusion of the 7-diethylamino-4-methylcoumarin C1 dye molecule in polar protic and aprotic solvents, *Photochem. Photobiol. Sci.,* 2 (2003) 329-341.

[27] T.K. Nyholm, Lipid-protein interplay and lateral organization in biomembranes, *Chem. Phys. Lipids,* 189 (2015) 48-55.

[28] R.C. Hresko, T.E. Kraft, A. Quigley, E.P. Carpenter, P.W. Hruz, Mammalian glucose transporter activity is dependent upon anionic and conical phospholipids, *J. Biol. Chem.,* 291 (2016) 17271-17282.

[29] R. Lipowsky, Remodeling of membrane compartments: some consequences of membrane fluidity, *Biol. Chem.,* 395 (2014) 253-274.

[30] N.J. Russell, Mechanisms of thermal adaptation in bacteria: Blueprints for survival, *Trends. Biochem. Sci.*, 9 (1984) 108-112.

[31] L. Vigh, D.A. Los, I. Horvath, N. Murata, The primary signal in the biological perception of temperature: Pd-catalyzed hydrogenation of membrane lipids stimulated the expression of the desA gene in Synechocystis PCC6803, *Proc. Natl. Acad. Sci. U.S.A.*, 90 (1993) 9090-9094.

[32] P. Ball, Water is an active matrix of life for cell and molecular biology, *Proc. Natl. Acad. Sci. U.S.A.*, 114 (2017) 13327-13335.

[33] J.B. Engberts, D. Hoekstra, Vesicle-forming synthetic amphiphiles, *Biochim. Biophys. Acta, Rev. Biomembr.*, 1241 (1995) 323-340.

[34] J.H. Fendler, Membrane mimetic chemistry: Characterizations and applications of micelles, microemulsions, monolayers, bilayers, vesicles, host-guest systems, and polyions, *John Wiley & Sons Inc*, 1982.

[35] D.H. Hubert, M. Jung, P.M. Frederik, P.H. Bomans, J. Meuldijk, A.L. German, Morphology transformations of DODAB vesicles reminiscent of endocytosis and vesicular traffic, *Langmuir,* 16 (2000) 8973-8979.

[36] N. Duzgunes, J.A. Goldstein, D.S. Friend, P.L. Felgner, Fusion of liposomes containing a novel cationic lipid, N-[2, 3-(dioleyloxy) propyl]-N, N, N-trimethylammonium: Induction by multivalent anions and asymmetric fusion with acidic phospholipid vesicles, *Biochemistry,* 28 (1989) 9179-9184.

[37] I.M. Oliveira, J.P. Silva, E. Feitosa, E.F. Marques, E.M. Castanheira, M.E.C.R. Oliveira, Aggregation behavior of aqueous dioctadecyldimethylammonium bromide/monoolein mixtures: A multitechnique investigation on the influence of composition and temperature, *J. Colloid Interface Sci.,* 374 (2012) 206-217.

[38] P. Singh, S. Choudhury, V. Sharma, S. Mitra, R. Mukhopadhyay, R. Das, S.K. Pal, Modulation of solvation and molecular recognition of a lipid bilayer under dynamical phase transition, *ChemPhysChem,* 19 (2018) 2709-2716.

[39] N.C. Maiti, M. Krishna, P. Britto, N. Periasamy, Fluorescence dynamics of dye probes in micelles, *J. Phys. Chem. B,* 101 (1997) 11051-11060.

[40] D.J. Birch, R.E. Imhof, Time-domain fluorescence spectroscopy using time-correlated single-photon counting, in: Topics in fluorescence spectroscopy, *Springer*, 2002.

[41] G. Dutt, Are the experimentally determined microviscosities of the micelles probe dependent?, *J. Phys. Chem. B,* 108 (2004) 3651-3657.

[42] H. Walderhaug, O. Soederman, P. Stilbs, Micellar dynamics and organization. A multifield carbon-13 NMR spin-lattice relaxation and {proton} carbon-13 nuclear Overhauser effect study, *J. Phys. Chem.,* 88 (1984) 1655-1662.

[43] H. Nery, O. Soederman, D. Canet, H. Walderhaug, B. Lindman, Surfactant dynamics in spherical and nonspherical micelles. A nuclear magnetic resonance study, *J. Phys. Chem.,* 90 (1986) 5802-5808.

[44] E. Feitosa, C.R. Benatti, M.J. Tiera, Effect of sonication on the thermotropic behavior of DODAB vesicles studied by fluorescence probe solubilization, *J. Surfactants Deterg.,* 13 (2010) 273-280.

[45] T. Yamada, N. Takahashi, T. Tominaga, S.-i. Takata, H. Seto, Dynamical behavior of hydration water molecules between phospholipid membranes, *J. Phys. Chem. B,* 121 (2017) 8322-8329.

[46] Y. Levy, J.N. Onuchic, Water mediation in protein folding and molecular recognition, *Annu. Rev. Biophys. Biomol. Struct.,* 35 (2006) 389-415.

[47] L. Barbassa, E.M. Mamizuka, A.M. Carmona-Ribeiro, Supramolecular assemblies of rifampicin and cationic bilayers: Preparation, characterization and micobactericidal activity, *BMC Biotechnol.,* 11 (2011) 40-48.

[48] F. Rodríguez-Prieto, C.C. Corbelle, B. Fernández, J.A. Pedro, M.C.R. Rodríguez, M. Mosquera, Fluorescence quenching of the N-methylquinolinium cation by pairs of water or alcohol molecules, *Phys. Chem. Chem. Phys.,* 20 (2018) 307-316.

[49] M. Bermudez, E. Martinez, M. Mora, M. Sagristá, M. De Madariaga, Molecular and physicochemical aspects of the interactions of the tuberculostatics ofloxacin and rifampicin with liposomal bilayers: A 31P-NMR and DSC study, *Colloids Surf. A,* 158 (1999) 59-66.

[50] C. Rodrigues, P. Gameiro, M. Prieto, B. De Castro, Interaction of rifampicin and isoniazid with large unilamellar liposomes: Spectroscopic location studies, *Biochim. Biophys. Acta, Gen. Subj.*, 1620 (2003) 151-159.

[51] I. Drexler, C. Staib, W. Kastenmüller, S. Stevanović, B. Schmidt, F.A. Lemonnier, H.-G. Rammensee, D.H. Busch, H. Bernhard, V. Erfle, Identification of vaccinia virus epitope-specific HLA-A* 0201-restricted T cells and comparative analysis of smallpox vaccines, *Proc. Natl. Acad. Sci. U.S.A.*, 100 (2003) 217-222.

[52] F. Feixas, S. Lindert, W. Sinko, J.A. McCammon, Exploring the role of receptor flexibility in structure-based drug discovery, *Biophys. Chem.*, 186 (2014) 31-45.

[53] A.A. Gorfe, A. Caflisch, I. Jelesarov, The role of flexibility and hydration on the sequence-specific DNA recognition by the Tn916 integrase protein: A molecular dynamics analysis, *J. Mol. Recognit.*, 17 (2004) 120-131.

[54] G. Chillemi, T. Castrignano, A. Desideri, Structure and hydration of the DNA-human topoisomerase I covalent complex, *Biophys. J.*, 81 (2001) 490-500.

[55] V. Tsui, I. Radhakrishnan, P.E. Wright, D.A. Case, NMR and molecular dynamics studies of the hydration of a zinc finger-DNA complex1, *J. Mol. Biol*, 302 (2000) 1101-1117.

[56] P. Singh, V.K. Sharma, S. Singha, V. García-Sakai, R. Mukhopadhyay, R. Das, S.K. Pal, Unravelling the role of monoolein in fluidity and dynamical response of a mixed cationic lipid bilayer, *Langmuir*, 35 (2019) 4682-4692.

[57] V. Sharma, E. Mamontov, M. Tyagi, V. Urban, Effect of α-Tocopherol on the microscopic dynamics of dimyristoylphosphatidylcholine membrane, *J. Phys. Chem. B*, 120 (2015) 154-163.

[58] P. Dubey, H. Srinivasan, V. Sharma, S. Mitra, V.G. Sakai, R. Mukhopadhyay, Dynamical transitions and diffusion mechanism in DODAB bilayer, *Sci. Rep.*, 8 (2018) 1862.

[59] S. Busch, C. Smuda, L.C. Pardo, T. Unruh, Molecular mechanism of long-range diffusion in phospholipid membranes studied by quasielastic neutron scattering, *J. Am. Chem. Soc.*, 132 (2010) 3232-3233.

[60] V. Sharma, E. Mamontov, D. Anunciado, H. O'Neill, V. Urban, Nanoscopic dynamics of phospholipid in unilamellar vesicles: effect of gel to fluid phase transition, *J. Phys. Chem. B,* 119 (2015) 4460-4470.

[61] V.K. Sharma, E. Mamontov, D.B. Anunciado, H. O'Neill, V.S. Urban, Effect of antimicrobial peptide on the dynamics of phosphocholine membrane: Role of cholesterol and physical state of bilayer, *Soft Matter,* 11 (2015) 6755-6767.

[62] V. Sharma, E. Mamontov, M. Tyagi, S. Qian, D. Rai, V. Urban, Dynamical and phase behavior of a phospholipid membrane altered by an antimicrobial peptide at low concentration, *J. Phys. Chem. Lett.,* 7 (2016) 2394-2401.

[63] S. Singha, D. Kim, B. Roy, S. Sambasivan, H. Moon, A.S. Rao, J.Y. Kim, T. Joo, J.W. Park, Y.M. Rhee, A structural remedy toward bright dipolar fluorophores in aqueous media, *Chem. Sci.,* 6 (2015) 4335-4342.

[64] S. Choudhury, P.K. Mondal, V. Sharma, S. Mitra, V.G. Sakai, R. Mukhopadhyay, S.K. Pal, Direct observation of coupling between structural fluctuation and ultrafast hydration dynamics of fluorescent probes in anionic micelles, *J. Phys. Chem. B,* 119 (2015) 10849-10857.

[65] J. Maiti, V. Kalyani, S. Biswas, F. Rodriguez-Prieto, M. Mosquera, R. Das, Slow solvation dynamics in supramolecular systems based on bile salts: Role of structural rigidity of bile salt aggregates, *J. Photochem. Photobiol. A,* 346 (2017) 17-23.

[66] T. Li, A.A. Hassanali, S.J. Singer, Origin of slow relaxation following photoexcitation of W7 in myoglobin and the dynamics of its hydration layer, *J. Phys. Chem. B,* 112 (2008) 16121-16134.

[67] L. Nilsson, B. Halle, Molecular origin of time-dependent fluorescence shifts in proteins, *Proc. Natl. Acad. Sci. U.S.A.,* 102 (2005) 13867-13872.

Chapter 5

Spectroscopic Studies on Photosensitization of a Biomimetic System and its Interaction with Biological Cell Lines

5.1. Introduction: Potential therapeutic (cargo drug) encapsulation coupled with stimuli responsiveness of drug delivery systems (DDS) have gained tremendous attention in recent years [1, 2]. It not only eludes the possibilities of premature drug release but also improves the therapeutic efficacy by the means of enhanced spatio-temporal accumulation of the therapeutic payload [3, 4]. This further lowers the cytotoxic effect of the therapeutic drug other than the tumor sites and also favors overcoming the drug resistance [5, 6]. These classes of DDS are mostly composed of three ingredients (i) a tumor targeting therapeutic carrier (ii) an external stimuli sensitive agents that can destabilize therapeutic carrier for efficient drug delivery (iii) a drug capable for tracking the spatial distribution, localization, and depletion from the DDS. Owing to the encapsulation characteristics and biocompatibility, liposomes recommend them as efficient carriers for therapeutic agents [7]. Out of the various published methods for triggering the release of drug molecules from liposome, photoinduced destabilization is a particularly attractive method for providing fast reaction rates [8]. Photo induction or light triggering generally offers the great benefit of not affecting physiological parameters such as temperature, pH and ionic strength, a fundamental requisite for biomedical applications [9, 10]. Liposome can be made photosensitive by using photochromic agents that isomerize [11-13], polymerize [14-16], fragment [17] or induce oxidative reactions [18, 19] upon irradiation [20, 21].

Many studies have reported changes in the permeability of vesicles toward ions and low molecular weight water-soluble compounds upon

irradiation [14, 22]. In contrast, biopolymers do not easily cross the membrane owing to the combined effects of conformation [23] and electric charge [24] and a drastic change in liposome morphology is required. Riske and co-workers reported morphological changes (bi-layer destabilization) in vesicles of mixtures of phosphatidylcholine and amphiphilic porphyrin which works as a photosensitizer [19]. Although the morphological changes observed are remarkable but their system has a high molar ratio of photoresponsive amphiphile to membrane lipid (>40 mol%), which is in comparable to the composition of biomembranes. In this regard, investigations have been conducted on liposomes containing photoresponsive compounds such as azobenzene, stilbene, spiropyran [22, 25, 26], and photo-polymerizable lipids [14, 15], wherein the lipid membrane is destabilized by light. Photosensitive proton sources such as 3,3-dicarboxydiphenyliodonium salts allow for efficient destabilization of the phosphatidylcholine bilayer by adsorption of the hydrophobic polyelectrolyte, but result in vesicle-to-micelle transition, and consequently, corroborate complete solubilization of the membrane [27]. Since solubilization of the vesicles results in cytotoxicity, cellular uptake of drugs in the targeted domain without any solubilization is desired for ideal drug delivery systems. Therefore, it is necessary to ensure photo-triggered destabilization of phosphatidylcholine membrane without disruption of the liposome structure.

Herein, we have used a synthesized photochromic dye dihydroindolizine (DHI) to investigate its efficacy in photoresponsive destabilization of phosphatidylcholine liposome, which is used as potential drug delivery vehicles. Photochromic DHI dye has received much attention owing to its remarkable photo-fatigue resistance and broad range of absorption. Specifically, DHI can undergo a reversible transformation from light yellow colored isomer to red-colored betaine isomer upon UVA irradiation with an increase in the polarity associated with the structural conversion from neutral (closed form) to charge-separated zwitterions (open form) (Scheme 5.1) [28, 29]. This structural conversion of DHI from closed to

open isomer can fluctuate or defect the liposomal membrane by mechanical stress and leads photoresponsive destabilization to liposome. Besides destabilization, photochromic agents can affect the liposome by various processes including aggregation [30, 31], fusion [22, 32, 33], and total membrane disruption [34]. Hence, we have monitored the entire possible phenomena by using time resolved fluorescence spectroscopy by labelling the liposome with fluorescent probe 8-anilino-1-naphthalenesulfonic acid ammonium salt (ANS). The picosecond resolved fluorescence transients and

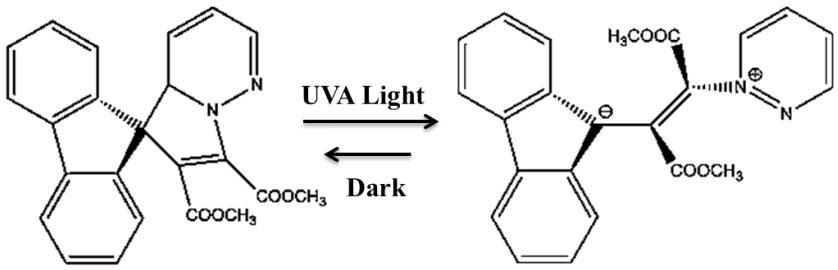

Scheme 5.1. *Structures of the closed and open isomers of DHI.*

polarization gated spectroscopy studies of ANS attached to hydrophobic core of liposome confirm higher permeability of liposome upon closed to open isomerization of DHI. The solvatochromic property of ANS has been used to study the dynamics of solvation and also to eliminate the possible existence of membrane disruption (like membrane solubilisation and vesicles to micelles conversion) in the studied systems upon light irradiation. Förster resonance energy transfer (FRET) techniques between the FRET pair ANS (incorporated to one set of liposome) and doxorubicin (encapsulated to other liposome system) have successfully manifested the possibility of liposome fusion by the course of photo triggered bilayer destabilization. Based on these photoresponsive microstructural changes of liposome, the *in vitro* drug release profile of cargo drug (DOX) has been studied through dialysis method. We have also investigated the therapeutic efficacy of DOX delivery from liposome to cervical cancer cell line HeLa. Our FACS, confocal fluorescence microscopic and MTT assay based studies reveal an enhanced cellular uptake of DOX

leading to significant reduction in cell viability of HeLa due to photoresponsive destabilization of liposome. Hence, we successfully established the DHI encapsulated liposome as a promising and model drug delivery vehicle.

5.2. Results and Discussion:

5.2.1. Photo-triggered Destabilization of Nanoscopic Vehicles by Dihydroindolizine for Enhanced Anticancer Drug Delivery in Cervical Carcinoma [35]: To elucidate the consequence of photo-sensitive isomerization of DHI to liposome bilayer, primarily the interaction of DHI with liposome

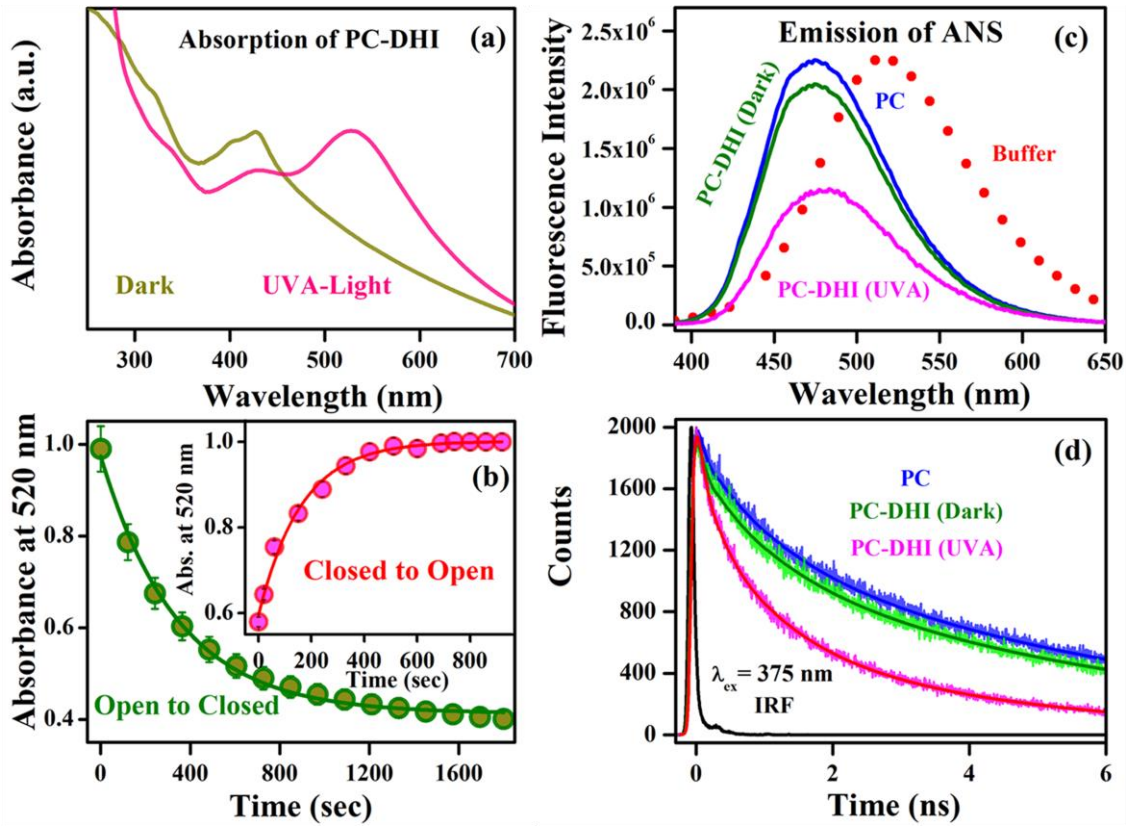

Figure 5.1. *(a) Absorption spectra of DHI in liposome: closed and open isomers. (b) Kinetics of the open to closed transition of DHI in liposome (SD = ± 0.008, n = 3). Inset shows the corresponding closed to open conversion rate (SD = ± 0.003, n = 3). (c) Steady state emission spectra of ANS in buffer, ANS bound to PC and PC-DHI in presence and absence of UVA light. (d) Time-resolved transients of ANS, ANS bound to PC and ANS bound to PC-DHI in the presence and absence of UVA light.*

(PC) was studied. Figure 5.1.a represents the optical absorption spectrum of the neutral form of DHI in liposome bilayer having peak maxima at 410 nm. A redshift in the absorption spectra of DHI relative to that in acetonitrile solution

having absorption maxima at 390 nm confirms the ground-state complexation of the photochromic dye with the liposome [36]. The reversible transformation of DHI from closed to open configurations in the liposome was evident from the decrease of the absorption peak at 410 nm and the concurrent increase of the strong peak at 520 nm. These absorption bands can be assigned to the locally excited π-π* transition that occurs in the butadienyl-vinyl-amine chromophores. To evaluate the photochromic behavior of DHI in liposome, photo isomerization reaction kinetics was monitored by measuring the change in absorbance at 520 nm. While UVA triggered closed to open transition of DHI corroborates increased in absorbance at 520 nm (shown in inset of Figure 5.1.b), whereas thermal relaxation leading open to closed transition of DHI was confirmed by decrease in absorbance at 520 nm (shown in Figure 5.1.b). The values of rate constant (*t*) for closed to open and open to closed isomerization of DHI were found to be 150 s and 340 s, respectively. The significant increase of *t* for DHI in liposome with respect to acetonitrile solution was thought to be resulted from hindered and slowed isomerization process due to the incorporation of DHI into the liposomes bilayer.

After subsequent validation of the DHI incorporation to liposome, consequence of different isomerization of DHI on liposome stability is monitored by using fluorescent probe 8-anilino-1-naphthalenesulfonic acid ammonium salt (ANS) which is commonly used to monitor the structural changes of proteins and membranes [37]. Figure 5.1.c represents the steady-state fluorescence spectra of ANS in liposome (~480 nm) which is found to be markedly blue shifted compared to buffer (~520 nm) indicating that the local polarity around ANS is lower than that of bulk water. Furthermore, the similarity in the position of the emission peak maximum of ANS in the liposome to that in CHT protein (~ 480 nm) is consistent with the fact that the dye resides in the hydrophobic bilayers of the liposome [38]. The fluorescence intensity as well as emission peak maximum of ANS-PC is observed to be similar to ANS-PC-DHI complex under dark condition, revealing the fact that ANS molecules are not detached from PC upon encapsulation of DHI to same

hydrophobic bilayer of the liposome. However, the fluorescence intensity of ANS-PC-DHI is found to be decreased along with a small red-shift (~ 5 nm) in emission maximum upon UVA irradiation. This suggests that ANS is now experiencing higher polarity upon closed to open transition of DHI. The higher

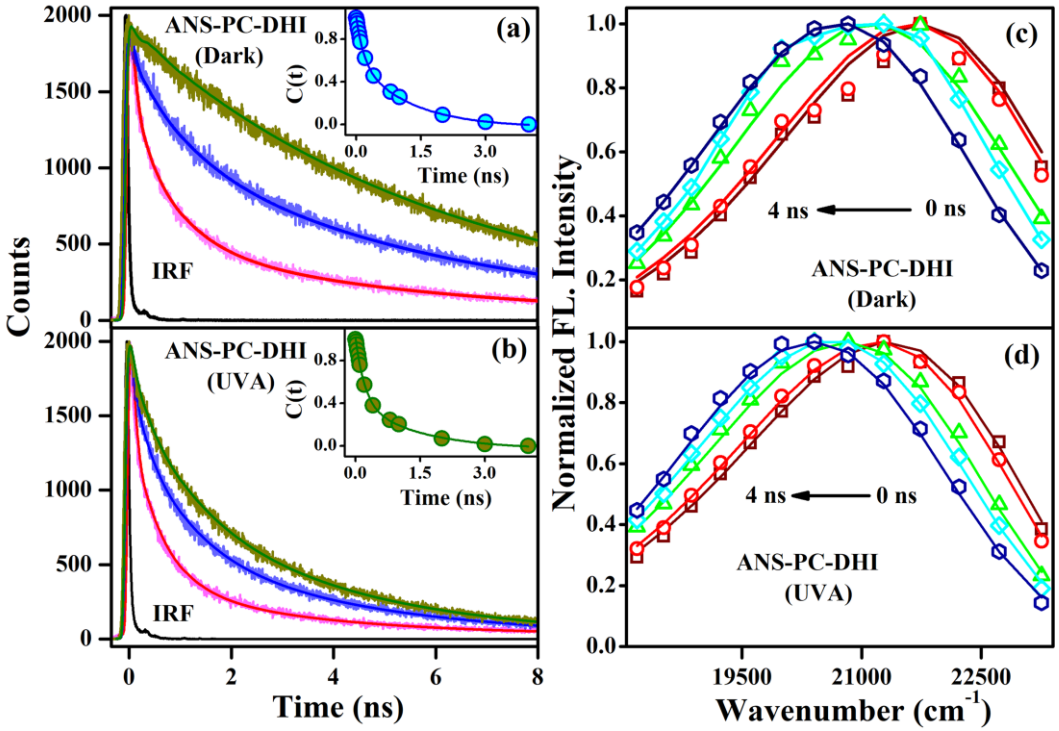

***Figure* 5.2.** *Picosecond-resolved transient of ANS at three different wavelengths in (a) PC-DHI in dark condition and (b) PC-DHI in presence of UVA light. (c, d) Time-resolved emission spectra (TRES) of corresponding systems are shown. Insets depict the corresponding solvation correlation decay profile of ANS.*

polarity around ANS due to UVA irradiation on DHI could occurs either due to displacement of some ANS toward bulk solution or due to increase in permeability of liposome because of its destabilization. Figure 5.1.d shows picosecond-resolved transients of ANS bound PC which is found to be multi-exponential in nature with average decay time constant of 3.0 ns. The fluorescence transient of the ANS-PC-DHI complex is found to be faster upon UVA irradiation (average decay time of 1.3 ns) than that of the dark condition (average decay time of 2.8 ns). The faster fluorescence decay along with the reduced quantum yield of ANS-PC-DHI upon UVA irradiation also indicates the enhancement of non-radiative relaxation due to increase in mobility of the solvating species. The enhancement of polarity around ANS could occur due to

photoresponsive destabilization of liposome. As DHI is hydrophobic under dark conditions, it used to encapsulate in the lipid bilayer of liposome. Once irradiated by UVA light, DHI isomerize from closed form to open form. Since the size and polarity of open form of DHI is different (higher) hence the orientation of open form will be different from that of closed form of DHI. Thus, under UVA irradiation, the liposomal membrane would be disturbed by the reorientation of open isomer and leads to increase in membrane permeability by mixing the inner components of the liposomes with outer components in aqueous solution.

Table 5.1. *Fluorescence lifetimes of ANS in different systems.*

System/Wavelength	$\tau_1 \pm$ SD ns [%]	$\tau_2 \pm$ SD ns[%]	$\tau_3 \pm$ SD ns [%]	τ_{avg} ns	χ^2
PC/480 nm	0.12±0.01(33)	1.04±0.05 (22)	6.22±0.21 (45)	3.07	1.03
PC-DHI/430 nm	0.13±0.01(58)	0.92±0.04 (27)	5.71±0.28 (15)	1.17	1.04
PC-DHI/480 nm	0.12±0.01(35)	1.08±0.05 (23)	6.00±0.30 (42)	2.82	1.05
PC-DHI/550 nm	0.17± 0.02 (-5)	0.16±0.01 (29)	6.17±0.31 (76)	4.72	1.05
PC-DHI-UVA/430 nm	0.12±0.01(68)	0.84±0.04 (25)	4.38±0.21 (7)	0.61	1.08
PC-DHI-UVA/480 nm	0.15±0.01(46)	1.04±0.05 (31)	3.99±0.19 (23)	1.31	1.04
PC-DHI-UVA/550 nm	0.18±0.01(38)	1.26±0.06 (28)	3.77±0.18 (34)	1.70	1.03

For various systems, the wavelengths (nm) and standard deviation (SD) of time-resolved decay measurements are shown. The amplitudes corresponding to the relevant decay components are shown within the parentheses.

The ability to induce destabilization by light suggests many interesting primary processes involved in changing the liposome reconstruction. Beside bilayer destabilization, photoresponsive agent have various effects on liposomes, including fusion [32, 33, 39], rearrangement of bilayer [30, 31] and total membrane perturbation (i.e. transformation into micelles or solubilization of the lipid membrane) [34, 40]. However the eminent role of water during the course of perturbation/rearrangement cannot be neglected as it plays a major role in assembly of macromolecular structure and dynamics. Hence to understand the dynamic nature of water molecules at the liposome bilayer during photoresponsive destabilization, time resolved Stokes shift (TRSS) could be useful techniques to estimate the environmental relaxation of

biomolecules over a broad time scale. Figure 5.2.a shows the wavelength-dependent emission transients of ANS in PC-DHI complex under dark condition at three characteristic wavelengths. The time resolved fluorescence at the blue and the red end is characterized by decay and a rise, respectively, indicating the picture of solvation dynamics, a phenomenon which represents the rate at which the solvent dipoles/charged species are rearranged, surrounding an instantaneously created dipole. Upon UVA irradiated closed to open transition of DHI, the transients of ANS in PC still show wavelength dependency, however, with a decrease in the time constants as shown in Figure 5.2.b (Table 5.1). Figure 5.2.c and Figure 5.2.d show the constructed time-resolved emission spectra (TRES) of ANS-PC-DHI with a spectral shift of 1012 cm^{-1} and 959 cm^{-1} in dark and UVA irradiated condition, respectively, in a 4 ns time window. ANS bound to PC-DHI in dark (inset of Figure 5.2.a) exhibits bimodal solvation dynamics with time components of 0.17 ns (40%) and 1.24 ns (60%), respectively. which are consistent with our previous studies on the solvation dynamics of liposome [41]. Upon UVA irradiation, both the two time components becomes faster, indicating increased polarity in the bilayers however presence of longer component represents ANS is still attached to the liposome systems. As both these components are slower than the sub picosecond solvation time scale reported for the bulk water [42] hence we can conclude that UVA irradiated isomerization of DHI could destabilized bilayer without any membrane disruption. This observation confirms the absence of membrane disruption i.e. liposome to micelle transition upon UVA irradiation.

To ascertain the geometrical restriction of the probe in the bilayer region, we measure the time-resolved rotational anisotropy of the ANS in dark and UVA irradiated PC-DHI complex (Table 5.2). The time-resolved anisotropy decay of ANS-PC-DHI, shown in Figure 5.3.a, revealed a rotational time constant of 8.09 ns attributed to the overall global tumbling motion of the liposome. With UVA irradiation the r(t) decay of the ANS-PC-DHI complex (Figure 5.3.b) exhibited one faster component of 0.71 ns due to the internal rotation of the fluorophore relative to the liposome (wobbling of the probe),

indicating a progressive release of restriction on the probe might be due to increase in the mobility of solvating species. However presence of a slow component of the rotational time constant indicates ANS is still bound to the

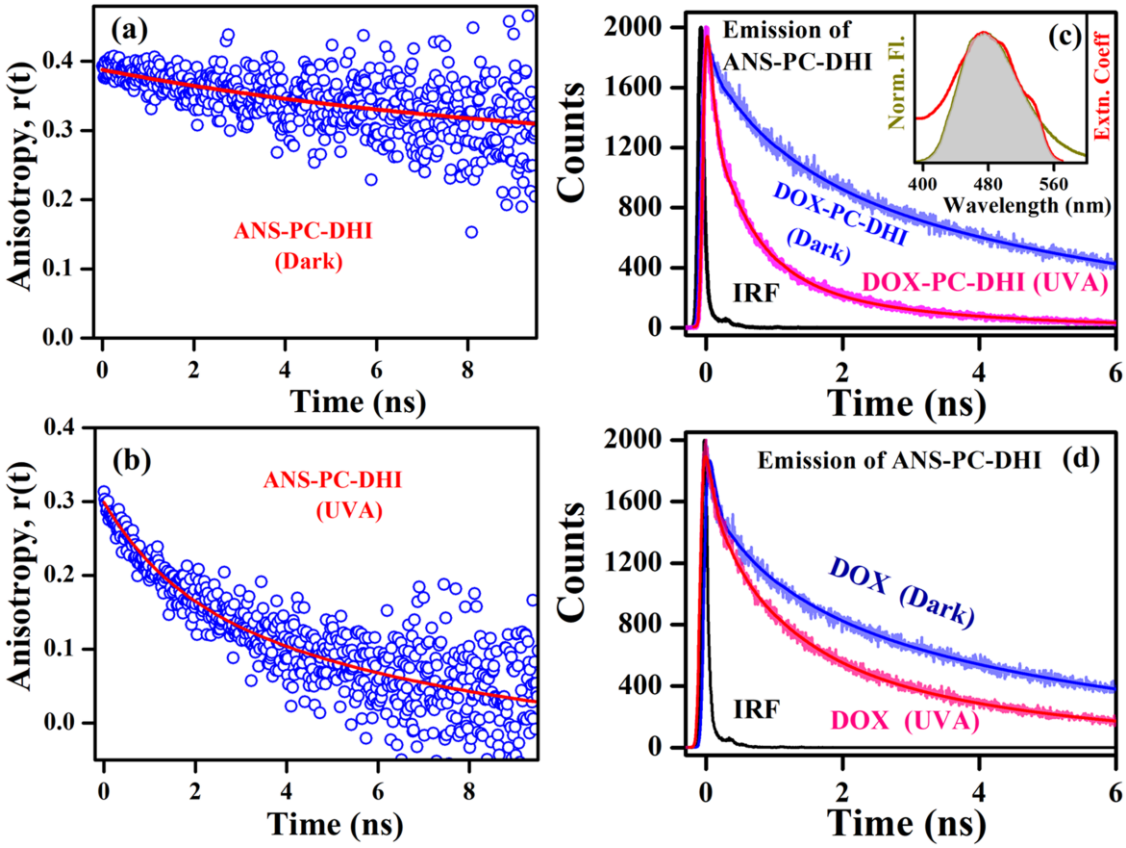

Figure 5.3. *Time-resolved anisotropy of ANS bound to PC-DHI in presence of (a).dark and (b) UVA light. Picosecond-resolved transients of the donor-acceptor in the absence and presence of UVA light, (c) donor is (ANS-PC-DHI) and acceptor is (DOX-PC-DHI) and (d) donor is (ANS-PC-DHI) and acceptor is free DOX. Insets depict the corresponding spectral overlap between donor (ANS-PC-DHI complex) emission and acceptor (DOX-PC-DHI) absorbance.*

surface of the liposome. This change is also manifested in the observed faster solvation dynamics of ANS bound to PC at UVA irradiated closed to open transition of DHI. Thus, the observed correlation between faster solvation dynamics and flexible internal motion of liposome corroborates that UVA irradiated isomerisation of DHI destabilizes the local environment of the bilayers of liposome without membrane disruption. In the latter case the dynamics of solvation is expected to be much faster (bulk water type) than the observed change of average solvation time constant from ~ 810 ps to 580 ps upon UVA exposure.

Table 5.2. *Solvation correlation time constants and rotational time constants of ANS encapsulated in PC-DHI at different conditions.*

System	Solvation time constants		Rotational time constants		χ^2
	$\tau_1 \pm$ SD ns [%]	$\tau_2 \pm$SD ns[%]	$\tau_1 \pm$ SD ns [%]	$\tau_2 \pm$ SD ns [%]	
Dark	0.17±0.01(40)	1.24±0.06(60)	-	8.09±0.24(100)	0.96
UV	0.15±0.01(43)	0.91±0.04(57)	0.71±0.0 3(17)	4.66±0.09(83)	0.88

For various systems, the standard deviation (SD) of time-resolved decay measurements is shown. The amplitudes corresponding to the relevant solvation and rotational components are shown within the parentheses.

After revealing that the irradiation of DHI induces liposome destabilization in the absence of total solubilization of the lipid membrane, we examined the possibility of other two processes i.e. rearrangement of bilayer and fusion between liposomes, induced by DHI. To understand the fusion phenomenon, Förster resonance energy transfer (FRET) techniques was used which offers a unique opportunity to measure an efficiency of energy transfer when donor and acceptor comes in proximity of each other. In order to monitor the fusion process, ANS was encapsulated in a group of liposome and doxorubicin (DOX) was encapsulated in another were both the two type of liposome was having DHI. Inset of Figure 5.3.c shows a spectral overlap between ANS-PC-DHI emission and the absorption of the DOX-PC-DHI ($J(\lambda) = 4.4X10^{14}$) suggests a possibility of FRET from ANS to DOX. The average lifetime of ANS in presence of mixer of two liposome decreased from 2.40 ns in dark condition to 0.47 ns upon UVA irradiated (Table 5.3). The energy-transfer efficiency was calculated to be 80%, as a consequence, the ANS-DOX distance is found to be 2.6 nm. We confirmed in a separate experiment that simple dilution of DOX in the medium containing ANS-PC-DHI does not cause the quenching of ANS fluorescence outside the liposome upon UVA irradiation (Figure 5.3.d). It has to be noted that the marginally faster time constant of ANS-PC-DHI in presence of free DOX upon UVA irradiation is the signature of fast relaxation of ANS due to destabilization of bilayer. Therefore, the quenching of ANS fluorescence may take place when the ANS-encapsulating liposomes are fused together with the DOX-encapsulating liposome in presences of UVA light. The finding also indicates that UVA irradiated DHI

sensitized liposome could not induce the rearrangement leading to inclusion of lipids from external sources. The rearrangement would not cause quenching of ANS emission.

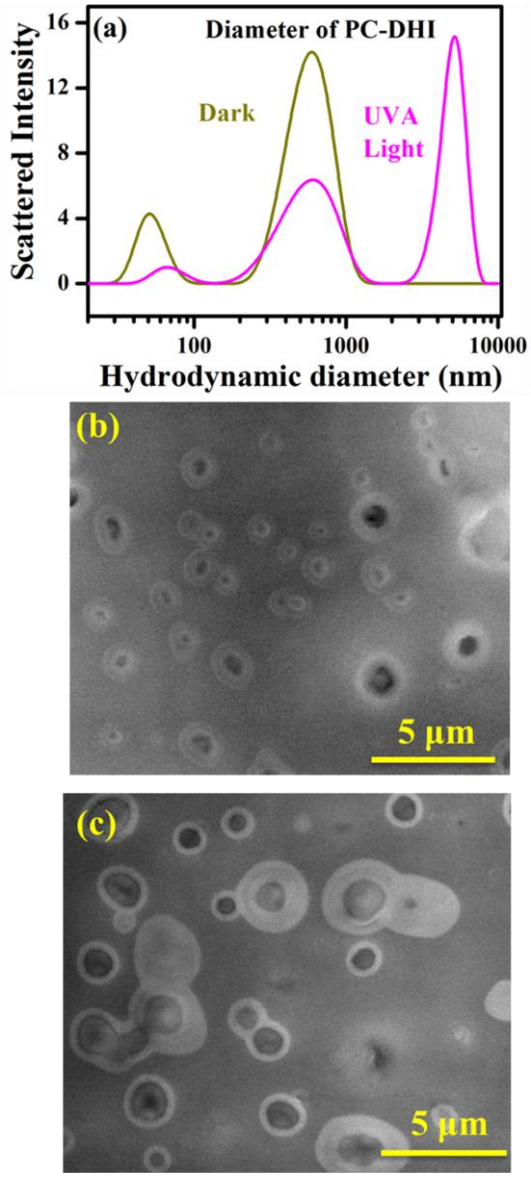

Figure 5.4. *(a) Hydrodynamic diameter of PC-DHI in absence and presence of UVA light. SEM images of PC-DHI in (b) dark condition and (c) upon UVA-irradiation.*

The effect of photoresponsive membrane destabilization on the change in liposome morphology was also monitored by investigating the size of liposomes before and after UVA-irradiation. Figure 5.4.a show the DLS spectra of liposome which was found to be polydispersed with ~40–500 nm of size distribution. Due to UVA-irradiation, these peaks had divided into three peaks at 40 nm, 500 nm and 3000 nm. The significant increase in size also indicates

not only the expansion but also the possibilities of fusion of liposomes. The size distribution of liposomes verified the vesicle structures existed in both conditions. Moreover, in order to investigate the liposome fusion at lower concentration, we have performed DLS experiment with lower PC concentration values (data not shown). It is observed that the DHI-sensitized liposomes of ~ 50 μm PC concentration, undergo fusion upon UVA exposure with relatively lower degree of fusion due to dilution leading to higher inter-liposome distance. Figure 5.4.b and Figure 5.4.c gave the morphological changes of liposomes due to UVA irradiation. Figure 5.4.b shows the spherical shape of liposomes in dark which confirmed that encapsulation of DHI doesn't hampered the morphology of liposome. When irradiated with UVA light, the liposomes of larger sizes and distorted shapes had been observed after photo isomerization. In a word, their liposome structures were still intact and exhibited no solubilized membrane even after being irradiated by UVA light. This finding is consistent with the results obtained by our time resolved spectroscopic studies.

Table 5.3. *Fluorescence lifetimes of ANS-PC-DHI in different systems.*

System	$\tau_1 \pm$ SD ns [%]	$\tau_2 \pm$ SD ns [%]	$\tau_3 \pm$ SD ns [%]	τ_{avg} ns	χ^2
DOX-PC-DHI	0.11±0.01(47)	1.08± 0.05(19)	6.04± 0.30(34)	2.40	1.05
DOX-PC-DHI (UVA)	0.09±0.01(60)	0.59± 0.02(29)	2.36± 0.11(11)	0.47	1.02
DOX	0.13±0.02(40)	1.06± 0.05(25)	5.29± 0.26(35)	2.3	1.03
DOX-UVA	0.14±0.01(45)	1.00± 0.05(32)	4.26± 0.21(23)	1.37	0.99

For various systems, the standard deviation (SD) of time-resolved decay measurements is shown. The amplitudes corresponding to the relevant decay components are shown within the parentheses.

Based on the photoresponsive properties and microstructural change investigated above, DHI-liposome could be considered as photoresponsive drug delivery system. As the liposome were closed and contained an inner aqueous compartment hence they showed the ability to entrap water-soluble dyes. The hydrophilic cargo drug DOX was used as a model drug, which was loaded into the internal aqueous phase of the liposome. Figure 5.5.a shows the

release behavior of DOX from PC by UVA irradiation. The amount of DOX released out from the PC into the external medium was proportional to the change in fluorescence intensity. A burst release is found to occurred upon UVA irradiation at the 30 minutes followed by a slower sustained release up to 1 h, which is comparable to the other drug delivery systems [8, 43]. We have found the spontaneous release of DOX was observed in the group without UVA irradiation as DOX absorbed on the surface of the liposome diffused to the outside medium when the samples were dispersed in aqueous solution. It has to be noted that, the leakage of DOX in the group without UVA irradiation was not entirely attributed to the burst release. Although HeLa cell is quite older but still drug release from vehicles has been executed on HeLa as model cancer cell [44]. As our judgement is along the line of recent literature hence we have considered HeLa as model cancer cell. Safety and efficacy are the necessary features that to be taken care of when investigating the potential use of the PC-DHI liposome as a drug delivery system. From the decades, liposomes are used for the drug delivery system because of its low toxicity, however photochromic agents used for triggering delivery vehicles are not always found to be biocompatible [45]. Hence, the cytocompatibility of the carrier PC-DHI was first evaluated against human epidermal keratinocyte cells (HaCaT cell line). The power of the UVA source and time of UVA exposure was also optimized using the same cell line (data not shown). The therapeutic efficacy of the drug loaded liposome was evaluated against cervical cancer cell line HeLa by exposing the cells directly to the PC-DHI-DOX in presence or absence of UVA (Figure 5.5.b). In this case also, the cell viability for PC-DHI was reduced only by 6 percentages than that of control indicating the cytocompatibility of PC-DHI formulation. It was observed that the cytotoxicity of DOX loaded-liposome (PC-DHI-DOX) was markedly enhanced following UVA irradiation in HeLa cells. Cell viabilities were about 60% after 24 h incubation with PC-DHI-DOX without UVA irradiation. In comparison, they decreased by more than 40% with UVA irradiation. UVA light induced a low cytotoxicity, only 5% compared to PC-DOX in dark, indicating DHI is solely

responsible for higher delivery of the drug to the cell leading to more cytotoxicity upon UVA exposure.

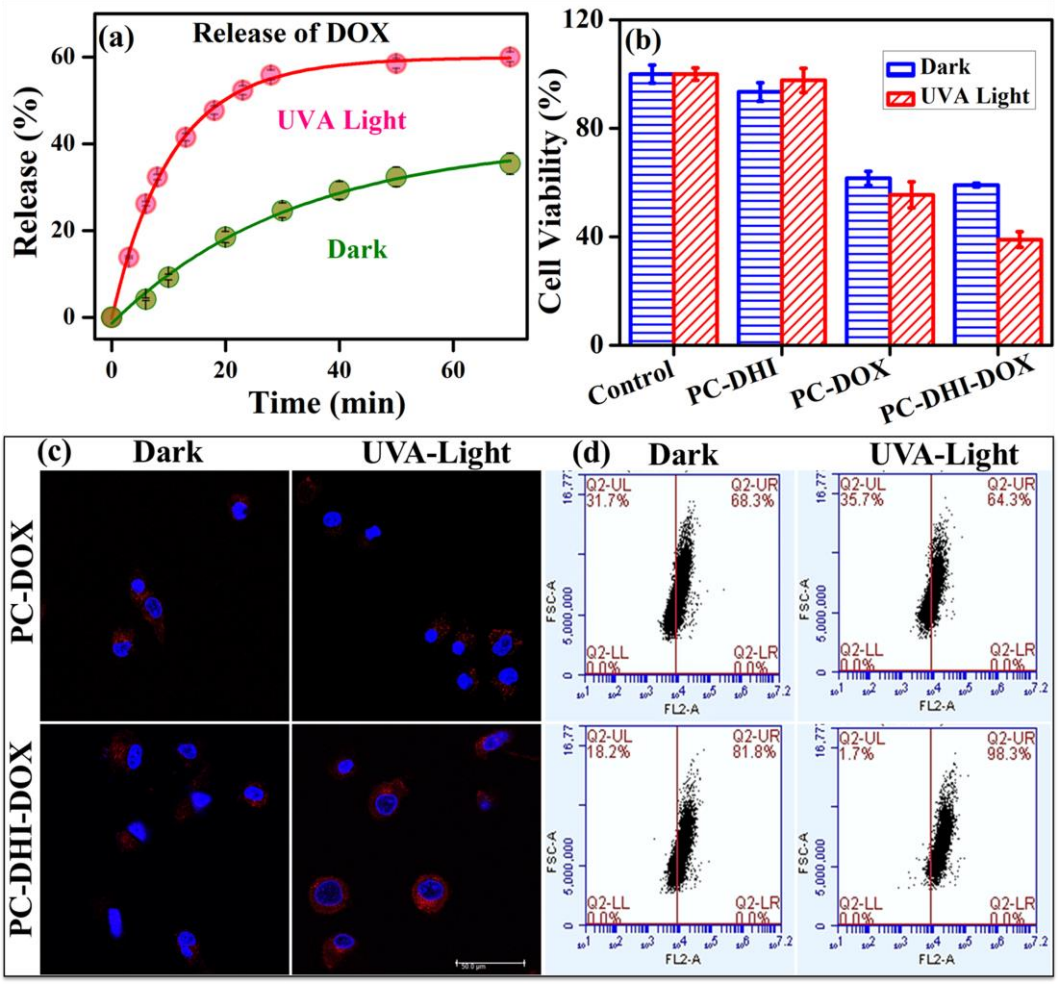

Figure 5.5. *(a) Release profile of DOX from PC-DHI in absence (SD = ± 0.4, n=3) and presence of UVA light (SD = ± 0.9, n=3). (b) Cytotoxicity assay in HeLa cells with PC-DHI, PC-DOX, and PC-DHI-DOX with MTT as an indicator dye in the presence and absence of UV light. (c) Confocal microscopy images of HeLa cells treated with PC-DOX liposome and PC-DHI-DOX liposome both in absence and presence of UVA light (d) Flow cytometry of HeLa cells treated with PC-DOX liposome and PC-DHI-DOX liposome both in absence and presence of UVA light.*

Further, the DHI-assisted delivery of the drug to the cells under UVA exposure was confirmed both qualitatively as well as quantitatively by the help of confocal microscopy and flow cytometry. Qualitative analysis of the confocal fluorescence micrographs clearly showed that under UVA exposure, cellular uptake of DOX in the HeLa cells treated with PC-DHI-DOX was quite higher with respect to the other three systems as evident from the variation in intensity of red colour in Figure 5.5.c. The flow cytometry based quantitative

analysis (Figure 5.5.d) revealed that % of cell populations that underwent DOX uptake was higher (98.3%) in the case cells treated with PC-DHI-DOX under UVA exposure in comparison to PC-DHI-DOX treated cells in dark condition (81.8%). Cells treated with PC-DOX shows no significant changes upon UVA irradiation. These findings altogether indicates higher DOX delivery by UVA trigger PC-DHI liposome (Scheme 5.2). The results presented in this study indicated that DHI encapsulated liposome could serve as a safe and promising drug delivery vehicle.

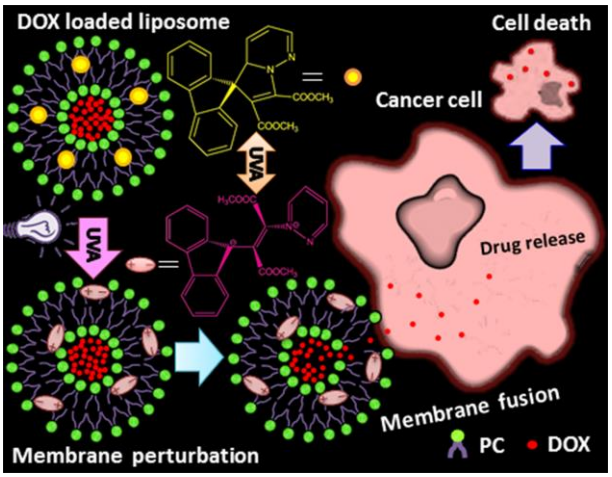

***Scheme* 5.2.** *Schematic representation of the photo-triggered release of DOX payload from PC liposome controlled drug delivery.*

5.3. Conclusion: In this study, we have investigated the photo-controlled alteration of liposome (L-α-phosphatidylcholin) dynamics and morphology via the incorporation of a new class of synthesized photochromic material, dihydroindolizine (DHI). The light-induced reversible pyrroline ring opening (zwitterion form) and the thermal back recovery reaction are responsible for its photochromism. We have demonstrated that structural conversion of DHI from closed to open isomer can fluctuate or defect the liposomal membrane by mechanical stress and hence responsible for fabrication of light trigger drug delivery systems. This destabilization causes an increase in the membrane permeability without complete disruption or solubilization of the liposome under irradiated conditions was manifested by time-resolved fluorescence spectroscopy of ANS bounded to liposome. A faster solvation dynamics in liposome upon light exposure compared to the dark condition rules out the

presence of membrane destruction which has also been evidenced by time resolved polarization gated spectroscopy studies. Absence of an isoemissive point in TRANES further rules out the heterogeneity in the residence of ANS molecules upon destabilization of bilayer. The fusion between the liposomes leading to morphological changes under UVA irradiation was confirmed by using SEM as well as by FRET technique by incorporating ANS and DOX in different sets of liposome. The ability of DHI toward its photoresponsive properties and subsequently leading to microstructural change fabricates it to be considered for potential photoresponsive drug delivery system. Furthermore, the liposome had a strong and quick interaction with HeLa cells and enhanced significant cytotoxicity to the cells upon UVA irradiation. Confocal fluorescence microscopic and flow cytometry studies also revealed that the light triggered DHI encapsulated liposome have high drug delivery efficiency into HeLa cells. Overall, our study showed that these DHI encapsulated liposomes have potential application as a smart photosensitive drug delivery system for cervical carcinoma.

References

[1] J.A. Kemp, M.S. Shim, C.Y. Heo, Y.J. Kwon, "Combo" nanomedicine: Co-delivery of multi-modal therapeutics for efficient, targeted, and safe cancer therapy, *Adv. Drug Deliv. Rev.,* 98 (2016) 3-18.

[2] A. Barhoumi, Q. Liu, D.S. Kohane, Ultraviolet light-mediated drug delivery: Principles, applications, and challenges, *J. Control. Release,* 219 (2015) 31-42.

[3] S. Dai, P. Ravi, K.C. Tam, Thermo-and photo-responsive polymeric systems, *Soft Matter,* 5 (2009) 2513-2533.

[4] S. Mura, J. Nicolas, P. Couvreur, Stimuli-responsive nanocarriers for drug delivery, *Nat. Mater.,* 12 (2013) 991-1003.

[5] Z. Yang, J.H. Lee, H.M. Jeon, J.H. Han, N. Park, Y. He, H. Lee, K.S. Hong, C. Kang, J.S. Kim, Folate-based near-infrared fluorescent theranostic gemcitabine delivery, *J. Am. Chem. Soc.,* 135 (2013) 11657-11662.

[6] S. Maiti, N. Park, J.H. Han, H.M. Jeon, J.H. Lee, S. Bhuniya, C. Kang, J.S. Kim, Gemcitabine–coumarin–biotin conjugates: A target specific theranostic anticancer prodrug, *J. Am. Chem. Soc.,* 135 (2013) 4567-4572.

[7] B. Bondurant, A. Mueller, D.F. O'Brien, Photoinitiated destabilization of sterically stabilized liposomes, *Biochim. Biophys. Acta, Biomembr.,* 1511 (2001) 113-122.

[8] H.J. Seo, J.-C. Kim, 7-acetoxycoumarin dimer-incorporated and folate-decorated liposomes: Photoresponsive release and in vitro targeting and efficacy, *Bioconjugate Chem.,* 25 (2014) 533-542.

[9] N. Kandoth, M. Malanga, A. Fraix, L. Jicsinszky, É. Fenyvesi, T. Parisi, I. Colao, M.T. Sciortino, S. Sortino, A host–guest supramolecular complex with photoregulated delivery of nitric oxide and fluorescence imaging capacity in cancer cells, *Chem. Asian J.,* 7 (2012) 2888-2894.

[10] R.M. Uda, E. Hiraishi, R. Ohnishi, Y. Nakahara, K. Kimura, Morphological changes in vesicles and release of an encapsulated compound triggered by a photoresponsive malachite green leuconitrile derivative, *Langmuir,* 26 (2010) 5444-5450.

[11] Y. Sasaki, S. Iwamoto, M. Mukai, J.-i. Kikuchi, Photo-and thermo-responsive assembly of liposomal membranes triggered by a gemini peptide lipid as a molecular switch, *J. Photochem. Photobiol. A,* 183 (2006) 309-314.

[12] T. Hamada, Y.T. Sato, K. Yoshikawa, T. Nagasaki, Reversible photoswitching in a cell-sized vesicle, *Langmuir,* 21 (2005) 7626-7628.

[13] K.i. Ishii, T. Hamada, M. Hatakeyama, R. Sugimoto, T. Nagasaki, M. Takagi, Reversible control of exo-and endo-budding transitions in a photosensitive lipid membrane, *ChemBioChem,* 10 (2009) 251-256.

[14] A. Mueller, B. Bondurant, D.F. O'Brien, Visible-light-stimulated destabilization of PEG-liposomes, *Macromolecules,* 33 (2000) 4799-4804.

[15] B. Bondurant, D.F. O'Brien, Photoinduced destabilization of sterically stabilized liposomes, *J. Am. Chem. Soc.,* 120 (1998) 13541-13542.

[16] T.M. Sisson, H.G. Lamparski, S. Kölchens, A. Elayadi, D.F. O'Brien, Cross-linking polymerizations in two-dimensional assemblies, *Macromolecules,* 29 (1996) 8321-8329.

[17] A. Veronese, N. Berclaz, P.L. Luisi, Photoinduced formation of bilayer vesicles, *J. Phys. Chem. B,* 102 (1998) 7078-7080.

[18] W. Caetano, P.S. Haddad, R. Itri, D. Severino, V.C. Vieira, M.S. Baptista, A.P. Schröder, C.M. Marques, Photo-induced destruction of giant vesicles in methylene blue solutions, *Langmuir,* 23 (2007) 1307-1314.

[19] K.A. Riske, T.P. Sudbrack, N.L. Archilha, A.F. Uchoa, A.P. Schroder, C.M. Marques, M.S. Baptista, R. Itri, Giant vesicles under oxidative stress induced by a membrane-anchored photosensitizer, *Biophys. J.,* 97 (2009) 1362-1370.

[20] Y. Sun, Y. Ji, H. Yu, D. Wang, M. Cao, J. Wang, Near-infrared light-sensitive liposomes for controlled release, *RSC Adv.,* 6 (2016) 81245-81249.

[21] J. Massiot, A. Makky, F. Di Meo, D. Chapron, P. Trouillas, V. Rosilio, Impact of lipid composition and photosensitizer hydrophobicity on the efficiency of light-triggered liposomal release, *Phys. Chem. Chem. Phys.,* 19 (2017) 11460-11473.

[22] Y. Lei, J.K. Hurst, Photoregulated potassium ion permeation through dihexadecyl phosphate bilayers containing azobenzene and stilbene surfactants, *Langmuir,* 15 (1999) 3424-3429.

[23] M.J. Zuckermann, T. Heimburg, Insertion and pore formation driven by adsorption of proteins onto lipid bilayer membrane–water interfaces, *Biophys. J.,* 81 (2001) 2458-2472.

[24] P. Fromherz, Lipid-vesicle structure: Size control by edge-active agents, *Chem. Phys. Lett.,* 94 (1983) 259-266.

[25] H. Sakai, A. Matsumura, S. Yokoyama, T. Saji, M. Abe, Photochemical switching of vesicle formation using an azobenzene-modified surfactant, *J. Phys. Chem. B,* 103 (1999) 10737-10740.

[26] R.F. Khairutdinov, J.K. Hurst, Photocontrol of ion permeation through bilayer membranes using an amphiphilic spiropyran, *Langmuir,* 17 (2001) 6881-6886.

[27] H. You, D.A. Tirrell, Photoinduced, polyelectrolyte-driven release of contents of phosphatidylcholine bilayer vesicles, *J. Am. Chem. Soc.,* 113 (1991) 4022-4023.

[28] A. Fernando, A.P. Malalasekera, J. Yu, T.B. Shrestha, E.J. McLaurin, S.H. Bossmann, C.M. Aikens, Refined insights in the photochromic spiro-dihydroindolizine/betaine system, *J. Phys. Chem. A,* 119 (2015) 9621-9629.

[29] A. Fernando, T.B. Shrestha, Y. Liu, A.P. Malalasekera, J. Yu, E.J. McLaurin, C. Turro, S.H. Bossmann, C.M. Aikens, Insights from theory and experiment on the photochromic spiro-dihydropyrrolo–pyridazine/betaine system, *J. Phys. Chem. A,* 120 (2016) 875-883.

[30] A. Yaroslavov, A. Efimova, V. Lobyshev, V. Kabanov, Reversibility of structural rearrangements in the negative vesicular membrane upon electrostatic adsorption/desorption of the polycation, *Biochim. Biophys. Acta, Biomembr.,* 1560 (2002) 14-24.

[31] L. Ge, H. Möhwald, J. Li, Phospholipid liposomes stabilized by the coverage of polyelectrolyte, *Colloids Surf., A,* 221 (2003) 49-53.

[32] J. Lee, B.R. Lentz, Secretory and viral fusion may share mechanistic events with fusion between curved lipid bilayers, *Proc. Natl. Acad. Sci. U.S.A.*, 95 (1998) 9274-9279.

[33] A.A. Yaroslavov, A.V. Sybachin, E. Kesselman, J. Schmidt, Y. Talmon, S.A. Rizvi, F.M. Menger, Liposome fusion rates depend upon the conformation of polycation catalysts, *J. Am. Chem. Soc.,* 133 (2011) 2881-2883.

[34] M. Takayama, S. Itoh, T. Nagasaki, I. Tanimizu, A new enzymatic method for determination of serum choline-containing phospholipids, *Clin. Chim. Acta,* 79 (1977) 93-98.

[35] P. Singh, S. Choudhury, S. Kulanthaivel, D. Bagchi, I. Banerjee, S.A. Ahmed, S.K. Pal, Photo-triggered destabilization of nanoscopic vehicles by dihydroindolizine for enhanced anticancer drug delivery in cervical carcinoma, *Colloids Surf. B,* 162 (2018) 202-211.

[36] D. Bagchi, A. Ghosh, P. Singh, S. Dutta, N. Polley, I.I. Althagafi, R.S. Jassas, S.A. Ahmed, S.K. Pal, Allosteric inhibitory molecular recognition of a photochromic dye by a digestive enzyme: Dihydroindolizine makes α-Chymotrypsin photo-responsive, *Sci. Rep.*, 6 (2016) 34399.

[37] B. Biswas, S. Roy, Proteins: structure, function, and engineering, *Springer Science & Business Media*, 2013.

[38] S.S. Narayanan, S.K. Pal, Nonspecific protein− DNA interactions: Complexation of α-Chymotrypsin with a genomic DNA, *Langmuir,* 23 (2007) 6712-6718.

[39] J.G. Linhardt, D.A. Tirrell, pH-induced fusion and lysis of phosphatidylcholine vesicles by the hydrophobic polyelectrolyte poly (2-ethylacrylic acid), *Langmuir,* 16 (2000) 122-127.

[40] K. Zasada, M. Łukasiewicz-Atanasov, K. Kłysik, J. Lewandowska-Łańcucka, B. Gzyl-Malcher, A. Puciul-Malinowska, A. Karewicz, M. Nowakowska, 'One-component'ultrathin multilayer films based on poly (vinyl alcohol) as stabilizing coating for phenytoin-loaded liposomes, *Colloids Surf., B,* 135 (2015) 133-142.

[41] S.K. Pal, D. Sukul, D. Mandal, K. Bhattacharyya, Solvation dynamics of DCM in lipid, *J. Phys. Chem. B,* 104 (2000) 4529-4531.

[42] R. Jimenez, G.R. Fleming, P. Kumar, M. Maroncelli, Dynamics of water, *Nature,* 369 (1994) 471-473.

[43] S. Geng, Y. Wang, L. Wang, T. Kouyama, T. Gotoh, S. Wada, J.-Y. Wang, A light-responsive self-assembly formed by a cationic azobenzene derivative and SDS as a drug delivery system, *Sci. Rep.,* 7 (2017) 39202.

[44] N. Gao, W. Yang, H. Nie, Y. Gong, J. Jing, L. Gao, X. Zhang, Turn-on theranostic fluorescent nanoprobe by electrostatic self-assembly of carbon dots with doxorubicin for targeted cancer cell imaging, in vivo hyaluronidase analysis, and targeted drug delivery, *Biosens. Bioelectron.,* 96 (2017) 300-307.

[45] J.R. Nilsson, S. Li, B. Önfelt, J. Andréasson, Light-induced cytotoxicity of a photochromic spiropyran, *Chem. Commun.,* 47 (2011) 11020-11022.

Chapter 6

Spectroscopic Studies on a Novel Fluorescence Probe for Interfacial Biomolecular Recognition

6.1. Introduction: Understanding complex phenomena emerging as a result of multi-scale dynamic biological interactions is one of the major challenges in contemporary biology [1-3]. Solvation dynamics is a powerful technique for the quantification of relaxation phenomena of biological macromolecules and have found increasing use in the study of biomolecular surfaces and interfaces [4-10]. In a typical solvation dynamics experiment the relaxation of a fluorophore is carefully monitored following photo excitation by a femtosecond/picosecond laser pulse [11, 12]. For an ideal fluorophore with less complicated excited state events, the relaxation dynamics is essentially governed by the solvent molecules in the immediate vicinity of the probe [13]. In case of a fluorophore covalently attached to the biological macromolecules the surface exposure is found to be an issue for the investigation of relaxation dynamics [14]. The issue becomes more vital in the case of interfacial relaxation dynamics of a biological macromolecule in contact with other biological and biomimetic surfaces. While indigenous fluorophores (fluorescent amino acids in protein and bases in DNA) are suffering from complicated excited state photo-physics, attachment of extrinsic probes may perturb the local structure of biomolecules [15, 16]. Sometimes non-covalently bound fluorophores become very effective in the investigation of biological surfaces, because of their selective attachment being governed by specific physical forces which includes Coulombic, hydrophobic or dipolar interaction [17]. But, for the obvious reason, a non-covalent solvation probe for the surface of a biomolecule may not be useful for the investigation of the interface of the biomolecule with another biological or biomimetic surface. For example in a study, electrostatically bound 2-(p-toluidino) naphthalene-6-sulfonate (TNS) has been

used to investigate the surface polarity of Histone 1 (H1) protein, which is found to be displaced to bulk water upon complexation of the protein with genomic DNA [18]. Thus investigation of surface and interface of a biological macromolecule using a non-covalently bound fluorophore is quite challenging and such reports are sparse in the literature.

Here, we have synthesized a fluorescent probe 6-acetyl-(2-((4-hydroxycyclohexyl) (methyl) amino) naphthalene (ACYMAN), which is a derivative of Acedan [19] for the investigation of biological interface. ACYMAN is moderately polar in the ground state (ground state dipole moment ~ 2.0 D), however, upon UV excitation, undergoes an intramolecular charge transfer (ICT) reaction to become highly polar in the excited state (excited state dipole moment ~ 7.1 D) and is known to display solvent-polarity sensitive fluorescence similar to Acedan [19]. The dye (ACYMAN) has a moderate fluorescence quantum yield in water (10%), and possesses good solubility in water (~ 10^{-4} M) which makes it suitable for studying the protein-water interfaces. For the present study, we have taken the interface of a nuclear protein H1 (cationic) and an anionic surfactant (SDS) as model system for the investigation of interfacial solvation dynamics and compared the same with that at the micellar surface. The H1-SDS (much below the critical micellar concentration (CMC) of the anionic surfactant) system under investigation is also biologically important as the interaction with the anionic SDS monomers induces helical structure in the H1 protein as evidenced from our CD studies. Such observation of induction of the helix structure in protein upon electrostatic interaction with DNA has been reported [20, 21], which is concluded to be one of the key factors in chromatin condensation [4, 22]. While the dynamics of hydration at the surface of H1 is reported to be ultrafast (up to few picoseconds) in nature, the interfacial dynamics upon the formation of electrostatically driven interface is sparse in the literature. One of the earlier studies concluded that the interfacial dynamics at the junction of H1-DNA complex is not much different from that of the protein surface itself [18]. However, the femtosecond resolved experiment was performed with

covalently labeled dansyl probe inviting the possibility of local structural perturbation in addition to losing information on the slower dynamics of structurally ordered water (SOW) molecules which are relevant to the structural transition of the biomolecule [23]. We have used the noncovalent novel fluorescent dye ACYMAN to probe the H1-SDS interface, especially the SOW and associated environmental dynamics upon the structural transition from random coil to α-helix with picosecond resolution in an experimental window of several nanoseconds. We have also compared the dynamics with those at the surface of H1 protein and micelles formed by the SDS monomers. The geometrical restriction of the dye in the microenvironments has been explored from polarization gated fluorescence studies. In order to establish the efficacy of ACYMAN in the exploration of interfacial solvation dynamics, we have compared the dynamics with other commercially available fluorescence reporters (dyes).

6.2. Results and Discussion:

6.2.1. A Sensitive Fluorescence Probe for the Polar Solvation Dynamics at Protein- Surfactant Interface [24]: ACYMAN is known to display strong polarity sensitive fluorescence. For example, the steady state emission peak maximum of the dye is significantly red shifted from 427 nm in cyclohexane to 517 nm in water [19]. This is attributed to a highly polar excited state originating from an intramolecular charge transfer (ICT) process, which is corroborated from theoretical calculations. On photo-excitation, the dipole moment of ACYMAN is found to change *in vacuo* from 2.0 D in the ground state to 7.1 D in the excited state, whereas, in ethanol it is found to be 4.03 D and 9.30 D, respectively, in the ground and the excited states. Such a moderate change in dipole moment ($\Delta\mu \sim 5$ D) upon photo-excitation is the signature of an intramolecular charge transfer (ICT) process rather than a twisted intramolecular charge transfer (TICT), where usually a large change in dipole moment (~16 D) of the fluorophore is involved [25]. Figure 6.1.a shows the steady-state fluorescence spectra of the dye in DMF, aqueous buffer and 100

mM SDS solution (micelles). The emission maximum and quantum yield of the dye in DMF (455 nm and 0.53, respectively) compared to those in aqueous buffer (517 nm and 0.09, respectively) indicate stabilization of the ICT state in polar solvent. In comparison to DMF, the steady state emission peak maximum is significantly red shifted (~50 nm) to 502 nm in the anionic SDS

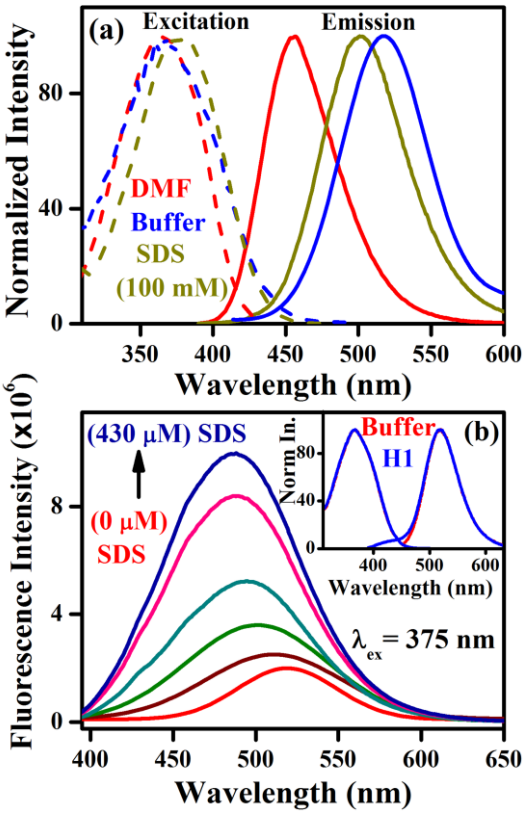

Figure 6.1. *(a) Steady state excitation and emission spectra of ACYMAN in various solvent and in presence of SDS micelles (100 mM). (b) Fluorescence emissions spectra of ACYMAN in Histone-1 (110 μM) with increasing concentrations of SDS: Inset shows excitation and emission spectra in H1 and aqueous buffer.*

micelles. The significant red shift in the position of the emission peak maximum of ACYMAN in the SDS micelles compared to DMF and its moderate blue shift compared to aqueous buffer reveal the location of the dye at the water-head-group interface of the micelle. Furthermore, the similarity in the position of the steady state emission peak maximum of ACYMAN in the SDS micelles to that in methanol ($\lambda_{em.}$ ~ 497 nm) (data not shown) is also consistent with the fact that the dye resides in the Stern layer of the anionic micelles, which is moderately polar and hydrogen bond donating. The steady

state fluorescence spectrum of ACYMAN in the Histone-1 (H1) protein (110 μM) is similar to that in aqueous buffer (inset, Figure 6.1.b) indicating the absence of any interaction between the protein and the dye. Upon the addition of SDS (430 μM), a marked blue shift (~35 nm) in the steady state fluorescence spectrum of the dye in H1-protein is observed, along with a significant increase in emission intensity. The blue shifted emission spectrum of ACYMAN at 485 nm compared to those in the protein (517 nm) and 430 μM SDS (517 nm, data not shown) solutions clearly indicates that the local environment around the dye significantly changed (lower polarity) in the protein surfactant complex. It is well-known that the anionic SDS surfactants strongly interact with the cationic nucleic protein H1 leading to the formation of protein-surfactant interface [21]. Our observation indicates that binding of the SDS molecules to the protein (H1) reduces the number of water molecules accessible to the protein surface, resulting in a decrease of the local polarity of the protein-surfactant interface in comparison to the protein-water interface (Figure 6.1.b). Furthermore, the binding constant for ACYMAN to the host protein-SDS interface has been estimated to be $7.51X10^{3}$ M^{-1} following Benesi Hildebrand plot [26] as shown in the inset of Figure 6.2.a. From this binding constant data, we have estimated that essentially all the dye molecules would remain bound to the protein-surfactant complex considering the concentrations of the dye and complex (equal to the concentration of the protein) to be 1 μM and 110 μM, respectively.

It is known that following the formation of protein-surfactant complex upon addition of SDS to the H1 protein solution, significant structural change in the protein is induced [27], especially in the N-terminal domain, which likely modifies the interface of the protein-surfactant complex compared to that of the protein. Both the CD-spectra and the fluorescence spectra of the single tyrosine (Tyr 72) residue of the H1-protein confirm such structural transition of the protein induced by SDS (Figure 6.2.a and Figure 6.2.b). As shown in Figure 6.2.a, a significant ellipticity in the whole protein is induced in the complex,

which is consistent with an increase in the α-helix content of the protein [20, 21]. Moreover, a large enhancement of the fluorescence emission of the single tyrosine residue (Tyr 72) of the protein at 305 nm is observed on the addition of SDS and was ascribed to transfer of Tyr 72 to a more hydrophobic environment [28]. As the H1 protein is known [20, 27] to comprise a central globular domain flanked by a short amino-terminal domain (NTD) and a long carboxyl-terminal domain (CTD), anionic SDS causes electrostatic charge compensation of the positively charged lysine residues in NTD and CTD through electrostatic interactions and leads to folding of these positively charged domains via hydrophobic interactions [21]. In consequence, Tyr 72 residue likely buries itself in a more hydrophobic region of the central globular domain of the protein resulting in significantly enhanced fluorescence intensity as shown in Figure 6.2.b.

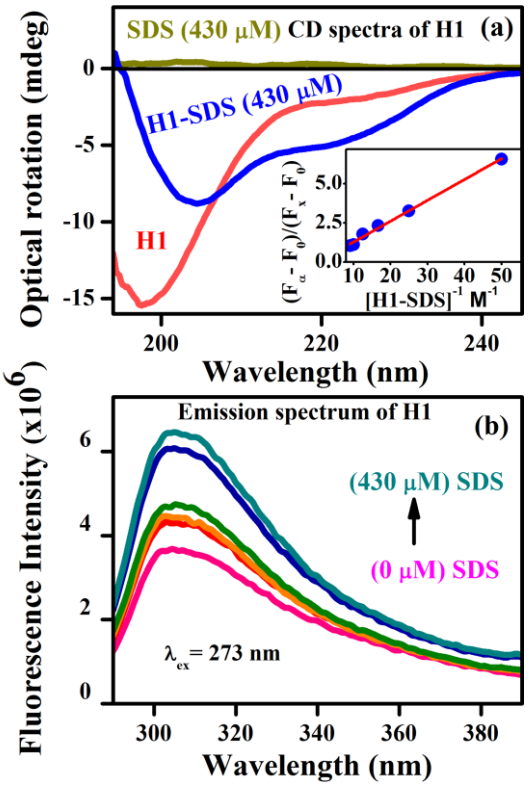

Figure 6.2. *(a) Far UV-CD (circular dichroism) spectra of Histone-1 (110 μM), SDS (430 μM) and Histone-1-SDS (430 μM) complex. Binding constant for ACYMAN to the H1-SDS interface is shown in inset. (b) Effect of SDS on the fluorescence emission of H1.*

Time-resolved fluorescence decay of ACYMAN in aqueous buffer (Figure 6.3.a) is characterized by a bi-exponential decay with a faster

component of 0.27 ns (78%) and a longer component of 0.6 ns (22%), (Table 6.1). Such bi-exponential decay of the probe in a homogeneous medium like aqueous buffer is also observed for several fluorescent dyes including some coumarins [29-32], and does not imply partitioning of the probe in two different environments [30, 33, 34].

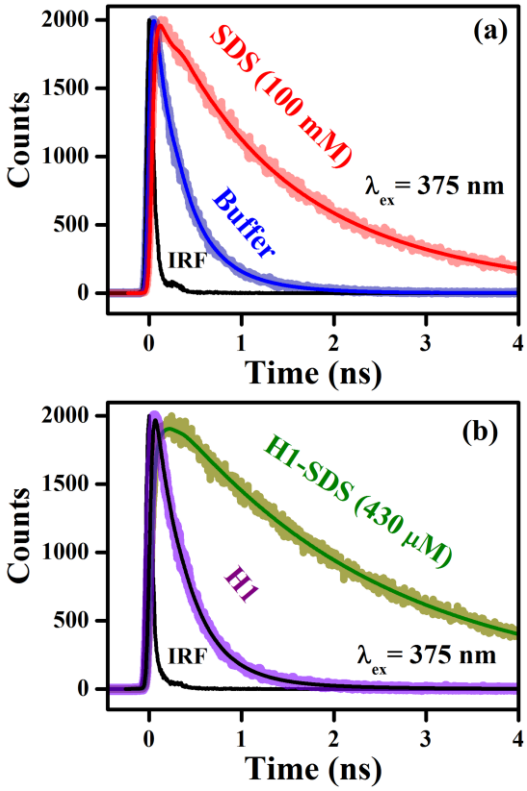

Figure 6.3. *(a) Picosecond-resolved fluorescence transients of the ACYMAN in aqueous buffer (χ^2= 1.03) and SDS micelles (100 mM) (χ^2= 1.07). (b) Picosecond-resolved fluorescence transients of the ACYMAN in Histone-1 (110 μM) (χ^2= 1.09) and Histone-1-SDS (430 μM) (χ^2= 1.05).*

This is indicative of the presence of different channels of radiative and non-radiative relaxation processes of the dye in polar solvents [29]. Following photo-excitation, ACYMAN is promoted to the locally excited state (LE) which is rapidly transferred to the intramolecular charge-transferred state (ICT) in polar solvents via ultrafast solvation and intramolecular charge transfer [18, 29]. This ICT state of ACYMAN undergoes a rapid non-radiative relaxation in water which give rise to the faster decay of (~270 ps) with a major contribution (78%). The longer component of ~ 600 ps may be attributed to the lifetime of the ICT state in water. For the H1-protein, the fluorescence decay of the probe

is very similar to aqueous buffer being characterized by two decay components identical to aqueous buffer, which excludes the possibility of any interaction between the probe and the host protein (Figure 6.3.b). Unlike aqueous buffer and protein (H1), the fluorescence decay components and their relative amplitudes vary continuously in going from the blue edge to the red edge of the emission spectra and the faster component at the blue end becomes a rise at the red end for the SDS micelles and the H1/SDS complex (Table 6.1). This is a manifestation of solvation dynamics in the SDS micelles as well as in the protein-surfactant complex as discussed later [35]. The fluorescence decays of ACYMAN in SDS micelles and H1-SDS complex at their corresponding emission maxima are shown in Figure 6.3.a and Figure 6.3.b, respectively. It has to be noted that the one extra longer component of fluorescence lifetime has been observed in SDS micelles as well as in H1-SDS complex compared to aqueous buffer and H1 protein systems, while the contribution of the shorter component of the fluorescence life time in SDS micelles and H1-SDS complex decreased significantly with respect to aqueous buffer and H1 protein.

Table 6.1. *Fluorescence lifetimes of ACYMAN in different systems.*

System/Wavelength (nm)	τ_1 ns [%]	τ_2 ns [%]	τ_3 ns [%]
Buffer/517 nm	0.27 (78)	0.59 (22)	-
Histone/517 nm	0.28 (80)	0.63 (20)	-
SDS micelles/450 nm	0.025 (76)	0.24 (18)	1.55 (6)
SDS micelles/500 nm	0.032 (38)	0.74 (18)	1.78 (44)
SDS micelles/550 nm	0.25 (-11)	1.29 (59)	2.31 (30)
Histone-SDS/430 nm	0.116 (48)	0.76 (37)	2.34 (15)
Histone-SDS/480 nm	0.030 (-2)	1.10 (31)	2.37 (67)
Histone-SDS/520 nm	0.050 (-19)	0.12 (15)	2.48 (66)

For various systems, the wavelength (nm) of time-resolved decay measurements are shown. The amplitudes corresponding to the relevant decay components are shown within the parentheses.

To better assess the interactions of the probe with the hosts (SDS/H1) time-resolved fluorescence anisotropy decay, r(t), measurements were carried out. For aqueous buffer (Figure 6.4.a) and the protein (H1) (Figure 6.4.b), the anisotropy decays are mono-exponential with similar rotational correlation

times (Table 6.2), indicating the absence of any interaction between the probe ACYMAN and the H1-protein. Time-resolved anisotropy decay, r(t), of ACYMAN are bi-exponential in the SDS micelles and in the H1-protein in presence of SDS (430 µM), and can be described by equation 2.37 in accordance with the ''two-step'' in combination with the ''wobbling-in-cone'' model [36]. For the SDS micelles, the anisotropy decay is significantly retarded compared to aqueous buffer (Table 6.2) and is characterized by two rotational time constants of 250 ps (23%) and 1.03 ns (77%), indicating strong interaction of the probe with the micelles (Figure 6.4.c). In accordance with the two-step model in combination with the wobbling-in-cone model, the shorter time constant of 250 ps may be attributed to the local motion of the probe within the micelle, whereas, the longer constant corresponds to the global tumbling motion of the entire micelle. The marked difference of the rotational time constants of the probe from aqueous buffer (~130 ps) corresponds to significant restriction of the orientational motion of the dye in the stern layer at the micelle-water interface. Time-resolved anisotropy decay of the probe in H1-protein becomes remarkably slow (Figure 6.4.d) upon the addition of SDS (430 µM) (Table 6.2) indicating strong interaction of the ACYMAN probe with the H1-protein in the presence of SDS monomers. The time constants of 530 ps (12%) and 4.8 ns (88%) are consistent with the restricted local motion of the probe in the protein surfactant interface, and global tumbling motion of the protein-surfactant complex, respectively. The generalized order parameter, S, which provides information about the packing in the vicinity of the probe molecule is remarkably high for both SDS micelles (0.88) and the H1-SDS complex (0.94) and is consistent with location of the probe at the micelle-water interface and the protein-surfactant interface, respectively. Furthermore, higher value of S and lower value of the semi-cone angle θ_0 for the H1-SDS complex compared to the SDS micelles indicates greater restriction of the orientational motion of the probe at the protein-surfactant interface than the micelle-water interface. This is consistent with the presence of highly rigid layer of water molecules in the protein-surfactant interface than the micelle-water interface.

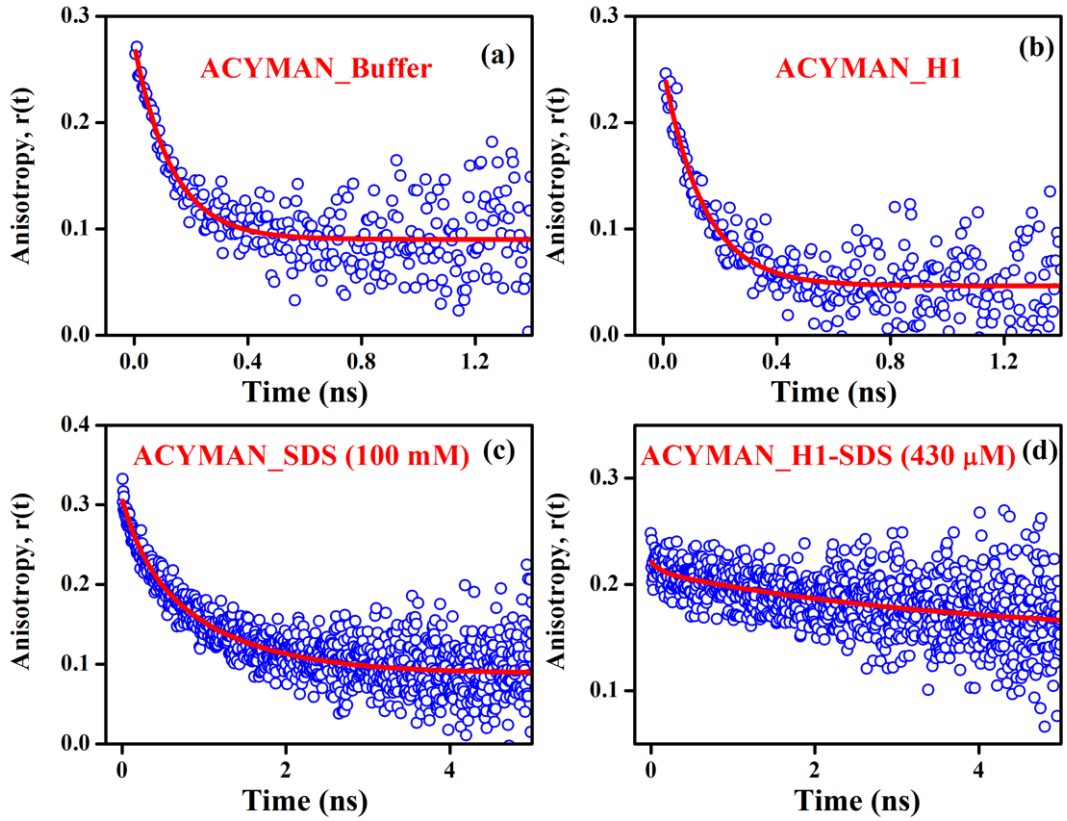

Figure 6.4. *Temporal decay of fluorescence anisotropy, r(t) of ACYMAN in (a) aqueous buffer (χ^2= 1.10), (b) Histone-1(110 μM) (χ^2= 1.2), (c) SDS micelles (100 mM) (χ^2= 1.5) and (d) Histone-1-SDS (430 μM) complex (χ^2= 1.0).*

Figure 6.5.a and Figure 6.6.a show the wavelength-dependent emission transients of ACYMAN in SDS micelles and in the H1/SDS complex at three characteristic wavelengths, from the blue end to the red end of the steady state fluorescence spectrum. Time-resolved fluorescence at the blue and the red end are characterized by a decay and a rise, respectively, indicating reorganization of the surrounding water molecules around the excited state dipole of the fluorophore which is manifested as the time-dependent shift of the fluorescence spectrum to the red (Figure 6.5.b and Figure 6.6.b). The heterogeneity of the environments around the probe in the micelle and in the protein-surfactant complex is ruled out as no iso-emissive point in the time resolved area normalized emission spectra (TRANES) [37] are observed as shown in the insets of Figure 6.5.c and Figure 6.6.c. For the SDS micelles, the solvation correlation function, C(t), decays (Figure 6.5.c) with two time constants of 50 ps (76%) and 800 ps (24%), indicating mediation of two types of water trajectories in the solvent relaxation in the micelle-water interface.

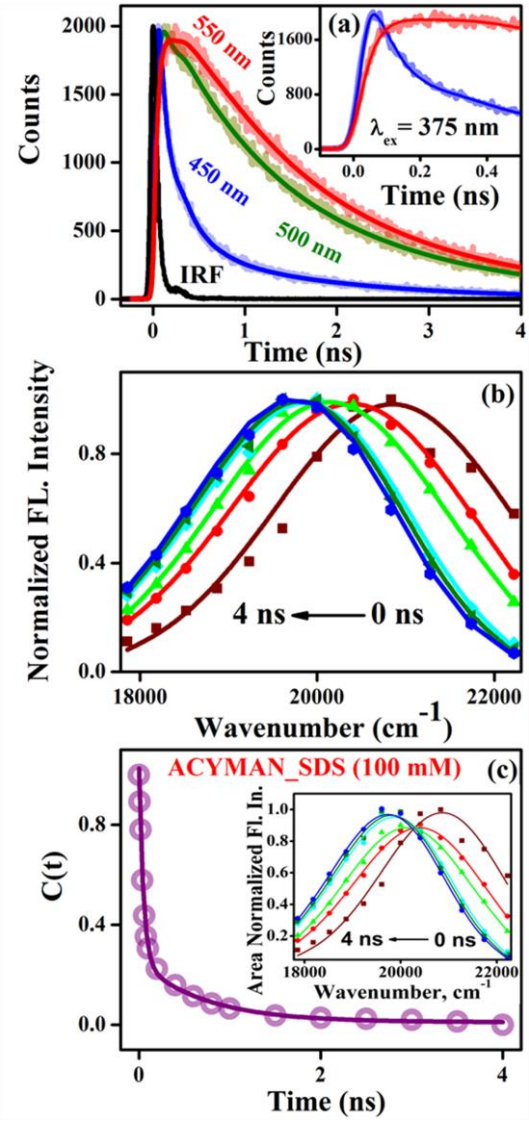

Figure 6.5. *(a) Picosecond-resolved transient of ACYMAN in SDS micelles (100 mM) at 450 nm (χ^2= 1.1), 500 nm (χ^2= 1.07) and 550nm (χ^2= 1.03). (b) Time-resolved emission spectra (TRES) of corresponding systems are shown. (c) Decay of the solvation correlation function, C(t) with time. Time-resolved area normalized emission spectra (TRANES) is shown in inset.*

Similar bimodality with time constants of 140 ps (77%) and 2.14 ns (23%) was observed by other studies on the solvation dynamics of various fluorescent probes in the anionic SDS micelles [7, 38]. In accordance with Zewail et al. [39] the faster component (50 ps) may be attributed to the micelle surface-bound water molecules, whereas, the slower component of few hundreds of picoseconds (800 ps) reflects coupling of the internal motion of the surfactant molecules with the water molecules of the Stern layer [40]. In sharp contrast to the micelles, the picosecond-resolved emission transients of ACYMAN in H1-protein monitored at the blue and the red end of the fluorescence spectrum are

more or less similar (data not shown) and no rise is observed in the emission transient at the red end. This observation is consistent with very fast solvation of ACYMAN in the protein-water interface due to bulk type water molecules similar to the observations of Zewail et al. [39].

Table 6.2. *Time-resolved anisotropy parameters of ACYMAN in different systems.*

System	ϕ_1 ns [%]	ϕ_2 ns [%]	S	θ_0
Aqueous buffer	0.13 (100)	-	-	-
SDS micelles (100 mM)	0.25 (23)	1.03 (77)	0.88	23.07
Histone (110 µM)	0.14 (100)	-	-	-
Histone-SDS (430 µM)	0.53 (12)	4.80 (88)	0.94	16.26

ϕ_1, and ϕ_2 are the rotational correlation times with corresponding amplitudes shown within parentheses. S is the order parameter and θ_0 is the semicone angle in the wobbling-in-cone model.[36]

In consequence no rise component associated with solvent relaxation could be detected in our TCSPC set up with a time resolution of 20 ps. The emission transients of the probe in H1-protein become dramatically different (Figure 6.6.a) upon interaction with SDS. The solvation correlation function, C(t) for the H1-SDS interface is characterized by two time constants, 110 ps (40%) and 1.0 ns (60%). This bimodal solvation dynamics in the H1-SDS interface indicates significant contributions of the surface-bound water molecules and structural fluctuation of the protein-surfactant complex in contrast to the significant role of the bulk type water molecules in the solvation dynamics at the protein (H1)-water interface. The subtle but distinct differences between the micelle-water and protein-surfactant interfaces are noted, warranting further discussion. First of all, the faster component of solvation (τ_1) increases more than two-fold in going from the Stern layer of the SDS micelles to the protein-surfactant interface of the H1-SDS complex (Table 6.3). In addition, there is a significant increase (from 24% to 60%) in the contribution of the slower component (τ_2) as well as its magnitude. The two-fold increase in the faster component may be ascribed to the exertion of stronger electrostatic field on the water molecules in the protein-surfactant interface than the micelle-water interface. The binding surface of the H1-protein is positively charged due

to the presence of a large number of positively charged residues in its N- and C-terminal domains, whereas the surfactant (SDS) is negatively charged owing to the presence of negatively charged sulfate head group. As the anionic surfactants anchor to the positively charged lysine residues on the terminal

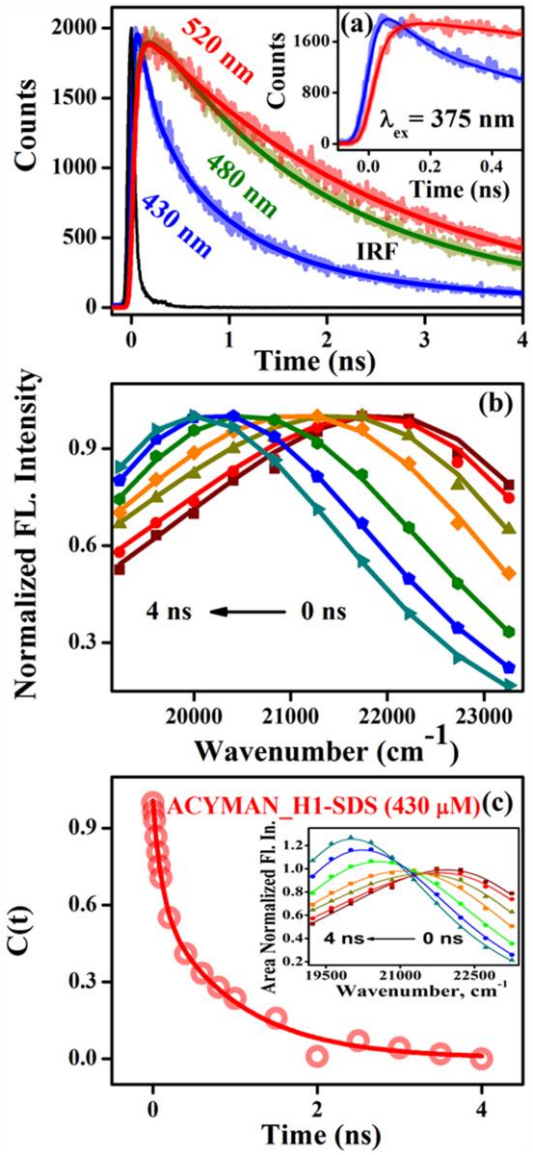

Figure 6.6. *(a) Picosecond-resolved transient of ACYMAN in Histone-1-SDS (430 μM) complex at 430nm (χ^2= 1.06), 480nm (χ^2= 1.09) and 520 nm (χ^2= 1.05). (b) Time-resolved emission spectra (TRES) of corresponding systems are shown. (c) Decay of the solvation correlation function, C(t) with time. Time-resolved area normalized emission spectra (TRANES) is shown in inset.*

domains of the protein, mutual electrostatic interaction between them gives rise to a strong electrostatic field that significantly slows down the dynamics of the interfacial water in the protein-surfactant interface compared to the micelle-

water interface. In addition, due to the anchoring of the negatively charged surfactant molecules on the positively charged surface of the H1 protein, hydrophobicity of the lysine side-chains increases as a result of electrostatic charge compensation followed by folding of the CTD and NTD in the H1-SDS complex [20, 27]. This in turn likely induces a crowded environment of the lysine side-chains and the surfactant molecules anchored to the surface of the protein, which imposes significant restriction on the structural fluctuation of the surfactant molecules in the H1-SDS complex compared to the SDS micelles. In consequence, the contribution of the slower solvation component (τ_2) increases significantly along with its magnitude in going from the Stern layer of the SDS micelles to the protein-surfactant interface of the H1-SDS complex.

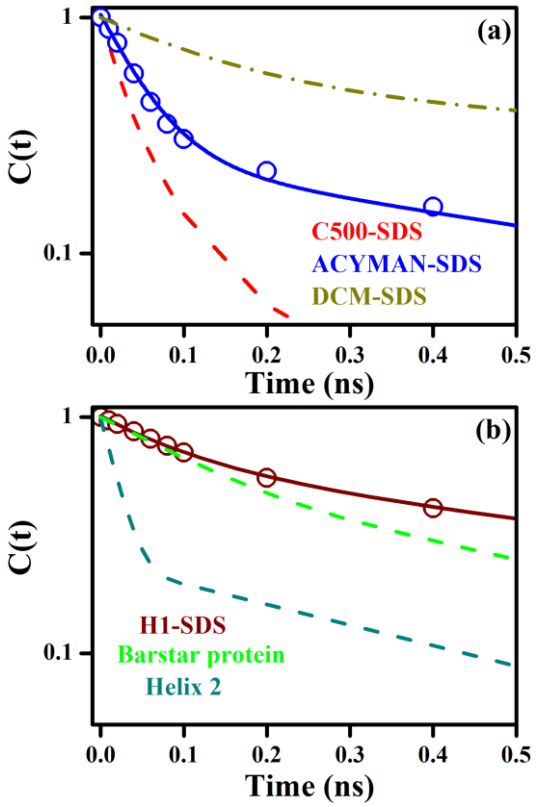

Figure 6.7. *(a) Solvation correlation function, C(t) of C500, ACYMAN and DCM in SDS micelles. (b) Shows decay of solvation correlation function, C(t) of the H1-SDS complex, dotted line represents C(t) of a Helix-2 and Barstar protein.*

In order to compare the sensitivity of ACYMAN toward the biomolecular interfaces, some other non-covalent solvation probe, coumarin 500 (C500) and DCM were also used for the studies. The reason behind the

choice of the two specific probes lies in the fact that C500 is a polar probe which is soluble in water and can be incorporated at the SDS micellar surface [40]. On the other hand DCM is hydrophobic and completely insoluble in water, however, can also be incorporated at the same micellar surface [41, 42]. The time scales of solvation dynamics obtained from these two probes at the micellar surface are found to be significantly different. While the reported average time constant of DCM solvation at SDS micellar surface is 1.4 ns [42] the observed average time constant of C500 solvation is 0.07 ns (Figure 6.7.a). The difference of the local environments around the probes for the same micellar surface can easily be concluded from the time constants of solvation, because of the nature of the probes as discussed earlier. In other words, whereas C500 is more compatible to be localized on the polar side (headgroup region) of the micellar surface, DCM prefers to reside in the more hydrophobic portion of the surface of the micelles [43]. From Figure 6.7.a it is also clear that the time scale of solvation dynamics of ACYMAN lies between that of C500 and DCM. Thus it is interesting to note which variety of the above dyes is eligible to probe the interfacial solvation dynamics. We have observed that C500 reveals bulk water type solvation dynamics for the H1 protein in presence of SDS below critical micellar concentration (cmc), and the dynamics is also insensitive to the formation of the H1-SDS interface. On the other hand, the dye DCM remains insoluble in H1, SDS below the cmc and even at the protein-surfactant interface after the formation of the H1-SDS complex. In the case of ACYMAN, the dynamics of solvation is distinct in the H1-SDS interface from that in SDS below or above the cmc as described earlier.

Table 6.3. *Solvation correlation data for ACYMAN in different systems.*

System	τ_1 ns [%]	τ_2 ns [%]	τ_{avg} ns
SDS micelles (100 mM)	0.05 (76)	0.80 (24)	0.23
Histone-SDS (430 μM)	0.11 (40)	1.00 (60)	0.64

A comparative study of solvation dynamics of the interface after the formation of an α-helix in the protein H1 to that of the hydration dynamics of

other α-helix protein is evident in the Figure 6.7.b in a time window of 500 ps. Molecular dynamics simulation on α-Helix containing protein shows that the dynamics of hydration in the close proximity of a α-Helix reveals ultrafast time components (75%) with a longer component of 500 ps (25%) [14, 44]. In another femtosecond resolved time-dependent dynamic stocks shift (TDSS) studies on α-helix containing barstar protein, a slower component of 578 ps (59%) is manifested in the hydration dynamics [45]. The faster portion of the dynamics is concluded to be the rotational motion of the water molecules in the close proximity of α-helix. Thus slower components of hydration dynamics in the α-helix portion of different proteins are consistent with our studies.

6.3. Conclusion: Time-resolved fluorescence studies of a new, dipolar fluorophore 6-acetyl-(2-((4 hydroxycyclohexyl) (methyl) amino) naphthalene (ACYMAN) unveils interesting features of solvation dynamics and local molecular dynamics in different interfaces of H1-protein, SDS micelles and H1-SDS complex. Time-resolved anisotropy decay of the dye is characterized by a time constant of ~130-140 ps in aqueous buffer and protein, but the decay becomes slower in SDS micelles than aqueous buffer or H1-protein, indicating to stronger interaction of the dye with the micelles than the protein. Upon the addition of SDS surfactants, the anisotropy decay becomes significantly retarded in the H1-SDS interface compared to the SDS micelles, which indicates to significantly stronger interaction of the dye with the H1-SDS complex than the micelles. Our studies also demonstrate that other well-known commercially available solvation dyes including C500 and DCM fail to probe the protein-surfactant interface of the H1-SDS complex. We have also compared the observed solvation dynamics of the interface with those from MD simulations and femtosecond resolved studies reported in the literature. The observed time scale of solvation dynamics for ACYMAN is consistent with the slower components of the hydration dynamics as mentioned in the literature. This slower dynamics of ACYMAN likely originates from the structurally ordered water molecules (SOW) in the helix-surfactant interface.

References

[1] W. Dubitzky, J. Southgate, H. Fuss, Understanding the dynamics of biological systems: Lessons learned from integrative systems biology, *Springer Science & Business Media*, 2011.

[2] J.A. Rupley, G. Careri, Protein hydration and function, *Adv. Protein Chem.,* 41 (1991) 37-172.

[3] B. Halle, Protein hydration dynamics in solution: A critical survey, *Philos. Trans. R. Soc. Lond., B, Biol. Sci.,* 359 (2004) 1207-1224.

[4] J.-M. Zanotti, G. Gibrat, M.-C. Bellissent-Funel, Hydration water rotational motion as a source of configurational entropy driving protein dynamics. Crossovers at 150 and 220 K, *Phys. Chem. Chem. Phys.,* 10 (2008) 4865-4870.

[5] R. Jimenez, G.R. Fleming, P. Kumar, M. Maroncelli, dynamics of water, *Nature,* 369 (1994) 471-473.

[6] M. Maroncelli, G.R. Fleming, Picosecond solvation dynamics of coumarin 153: The importance of molecular aspects of solvation, *J. Chem. Phys.,* 86 (1987) 6221-6239.

[7] N. Nandi, K. Bhattacharyya, B. Bagchi, Dielectric relaxation and solvation dynamics of water in complex chemical and biological systems, *Chem. Rev.,* 100 (2000) 2013-2046.

[8] K. Bhattacharyya, Solvation dynamics and proton transfer in supramolecular assemblies, *Acc. Chem. Res,* 36 (2003) 95-101.

[9] A.H. Zewail, Femtochemistry: Atomic-scale dynamics of the chemical bond using ultrafast lasers (Nobel Lecture), *Angew. Chem. Int. Ed.,* 39 (2000) 2586-2631.

[10] B. Born, H. Weingärtner, E. Bründermann, M. Havenith, Solvation dynamics of model peptides probed by terahertz spectroscopy. Observation of the onset of collective network motions, *J. Am. Chem. Soc.,* 131 (2009) 3752-3755.

[11] S.K. Pal, A.H. Zewail, Dynamics of water in biological recognition, *Chem. Rev.,* 104 (2004) 2099-2124.

[12] E. Potter, J. Herek, S. Pedersen, Q. Liu, A. Zewail, Femtosecond laser control of a chemical reaction, *Nature,* 355 (1992) 66–68.

[13] S. Choudhury, S. Batabyal, P.K. Mondal, P. Singh, P. Lemmens, S.K. Pal, Direct observation of kinetic pathways of biomolecular recognition, *Chem. Eur. J.,* 21 (2015) 16172-16177.

[14] S. Bandyopadhyay, S. Chakraborty, S. Balasubramanian, B. Bagchi, Sensitivity of polar solvation dynamics to the secondary structures of aqueous proteins and the role of surface exposure of the probe, *J. Am. Chem. Soc,* 127 (2005) 4071-4075.

[15] D.R. Buckler, E. Haas, H.A. Scheraga, Analysis of the structure of ribonuclease A in native and partially denatured states by time-resolved nonradiative dynamic excitation energy transfer between site-specific extrinsic probes, *Biochemistry,* 34 (1995) 15965-15978.

[16] E.M. Kirilova, I. Kalnina, T. Zvagule, N. Gabruseva, N. Kurjane, I.I. Solomenikova, Fluorescent study of human blood plasma albumin alterations induced by ionizing radiation, *J. Fluoresc.,* 21 (2011) 923-927.

[17] R.W. Sinkeldam, N.J. Greco, Y. Tor, Fluorescent analogs of biomolecular building blocks: Design, properties, and applications, *Chem. Rev.,* 110 (2010) 2579-2619.

[18] D. Zhong, S.K. Pal, A.H. Zewail, Femtosecond studies of protein–DNA binding and dynamics: Histone I, *ChemPhysChem,* 2 (2001) 219-227.

[19] S. Singha, D. Kim, B. Roy, S. Sambasivan, H. Moon, A.S. Rao, J.Y. Kim, T. Joo, J.W. Park, Y.M. Rhee, A structural remedy toward bright dipolar fluorophores in aqueous media, *Chem. Sci.,* 6 (2015) 4335-4342.

[20] A. Roque, I. Ponte, P. Suau, Role of charge neutralization in the folding of the carboxy-terminal domain of histone H1, *J. Phys. Chem. B,* 113 (2009) 12061-12066.

[21] S. Bathaie, A. Moosavi-Movahedi, B. Ranjbar, A. Saboury, A mechanistic study of the histone H1-DNA complex dissociation by sodium dodecyl sulfate, *Colloids Surf., B,* 28 (2003) 17-25.

[22] J. Bednar, R.A. Horowitz, S.A. Grigoryev, L.M. Carruthers, J.C. Hansen, A.J. Koster, C.L. Woodcock, Nucleosomes, linker DNA, and linker histone form

a unique structural motif that directs the higher-order folding and compaction of chromatin, *Proc. Natl. Acad. Sci. U.S.A.*, 95 (1998) 14173-14178.

[23] J.R. Errington, P.G. Debenedetti, Relationship between structural order and the anomalies of liquid water, *Nature,* 409 (2001) 318-321.

[24] P. Singh, S. Choudhury, S. Singha, Y. Jun, S. Chakraborty, J. Sengupta, R. Das, K.-H. Ahn, S.K. Pal, A sensitive fluorescent probe for the polar solvation dynamics at protein–surfactant interfaces, *Phys. Chem. Chem. Phys.*, 19 (2017) 12237-12245.

[25] Z.R. Grabowski, K. Rotkiewicz, W. Rettig, Structural changes accompanying intramolecular electron transfer: Focus on twisted intramolecular charge-transfer states and structures, *Chem. Rev.*, 103 (2003) 3899-4032.

[26] A. Mallick, B. Haldar, N. Chattopadhyay, Spectroscopic investigation on the interaction of ICT probe 3-acetyl-4-oxo-6, 7-dihydro-12H indolo-[2, 3-a] quinolizine with serum albumins, *J. Phys. Chem. B,* 109 (2005) 14683-14690.

[27] A. Roque, N. Teruel, R. López, I. Ponte, P. Suau, Contribution of hydrophobic interactions to the folding and fibrillation of histone H1 and its carboxy-terminal domain, *J. Struct. Biol.,* 180 (2012) 101-109.

[28] J.G. Gavilanes, M.A. Lizarbe, A.M. Munico, M. Onnaderra, Interaction of dipalmitoyl-phosphatidylcholine with calf thymus histone H1, *Int. J. Pept. Protein Res.*, 26 (1985) 187-194.

[29] J. Dana, T. Debnath, P. Maity, H.N. Ghosh, Restriction of molecular rotation and intramolecular charge distribution in the photoexcited state of coumarin dyes on gold nanoparticle surface, *J. Phys. Chem. C,* 119 (2015) 2046-2052.

[30] A. Chatterjee, D. Seth, Photophysical properties of 7-(diethylamino) coumarin-3-carboxylic acid in the nanocage of cyclodextrins and in different solvents and solvent mixtures, *Photochem. Photobiol.*, 89 (2013) 280-293.

[31] A. Chatterjee, B. Maity, D. Seth, The photophysics of 7-(N, N′-diethylamino) coumarin-3-carboxylic acid in water/AOT/isooctane reverse

micelles: an excitation wavelength dependent study, *Phys. Chem. Chem. Phys.,* 15 (2013) 1894-1906.

[32] P. Verma, H. Pal, Intriguing H-aggregate and H-dimer formation of coumarin-481 dye in aqueous solution as evidenced from photophysical studies, *J. Phys. Chem. A,* 116 (2012) 4473-4484.

[33] A. Mishra, G. Behera, M. Krishna, N. Periasamy, Time-resolved fluorescence studies of aminostyryl pyridinium dyes in organic solvents and surfactant solutions, *J. Lumin.,* 92 (2001) 175-188.

[34] G. Saroja, B. Ramachandram, S. Saha, A. Samanta, The fluorescence response of a structurally modified 4-aminophthalimide derivative covalently attached to a fatty acid in homogeneous and micellar environments, *J. Phys. Chem. B,* 103 (1999) 2906-2911.

[35] E. Middelhoek, H. Zhang, J. Verhoeven, M. Glasbeek, Subpicosecond studies of the solvation dynamics of fluoroprobe in liquid solution, *Chem. Phys.,* 211 (1996) 489-497.

[36] E.L. Quitevis, A.H. Marcus, M.D. Fayer, Dynamics of ionic lipophilic probes in micelles: Picosecond fluorescence depolarization measurements, *J. Phys. Chem.,* 97 (1993) 5762-5762.

[37] A. Koti, M. Krishna, N. Periasamy, Time-resolved area-normalized emission spectroscopy (TRANES): A novel method for confirming emission from two excited states, *J. Phys. Chem. A,* 105 (2001) 1767-1771.

[38] Y. Tamoto, H. Segawa, H. Shirota, Solvation dynamics in aqueous anionic and cationic micelle solutions: sodium alkyl sulfate and alkyltrimethylammonium bromide, *Langmuir,* 21 (2005) 3757-3764.

[39] L. Zhao, S.K. Pal, T. Xia, A.H. Zewail, Dynamics of ordered water in interfacial enzyme recognition: Bovine pancreatic phospholipase A2, *Angew. Chem. Int. Ed.,* 43 (2004) 60-63.

[40] S. Choudhury, P.K. Mondal, V. Sharma, S. Mitra, V.G. Sakai, R. Mukhopadhyay, S.K. Pal, Direct observation of coupling between structural fluctuation and ultrafast hydration dynamics of fluorescent probes in anionic micelles, *J. Phys. Chem. B,* 119 (2015) 10849-10857.

[41] R. Sarkar, A.K. Shaw, M. Ghosh, S.K. Pal, Ultrafast photoinduced deligation and ligation dynamics: DCM in micelle and micelle-enzyme complex, *J. Photochem. Photobiol., B,* 83 (2006) 213-222.

[42] S.K. Pal, D. Sukul, D. Mandal, S. Sen, K. Bhattacharyya, Solvation dynamics of DCM in micelles, *Chem. Phys. Lett.*, 327 (2000) 91-96.

[43] S.K. Pal, D. Sukul, D. Mandal, K. Bhattacharyya, Solvation dynamics of DCM in lipid, *J. Phys. Chem. B,* 104 (2000) 4529-4531.

[44] S. Bandyopadhyay, S. Chakraborty, S. Balasubramanian, S. Pal, B. Bagchi, Atomistic simulation study of the coupled motion of amino acid residues and water molecules around protein HP-36: Fluctuations at and around the active sites, *J. Phys. Chem. B,* 108 (2004) 12608-12616.

[45] A. Jha, K. Ishii, J.B. Udgaonkar, T. Tahara, G. Krishnamoorthy, Exploration of the correlation between solvation dynamics and internal dynamics of a protein, *Biochemistry,* 50 (2010) 397-408.

Chapter 7

Spectroscopic Studies on DNA-Surfactant Interaction for a Specific Biological Function

7.1. Introduction: The search for harmless synthetic vectors that allow an efficient delivery of genes for the treatment of genetic and acquired diseases lead to intense research activities and a wealth of literature in the last two decades [1-5]. Circumventing limitations associated with the viral vectors, e.g. packaging DNA with particular size, immunogenicity and mutagenicity, were the main motives of those studies. DNA condensate (complexes) with cationic surfactants/lipids are considered to be efficient candidates for gene-delivery (transfection) applications [6]. Among other obvious requirements for achieving efficient transfection, the most important factor is that the interaction of DNA with the vectors should yield a nanometer size close to that of viruses [4, 7]. This requirement is closely related to the fact that the critical size limit for endocytosis is 150 nm and the condensate is expected to be escape from the blood vessel if its size is beyond a limit [4, 7]. Another important factor is the intactness of the duly hydrated B-form of the gene carrying DNA in the synthetic vector [5, 8]. While the above important considerations limit the efficiency of cationic polymers and cationic lipids [9, 10], cationic detergent cetyltrimethylammonium bromide (CTAB) is found to condense DNA into discrete particles containing even single nucleic acid molecule [11-13]. One of the notable properties of CTAB is the discrete first order phase transition of DNA between elongated coils and collapsed globules [12] well below the critical micellar concentration (CMC) of the surfactant and the formation of aggregates [12]. The interesting structure of the CTAB-DNA condensate is thought to result from the interaction of the negatively charged DNA phosphate groups with cationic surfactants and a further stabilization by the hydrophobic tails of the CTAB molecules [14].

Despite the unique feature of the CTAB-DNA condensate, the surfactant CTAB is found to be poorly efficient in transfection *in vitro* [15, 16]. In order to study the sole role of CTAB in the stabilization of the CTAB-DNA condensate, in non-polar solvents rather than polar water media are the choice. The high solubility of the complex makes the contribution of parents (DNA and/or CTAB) inconclusive in the stability of the condensate in aqueous conditions. It was also concluded that due to higher solubility of the condensate, the complex in the cells is thought to induce fast release of CTAB revealing detergent related toxicity [4]. Earlier it has been shown that DNA-surfactant complexes are soluble in low-polarity organic solvents [3, 17-19]. In one of these reports the structural properties of a genomic DNA upon complexation with CTAB in non-aqueous solvents of different degrees of polarity have been studied in details [3]. By using UV, CD spectroscopy and fluorescence microscopy, the study has concluded that DNA-CTAB condensate dissociates into their initial components at concentrations of 40-60% (v/v) for ethanol or 30-50% (v/v) for 2-propanol, while conserving the double-stranded structure of the native DNA. Several other recent studies [20, 21] unravel structural aspects of the genomic DNA in the condensate. However, the molecular recognition properties (both specific; intercalation, and non-specific; coulombic) of the gene carrying DNA in the condensate are sparsely covered in the literature. In our earlier reports, the DNA-binding drugs Hoechest 33258 (non-specific) [22] and ethidium bromide (specific) [23] appear to be promising DNA-probes in the condensate. Ethidium bromide (EB) intercalates into the genomic DNA and provides the structural details of DNA even when it is in condensed form in a self-assembled reverse micellar nanocage. On the other hand, Hoechest 33258, a well-known DNA minor groove binder, provides dynamical and structural information of the condensed DNA either bound to nucleic acid binding protein or CTAB surfactant [24]. It is important to note that the functional properties of gene carrying DNA (molecular recognition) in the condensate will dictate the overall activity of the gene after delivery in the target cells. A detailed investigation on the structural and functional properties (intercalation and electrostatic binding) of a genomic DNA (calf thymus; CT-DNA) in its condensate

form in a non-aqueous solvent (butanol), where stabilization of the condensate is essentially governed by the hydrophobic tails of the CTAB surfactant, is the main motive of our present studies.

In the present work, we have synthesized a condensate of CT-DNA and CTAB in butanol. While dynamic light scattering (DLS) studies confirm the size of the condensate in the solution to be less than 100 nm, circular dichroism (CD) spectroscopy reveals the intactness of B-form structure of the genomic DNA in the condensate. Picosecond resolved fluorescence of a well-known DNA intercalator EB to the nucleic acid in the condensate clearly shows some degree of perturbation of the intercalative binding of the genomic DNA in the condensate compared to that in aqueous solution. We have measured the temperature dependent binding constant of the EB with the genomic DNA in the condensate in butanol and compared with that in aqueous solution. A detailed analysis of thermodynamical parameters from the Van't Hoff plots reveals that the EB-binding to the genomic DNA in the condensate is significantly different from that of the DNA in aqueous solution. In order to probe the interaction of CTAB in the condensate, we have used nonyl acridine orange (NAO) as model cationic surfactant with a fluorescence acridine moiety [25, 26]. Picosecond resolved polarization gated anisotropy of NAO in the condensate shows a hydrodynamic rotation of the surfactant in the condensate and reveals an activation energy for the viscous flow [27, 28]. Strong spectral overlap of NAO emission and absorption spectrum of intercalating EB also offers the opportunity to measure the distance between cationic surfactant and the intercalator (EB) in the condensate with molecular precision employing Förster resonance energy transfer (FRET) strategy. We have also used FRET between NAO and another electrostatic DNA binder, crystal violet (CV) in the condensate. The constructed probability distribution functions of FRET distance between NAO and either EB (intercalator) or CV (electrostatic binder) at various temperatures in the condensate unravel the efficacy of molecular recognition of the genomic DNA by small ligands. Our

studies are expected to find relevance in the investigation of functionality of DNA molecules in condensate for potential gene-delivery application.

7.2. Results and Discussion:

7.2.1. Molecular Recognition of Genomic DNA in a Condensate with a Model Surfactant for Potential Gene-delivery Applications [29]: The normalised intensity distribution of scattered light from DLS on aqueous CTAB micelles and DNA are shown in Figure 7.1.a. Hydrodynamic diameters for CTAB micelles (aqueous) and DNA (aqueous) are measured to be 4.8 nm and 187.0 nm, respectively, which are consistent with the reported literature [30-32].

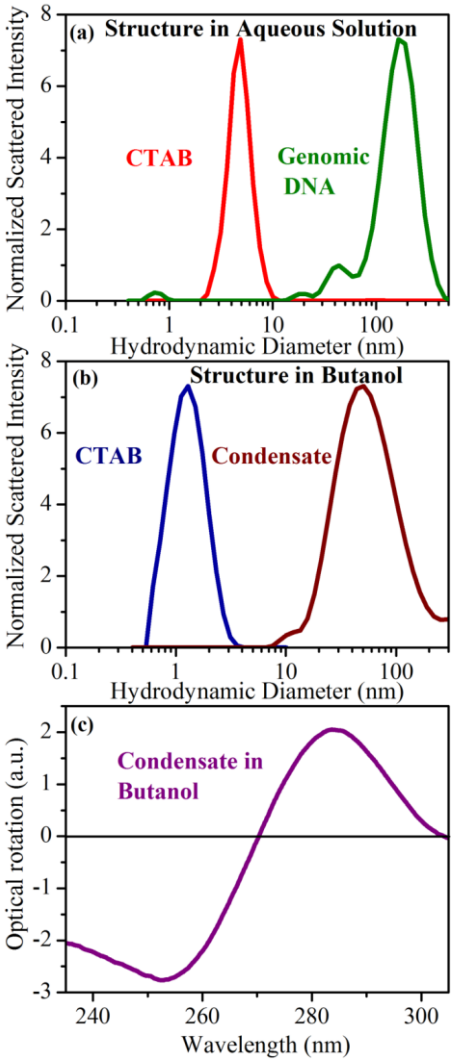

Figure 7.1. *Dynamic Light Scattering (DLS) of (a) CTAB micelle and DNA in aqueous solution (b) CTAB and the condensate (DNA-CTAB complex) in butanol. (c) CD spectra of DNA in condensate.*

However, the hydrodynamic diameter of CTAB in butanol is found to be 1.2 nm, which is the estimated length of the surfactant itself, indicating insignificant possibility of CTAB to form micelles in butanol. The diameter of the DNA-CTAB condensate is found to be 50 nm in butanol (Figure 7.1.b). During complexation the phosphate groups of DNA interact with the positive head group of CTAB resulting to a decrease in hydrodynamic diameter of the DNA-CTAB condensate. In order to understand structural perturbation of DNA due to its compactness in the condensate, we have performed circular dichroism (CD) spectroscopic studies. Figure 7.1.c shows the CD spectrum of the condensate in which the positive peak at 284 nm and negative peak at 253 nm are the signature of the B-form DNA in the condensate [20]. The structural integrity of the genomic DNA (B-form) in the condensate with respect to that in the aqueous buffer solution [24] is also clearly evident from the Figure.

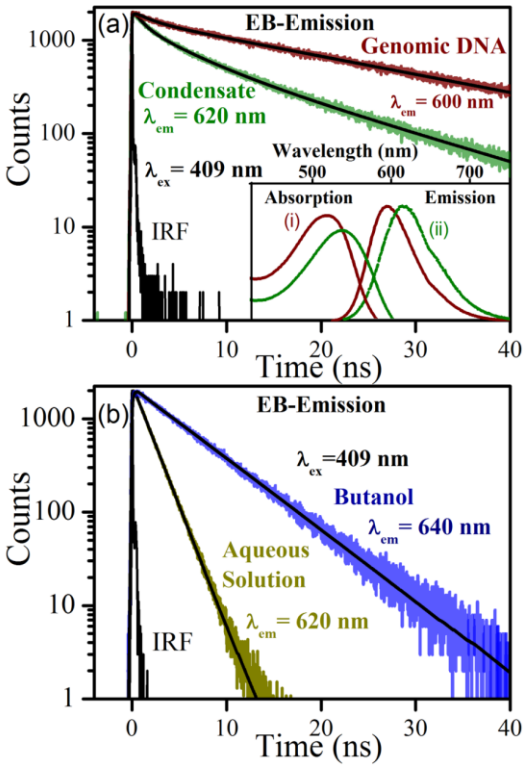

Figure 7.2. *(a) Picosecond resolved fluorescence transients of EB in DNA and in the condensate are shown. Inset shows the steady state spectra of EB in (i) DNA and (ii) the condensate. (b) Picosecond resolved fluorescence transients of EB in aqueous and in butanol are shown.*

Upon confirmation of the structural integrity, functional properties (molecular recognition) of DNA in the condensate were investigated through

intercalation of EB. Inset of Figure 7.2.a shows absorption and emission spectra of EB in DNA in aqueous solution and in the condensate. The red shift in absorption and emission maxima of EB in the condensate with respect to buffer, indicating more polar environment in the vicinity of the probe in the genomic DNA upon complexation with CTAB [33]. Picosecond resolved fluorescence transients of EB in DNA (aqueous) and in condensate (butanol) are shown in Figure 7.2.a. The bi-

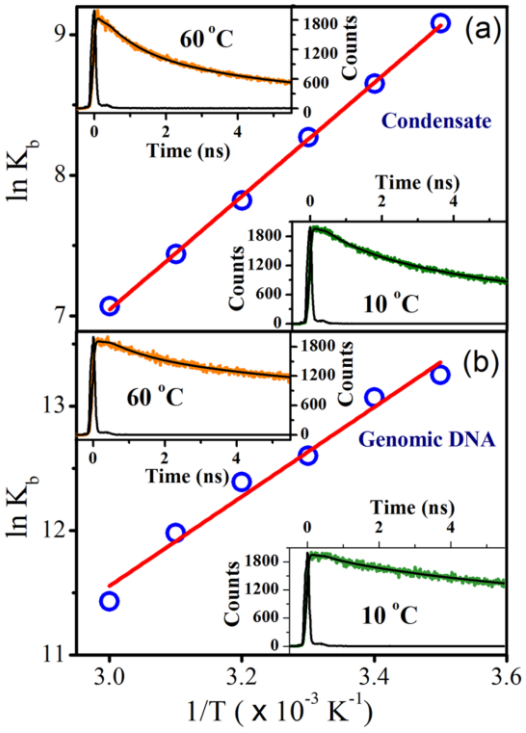

Figure 7.3. *The Van't Hoff plot of ln K vs. 1/T for binding of EB to (a) the condensate and to (b) DNA and picosecond resolved fluorescence transient at 10 ^{0}C and 60 ^{0}C for EB in condensate and in the genomic DNA are shown in inset of panel (a) and (b).*

exponential fitting of the fluorescence decay of EB in DNA (aqueous) revealing ~22 ns as major component indicates that most of the EB is intercalated to the genomic DNA [23]. The shorter time constant (minor component) of ~1.8 ns is due to unbound EB in the aqueous solution [23]. The time constant is consistent with that of the free EB in aqueous solution revealing a ~1.6 ns component as shown in Figure 7.2.b and Table 7.1. The fluorescence transient of the DNA-bound EB in the condensate shows triple exponential decay revealing typically time constants of ~1 ns (4%), 4.3 ns (21%) and 14 ns (75%). While the longer time constant (~14 ns) is the indicative of the DNA bound EB in the condensate, other two faster

components indicate the population of loosely bound/free EB in the butanol solution. Our measurement of fluorescence transient of EB in bulk butanol reveals time constants of ~1 ns and 5 ns as shown in Figure 7.2.b and Table 7.1.

Table 7.1. *The fluorescence life time of ethidium bromide (EB) in various systems.*

system	τ_1 [ns] ([%])	τ_2 [ns] ([%])	τ_3 [ns] ([%])	τ_{avg} [ns]
DNA	1.8 (2.04)	22.0 (97.96)	-	21.6
Condensate	0.9 (3.75)	4.3 (21.13)	13.8 (75.11)	11.3
Aqueous	1.6 (100.0)	-	-	1.6
Butanol	0.9 (1.01)	5.5 (98.99)	-	5.4

To gain insight into the thermal stability of the condensate, we have performed molecular recognition studies on the genomic DNA in the condensate at different temperatures. Upon increasing temperatures (10 ^{0}C to 60 ^{0}C) the relative percentage of the shorter components of EB-DNA fluorescence decays in aqueous solution and in the condensate are gradually increased. This observation is consistent with the fact that EB molecules are exposed towards the polar environments with increasing temperature. As evident from the insets of Figure 7.3.a the average lifetime for EB in the condensate is decreased from 11.9 ns at 10 ^{0}C to 8.2 ns at 60 ^{0}C, whereas average lifetime of EB in aqueous DNA is decreased from 22.0 ns at 10 ^{0}C to 19.2 ns at 60 ^{0}C (insets of Figure 7.3.b). We have estimated the binding constant *K* of EB with the genomic DNA and the condensate at different temperatures by using the following equation [23],

$$K = \frac{[EB-DNA]}{([EB]-[EB-DNA])\times([DNA]-[EB-DNA])} \qquad (7.1)$$

where [EB-DNA], [EB] and [DNA] represent the concentration of EB-DNA complexes, EB and the genomic DNA, respectively. The relative weighting of the longer and shorter components of EB fluorescence decays in the corresponding systems are indicative of bound and free population of the EB molecules, respectively. At room temperature, the binding constants of EB in two systems are found to be 470X10^{-3} μM^{-1} (aqueous DNA) and 5.7X10^{-3} μM^{-1} (condensate in butanol) indicating that EB binds to the DNA in aqueous solution more strongly than that in the condensate. The binding constant for the two systems were

calculated at six different temperatures and has been plotted against the inverse of temperature as shown in Figure 7.3.a and Figure 7.3.b. The plotted data were fitted following the Van't Hoff equation [34, 35],

$$\ln(K) = \frac{-\Delta H}{RT} + \frac{\Delta S}{R} \qquad (7.2)$$

where R is the gas constant and T is the temperature in Kelvin. ΔH and ΔS were obtained from the slope and intercept of the linear Van't Hoff plot and ΔG can be obtained from the Gibbs Helmholtz equation [36].

$$\Delta G = \Delta H - T\Delta S = - RT\ln K \qquad (7.3)$$

The calculated value of ΔG, ΔH and ΔS are tabulated in Table 7.2. Negative values of both ΔG and ΔH for the two systems (genomic DNA and condensate) indicate that interactions are spontaneous and exothermic in nature. However, ΔS is found to be positive for DNA (aqueous) and negative for the condensate. Negative value of ΔH and positive value of ΔS in DNA (aqueous) indicate that EB binds through electrostatic interaction. For the condensate both ΔH and ΔS are negative, which corroborate that EB binds to the genomic DNA in the condensate through van der Waals forces [37].

Table 7.2. *Thermodynamic parameters of the binding of ethidium bromide to DNA and their condensate.*

System	ΔH_{obs} (kcal mol^{-1})	ΔG_{obs} (kcal mol^{-1})	$T\Delta S_{obs}$ (kcal mol^{-1})
DNA	-6.69	-7.56	0.87
Condensate	-7.57	-5.05	-2.52

In order to study DNA-CTAB interactions in the condensate from the view point of the cationic surfactant (CTAB), we have used a fluorescent cationic surfactant NAO (acridine orange 10-nonyl bromide), having an acridine head group and a long alkyl tail in the condensate [38]. Absorption and emission spectra of NAO in the condensate are shown in the inset of Figure 7.4.a. Time resolved fluorescence transient of NAO in the condensate is shown in Figure 7.4.a. The three exponential fitting of the decay reveals and average time constant of 2.6 ns, which is much longer than that of free NAO in butanol (data not shown), indicating that NAO is attached to the condensate. For further confirmation of the

binding of NAO with the condensate, we have performed temperature dependent polarization-gated fluorescence anisotropy measurements. The anisotropy decays of NAO in the condensate at two temperatures (20 ^{0}C and 70 ^{0}C) are shown in the insets of Figure 7.4.b. As evident from Figure 7.4.b the rotational time constant (τ_{rot}) becomes faster upon increasing the temperature. We have estimated the

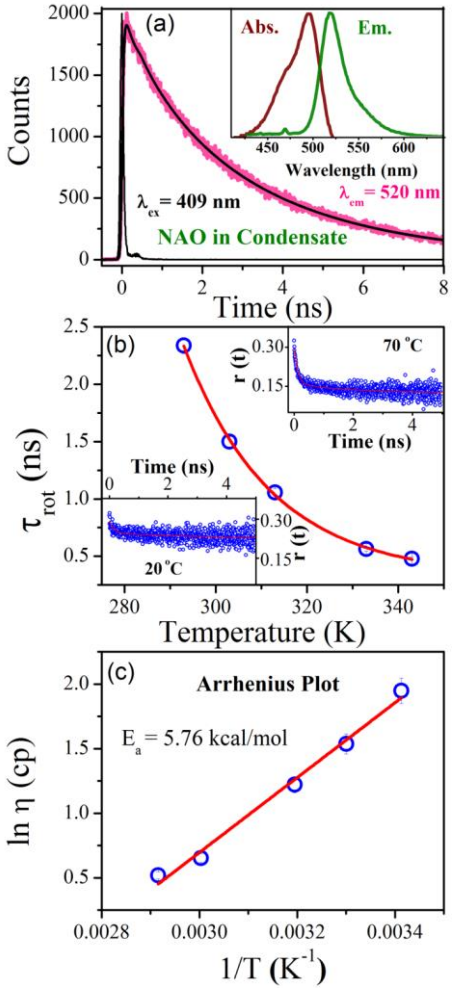

Figure 7.4. *(a) Picosecond resolved fluorescence transients of NAO in the condensate. Inset shows steady state spectra of NAO in condensate. (b) Plot of rotational time constants (τ_{rot}) against temperature for NAO in condensate. (c) Arrhenius plot of microviscosities of NAO in condensate.*

microviscosities at different temperatures for the corresponding systems, using hydrodynamic radius of the probe to be 6.8 Å and plotted with 1/T (K^{-1}) as shown in Figure 7.4.c. A linear fit of the plot to the data provides an activation energy of 5.76 kcal/mol from the equation [39], $\eta = \eta_0 \exp[E_n/(RT)]$, where E_n is the activation energy for the viscous flow. The estimated binding constant is

consistent with the fact that NAO is electrostatically bound to the genomic DNA in the condensate [40].

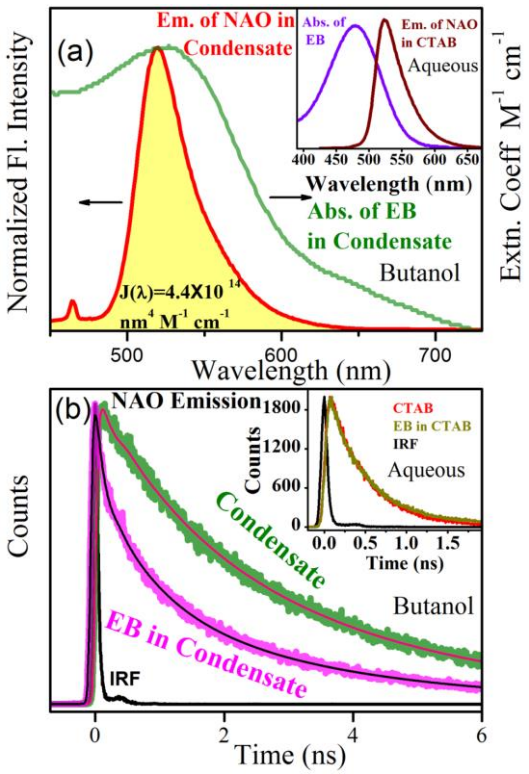

Figure 7.5. *(a) Spectral overlap of donor (NAO) and acceptor (EB) in condensate. Inset shows the spectral overlap of donor (NAO in CTAB micelles) and acceptor (EB) in aqueous solution. (b) Picosecond resolved transients of NAO in condensate in presence and absence of EB. Inset shows picosecond resolved transients of NAO in CTAB micelles in presence and absence of EB.*

To study the specific interaction of the genomic DNA in the condensate with cationic surfactant NAO, the nucleic acid was first labelled by the intercalator EB. Figure 7.5.a shows that emission spectrum of NAO broadly overlaps with absorption spectra of EB in the condensate without EB and NAO, respectively, revealing EB and NAO to be a possible FRET pair. Figure 7.5.b shows that the fluorescence transient of NAO in the condensate is decreased by addition of EB due to efficient energy transfer from NAO (donor) to EB (acceptor) in the condensate. The efficiency of energy transfer is found to be 57%. At room temperature (20 ^{0}C), the estimated Förster distance (R_0) and donor-acceptor distance are found to be 35 Å and 33 Å, respectively. The observation indicates that donor and acceptor are in close proximity revealing strong interactions between DNA and the cationic surfactant (NAO) to form the condensate. In order

to confirm that FRET is solely due to interaction of DNA (intercalated with EB) with the CTAB mimic NAO, a control experiment has been performed, where EB was added in aqueous solution of NAO in CTAB micelles. The inset of Figure 7.5.a shows that the emission of NAO in the CTAB micelles significantly overlaps with the absorption spectrum of EB in aqueous solution. However, the inset in Figure 7.5.b shows that fluorescence transient of NAO in CTAB micelles (aqueous) has no temporal quenching in presence of EB (without DNA), revealing that the quenching of fluorescence transients of NAO in the condensate is due to DNA-mediated energy transfer from NAO to EB. In presence of DNA, both positively charged CTAB and NAO are electrostatically bound to the nucleic acid and approach in the proximity of DNA-bound EB. However, the possibility of proximity of NAO to the energy acceptor EB in absence of DNA is completely absent (inset of Figure 7.5.b).

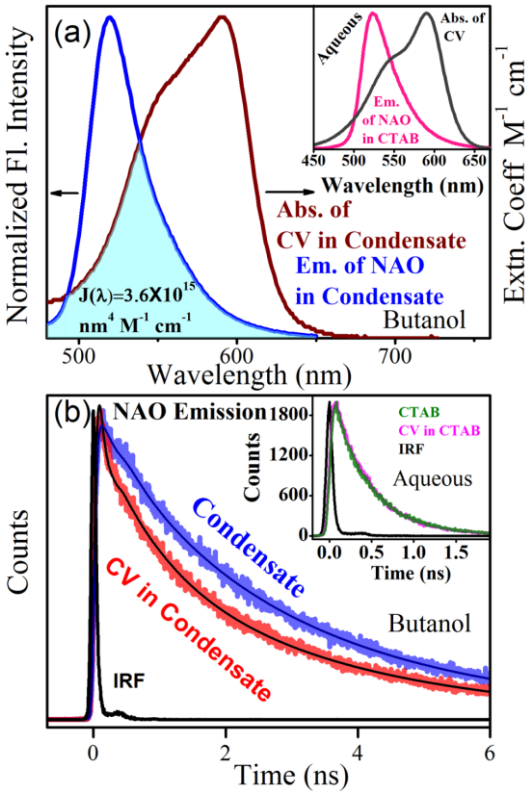

Figure 7.6. *(a) Spectral overlap of donor (NAO) and acceptor (CV) in condensate. Inset shows the spectral overlap of donor (NAO in CTAB micelles) and acceptor (CV) in aqueous solution. (b) Picosecond resolved transients of NAO in condensate in presence and absence of CV. Inset shows picosecond resolved transients of NAO in CTAB micelles in presence and absence of CV.*

In order to study the nonspecific molecular recognition of a cationic dye (CV) by the genomic DNA in the condensate, we have performed the FRET studies to investigate the energy transfer from NAO to CV in the condensate. Figure 7.6.a shows that the emission spectrum of NAO overlaps (in condensate) with the absorption spectrum of CV (in the condensate). The fluorescence transient of NAO in the condensate is quenched in presence of CV as shown in Figure 7.6.b. The efficiency of energy transfer in the above system

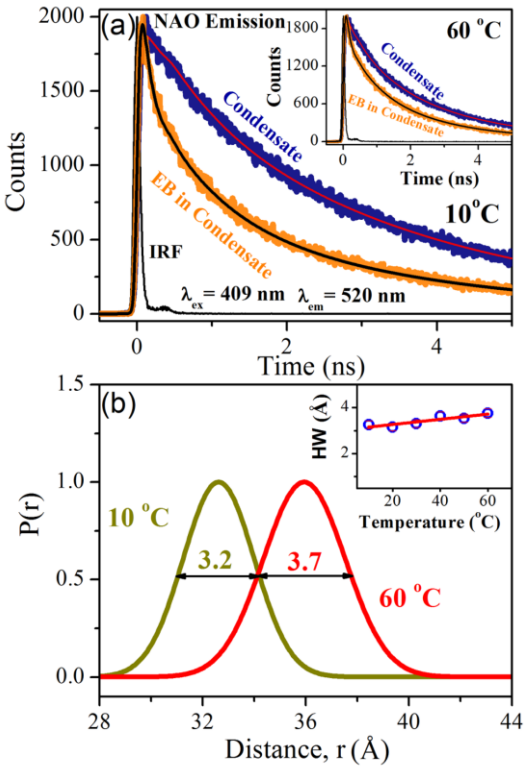

Figure 7.7. *(a) Picosecond resolved fluorescent transients of NAO in condensate in absence and presence of EB at 10 ^{0}C and at 60 ^{0}C are shown in inset, respectively. (b) Shows distribution of donor-acceptor distances of NAO and EB in condensate at 10 ^{0}C and at 60 ^{0}C. Inset shows plot of HW vs. temperature for the corresponding system.*

is found to be 32%, which is lower than that in the case of EB as energy acceptor. The lower efficiency of energy transfer in non-specific interaction compared to that in the case of specific interaction (intercalation) may be due to higher mutual coulombic repulsion of donor and acceptor having similar charges (cationic). The effect of the repulsion in the case of intercalated EB is lesser (Figure 7.5.b) than that of the loosely bound CV (Figure 7.6.b) [41]. The estimated Förster distance

and donor (NAO)-acceptor (CV) distances are found to be 49 Å and 56 Å, respectively. Furthermore, in order to confirm that FRET is exclusively DNA-mediated, some control experiment has been done as shown in insets of Figure 7.6.a and Figure 7.6.b revealing no FRET in the absence of DNA in the micellar system in aqueous solution.

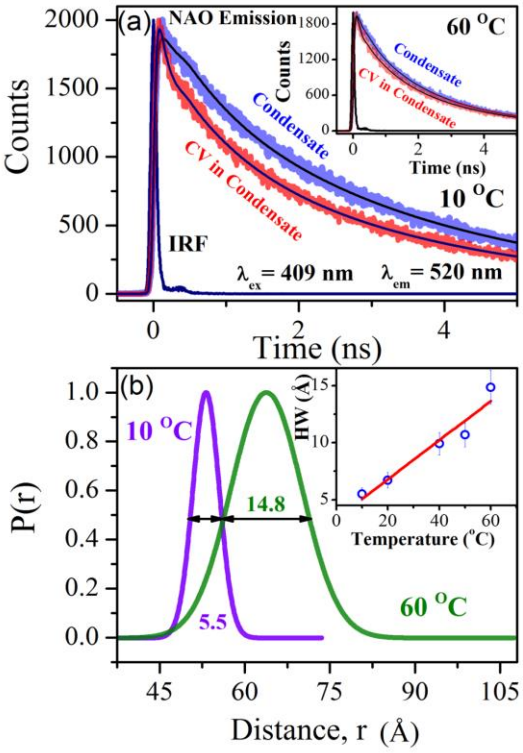

Figure 7.8. *(a) Picosecond resolved fluorescent transients of NAO in condensate in absence and presence of CV at 10 ^{0}C and at 60 ^{0}C are shown in inset. (b) Shows distribution of donor-acceptor distances of NAO and CV in condensate at 10 ^{0}C and at 60 ^{0}C. Inset shows a plot of HW vs. temperature for the corresponding system.*

To study the fluctuation of the donor-acceptor distance we have performed picosecond resolved temperature dependent FRET study for the corresponding systems. Figure 7.7.a and the inset show temperature dependent FRET between NAO and EB in the condensate at 10 ^{0}C and at 60 ^{0}C, respectively, clearly revealing that FRET efficiency is decreasing upon increasing temperature. The calculated donor-acceptor distance at the above two temperatures are found to be 33 Å and 36 Å, respectively. We have also calculated the distance distribution (p(r)) of donor-acceptor distance at different temperatures following the procedure reported earlier [42]. The distributions of NAO-EB distances in the

condensate at temperatures 10 ^{0}C and 60 ^{0}C are shown in Figure 7.7.b, which reveal that the distribution at lower temperature (half width, HW = 3.2 Å) is comparable to higher one (HW = 3.7 Å). The HW of the NAO-EB distances in the condensate are plotted against temperature yielding a linear thermal dependency of HW. With increasing temperatures, only distances between NAO and EB are found to be increased, however, the patterns of distributions (HW) of the distances are changed insignificantly (with experimental uncertainty of 5%) revealing the thermal stability, probably due to the fact that EB is strongly intercalated to DNA in the condensate.

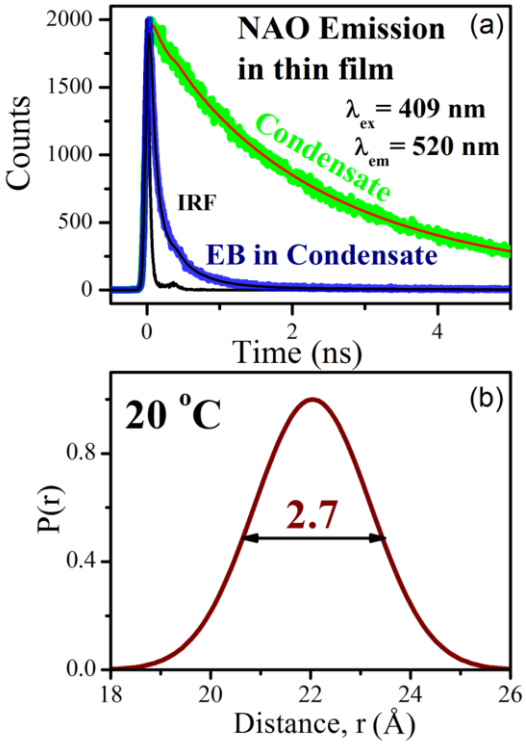

***Figure 7.9**. (a) Picosecond resolved fluorescent transients of NAO in condensate in film form in absence and presence of EB. (b) Distribution of donor-acceptor distance of NAO and EB in condensate at room temperature (20 ^{o}C).*

Picosecond resolved temperature dependent FRET between CV and NAO in the condensate at 10 ^{0}C and at 60 ^{0}C are shown in Figure 7.8.a and in the inset, respectively. The FRET efficiency decreased significantly as compared to above system with increasing temperatures and the calculated donor-acceptor distances are found to be 53 Å and 64 Å at 10 ^{0}C and 60 ^{0}C, respectively. The distributions of donor-acceptor distances at the above temperatures are shown in Figure 7.8.b,

which reveal that the distribution at 60 ^{0}C (HW = 14.8 Å) is much broader than that of at 10 ^{0}C (HW = 5.5 Å). The plot of HW verses temperature provides the linear increment as shown in the inset of Figure 7.8.b. The observation demonstrates that thermal fluctuations of the NAO-CV distances at higher temperatures increases in contrary to the earlier case of NAO-EB system in the condensate [43]. It has to be noted that the fluctuation is not due to the instability of position of NAO in the DNA rather it is due to a relocation of CV at higher temperature. This is due to the fact that the observed insignificant fluctuation is present in the NAO-EB system, where EB was bound by intercalation to the genomic DNA in the condensate. As the condensate is found to be an attractive system for bioelectronics as thin films [44], we have also performed FRET studies on the efficacy of energy migration from NAO to DNA bound EB in the condensate as thin films. The efficient energy transfer from NAO to the acceptor EB is clearly evident from Figure 7.9.a. Figure 7.9.b shows the distribution (HW = 2.7 Å) of donor-acceptor distance in thin film, which is lower than that of the solution phase may be due to the fact that in solid state the donor acceptor pair becomes less flexible.

7.3. Conclusion: In conclusion, we have performed a detailed study of an efficient gene-delivery system DNA-CTAB condensate. DLS experiments clearly show that DNA upon complexation with CTAB becomes compact in non-polar solvents. CD spectroscopy reveals that the B-structure of DNA remains unperturbed upon complexation with the CTAB surfactant. Using Van't Hoff equation, we have calculated binding constant of EB in DNA and the condensate at different temperature and found that EB binds strongly to DNA in compared to the condensate. The mode of binding of EB in DNA is electrostatic whereas in the condensate it binds through van der Waals forces. We have also used polarization gated fluorescence anisotropy for the estimation of fluctuations of NAO in the condensate. In DNA-CTAB interaction we have found that FRET efficiency is higher when EB is used as acceptor instead of CV. The picosecond resolved temperature dependent FRET study for the corresponding system reveals that the

distance between the donor and the acceptor increases significantly with increasing temperatures in case of CV compared to that of EB used as an acceptor. The fluctuation of donor acceptor distance is also higher in the case of a non-specific binding (CV) in comparison to specific binding (EB). Thus our findings are important to the future investigation on molecular recognition of DNA in the condensate and may find relevance in the design of an efficient gene-delivery agent.

References

[1] I. Koltover, T. Salditt, J.O. Rädler, C.R. Safinya, An inverted hexagonal phase of cationic liposome-DNA complexes related to DNA release and delivery, *Science,* 281 (1998) 78-81.

[2] B. Pitard, O. Aguerre, M. Airiau, A.-M. Lachagès, T. Boukhnikachvili, G. Byk, C. Dubertret, C. Herviou, D. Scherman, J.-F. Mayaux, Virus-sized self-assembling lamellar complexes between plasmid DNA and cationic micelles promote gene transfer, *Proc. Natl. Acad. Sci. U.S.A.,* 94 (1997) 14412-14417.

[3] V.G. Sergeyev, S.V. Mikhailenko, O.A. Pyshkina, I.V. Yaminsky, K. Yoshikawa, How does alcohol dissolve the complex of DNA with a cationic surfactant?, *J. Am. Chem. Soc.,* 121 (1999) 1780-1785.

[4] J. Clamme, S. Bernacchi, C. Vuilleumier, G. Duportail, Y. Mély, Gene transfer by cationic surfactants is essentially limited by the trapping of the surfactant/DNA complexes onto the cell membrane: A fluorescence investigation, *Biochim. Biophys. Acta, Biomembr.,* 1467 (2000) 347-361.

[5] C.R. Safinya, K. Ewert, A. Ahmad, H.M. Evans, U. Raviv, D.J. Needleman, A.J. Lin, N.L. Slack, C. George, C.E. Samuel, Cationic liposome–DNA complexes: From liquid crystal science to gene delivery applications, *Phil. Trans. R. Soc. A,* 364 (2006) 2573-2596.

[6] J.P. Behr, Synthetic gene-transfer vectors, *Acc. Chem. Res.,* 26 (1993) 274-278.

[7] C. Watts, M. Marsh, Endocytosis: what goes in and how, *J. Cell Sci.,* 103 (1992) 1-8.

[8] J.O. Rädler, I. Koltover, T. Salditt, C.R. Safinya, Structure of DNA-cationic liposome complexes: DNA intercalation in multilamellar membranes in distinct interhelical packing regimes, *Science,* 275 (1997) 810-814.

[9] D.D. Lasic, Liposomes within liposomes, *Nature,* 387 (1997) 26-27.

[10] J. Zabner, A.J. Fasbender, T. Moninger, K.A. Poellinger, M.J. Welsh, Cellular and molecular barriers to gene transfer by a cationic lipid, *J. Biol. Chem.,* 270 (1995) 18997-19007.

[11] M. Reichmann, S. Rice, C. Thomas, P. Doty, A further examination of the molecular weight and size of desoxypentose nucleic acid, *J. Am. Chem. Soc.,* 76 (1954) 3047-3053.

[12] S.M. Mel'nikov, V.G. Sergeyev, K. Yoshikawa, Transition of double-stranded DNA chains between random coil and compact globule states induced by cooperative binding of cationic surfactant, *J. Am. Chem. Soc.,* 117 (1995) 9951-9956.

[13] S.M. Mel'nikov, V.G. Sergeyev, Y.S. Mel'nikova, K. Yoshikawa, Folding of long DNA chains in the presence of distearyldimethylammonium bromide and unfolding induced by neutral liposomes, *J. Chem. Soc., Faraday Trans.,* 93 (1997) 283-288.

[14] S. Marchetti, G. Onori, C. Cametti, DNA condensation induced by cationic surfactant: A viscosimetry and dynamic light scattering study, *J. Phys. Chem. B,* 109 (2005) 3676-3680.

[15] P. Pinnaduwage, L. Schmitt, L. Huang, Use of a quaternary ammonium detergent in liposome mediated DNA transfection of mouse L-cells, *Biochim. Biophys. Acta, Biomembr.,* 985 (1989) 33-37.

[16] J.K. Rose, L. Buonocore, M.A. Whitt, A new cationic liposome reagent mediating nearly quantitative transfection of animal cells, *Biotechniques,* 10 (1991) 520-525.

[17] V. Sergeev, O. Pyshkina, A. Zezin, V. Kabanov, DNA-surfactant complexes soluble in low-polarity organic liquids, *Polym. Sci. Ser. A, Chem. Phys.,* 39 (1997) 12-16.

[18] K. Ijiro, Y. Okahata, A DNA–lipid complex soluble in organic solvents, *J. Chem. Soc., Chem. Commun.,* (1992) 1339-1341.

[19] K. Tanaka, Y. Okahata, A DNA-Lipid Complex in Organic Media and Formation of an Aligned Cast Film1, *J. Am. Chem. Soc.,* 118 (1996) 10679-10683.

[20] S. Marchetti, G. Onori, C. Cametti, Calorimetric and dynamic light-scattering investigation of cationic surfactant-DNA complexes, *J. Phys. Chem. B,* 110 (2006) 24761-24765.

[21] R. Marty, C.N. N'soukpoé-Kossi, D. Charbonneau, C.M. Weinert, L. Kreplak, H.-A. Tajmir-Riahi, Structural analysis of DNA complexation with cationic lipids, *Nucleic Acids Res.,* 37 (2009) 849-857.

[22] R. Sarkar, S.K. Pal, Interaction of Hoechst 33258 and ethidium with histone1-DNA condensates, *Biomacromolecules,* 8 (2007) 3332-3339.

[23] R. Sarkar, S.K. Pal, Ligand–DNA interaction in a nanocage of reverse micelle, *Biopolymers,* 83 (2006) 675-686.

[24] S. Choudhury, S. Batabyal, T. Mondol, D. Sao, P. Lemmens, S.K. Pal, Ultrafast dynamics of solvation and charge transfer in a DNA- based biomaterial, *Chem. Asian J.,* 9 (2014) 1395-1402.

[25] T.H. Haines, N.A. Dencher, Cardiolipin: A proton trap for oxidative phosphorylation, *FEBS Lett.,* 528 (2002) 35-39.

[26] J.M. Petit, A. Maftah, M.H. Ratinaud, R. Julien, 10N- Nonyl acridine orange interacts with cardiolipin and allows the quantification of this phospholipid in isolated mitochondria, *Eur. J. Biochem.,* 209 (1992) 267-273.

[27] P.K. Verma, R.K. Mitra, S.K. Pal, A molecular picture of diffusion controlled reaction: role of microviscosity and hydration on hydrolysis of benzoyl chloride at a polymer hydration region, *Langmuir,* 25 (2009) 11336-11343.

[28] S. Patel, A. Datta, Fluorescence investigation of the binding of model PDT drugs to nonionic and zwitterionic surfactants, *Photochem. Photobiol. Sci.,* 85 (2009) 725-732.

[29] P. Singh, S. Choudhury, G.K. Chandra, P. Lemmens, S.K. Pal, Molecular recognition of genomic DNA in a condensate with a model surfactant for potential gene-delivery applications, *J. Photochem. Photobiol., B,* 157 (2016) 105-112.

[30] A.M. Wiosetek-Reske, S. Wysocki, Spectral studies of N-nonyl acridine orange in anionic, cationic and neutral surfactants, *Spectrochim. Acta, Part A,* 64 (2006) 1118-1124.

[31] M. Cárdenas, K. Schillén, T. Nylander, J. Jansson, B. Lindman, DNA Compaction by cationic surfactant in solution and at polystyrene particle solution interfaces: a dynamic light scattering study, *Phys. Chem. Chem. Phys.,* 6 (2004) 1603-1607.

[32] T. Movchan, I. Soboleva, E. Plotnikova, A. Shchekin, A. Rusanov, Dynamic light scattering study of cetyltrimethylammonium bromide aqueous solutions, *Colloid J.,* 74 (2012) 239-247.

[33] R. Bera, B.K. Sahoo, K.S. Ghosh, S. Dasgupta, Studies on the interaction of isoxazolcurcumin with calf thymus DNA, *Int. J. Biol. Macromol.,* 42 (2008) 14-21.
[34] G. Zhang, X. Hu, P. Fu, Spectroscopic studies on the interaction between carbaryl and calf thymus DNA with the use of ethidium bromide as a fluorescence probe, *J. Photochem. Photobiol., B,* 108 (2012) 53-61.
[35] N. Akbay, Z. Seferoğlu, E. Gök, Fluorescence interaction and determination of calf thymus DNA with two ethidium derivatives, *J. Fluoresc.,* 19 (2009) 1045-1051.
[36] R.K. Nanda, N. Sarkar, R. Banerjee, Probing the interaction of ellagic acid with human serum albumin: A fluorescence spectroscopic study, *J. Photochem. Photobiol. A,* 192 (2007) 152-158.
[37] P.D. Ross, S. Subramanian, Thermodynamics of protein association reactions: forces contributing to stability, *Biochemistry,* 20 (1981) 3096-3102.
[38] E. Mileykovskaya, W. Dowhan, R.L. Birke, D. Zheng, L. Lutterodt, T.H. Haines, Cardiolipin binds nonyl acridine orange by aggregating the dye at exposed hydrophobic domains on bilayer surfaces, *FEBS Lett.,* 507 (2001) 187-190.
[39] R.K. Mitra, P.K. Verma, S.K. Pal, Exploration of the dynamical evolution and the associated energetics of water nanoclusters formed in a hydrophobic solvent, *J. Phys. Chem. B,* 113 (2009) 4744-4750.
[40] M. Eftink, C. Ghiron, Dynamics of a protein matrix revealed by fluorescence quenching, *Proc. Natl. Acad. Sci. U.S.A.,* 72 (1975) 3290-3294.
[41] W. Müller, F. Gautier, Interactions of heteroaromatic compounds with nucleic acids. A-T-specific non-intercalating DNA ligands, *Eur. J. Biochem.,* 54 (1975) 385-394.
[42] S. Choudhury, P.K. Mondal, V.K. Sharma, S. Mitra, V.G. Sakai, R. Mukhopadhyay, S.K. Pal, Direct observation of coupling between structural fluctuation and ultrafast hydration dynamics of fluorescent probes in anionic micelles, *J. Phys. Chem. B,* 34 (2015) 10849-10857.
[43] S. Nag, B. Sarkar, M. Chandrakesan, R. Abhyanakar, D. Bhowmik, M. Kombrabail, S. Dandekar, E. Lerner, E. Haas, S. Maiti, A folding transition underlies the emergence of membrane affinity in amyloid-β, *Phys. Chem. Chem. Phys.,* 15 (2013) 19129-19133.
[44] A.J. Steckl, DNA–a new material for photonics?, *Nature Photon.,* 1 (2007) 3-5.

Chapter 8

Spectroscopic Studies on Protein-DNA Interaction in a Physiologically Relevant Environment

8.1. Introduction: Many *in vivo* enzymatic processes including repression or activation of transcription in gene regulatory network are triggered by binding of proteins to their respective target sites on DNA. However the study of enzyme-DNA interactions have been usually designed as dilute solution experiments, which differ substantially from *in vivo* conditions as 40% volume of cytosol is occupied by a wide variety of macromolecules and solutes [1-3]. Due to this reason, the diffusion of any solutes in intracellular environment is get affected either being reduced or presenting anomalous diffusion at short times [4-8]. Contemporary studies have revealed that macromolecular crowding inside the cell does not only affect diffusion processes but also biochemical reaction processes by inducing the enzyme to undergo protein folding, self-association, or protein-binding processes, which in turn may alter the activity of the enzyme [9-12]. Thus, in order to obtain more accurate rates for enzymatic reactions, it is important to perform the studies of biochemical processes in nature-like microenvironments that try to mimic the effect of macromolecular crowding.

As the quantitative studies of enzyme-DNA interactions within a living cell are challenging, subsequently to mimic the intracellular like environment the high concentration of crowding agents are often used in the *in vitro* studies. For this purpose polyethylene glycol and polysaccharides are often considered as a convenient macromolecular crowder as it is highly soluble in water, it does not precipitate the biological macromolecules used for the study and also it does not bind with the biological macromolecules before and after the reaction [13]. Polymer cosolutes (PEG) usually generate an area inaccessible to other biological macromolecules known as excluded volume and these excluded

volume per cosolutes increases as size of cosolutes increases. Apart from this, inclusion of cosolutes causes the decrease of water activity of solution and hence generates an osmotic pressure [14, 15]. The dependence of the equilibrium binding constant, (K), of the biomolecular reaction on the water activity (a_w) is related to the number of water molecules released (Δn_w) during the reaction represented by the equation, $-\Delta n_w = \delta \log K / \delta \log a_w$. Based on this thermodynamic model, the equilibrium constant of a reaction accompanied by the released of water molecules is found to be 10 to 100 times higher in solution with water activity less than one [13, 16]. The excluded volume of protein in macromolecular crowding can be minimized either by changes in the hydrodynamic volume or via changes in its association state [17, 18], which are promoted by modulation of the biological equilibria of protein that would affect protein folding, conformational stability, protein-protein interactions and protein-nucleic acid interactions [18-20].

Zimmerman and Minton have shown in number of experimental systems which support that crowding promotes molecular association and hence the enzymatic activity [21, 22]. In one of the contemporary literature they have shown that in presence of several macromolecules the enzymatic activity of DNA ligases from both rat liver and *Escherichia coli* increases by several orders [23]. Naoki Sugimoto and co-workers have shown that molecular crowding increases the activity of endonucleases but not affect exonucleases [24]. All these studies furnish amendment of catalytic activity of the enzyme as a consequence of molecular crowding. However, the exact role of structure, function and dynamics of enzyme triggering in alteration of enzymatic activity in molecular crowding condition are still poorly understood and a detailed understanding in this field is highly demanding due to the highly compact packing *in vivo* condition.

Here, we systemically study the role of molecular crowding such as polyethylene glycol (PEG) on the structure, functionality, substrate binding and dynamic of endonuclease glycoprotein known as bovine pancreatic

deoxyribonuclease I (DNase I). DNase I is a secretory glycoprotein that hydrolysed the P-O3'-bond of double-stranded DNA predominantly by single-stranded nicking mechanism under physiological condition in presence of Mg^{2+} and Ca^{2+} [25]. Like many of the non-specific protein-DNA interaction, crystal structure showed that the unspecific DNase I bind tightly in the minor groove and to the sugar-phosphate backbone of both strands of the DNA [25]. In the present study the enzymatic activity of DNase I on the hydrolysis of 20-mer double stranded DNA is found to increase with increasing PEG concentrations through intact structural integrity as revealed from CD in the solution. To corroborate the change in activity and binding of DNase I towards DNA as a function of the concentration of PEG, time resolved fluorescence spectroscopy study was followed. While picosecond resolved transients of EB intercalated to DNA upon interaction with DNase I revealed the extent of DNA cleavage by enzyme in presence and absence of PEG, Förster resonance energy transfer **(**FRET) studies from 8-anilino-1-naphthalenesulfonic acid ammonium salt (ANS) attached with DNase I to EB intercalated to DNA confirm more efficient binding between DNase I and DNA in presence of PEG. Further, the change in protein dynamics, responsible for the association of DNase I and DNA has been monitored by rotational dynamics as well as picosecond resolved transients of ANS attached to DNase I. We have also confirmed the enhanced activity of DNase I in presence of molecular crowding through conventional way of agarose gel electrophoresis in order to evaluate the hydrolysis of both large (calf thymus) DNA as well as for 20-mer dsDNA.

8.2. Results and Discussion:

8.2.1. Ultrafast Spectroscopy on DNA-Cleavage by Endonuclease in Molecular Crowding [26]: The kinetics of hydrolysis of the substrate dsDNA-EB by DNase I has been measured by steady state fluorescence technique and is found that the rate of exclusion of the EB from DNA upon hydrolysis by DNase I increases gradually as the concentration of PEG increases in the solution. Figure 8.1.a shows that in absence of PEG the amount of residual

dsDNA after 300 sec is estimated to be 67%; however it reduced to 57%, 49% and 48% in presence of 5, 10 and 15 wt% PEG [27-29]. To calculate the rate constant and the maximum velocity, we have measured the kinetics at different substrate concentrations. Figure 8.1.b depicts the corresponding Lineweavere-

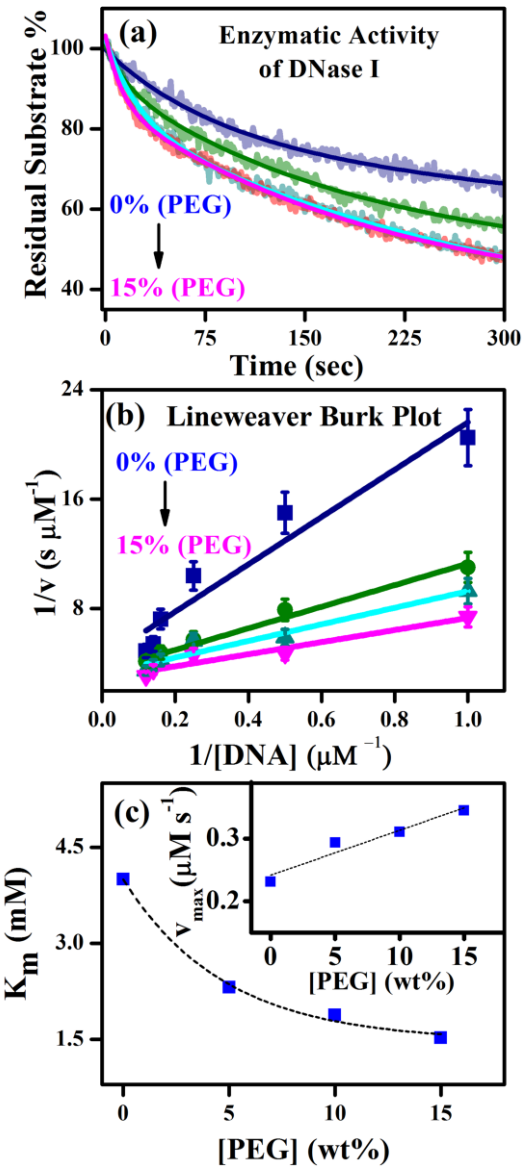

Figure 8.1. *(a) Amount of residual DNA upon hydrolysis by DNase I in the presence of 0, 5, 10 and 15 wt% of PEG. (b) A representative Lineweavere-Burk plot for the catalytic activity of DNase I on the substrate DNA in presence of 0, 5, 10 and 15 wt% PEG. (c) K_m for the catalytic activity of DNase I on the substrate DNA as a function of PEG concentrations. The plot of V_{max} against PEG concentration is shown in the inset.*

Burk plot for different PEG concentration, where the reciprocal of the reaction velocity (v) is plotted as a function of the reciprocal of the concentration of

DNA [30]. The curves produce good linear fits for all the systems and from the slope and intercept of the curves, we have calculated the Michaelise-Menten constant (K_m) and the maximum velocity (V_{max}) for all the systems. The calculated K_m, and V_{max} values for the three different PEG concentrations are presented in Figure 8.1.c which clearly indicates that with the increase in PEG concentration, V_{max} increases however, K_m for the enzymatic activities of DNase I for substrate DNA decreases. These kinetic parameters reveal that molecular crowding influences the hydrolytic activity of the DNase I by affecting catalytic activity as well as its binding affinity toward the substrate DNA, indicated by both increase of V_{max} and decrease of K_m [27, 31].

Table 8.1. *Fluorescence lifetimes of EB in different systems.*

System	τ_1 ns [%]	τ_2 ns [%]	τ_3 ns [%]	τ_{avg} ns
DNA	0.21 (27)	2.21 (19)	21.0 (54)	11.9
DNA-DNase I	0.50 (36)	2.57 (35)	21.0 (29)	7.2
DNA-PEG	0.26 (30)	2.70 (23)	20.40 (47)	10.4
DNA-DNase I-PEG	0.51 (42)	3.24 (40)	20.30 (18)	5.2
Water	0.47 (20)	1.68 (80)	-	1.4
PEG	0.93 (51)	3.46 (49)	-	2.1

In order to reveal whether the changes in catalytic activity induced by PEG are accompanied by alterations in the secondary structures of DNase I, CD spectroscopy were performed. As observed from Figure 8.2.a the aqueous DNase I solution displays CD features with minimum value at 208 and 215 nm (far UV-CD), corroborating the native secondary structures of the enzyme [32] which is observed to be insignificantly perturbed in presence of PEG, indicating that the secondary structure of the enzyme is preserved up to 15 wt% PEG concentration. Inset of Figure 8.2.a symbolize the percentage of α strand and β sheet in free DNase I in absence and presence of 15 wt% PEG which remain almost same in both the cases. To gain insight about the DNA structure perturbation by DNase I, we have next focused on conformational changes of 20-mer DNA, which exhibits two characteristics peaks (inset of

Figure 8.2.b); one positive band around 280 nm complemented to π-π base stacking, and one negative band around 245 nm for hellicity [33]. Upon addition of DNase I the band at 280 nm was insignificantly perturbed however,

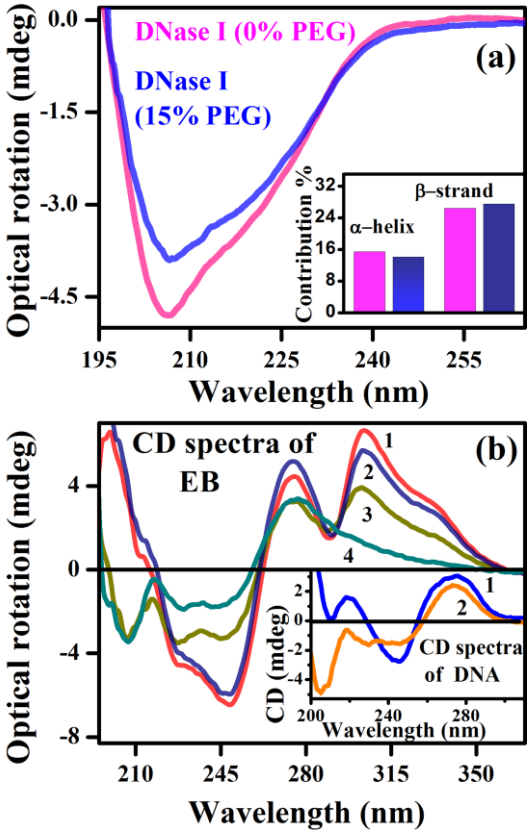

Figure 8.2. *(a) The far UV-CD (circular dichroism) spectra of DNase I at 0 and 15wt% PEG. Contribution of alpha strand and beta sheet at various wt% PEG is shown in inset. (b) Induced CD (circular dichroism) spectra of EB intercalated to DNA in 1) buffer, 2) 15 wt% PEG, 3) complexed with DNase I in buffer and 4) complexed with DNase I in 15 wt% PEG. CD spectra of 1) DNA and 2) DNA-DNase I complex are shown in inset.*

the band at 245 nm became less negative, this in turn attributed to partial B-to-A DNA transition upon protein interaction [34]. In order to explore the cleavage of DNA in presence and absence of PEG, DNA was intercalated with EB which generated induced CD signal near 303 nm along with and increasing helicity peak of DNA [35] as shown in Figure 8.2.b. In presence of PEG, an insignificant decrease in the induced CD spectra at 303 nm was observed may be due to osmotic stress of PEG, while the nature of the spectra remained nearly unchanged, demonstrating that DNA remained in B conformation upon addition of PEG. When DNase I is added to the DNA-EB system, decrease in

303 nm spectra is observed however, a commendable variation has been observed when DNase I is added to DNA-EB system containing 15 wt% of PEG, infers that cleavage has enhanced in presence of PEG. In this light of understanding, altered enzymatic activity offers a unique opportunity for correlating the function with the dynamics. For this reason fluorescence spectroscopic techniques can prove useful to understand bio-macromolecular dynamics over a broad time scale.

The enhanced hydrolysis (V_{max}) of DNA by DNase I in presence of PEG is established by monitoring the picosecond resolved transients of EB intercalated to DNA. The significant decrease in emission intensity and red shift of EB emission maxima in the DNA-DNase I complex compared to EB-DNA in buffer indicated the lowering of the contribution of EB binding to the DNA upon cleavage with DNase I (inset of Figure 8.3.a). Figure 8.3.a shows picosecond resolved transients of EB in buffer and in EB-DNA complexes in absence and presence of DNase I. The tri-exponential fitting of the fluorescence decay of EB in DNA revealing ~21 ns as major component (54%) indicates that most of the EB is intercalated to the DNA [36]. However, upon hydrolysis of EB-DNA complexes by DNase I the contribution of longer decay component ~21 ns (29%) decreases considerably, reflecting significant cleavage of DNA by DNase I in buffer solution as shown in Table 8.1. In order to investigate the effect of PEG in hydrolysis of DNA, picosecond resolved transients of all the system are studied in presence of 15 wt% PEG, shown in Figure 8.3.b. It is observed that the maximum population of the dye intercalated to the DNA in presence of PEG is slightly decreased (~21 ns (47%)) in contrast to that in DNA in buffer solution (~21 ns (54%)) which occurred may be due to osmotic stress created by PEG. The transient of EB in DNA upon hydrolysis by DNase I in presence of PEG shows that the contribution of a longer time component ~21 ns (18%) is extensively get lower than that of DNA in buffer solution (21 ns (29%)), corroborate the higher cleavage in presence of PEG. Inset of Figure 8.3.b shows the corresponding steady state emission of EB in DNA and DNA-DNase I complex in presence of PEG. It should be noted that decrease in emission

intensity and more red shift of EB emission maxima in the DNA-DNase I complex in presence of PEG compared to EB in DNA-DNase I complex in buffer revealing the further reduction of the contribution of EB binding to the DNA upon hydrolysis in presence of PEG.

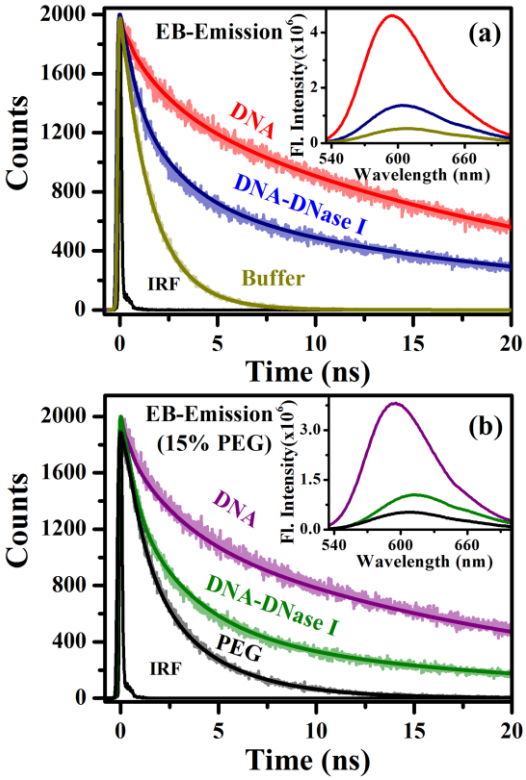

Figure 8.3. *Picosecond-resolved transient of free EB, EB in DNA and in DNA-DNase I complex in presence of (a) 0 wt% PEG and (b) 15 wt% PEG. Insets depict the corresponding steady state emission of free EB, EB in DNA and in DNA-DNase I complex.*

The binding affinity and dynamics of DNase I with DNA are monitored by using a biologically relevant probe 8-anilino-1-naphthalenesulfonic acid ammonium salt (ANS) which binds selectively to the enzymes in their hydrophobic sites [37]. The excitation spectrum of ANS in buffer shows a peak at 356 nm, which remains same when formed complexed with DNase I, however, the emission spectrum of the ANS-DNase I complex shows a blue shift (60 nm) compared to that in buffer as shown in Figure 8.4.a, indicate interaction of ANS to the hydrophobic sites of protein. Picosecond-resolved transients of ANS in buffer, DNase I-bound ANS and its complex with DNA are shown in Figure 8.4.b. ANS in complexed with DNase I show essentially fluorescence decays of average time constants 8.12 ns which is much slower

than ANS in buffer (0.23 ns). The longer life time of ANS-DNase I is observed to be similar to that of the ANS-DNase I-DNA complex, revealing the fact that ANS molecules are not detached from DNase I upon complexation (Table 8.2). Further, in order to understand the effect of confinement on the fate of ANS bound DNase I, similarly the picosecond transient of ANS in all the systems were performed in presence of PEG. The average fluorescence decays time constants of ANS in complexed with DNase I was found to be 5.66 ns, whereas an insignificant change in life time of ANS-DNase I-DNA in presence of PEG was observed shown in Figure 8.4.c.

Table 8.2. *Fluorescence lifetimes of ANS in different systems.*

System	τ_1 ns [%]	τ_2 ns [%]	τ_3 ns [%]	τ_{avg} ns
DNase I	0.15 (32)	1.52 (13.4)	14.42 (54.6)	8.12
DNaseI-DNA	0.14 (33.8)	1.32 (16.1)	13.90 (50.1)	7.22
DNase I-DNA-EB	0.11 (39.3)	1.15 (27.3)	11.74 (33.4)	4.28
DNase I-PEG	0.14 (32.6)	1.07 (27.2)	13.22 (40.2)	5.66
DNase I-PEG-DNA	0.14 (35.4)	1.16 (24.4)	12.59 (40.2)	5.39
DNase I-PEG-DNA-EB	0.13 (34.7)	0.83 (46.9)	10.85 (18.4)	2.43
Buffer	0.23 (100)	-	-	0.23
PEG	0.37 (48)	0.86 (52)	-	0.63

The intactness of ANS in DNase I upon complex with DNA has enabled us to carry out Förster resonance energy transfer (FRET) studies from the donor, ANS in DNase I, to another dye (acceptor), ethidium bromide (EB), intercalated in the DNA, which also corroborate the binding between enzyme and DNA. The significantly large spectral overlap (2.58×10^{14} M^{-1} cm^{-1} nm^4) of the donor (ANS) emission and acceptor (EB) absorption spectra favours energy transfer from the donor to the acceptor as shown in inset of Figure 8.5.a. The picosecond resolved transient (Figure 8.5.a) of the ANS in DNase I-DNA complex reveals an average decay time constant of 7.22 ns and 4.28 ns in the absence and presence of the acceptor (EB), respectively. The efficiency of energy transfer and donor–acceptor distance was calculated to be 40% and 28.7

Å, respectively. To gain insight into the effect of PEG in the binding between DNase I and DNA, we have executed the similar FRET study in presence of PEG. The absorption spectrum of EB bound to DNA has almost same spectral

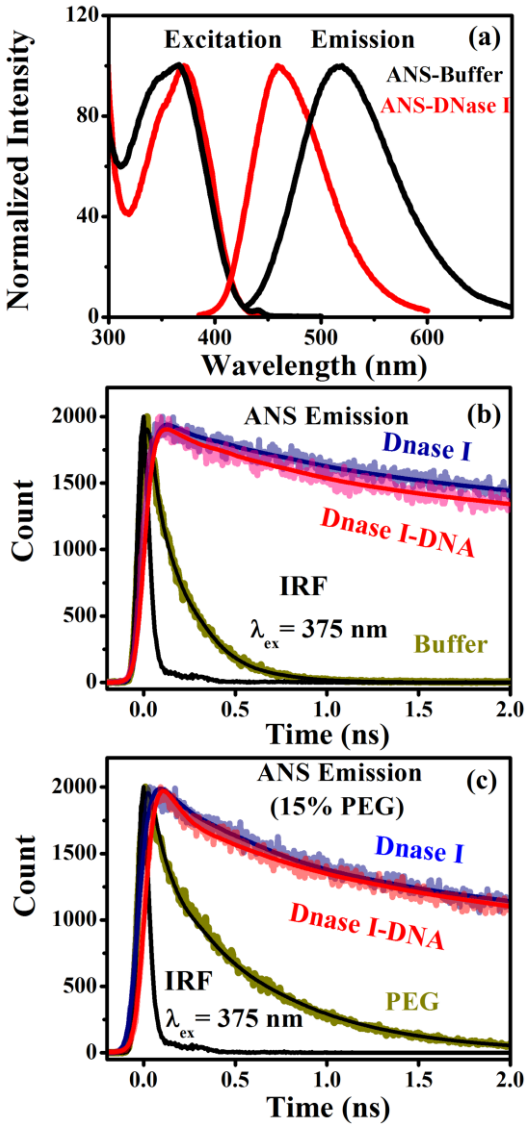

Figure 8.4. *(a) Steady state excitation and emission spectra of ANS in buffer and in complex with DNase I. Time-resolved transients of free ANS, ANS bound to DNase I in the presence and absence of DNA are shown in presence of (b) 0 wt% PEG and (c) 15 wt% PEG.*

overlap with the emission spectrum of ANS in DNase I in presence of PEG (inset of Figure 8.5.b). The fluorescence transient of ANS in DNase I in 15wt% PEG is quenched in presence of EB interacted to DNA as shown in Figure 8.5.b and Table 8.2 and the efficiency of energy transfer and ANS- EB distances in presence of PEG is found to be 54%, and 22.9 Å, respectively. The higher

efficiency of energy transfer leading to shorter FRET distance in presence of PEG corroborates higher binding between DNase I and DNA compared to that in absence of PEG, which is also consistent with our kinetics studies.

Table 8.3. *Rotational time constants of ANS at the enzyme (DNase I) surface at various concentrations of PEG.*

System	τ_1 ns [%]	τ_2 ns [%]	τ_{avg} ns
ANS-DNase I	1.32 (11.3)	45 (88.7)	39.6
ANS-DNase I-DNA	0.9 (14.7)	45 (85.3)	38.4
ANS-DNase I-PEG	0.20 (66.4)	40 (33.6)	13.5
ANS-DNase I-DNA-PEG	0.13 (70.8)	40 (29.2)	11.7
Buffer	0.07 (100)	-	0.07
PEG	0.19 (100)	-	0.19

In order to gain insight in the basis for higher binding between DNase I-DNA in presence of PEG, we compare the average lifetime of ANS bound to DNase I in presence and absence of PEG and found that the contribution of average time constant characteristic of ANS-DNase I adduct, decreases from 8.12 ns in the buffer to 5.66 ns in presence of 15 wt% PEG (as shown in Figure. 8.4.a and Figure 8.4.b). The observation is consistent with the fact that faster dynamics at the higher concentration of PEG suggests thinning of the hydration water shell around the enzyme due to decreased water activity and hence leads to higher binding between DNase I-DNA, which accelerates the hydrolysis of DNA (Scheme 8.1) [15]. Bagchi et al. earlier proposed the presence of at least two types of water molecules at the protein surface and these water molecules remain in a dynamic equilibrium with the bulk or free type water molecules (Water $_{\text{surface bound}}\leftrightarrow$ Water $_{\text{bulk}}$) [38, 39]. This equilibrium between the bound and bulk water is sensitive to the change in the microenvironment of the protein, e.g. temperature, pressure, additives etc. Hence, addition of PEG produces an osmotic stress in the hydration layer, which in turn shifts the equilibrium towards a less hydrated conformation and also increases the contribution of faster moving bulk water molecules around the enzyme's surface. This explains the observed decrease in the average time

constant of ANS bound to DNase I with increased in PEG concentration. The hydration shell formed by water molecules in the close vicinity of a protein molecule is crucial for protein structure and folding and defines the substrate binding, and molecular recognition [40]. Changes in the protein hydration are known to be related to changes in protein catalytic activity and also have a

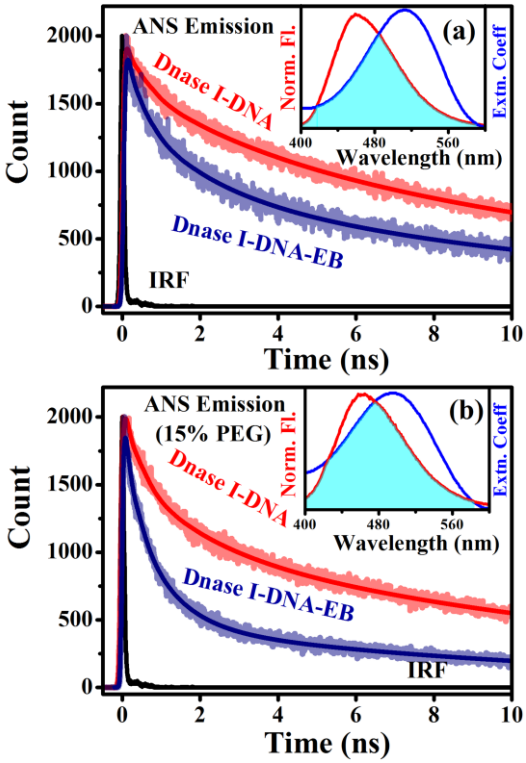

Figure 8.5. *Picosecond-resolved transients of the donor (ANS-DNase I-DNA complex) in the absence and presence of the acceptor (EB) in DNA in (a) 0 wt% PEG and (b) 15 wt% PEG. Insets depict the corresponding spectral overlap between donor (ANS-DNase I-DNA complex) emission and acceptor (ANS-DNase I with EB-bound DNA) absorbance.*

profound effect on protein conformational stability and dynamics [40-42]. As in our studies the changes in catalytic activity induced by PEG are not accompanied by change in conformation hence, in order to confirm the modification of the enzyme's dynamics with the addition of PEG, we measured the temporal anisotropy decay, r(t), of the probe ANS bound to DNase I in buffer and in presence of 15 wt% PEG concentrations. ANS in buffer exhibits a fast single exponential rotational decay [43] (inset of Figure 8.6.a), on the other hand the rotational relaxation of ANS bound to DNase I and upon

complexation with DNA has been found to be bi-exponential with comparable time constant, attributing that dynamics of DNase I was insignificantly perturbed when it form complex with DNA (Figure 8.6.a and Figure 8.6.b). Further, with the addition of PEG to ANS-DNase I complex, the components of

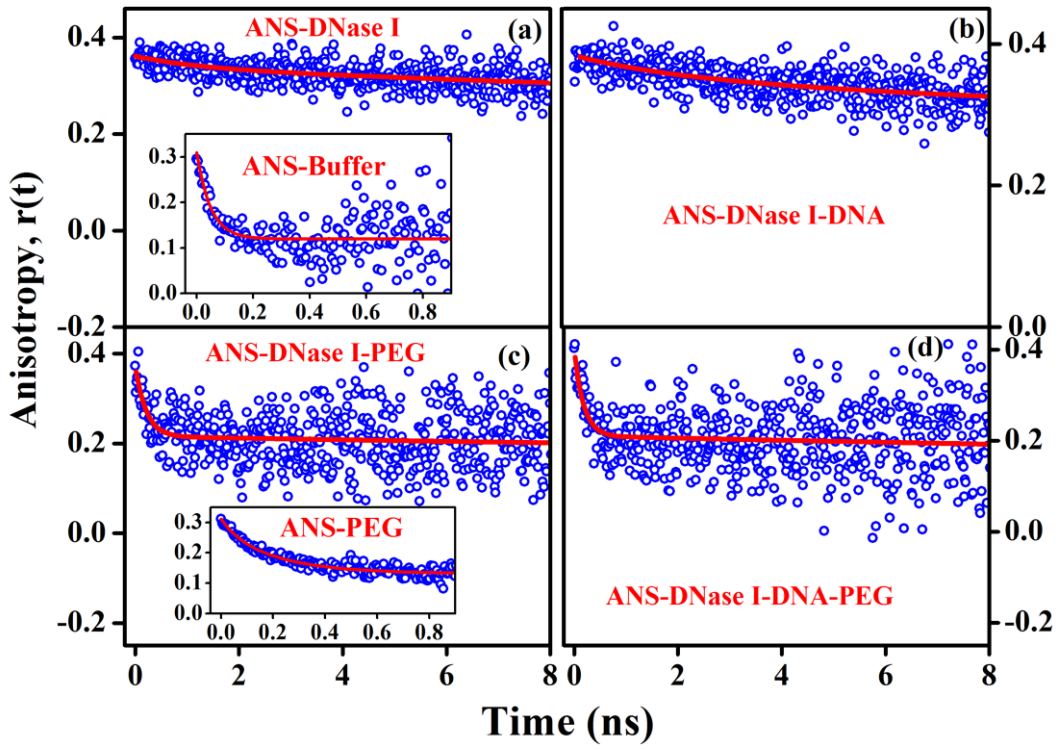

Figure 8.6. *Time-resolved anisotropy of ANS bound to DNase I in presence of (a) 0 wt% PEG and (c) 15 wt% PEG. Inset shows the corresponding time-resolved anisotropy of free ANS. Time-resolved anisotropy of ANS bound to DNase I in the presence of DNA in (b) 0 wt% PEG and (d) 15 wt% PEG.*

local and global tumbling motion of probe get faster indicating a greater contribution from the bulk type of water molecules in the proximity of the probe. However, ANS is still bound to the enzyme is evident from the presence of a slow component which was not found in 15 wt% PEG solution without the enzyme as shown in inset of Figure 8.6.c and Table 8.3. Similarly when ANS-DNase I formed complex with DNA in presence of PEG the rotational relaxation time constant of ANS was found to be insignificantly perturb in comparison to the rotational relaxation time constant of probe in ANS-DNase I complex (Figure 8.6.d). This observation clearly indicates that, flexibility of ANS attached to hydrophobic core of DNase I is much higher in presence of

PEG compared to in absence of PEG. It is worth mentioning that the result obtain from rotational dynamic of enzymes is also corroborated by time resolved measurement.

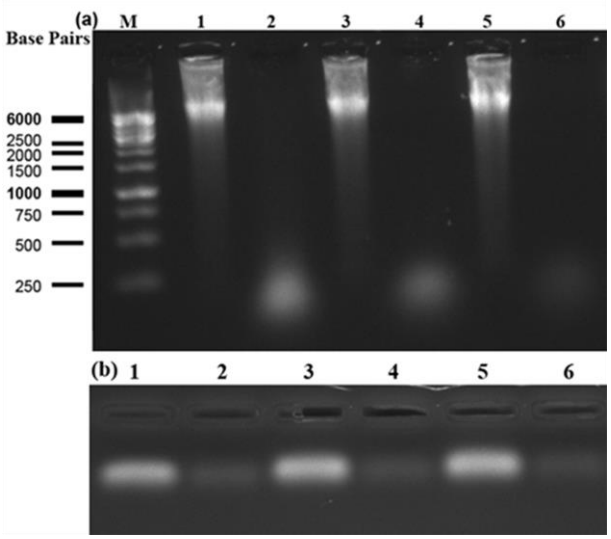

Figure 8.7. *(a) Hydrolysis of calf thymus DNA by DNase I at 25 ^{0}C. Lane M shows the DNA size marker. Lanes 1, 3 and 5 show DNA in presence of 0, 5 and 15 wt% PEG. Lanes 2, 4 and 6 shows hydrolysis by DNase I in the presence of 0, 5 and 15 wt% PEG. (b) Hydrolysis of a short oligonucleotide DNA (20-mer dsDNA) by DNase I at 25 ^{0}C. Lanes 1, 3 and 5 shows DNA in presence of 0, 5 and 15 wt% PEG. Lanes 2, 4 and 6 shows hydrolysis by DNase I in presence of 0, 5 and 15 wt% PEG.*

The effect of molecular crowding on the catalytic activity of DNase I was also analysed using agarose gel electrophoresis. Initially we examined the hydrolysis of larger genomic DNA (calf thymus) by DNase I at 25 ^{0}C in absence and presence of different PEG concentration. Before hydrolysis by DNase I the migration of substrate DNA in absence and presence of 5 and 15 wt% PEG were found to be same (Figure 8.7.a), validate PEG does not significantly affect the stability of DNA (lane 1, 3 and 5). Migration of bands were found to be faster (lane 2, 4 and 6) upon hydrolysis with DNase I with respect to substrate corroborate the formation of degraded product from the substrate. The diffused band of degraded product in absence of PEG were found to be smeared and of higher intensity, however, the smearing and intensity of bands were found to be decreased as the PEG wt% was increased corroborate the formation of higher degraded product from the substrate in presence of molecular crowding. To evaluate the effect of molecular crowding on

hydrolysis of short DNA using agarose gel electrophoresis, 20-mer dsDNA was used as a substrate shown in Figure 8.7.b. Like genomic DNA, the migration of

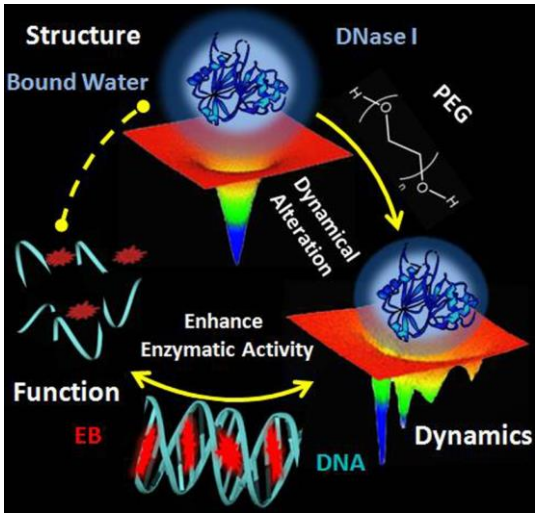

Scheme 8.1. *Schematic representation of the correlation between dynamics and function of DNase I in presence of PEG as molecular crowding.*

20-mer dsDNA was also found to be same in absence and presence of 5 and 15 wt% PEG (lane 1, 3 and 5). Upon hydrolysis by DNase I the intensity of substrate DNA was decreased as concentration of molecular crowding was increasing (lane 2, 4 and 6). The result shows that dsDNA hydrolysis by DNase I was greatly enhanced by the addition of 5 and 15 wt% PEG. Overall, molecular crowding increases the cleavage yield of DNase I not only for the large DNA (calf thymus) but also for the short (20-mer) DNA oligonucleotide.

8.3. Conclusion: Our results reveal that the enzymatic activity of DNase I has been increased in presence of a molecular crowding agent, PEG 3350. While, steady state and ultrafast time resolved spectroscopy on a florescence probe EB intercalated to substrate DNA reveal the hydrolysis of the substrate by DNase I, the spectroscopic information including picosecond resolved fluorescence polarization gated studies on the enzyme-bound fluorescence probe ANS shows enhanced surface flexibility of DNase I in the presence of PEG. The reduced water activity at the enzyme surface due to osmotic stress of the molecular crowding agent enhancing the dynamical flexibility of the

enzyme is concluded to increase the DNA binding eventually accelerate the hydrolysis reaction of DNase I. In summary the study attempts to unravel the molecular picture of DNA hydrolysis by an endonuclease in presence of an osmotic stress generating molecular crowding agent. A clear correlation of the flexibility of the endonuclease with the rate of DNA hydrolysis within the overall structural integrity of the enzyme has also been established.

References

[1] A.B. Fulton, How crowded is the cytoplasm? Minireviews, *Cell,* 30 (1982) 345-347.

[2] R.J. Ellis, Macromolecular crowding: Obvious but underappreciated, *Trends Biochem. Sci.,* 26 (2001) 597-604.

[3] L. Homchaudhuri, N. Sarma, R. Swaminathan, Effect of crowding by dextrans and Ficolls on the rate of alkaline phosphatase–catalyzed hydrolysis: A size-dependent investigation, *Biopolymers,* 83 (2006) 477-486.

[4] N. Muramatsu, A.P. Minton, Tracer diffusion of globular proteins in concentrated protein solutions, *Proc. Natl. Acad. Sci. U.S.A.,* 85 (1988) 2984-2988.

[5] M. Arrio-Dupont, G. Foucault, M. Vacher, P.F. Devaux, S. Cribier, Translational diffusion of globular proteins in the cytoplasm of cultured muscle cells, *Biophys. J.,* 78 (2000) 901-907.

[6] C. Balcells, I. Pastor, E. Vilaseca, S. Madurga, M. Cascante, F. Mas, Macromolecular crowding effect upon in vitro enzyme kinetics: Mixed activation–diffusion control of the oxidation of NADH by pyruvate catalyzed by lactate dehydrogenase, *J. Phys. Chem. B,* 118 (2014) 4062-4068.

[7] M. Weiss, M. Elsner, F. Kartberg, T. Nilsson, Anomalous subdiffusion is a measure for cytoplasmic crowding in living cells, *Biophys. J.,* 87 (2004) 3518-3524.

[8] H.-X. Zhou, G. Rivas, A.P. Minton, Macromolecular crowding and confinement: Biochemical, biophysical, and potential physiological consequences, *Annu. Rev. Biophys.,* 37 (2008) 375.

[9] N. Kozer, G. Schreiber, Effect of crowding on protein–protein association rates: Fundamental differences between low and high mass crowding agents, *J. Mol. Biol.,* 336 (2004) 763-774.

[10] A.P. Minton, Influence of macromolecular crowding upon the stability and state of association of proteins: predictions and observations, *J. Pharm. Sci.,* 94 (2005) 1668-1675.

[11] H. Dong, S. Qin, H.-X. Zhou, Effects of macromolecular crowding on protein conformational changes, *PLoS Comput. Biol.,* 6 (2010) 1-10.

[12] N. Chebotareva, B. Kurganov, N. Livanova, Biochemical effects of molecular crowding, *Biochemistry (Mosc.)*, 69 (2004) 1239-1251.

[13] S.-i. Nakano, D. Miyoshi, N. Sugimoto, Effects of molecular crowding on the structures, interactions, and functions of nucleic acids, *Chem. Rev.*, 114 (2013) 2733-2758.

[14] V. Parsegian, R. Rand, D. Rau, Osmotic stress, crowding, preferential hydration, and binding: a comparison of perspectives, *Proc. Natl. Acad. Sci. U.S.A.*, 97 (2000) 3987-3992.

[15] M.J. Blandamer, J.B. Engberts, P.T. Gleeson, J.C.R. Reis, Activity of water in aqueous systems; a frequently neglected property, *Chem. Soc. Rev.*, 34 (2005) 440-458.

[16] B. Schneider, H.M. Berman, Hydration of the DNA bases is local, *Biophys. J.*, 69 (1995) 2661.

[17] D. Homouz, M. Perham, A. Samiotakis, M.S. Cheung, P. Wittung-Stafshede, Crowded, cell-like environment induces shape changes in aspherical protein, *Proc. Natl. Acad. Sci. U.S.A.*, 105 (2008) 11754-11759.

[18] A.P. Minton, Implications of macromolecular crowding for protein assembly, *Curr. Opin. Struct. Biol.*, 10 (2000) 34-39.

[19] D.K. Eggers, J.S. Valentine, Molecular confinement influences protein structure and enhances thermal protein stability, *Prot. Sci.*, 10 (2001) 250-261.

[20] E. Bismuto, P.L. Martelli, A. De Maio, D.G. Mita, G. Irace, R. Casadio, Effect of molecular confinement on internal enzyme dynamics: Frequency domain fluorometry and molecular dynamics simulation studies, *Biopolymers*, 67 (2002) 85-95.

[21] S.B. Zimmerman, Macromolecular crowding effects on macromolecular interactions: some implications for genome structure and function, *Biochim. Biophys. Acta, Gene Struct. Expression*, 1216 (1993) 175-185.

[22] S.B. Zimmerman, A.P. Minton, Macromolecular crowding: Biochemical, biophysical, and physiological consequences, *Annu. Rev. Biophys. Biomol. Struct.*, 22 (1993) 27-65.

[23] S.B. Zimmerman, B.H. Pheiffer, Macromolecular crowding allows blunt-end ligation by DNA ligases from rat liver or Escherichia coli, *Proc. Natl. Acad. Sci. U.S.A.*, 80 (1983) 5852-5856.

[24] Y. Sasaki, D. Miyoshi, N. Sugimoto, Regulation of DNA nucleases by molecular crowding, *Nuc. Acids Res.*, 35 (2007) 4086-4093.

[25] M. Gueroult, D. Picot, J. Abi-Ghanem, B. Hartmann, M. Baaden, How cations can assist DNase I in DNA binding and hydrolysis, *PLoS Comput. Biol.*, 6 (2010) 1-11.

[26] P. Singh, S. Choudhury, S. Dutta, A. Adhikari, S. Bhattacharya, D. Pal, S.K. Pal, Ultrafast spectroscopy on DNA-cleavage by endonuclease in molecular crowding, *Int. J. Biol. Macromol.*, 103 (2017) 395-402.

[27] S.B. Zimmerman, B. Harrison, Macromolecular crowding increases binding of DNA polymerase to DNA: An adaptive effect, *Proc. Natl. Acad. Sci. U.S.A.*, 84 (1987) 1871-1875.

[28] J.R. Wenner, V.A. Bloomfield, Crowding effects on EcoRV kinetics and binding, *Biophys. J.*, 77 (1999) 3234-3241.

[29] X. Su, C. Zhang, X. Zhu, S. Fang, R. Weng, X. Xiao, M. Zhao, Simultaneous fluorescence imaging of the activities of DNases and 3′ exonucleases in living cells with chimeric oligonucleotide probes, *Anal. Chem.*, 85 (2013) 9939-9946.

[30] P.K. Verma, S. Rakshit, R.K. Mitra, S.K. Pal, Role of hydration on the functionality of a proteolytic enzyme α-Chymotrypsin under crowded environment, *Biochimie*, 93 (2011) 1424-1433.

[31] M.T. Morán-Zorzano, A.M. Viale, F.J. Muñoz, N. Alonso-Casajús, G.G. Eydallín, B. Zugasti, E. Baroja-Fernández, J. Pozueta-Romero, Escherichia coli AspP activity is enhanced by macromolecular crowding and by both glucose-1, 6-bisphosphate and nucleotide-sugars, *FEBS Lett.*, 581 (2007) 1035-1040.

[32] K. Ajtai, S.Y. Venyaminov, CD study of the actin DNase I complex, *FEBS Lett.*, 151 (1983) 94-96.

[33] Y.M. Evdokimov, T. Pyatigorskaya, O. Polyvtsev, N. Akimenko, V. Kadykov, D.Y. Tsvankin, Y.M. Varshavsky, A comparative X-ray diffraction

and circular dichroism study of DNA compact particles formed in water-salt solutions, containing poly (ediylene glycol), *Nuc. Acids Res.,* 3 (1976) 2353-2366.

[34] C. N'Soukpoe-Kossi, S. Diamantoglou, H. Tajmir-Riahi, DNase I-DNA interaction alters DNA and protein conformations, *Biochem. Cell Biol.,* 86 (2008) 244-250.

[35] D. Dalglkish, A. Peacocke, G. Fey, C. Harvey, The circular dichroism in the ultraviolet of aminoacridines and ethidium bromide bound to DNA, *Biopolymers,* 10 (1971) 1853-1863.

[36] R. Sarkar, S.K. Pal, Ligand–DNA interaction in a nanocage of reverse micelle, *Biopolymers,* 83 (2006) 675-686.

[37] S. Choudhury, S. Batabyal, P.K. Mondal, P. Singh, P. Lemmens, S.K. Pal, Direct observation of kinetic pathways of biomolecular recognition, *Chem. Eur. J.,* 21 (2015) 16172-16177.

[38] Y. Qin, L. Wang, D. Zhong, Dynamics and mechanism of ultrafast water–protein interactions, *Proc. Natl. Acad. Sci. U.S.A.,* 113 (2016) 8424-8429.

[39] N. Nandi, B. Bagchi, Dielectric relaxation of biological water, *J. Phys. Chem. B,* 101 (1997) 10954-10961.

[40] J. Partridge, P.R. Dennison, B.D. Moore, P.J. Halling, Activity and mobility of subtilisin in low water organic media: Hydration is more important than solvent dielectric, *Biochim. Biophys. Acta, Protein Struct. Mol. Enzymol.,* 1386 (1998) 79-89.

[41] Y. Pocker, Water in enzyme reactions: Biophysical aspects of hydration-dehydration processes, *Cell. Mol. Life Sci.,* 57 (2000) 1008-1017.

[42] J. Kornblatt, M. Kornblatt, Water as it applies to the function of enzymes, *Int. Rev. Cytol.,* 215 (2002) 49-73.

[43] S.K. Pal, J. Peon, A.H. Zewail, Ultrafast surface hydration dynamics and expression of protein functionality: α-Chymotrypsin, *Proc. Natl. Acad. Sci. U.S.A.,* 99 (2002) 15297-15302.

Chapter 9

Spectroscopic Studies on Biomolecular Recognition of an Enzyme in a Model Engineered Environment

9.1. Introduction: Enzymes are one of the most efficient catalysts known to date, enhancing the rate of a biochemical reaction by several orders of magnitude compared to uncatalyzed reactions [1, 2]. Enzyme mediated catalysis is attributed to direct structural interaction between the enzyme and the substrate through the 'induced fit' [3] or the 'conformational selection' [4-6] mechanisms, emphasizing the role of protein conformational transitions from unbound form of the enzyme to its ligand-bound forms [7, 8]. In the induced fit model, the ligand first binds loosely to the protein followed by a conformational relaxation in the macromolecule to give the final complex (Scheme 9.1). As for the conformational selection model, intrinsic dynamics of the protein structure causes a conformational transition in the macromolecule *prior* to ligand binding from the unbound-ground state conformation to a higher-energy conformation, to which the ligand then binds leading to the formation of the final protein-ligand complex (Scheme 9.1). Thus, dynamic nature of the protein structure plays a crucial role in enzyme catalysis through molecular recognition and substrate binding [9, 10]. Water plays a critical role in protein dynamics, because, conformational fluctuations result in large-scale protein motions, which are slaved or coupled to water motions [11-13]. Therefore, water dynamics likely plays a major role in the enzyme catalysis. It has been recently shown that slow water dynamics owing to coupled protein-water motions assist enzyme-substrate interactions leading to the formation of productive Michaelis complex during an enzymatic reaction [14]. In our recent study [15], two different pathways of molecular recognition, namely,

conformational selection and induced-fit mechanisms were recognized for the interaction of an enzyme α-Chymotrypsin with 8-anilino-1-naphthalenesulfonic acid ammonium salt at two different pH in a microfluidic channel. Whereas structural flexibility of the enzyme at pH 6.3 triggered conformational selections, restricted protein motion at pH 3.6 prompted the protein to adopt an induced-fit type of molecular recognition. However, experimental informations on correlating water dynamics and protein functional motion to enzymatic turnover is sparse [16-18]. Thus, it would be an intriguing to explore whether the contribution of water dynamics in large-scale protein motions might be essential to understand molecular recognition and substrate binding in enzyme mediated catalysis.

Here, we have explored the correlation between the dynamics of water molecules and the pathway of molecular recognition between an enzyme α-chymotrypsin (CHT) and a substrate Ala-Ala-Phe-7-amido-4-methylcoumarin (AMC) in the nanoscopic domain of the cationic reverse micelles of Benzyl-n-hexadecyldimethylammonium chloride (BHDC) and the anionic reverse micelles of Sodium bis (2-ethylhexyl) sulfosuccinate (AOT). We have directly monitored the interaction of CHT with AMC in a microfluidic channel equipped with a microscopic and spectroscopic attachment in conjunction with time-resolved fluorescence measurements of a polar fluorophore, Acedan (AC1), to probe the dynamics of nanoscopic water molecules confined within the reverse micelles. MIR FTIR spectroscopic measurements were also carried out to probe the structure of the water molecules confined within the core of the reverse micelles. From the kinetic profiles of fluorescence enhancement in the microfluidics channel, two distinct kinetic pathways of recognition between the enzyme (CHT) and the substrate (AMC) are manifest in two oppositely charged reverse micelles. Investigation of the kinetics of enzyme-substrate interactions in a microfluidic channel, in concert with FTIR and time-resolved fluorescence measurements, establish that modulation of the nanoscopic water dynamics is responsible for the manifestation of two different pathways of

molecular recognition in two oppositely charged reverse micelles of BHDC and AOT. This becomes further manifest in neutral reverse micelles of Brij-30 and Triton X-100. In the former, faster water dynamics aids the 'conformational selection' pathway, whereas in the latter significantly slower dynamics of water molecules become conducive to an 'induced fit' mechanism in the enzyme-substrate interaction.

9.2. Results and Discussion:

9.2.1. Modulation of Kinetic Pathways of Enzyme-Substrate Interaction in a Microfluidic Channel: Nanoscopic Water Dynamics as a Switch [19]: Figure 9.1.a shows the fluorescence micrographs of the microfluidics channel in the

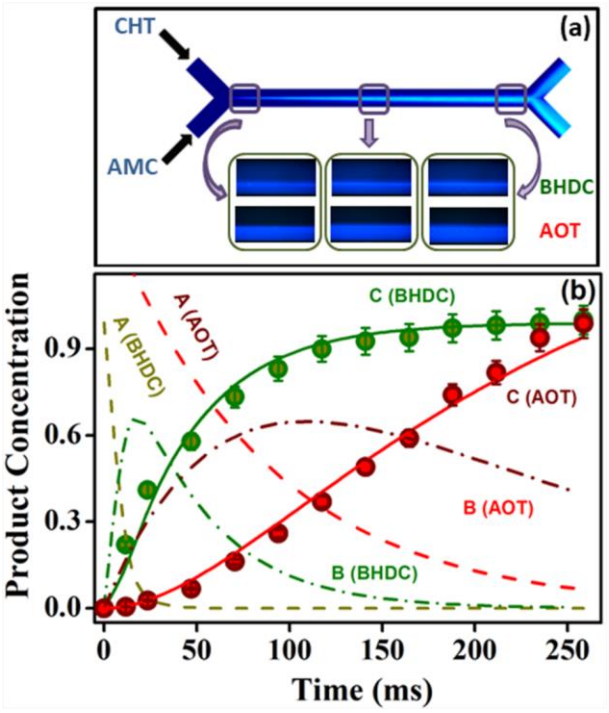

Figure 9.1. *The fluorescence and kinetic profile of hydrolysis of AMC catalysed by CHT are compared in presence of cationic (BHDC) and anionic (AOT) reverse micelles. (a) Micrographs of the microfluidics channel at different positions along the channel. (b) Evolution of the fluorescence intensity due to hydrolysis of AMC catalysed by CHT along the microfluidics channel (solid lines) (5% error bar). The substrate (A) and intermediate (B) concentrations are shown with dashed (----) and dashed-dotted lines (-...-..), respectively (5% error).*

cationic (BHDC/benzene) and the anionic (AOT/benzene) reverse micelles. The blue–cyan emission from the AMC–CHT complex increases along the

channel, because, the substrate (AMC) and the enzyme (CHT) have time to mix to form the AMC–CHT complex. Two distinct pathways are evident from the time-dependent fluorescence profiles along the microchannel (Figure 9.1.b). To explain the observed data, a simple kinetic scheme A→B→C is considered, for conversion of the unbound (without AMC) form of the enzyme (A) to the final CHT-AMC complex (C) via the intermediate (B) state of CHT with AMC, formed immediately following recognition. We have made two important approximations for the first order rate constants, k_1 and k_2, in the above

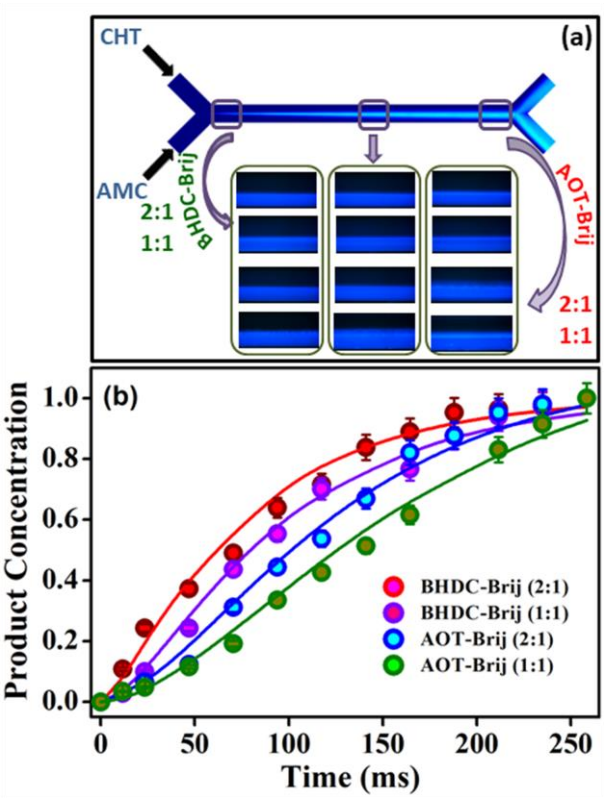

Figure 9.2. *Effect of the non-ionic surfactants (Brij 30) on the fluorescence kinetic profile in cationic (BHDC) and anionic (AOT) reverse micelles. (a) Micrographs of the microfluidics channel at different positions along the channel with different concentrations of non-ionic surfactant. (b) Comparison of normalised fluorescence intensity upon catalysis by CHT along the microfluidics channel at different concentration of non-ionic surfactants in cationic (BHDC) and anionic (AOT) reverse micelles (5% error bar).*

scheme. First of all, k_1 may be approximated as a pseudo-first-order rate constant since the enzyme concentration (CHT) was much larger than that of the substrate (AMC). Secondly, the rate of the reverse reaction is assumed to be slow enough to consider the two consecutive reactions to be irreversible, which

is in agreement with a steady-state approximation for the system. As a consequence, the time evolution of [C] can be expressed via equation 2.67, [20]. Numerical fitting of the experimental data with equation 2.67 reveals reasonable agreement with the proposed model for the formation of an intermediate-state complex (B). Whereas, k_1 and k_2 values (Table 9.1) for the cationic (BHDC/Benzene) reversemicelle were found to be 180 and 23.5 s^{-1}, respectively, those for the anionic (AOT/Benzene) reverse micelle are 11.9 and

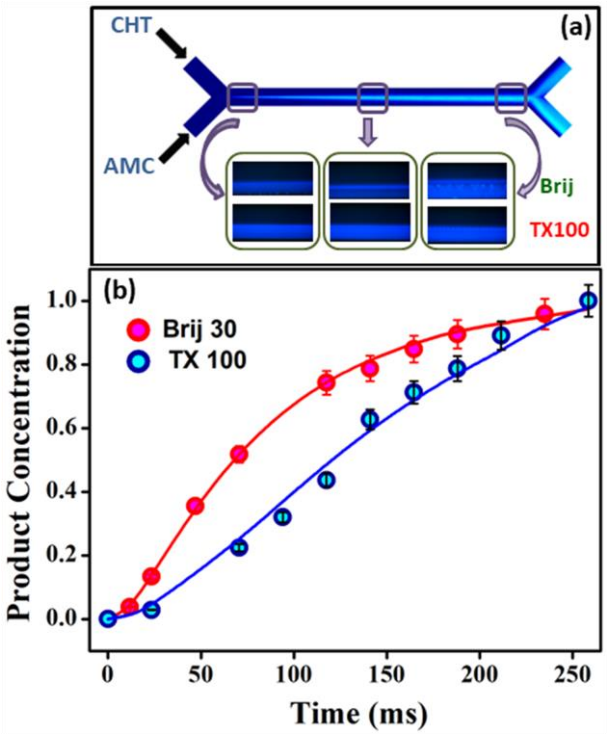

Figure 9.3. *The fluorescence and kinetic profile of hydrolysis of AMC catalysed by CHT are compared in presence of Brij 30 and TX-100 reverse micelles. (a) Micrographs of the microfluidics channel at different positions along the channel. (b) Evolution of the fluorescence intensity due to hydrolysis of AMC catalysed by CHT along the microfluidics channel (solid lines).*

7.0 s^{-1}. It is pertinent to mention that similar time constants (k_1 ~ 170 s^{-1} and k_2 ~ 24 s^{-1}) were also obtained for cationic (BHDC/Benzene) reverse micelle using another software (microcal-origin). In the cationic reverse micelle (BHDC/Benzene), first A transforms into B quite rapidly and B accumulates because it disappears slowly ($k_1 >> k_2$). As the concentration of A decreases, its rate of transformation into B decreases as well; at the same time the rate of

conversion of B to C increases as more B is formed with progress in time. As long as $k_1 \neq k_2$, the concentration of B decreases as shown in Figure 9.1.b. The kinetic signatures in the cationic RM (BHDC/benzene) indicate that the substrate AMC binds rapidly to an active conformation of the enzyme CHT to form a complex, which then undergoes structural reorganization to the final form of the CHT-AMC complex. This is consistent with molecular recognition of the enzyme by the substrate via the 'conformational selection' fit mechanism [21, 22]. From the magnitude of the pseudo-first-order reaction rate constant, the value of the corresponding second-order rate constant is found to be $1.8X10^7\ M^{-1}\ s^{-1}$ which agrees well with that ($\sim10^7\ M^{-1}\ s^{-1}$) for the interaction of ANS with CHT at pH 6.3 [15]. The first order rate constant, k_2, for structural reorganization of the enzyme is also of the same order as reported ($\sim10–100\ s^{-1}$) earlier [15, 21]. In the case of anionic reverse micelle (AOT/Benzene), the pseudo-first-order rate constant, k_1, is much smaller (Table 9.1) than that for the cationic reverse micelle and the estimated second-order rate constant is about $1.1X10^5\ M^{-1}\ s^{-1}$, which is consistent with weak binding interaction of AMC with CHT in the first stage [15, 21]. In the second step, structural reorganization is associated with a time constant (k_2) nearly 3-fold smaller than that for the cationic reverse micelles. Thus, the molecular recognition pathway in the anionic reverse micelle of AOT involves much weaker binding interaction between AMC and CHT in the first step than the cationic reverse micelle, followed by complexation through slow structural reorganization and is consistent with the induced-fit mechanism [3, 15].

The difference in the kinetic pathways of molecular recognition of the enzyme (CHT) by the substrate (AMC) between the cationic (BHDC/benzene) and the anionic (AOT/benzene) reverse micelles is quite intriguing and indicates a possible role of water dynamics in dictating the mechanism of recognition, given that the dynamics of water molecules in the nanoscopic domain of the anionic reverse micelles are significantly different from that of the cationic reverse micelles [22, 23]. Thus, it becomes necessary to probe further the role of water dynamics in dictating the kinetic pathways of

molecular recognition between CHT and AMC. For this purpose, we have monitored the binding interaction of CHT with AMC in the mixed cationic (BHDC/Brij-30) and mixed anionic (AOT/Brij-30) reverse micelles with a non-ionic surfactant (Brij-30), because, Brij-30 is known to modulate the dynamics and reactivity of water molecules within the core of the AOT-reverse micelles [24].

Table 9.1. *Numerically fitted kinetic parameters for enzyme-substrate interaction.*

Systems	k_1 [s^{-1}]	k_2 [s^{-1}]
BHDC	180.0± 9.0	23.5± 1.1
BHDC-Brij (2:1)	134.1± 6.7	14.0± 0.8
BHDC-Brij (1:1)	50.0± 3.5	12.9± 0.9
AOT	11.9± 0.9	7.0± 0.5
AOT-Brij (2:1)	16.9± 1.0	8.2± 0.6
AOT-Brij (1:1)	23.6± 1.6	10.5± 0.5
Brij 30	89.7± 7.1	11.3± 0.7
TX-100	12.2± 1.0	8.34± 0.4

In addition, we have probed the enzyme-substrate interactions in neutral reverse micelles of Brij-30 (benzene) and TX-100 (cyclohexane :benzene) (1:1) at the same W_0 value (= 8) as that for the other reverse micelles. Figure 9.2.a displays the fluorescence micrographs of the microfluidics channel at different mole fractions of the non- ionic surfactant. It becomes evident from the changes in the kinetic profiles of Figure 9.2.b along with changes in the values of k_1 and k_2 (k_1~50.0 s^{-1}, k_2~12.9 s^{-1}) that the nature of recognition of AMC by CHT in the enzymatic catalysis shifts from 'conformational selection fit' in pure BHDC reverse micelles to that of the induced-fit mechanism in the mixed cationic reverse micelles of BHDC/Brij-30 (1:1). On the other hand, the change in kinetic profiles (Figure 9.2.b) as well as k_1 and k_2 values (Table 9.1) in going from pure AOT to that of mixed anionic reverse micelles (AOT/Brij-30 = 1:1) is indicative of a shift in recognition from an 'induced fit' mechanism to that of 'conformational selection' in the enzyme-substrate interaction. These

observations led us to conjecture that modulation of the dynamics of water molecules upon incorporation of a non-ionic surfactant (Brij-30) likely modulates the kinetic pathway of molecular recognition of CHT by AMC from

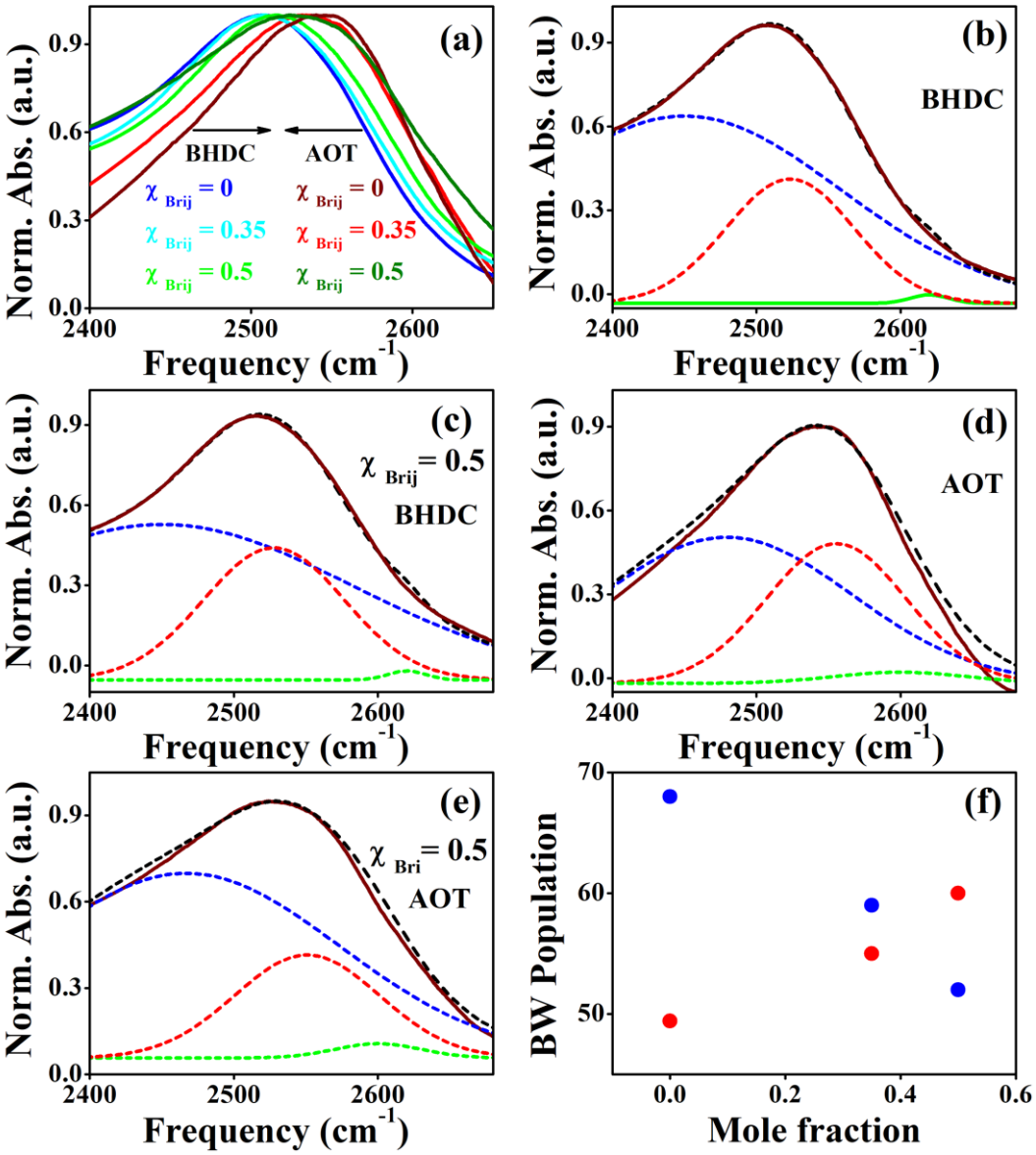

Figure 9.4. *(a) FTIR absorption spectra of the OD stretch of HOD in water for reverse micelles at different mole fractions of Brij-30. FTIR spectrum in (b) BHDC reverse micelles (c) BHDC reverse micelles in presence of Brij-30, (d) AOT reverse micelle and (e) AOT reverse micelle in presence of Brij-30. The spectrum is deconvoluted into three Gaussian curves peaking at 2450 cm-1 (blue), 2554 cm-1 (red) and ~2620 cm-1 (green).(f) Relative population of bound water for AOT (blue) and BHDC (red) as a function of Brij-30 mole fraction.*

those in the pure ionic reverse micelles. Our conjecture is further corroborated by an inspection of the kinetic profiles (Figure 9.3) and the rate constant values (k_1 and k_2) corresponding to enzyme-substrate interactions in the neutral

reverse micelles of Brij-30 and TX-100. In case of Brij-30, the kinetic profile as well as significantly larger k_1 value (k_1>>k_2, Table 9.1) is indicative of the 'conformational selection' fit mechanism. As for the reverse micelles of TX-100, the kinetic profile is distinctly different from that in Brij-30 (Figure 9.3.b) and the values of the rate constants (k_1 and k_2) are close to each other which is consistent with an 'induced fit' model for interaction of the enzyme (CHT) with the substrate (AMC) [3, 15]. As a consequence of the observed difference in molecular recognition of the substrate by the enzyme in different types of reverse micelles it becomes imperative to investigate both the physical properties and the dynamics of water molecules entrapped within the core of the reverse micelles.

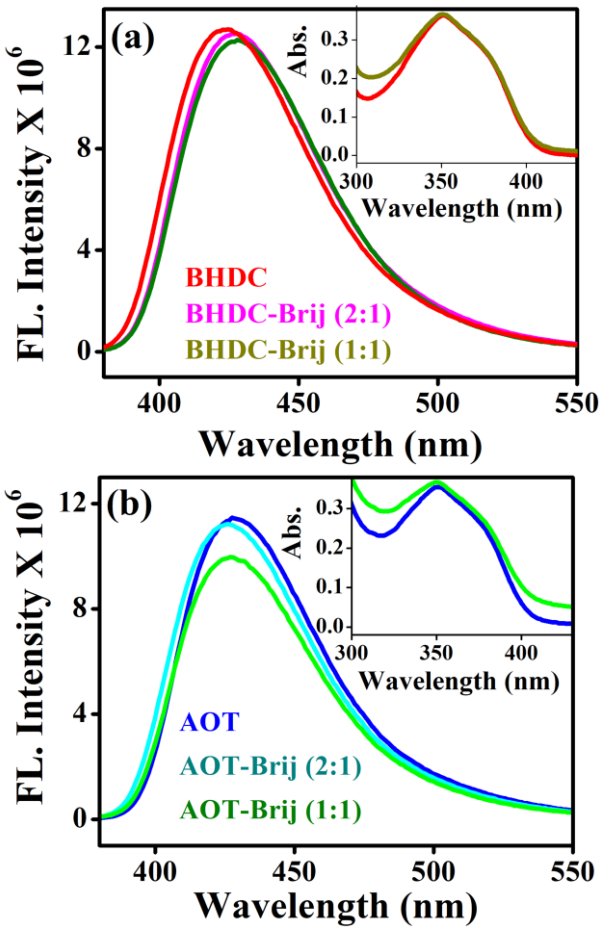

Figure 9.5. *Fluorescence emission spectra of AC1 in reverse micelles (20mM) at different mole fractions of Brij-30 i.e. (a) BHDC reverse micelle and (b) AOT reverse micelles. Inset depicts the corresponding absorption spectra of AC1 in mixed reverse micelles.*

In this regard, measurements of the OD stretching modes by FTIR provide information on the physical properties of water molecules entrapped within the core of the cationic and the anionic RMs in absence and presence of Brij-30. Figure 9.4.a displays the OD stretching of HOD in the cationic RM (BHDC/Benzene) at different mole-fractions (X_{brij}) of Brij-30. Pure water shows an absorption peak at 2505 cm^{-1}, which undergoes a progressive blue shift along with asymmetric deformation of the absorption profile when encapsulated in reverse micelles. The blue shift in the absorption peak is found to be higher in the anionic (AOT) reverse micelles than the cationic (BHDC) reverse micelles. In reverse micelles the FTIR absorption curves are broadened

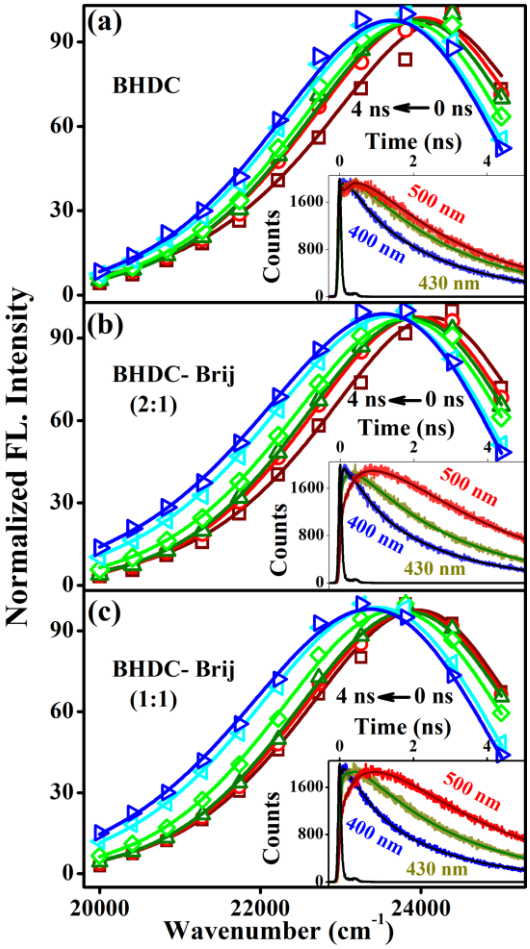

Figure 9.6. *Time-resolved emission spectra (TRES) of AC1 in BHDC reverse micelles in presence of different mole fraction of Brij-30 (a) 0, (b) 0.35 and (c) 0.5. Insets display picosecond-resolved emission transients of AC1 at three different wavelengths.*

and could be deconvoluted into three Gaussian sub-bands peaking at 2640 ± 10, 2545 ± 5 and 2450 cm^{-1}, respectively. The deconvolution of the FTIR spectra is displayed in Figure 9.4.(b-e) for pure BHDC, pure AOT as well as those in the presence of Brij-30. According to the 'three states model', the water in the nanoscopic domain of reverse micelles is identified as free water (FW), bound water (BW) and trapped water (TW) molecules [25]. The FW molecules (~2450 cm^{-1}), occupying the cores of the water pool of the reverse micelles engage in strong hydrogen bonding interaction with the neighbouring water molecules.

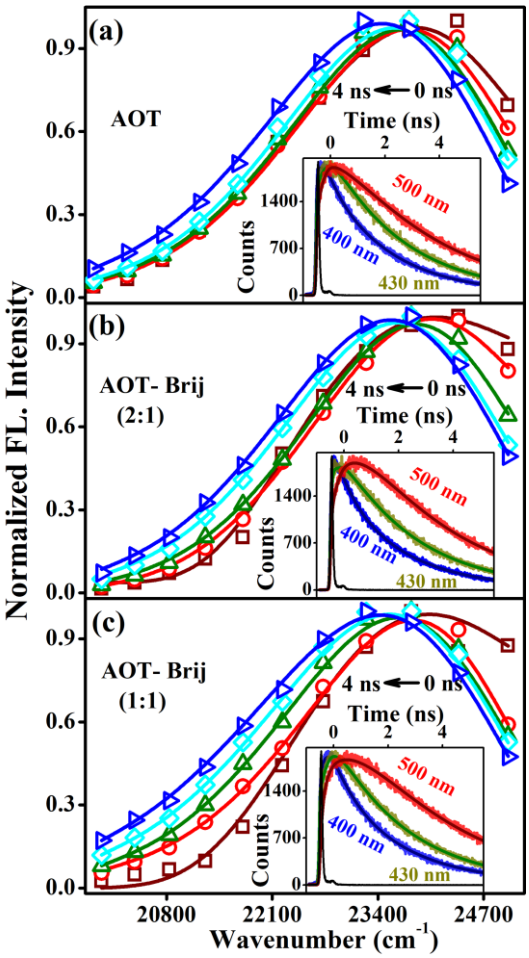

Figure 9.7. *Time-resolved emission spectra (TRES) of AC1 in AOT reverse micelles in presence of different mole fractions of Brij-30 (a) 0, (b) 0.35 and (c) 0.5. Insets depict picosecond-resolved fluorescence transients of AC1 at three different wavelengths.*

The second component peaking at ~2545 cm^{-1} involves the so-called bound water (BW) molecules incapable of forming fully developed hydrogen bonds and bound to the surfactant headgroups. The third type of water molecules

absorbing in the high-frequency region (~2640 cm^{-1}) is generally dispersed among the long hydrocarbon chains of the surfactant molecules. The relative area contribution of the BW towards the total spectra are calculated and shown as a function of the mole fraction of Brij-30 (Figure 9.4.f). In comparison to BHDC, a high abundance of the BW is observed in the case of the AOT reverse micelles. The relative abundance of the BW decreases for AOT, while that for BHDC increases with increasing mole-fraction of Brij-30. The relative abundance of the bound water molecules and its' variation in presence of a non-ionic surfactant likely affects the dynamics of water molecules within the reverse micelle core owing to the coupled nature of water and surfactant molecules [26].

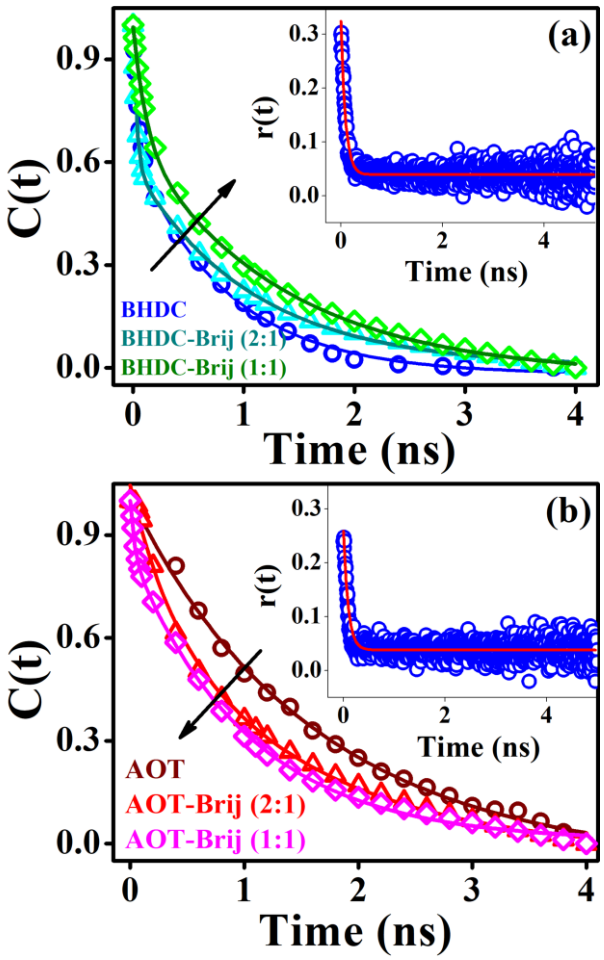

Figure 9.8. *(a) Solvation correlation function of AC1 in BHDC reverse micelles at different molar fraction of Brij-30. (b) Solvation correlation function of AC1 in AOT reverse micelles at different molar fraction of Brij-30. Inset depicts corresponding temporal decay of fluorescence anisotropy, r(t), of AC1 in BHDC and AOT reverse micelles.*

In order to probe the dynamics of water molecules entrapped within the core of reverse micelles, time-resolved fluorescence of AC1 dye were monitored. Figure 9.5.a and Figure 9.5.b exhibit the steady state emission spectra of AC1 in the reverse micelles of BHDC and AOT, respectively. The fluorescence peak maximum of AC1 in pure water (~515 nm, data not shown) is significantly blue shifted to 424 nm and 427 nm, respectively, in the reverse micelles (w_0 = 8) of BHDC/Benzene and AOT/Benzene, respectively. The observed blue shift in the cationic (BHDC/Benzene) reverse micelles relative to the anionic (AOT/benzene) likely originates from reduced polarity of its interface compared to the latter. However, upon the addition of Brij-30 to both BHDC and AOT reverse micelles, an insignificant shift in the emission peak maximum is observed.

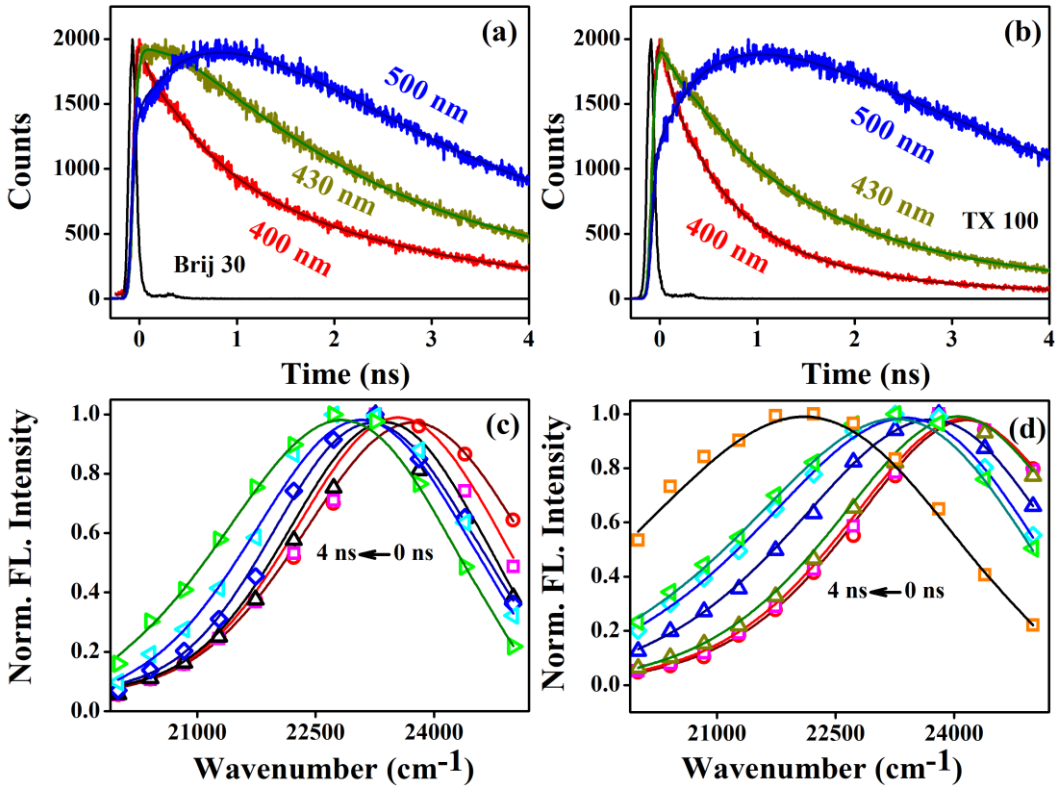

Figure 9.9. *Picosecond-resolved emission transients of AC1 at three different wavelengths in (a) Brij 30 and (b) TX-100 reverse micelles. Time-resolved emission spectra (TRES) of AC1 in (c) Brij 30 reverse micelles and (d) TX-100 reverse micelles.*

Inset of Figures 9.6 and Figure 9.7 display wavelength-dependent fluorescence transients of AC1 in BHDC and AOT reverse micelles at different mole-fractions of Brij-30 at three characteristic wavelengths. The transients at

the blue and the red end of the steady state fluorescence spectra are characterized by a decay and a rise, respectively, indicating reorganization of the local environment around the excited state dipole of the fluorophore and is characterized by a time-dependent fluorescence Stokes shift (TDFSS) (Figures 9.6 and Figure 9.7) [27-30]. The solvation correlation function, C(t), calculated from the TDFSS of AC1 decays (Figure 9.8) with two time constants indicats mediation of two types of water trajectories in the solvent relaxation. The faster component (τ_1) may be ascribed to loosely bound water molecules, whereas, the longer relaxation component (τ_2) likely originates from water molecules strongly bound to the surfactant headgroups [31]. The average

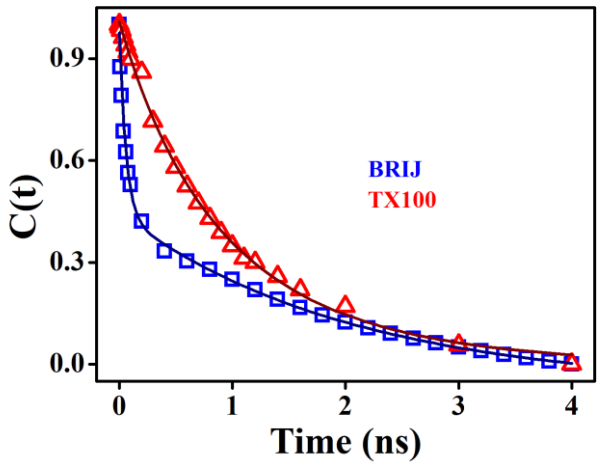

Figure 9.10. *Solvation correlation function of AC1 in Brij 30 reverse micelles and TX-100 reverse micelles.*

solvation time (Table 9.2) for the BHDC reverse micelle (~550 ps) is significantly faster than that for the AOT reverse micelle (~1630 ps) indicating to a significantly faster hydration dynamics in the cationic reverse micelle relative to the anionic reverse micelle. Upon an increase in content of Brij-30 in the mixed cationic reverse micelle (BHDC/Brij-30), the relaxation components become longer along with a significant increase in the average solvation time (~940 ps), whereas, in the case of mixed anionic reverse micelle (AOT/Brij-30) a decrease (~880 ps) is noted. A comparison of the results obtained from the microfluidics set up and time-resolved fluorescence measurements demonstrates clearly that faster hydration dynamics in the cationic (BHDC)

reverse micelles facilitates the mechanism of conformational selection, whereas, slower dynamics of water molecules in the anionic (AOT) reverse micelles aids the induced fit model in the kinetic pathway of recognition of CHT by AMC. This becomes further manifest in case of neutral reverse micelles (Figure 9.9 and Figure 9.10, Table 9.2), where remarkably faster solvation (~1000 ps) facilitates 'conformational selection' in Brij30 and significantly slower dynamics of hydration (~2500 ps) aids an 'induced fit' mechanism for the enzyme-substrate interaction leading to the formation of CHT-AMC complex.

Table 9.2. *Solvation time constant of Acedan in different systems.*

Systems	τ_1 ns (%)	τ_2 ns (%)	τ_{avg} ns (%)
BHDC	0.03 (36)	0.84 (64)	0.55
BHDC-Brij (2:1)	0.03 (41)	1.06 (59)	0.64
BHDC-Brij (1:1)	0.11 (31)	1.33 (69)	0.94
AOT	0.50 (03)	1.66 (97)	1.63
AOT-Brij (2:1)	0.34 (30)	1.45 (70)	1.11
AOT-Brij (1:1)	0.04 (15)	1.03 (85)	0.88
Brij 30	0.05 (50)	2.06 (50)	1.04
TX-100	0.67 (57)	5.04 (43)	2.52

In the 'conformational selection' model the unbound protein must undergo conformational transition from inactive to active form prior to the eventually successful encounter with the ligand resulting in the formation of the final protein-ligand complex, whereas, in the induced-fit mechanism the ligand binds transiently to the predominant free conformation followed by a conformational change in the protein to give the final complex [6]. As the protein motions are coupled to the water dynamics, [11-13] dynamics of the water molecules in the reverse micelle core likely drives the conformational transition in the enzyme (CHT) either prior to an encounter with AMC or following the formation of a transient enzyme-substrate complex. In the cationic (BHDC) reverse micelles, faster hydration dynamics (~550 ps) drives fast conformational rearrangements in the unbound form of the enzyme (CHT)

to pre-organize it into a conformation similar to that of the CHT-AMC complex prior to the binding of AMC (Scheme 9.1) and hence, facilitates the conformational selection model for the formation of the final enzyme-substrate complex. On the other hand, in the anionic (AOT) reverse micelles the substrate (AMC) transiently binds to CHT prior to conformational rearrangements in the enzyme forming a transient enzyme-substrate complex owing to significantly slower dynamics of hydration (~1630 ps). Then slower relaxation of the water molecules drives conformational rearrangements in the enzyme of the transient enzyme-substrate complex (Scheme 9.1) resulting in the formation of the final enzyme-substrate complex which is consistent with the induced fit model [3]. Thus, faster hydration dynamics in the cationic reverse micelles leads to the organization of a molecular recognition event following the 'conformational selection' model, whereas, an induced fit mechanism is favored in the anionic reverse micelles for recognition of the enzyme by the substrate as a consequence of significantly slower dynamics of water molecules.

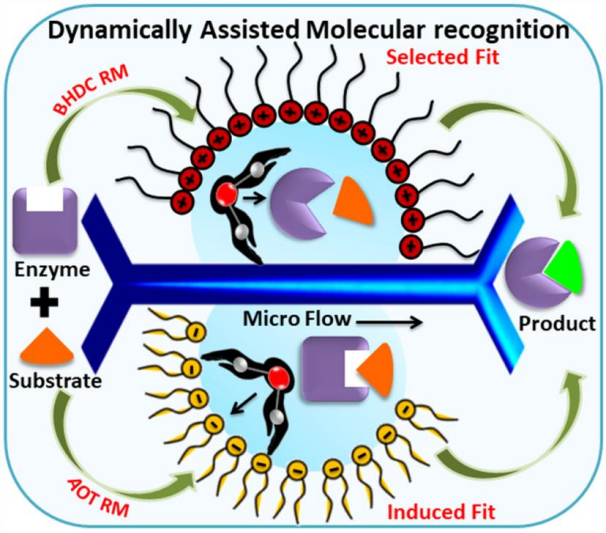

Scheme 9.1.*The overall schematic of the microfluidic based study: The water interactions with the enzyme more in BHDC reverse micelle (RM) compared to that in AOT RM eventually inferring conformational fitting of molecular recognition over induced fit.*

9.3. Conclusion: The kinetic signatures observed from a microfluidics channel demonstrate two different pathways of molecular recognition of an enzyme (CHT) by a substrate (AMC), viz. 'conformational selection' and 'induced-fit' in the nanoscopic domains of two oppositely charged reverse

micelles. When the dynamics of nanoscopic water is fast, as in the case of the cationic reverse micelles of BHDC (~550 ps), it drives fast conformational rearrangements in the unbound form of the enzyme (CHT) to pre-organize it into a conformation similar to that of the bound form prior to binding of the substrate (AMC) and thereby, facilitates the conformational selection model for the formation of the final CHT-AMC complex. In the case of the anionic reverse micelles of AOT, the dynamics of water is significantly slow (~1630 ps), which aids in transient binding of the substrate (AMC) to the enzyme (CHT) prior to conformational rearrangements in the unbound form of CHT, ultimately leading to the formation of the final enzyme-substrate complex via the induced fit model. The role of the dynamics of nanoscopic water molecules in modulating the mode of enzyme-substrate interaction becomes further evident on three instances: firstly, in the shift of molecular recognition from 'induced fit' in pure anionic (AOT) reverse micelles to that of 'conformational selection' in the mixed anionic (1:1) micelles of (AOT/Brij-30), as the hydration dynamics becomes remarkably faster (~880 ps) in the latter relative to that (~1630 ps) in the former and secondly, when the mode of molecular recognition is shifted from 'conformational selection' in pure cationic (BHDC) reverse micelles to that of 'induced fit' in the mixed cationic (1:1) reverse micelles (BHDC/Brij-30), upon a significant retardation (~70 %) in the nanoscopic water dynamics. Finally, in neutral reverse micelles of Brij-30, for which faster water dynamics (~1000 ps) is found to facilitate the 'conformational selection fit' mechanism, whereas the neutral reverse micelles of TX-100 becomes conducive to an 'induced fit' mechanism for recognition of the enzyme (CHT) by the substrate (AMC) on the account of significantly retarded water dynamics (~2500 ps). Taken together, our works based on a microfluidics channel and time-resolved fluorescence measurements, clearly demonstrates that the dynamics of nanoscopic water molecules acts as a switch in modulating the pathway of molecular recognition of an enzyme (CHT) by the substrate (AMC) within the core of reverse micelles.

References

[1] M. Garcia-Viloca, J. Gao, M. Karplus, D.G. Truhlar, How enzymes work: Analysis by modern rate theory and computer simulations, *Science,* 303 (2004) 186-195.

[2] R. Wolfenden, Degrees of difficulty of water-consuming reactions in the absence of enzymes, *Chem. Rev.,* 106 (2006) 3379-3396.

[3] D.E. Koshland, Application of a theory of enzyme specificity to protein synthesis, *Proc. Natl. Acad. Sci. U.S.A.,* 44 (1958) 98-104.

[4] T.R. Weikl, F. Paul, Conformational selection in protein binding and function, *Protein Sci.,* 23 (2014) 1508-1518.

[5] A.D. Vogt, N. Pozzi, Z. Chen, E. Di Cera, Essential role of conformational selection in ligand binding, *Biophys. Chem.,* 186 (2014) 13-21.

[6] H.-X. Zhou, From induced fit to conformational selection: A continuum of binding mechanism controlled by the timescale of conformational transitions, *Biophys. J,* 98 (2010) L15-L17.

[7] S.D. Schwartz, V.L. Schramm, Enzymatic transition states and dynamic motion in barrier crossing, *Nat. Chem. Biol.,* 5 (2009) 551–558.

[8] X. Du, Y. Li, Y.-L. Xia, S.-M. Ai, J. Liang, P. Sang, X.-L. Ji, S.-Q. Liu, Insights into protein–ligand interactions: mechanisms, models, and methods, *Int. J. Mol. Sci.,* 17 (2016) 144-178.

[9] E.Z. Eisenmesser, O. Millet, W. Labeikovsky, D.M. Korzhnev, M. Wolf-Watz, D.A. Bosco, J.J. Skalicky, L.E. Kay, D. Kern, Intrinsic dynamics of an enzyme underlies catalysis, *Nature,* 438 (2005) 117–121.

[10] A. Kohen, Role of dynamics in enzyme catalysis: Substantial versus semantic controversies, *Acc. Chem. Res,* 48 (2014) 466-473.

[11] P.W. Fenimore, H. Frauenfelder, B.H. McMahon, F.G. Parak, Slaving: Solvent fluctuations dominate protein dynamics and functions, *Proc. Natl. Acad. Sci. U.S.A.,* 99 (2002) 16047-16051.

[12] K. Wood, M. Plazanet, F. Gabel, B. Kessler, D. Oesterhelt, D. Tobias, G. Zaccai, M. Weik, Coupling of protein and hydration-water dynamics in biological membranes, *Proc. Natl. Acad. Sci. U.S.A.,* 104 (2007) 18049-18054.

[13] L. Zhao, W. Li, P. Tian, Reconciling mediating and slaving roles of water in protein conformational dynamics, *PloS one,* 8 (2013) 1-7.

[14] M. Grossman, B. Born, M. Heyden, D. Tworowski, G.B. Fields, I. Sagi, M. Havenith, Correlated structural kinetics and retarded solvent dynamics at the metalloprotease active site, *Nat. Struct. Mol. Biol.,* 18 (2011) 1102–1108.

[15] S. Choudhury, S. Batabyal, P.K. Mondal, P. Singh, P. Lemmens, S.K. Pal, Direct observation of kinetic pathways of biomolecular recognition, *Chem. Eur. J.,* 21 (2015) 16172-16177.

[16] C.R. Robinson, S.G. Sligar, Changes in solvation during DNA binding and cleavage are critical to altered specificity of the EcoRI endonuclease, *Proc. Natl. Acad. Sci. U.S.A.,* 95 (1998) 2186-2191.

[17] G. Durin, A. Delaunay, C. Darnault, D.J. Heyes, A. Royant, X. Vernede, C.N. Hunter, M. Weik, D. Bourgeois, Simultaneous measurements of solvent dynamics and functional kinetics in a light-activated enzyme, *Biophys. J,* 96 (2009) 1902-1910.

[18] R.M. Daniel, R.V. Dunn, J.L. Finney, J.C. Smith, The role of dynamics in enzyme activity, *Annu. Rev. Biophys. Biomol. Struct.,* 32 (2003) 69-92.

[19] P. Singh, D. Mukherjee, S. Singha, R. Das, S.K. Pal, Modulation of kinetic pathways of enzyme-substrate interaction in a microfluidic channel: Nanoscopic water dynamics as a switch, *Chem. Eur. J.,* (2019) doi: 10.1002/chem.201901751.

[20] P.W. Atkins, J. De Paula, J. Keeler, Atkins' Physical Chemistry: Thermodynamics and Kinetics, *Oxford University Press*, 2018.

[21] H.R. Bosshard, Molecular recognition by induced fit: How fit is the concept?, *Physiology,* 16 (2001) 171-173.

[22] F.M. Agazzi, N.M. Correa, J. Rodriguez, Molecular dynamics simulation of water/BHDC cationic reverse micelles. structural characterization, dynamical properties, and influence of solvent on intermicellar interactions, *Langmuir,* 30 (2014) 9643-9653.

[23] M.H. Pomata, D. Laria, M.S. Skaf, M.D. Elola, Molecular dynamics simulations of AOT-water/formamide reverse micelles: Structural and dynamical properties, *J. Chem. Phys.,* 129 (2008) 244503-244511.

[24] R.K. Mitra, S.S. Sinha, P.K. Verma, S.K. Pal, Modulation of dynamics and reactivity of water in reverse micelles of mixed surfactants, *J. Phys. Chem. B,* 112 (2008) 12946-12953.

[25] S. Bardhan, K. Kundu, S. Das, M. Poddar, S.K. Saha, B.K. Paul, Formation, thermodynamic properties, microstructures and antimicrobial activity of mixed cationic/non-ionic surfactant microemulsions with isopropyl myristate as oil, *J. Colloid Interface Sci.,* 430 (2014) 129-139.

[26] S. Choudhury, P.K. Mondal, V. Sharma, S. Mitra, V.G. Sakai, R. Mukhopadhyay, S.K. Pal, Direct observation of coupling between structural fluctuation and ultrafast hydration dynamics of fluorescent probes in anionic micelles, *J. Phys. Chem. B,* 119 (2015) 10849-10857.

[27] P. Singh, S. Choudhury, S. Singha, Y. Jun, S. Chakraborty, J. Sengupta, R. Das, K.-H. Ahn, S.K. Pal, A sensitive fluorescent probe for the polar solvation dynamics at protein–surfactant interfaces, *Phys. Chem. Chem. Phys.,* 19 (2017) 12237-12245.

[28] M. Maroncelli, G.R. Fleming, Picosecond solvation dynamics of coumarin 153: the importance of molecular aspects of solvation, *J. Chem. Phys.,* 86 (1987) 6221-6239.

[29] Š. Vajda, R. Jimenez, S.J. Rosenthal, V. Fidler, G.R. Fleming, E.W. Castner, Femtosecond to nanosecond solvation dynamics in pure water and inside the γ-cyclodextrin cavity, *J. Chem. Soc. Faraday Trans.,* 91 (1995) 867-873.

[30] J. Faeder, B.M. Ladanyi, Solvation dynamics in reverse micelles: The role of headgroup− solute interactions, *J. Phys. Chem. B,* 109 (2005) 6732-6740.

[31] T. Yamada, N. Takahashi, T. Tominaga, S.-i. Takata, H. Seto, Dynamical behavior of hydration water molecules between phospholipid membranes, *J. Phys. Chem. B,* 121 (2017) 8322-8329.

List of Publications

(Peer-reviewed journals)

1. **P. Singh**, S. Choudhury, V. K. Sharma, S. Mitra, R. Mukhopadhyay, R. Das and S. K. Pal
"Modulation of Solvation and Molecular Recognition of a Lipid Bilayer under Dynamical Phase Transition"
ChemPhysChem 19 (2018) 2709.

2. **P. Singh**, V. K. Sharma, S. Singha, V. G. Sakai, R. Mukhopadhyay, R. Das and S. K. Pal
"Unraveling the Role of Monoolein in Fluidity and Dynamical Response of a Mixed Cationic Lipid Bilayer"
Langmuir 35 (2019) 4682.

3. **P. Singh**, S. Choudhury, S. Kulanthaivel, D. Bagchi, I. Banerjee, S. A. Ahmed and S. K. Pal
"Photo-triggered Destabilization of Nanoscopic Vehicles by Dihydroindolizine for Enhanced Anticancer Drug Delivery in Cervical Carcinoma"
Colloids and Surfaces B: Biointerfaces 162 (2018) 202.

4. **P. Singh**, S. Choudhury, S. Singha, Y. Jun, S. Chakraborty, J. Sengupta, R. Das, K-Han Ahn and S. K. Pal
"A Sensitive Fluorescence Probe for the Polar Solvation Dynamics at Protein- Surfactant Interface"
Physical Chemistry Chemical Physics 19 (2017) 12237.

5. **P. Singh**, S. Choudhury, G. K. Chandra, P. Lemmens and S. K. Pal
"Molecular Recognition of Genomic DNA in a Condensate with a Model Surfactant for Potential Gene-delivery Applications"
Journal of Photochemistry and Photobiology B: Biology 157 (2016) 105.

6. **P. Singh**, S. Choudhury, S. Dutta, A. Adhikari, S. Bhattacharya, D. Pal and S. K. Pal
"Ultrafast Spectroscopy on DNA-Cleavage by Endonuclease in Molecular Crowding"
International Journal of Biological Macromolecules 103 (2017) 395.

7. **P. Singh**, D. Mukherjee, S. Singha, R. Das and S. K. Pal
"Modulation of Kinetic Pathways of Enzyme-Substrate Interaction in a Microfluidic Channel: Nanoscopic Water Dynamics as a Switch"
Chemistry – A European Journal (DOI: 10.1002/chem.201901751).

8. **P. Singh**, D. Bagchi and S. K. Pal
"Ultrafast Dynamics Driven Biomolecular Recognition where Fast Activities Dictate Slow Events"
Journal of Biosciences 43 (2018) 485.

9.* E. Khatun, A. Ghosh, P. Chakraborty, **P. Singh**, M. Bodiuzzaman, P. Ganesan, G. Nataranjan, J. Ghosh, S. K. Pal and T. Pradeep
"A Thirty-fold Photoluminescence Enhancement Induced by Secondary Ligands in Monolayer Protected Silver Clusters"
Nanoscale 10 (2018) 20033.

10.* D. Bagchi, S. Dutta, **P. Singh**, S. Chaudhuri and S. K. Pal
"Essential Dynamics of an Effective Phototherapeutic Drug in a Nanoscopic Delivery Vehicle: Psoralen in Ethosome for Biofilm Treatment"
ACS Omega 2 (2017) 1850.

11.* D. Bagchi, A. Ghosh, **P. Singh**, S. Dutta, N. Polley, I. I. Althagafi, R. S. Jassas, S. A. Ahmed and S. K. Pal
"Allosteric Inhibitory Molecular Recognition of a Photochromic Dye by a Digestive Enzyme: Dihydroindolizine makes Alpha-chymotrypsin Photo-responsive"
Scientific Reports (Nature Publications) 6 (2016) 34399.

12.* S. Choudhury, B. Ghosh, **P. Singh**, R. Ghosh, S. Roy and S. K. Pal
"Ultrafast Differential Flexibility of Cro-protein Binding Domains of Two Operator DNAs with Different Sequences"
Physical Chemistry Chemical Physics 18 (2016) 17983.

13.* S. Choudhury, G. Naiya, **P. Singh**, P. Lemmens, S. Roy and S. K. Pal
"Modulation of Ultrafast Conformational Dynamics in Allosteric Interaction of Gal Repressor Protein with Different Operator DNA Sequences"
ChemBioChem 17 (2016) 605 (Cover Article).

14.* S. Choudhury, S. Batabyal, P. K. Mondal, **P. Singh**, P. Lemmens and S. K. Pal
"Direct Observation of Kinetic Pathways of Biomolecular Recognition", ***Chemistry – A European Journal*** 21 (2015) 16172.

* Not included in the thesis.

List of International/ National Conferences

1. Poster entitled as "Dynamical perspective of protein-DNA interaction" by **P. Singh** and S. K. Pal, was presented in the conference named ***Advances in Spectroscopy and Ultrafast Dynamics (ASUD-2014)*** held at Indian Association for the Cultivation of Science, Kolkata during December 12-14, 2014.

2. Poster entitled as "Dynamical perspective of protein-DNA interaction" by **P. Singh** and S. K. Pal, was presented in the conference named ***Ultrafast Science- 2015*** held at S N Bose National Centre for Basic Sciences, Kolkata during November 9- 21, 2015.

3. Poster entitled as "Molecular Recognition of Genomic DNA in a Condensate with a Model Surfactant for Potential Gene-delivery Applications" by **P. Singh** and S. K. Pal, was presented in the conference named ***Ultrafast Science- 2016'*** held at BARC Mumbai during November 24-26, 2016.

4. Poster entitled as "Photo-triggered Destabilization of Nanoscopic Vehicles by Dihydroindolizine for Enhanced Anticancer Drug Delivery in Cervical Carcinoma" by **P. Singh** and S. K. Pal, was presented in the conference named ***NANOBIOTECK-2017*** held at KTDC - Samudra, Trivandrum during December 6-8, 2017.

5. Oral entitled as "Spectroscopic Characterization of a Novel Photoreponsive Nanomedicine for Potential use in Cervical Cancer" by **P. Singh** and S. K. Pal, was presented in the conference named ***27th IUPAC International Symposium in Photochemistry*** held at University College Dublin, Ireland during July 8-13, 2018.

6. Attended the conference named ***Industry Academia Meet 2018*** held at S. N. Bose National Centre for Basic Sciences, Kolkata on 6 October 2018.

7. Poster entitled as "Modulation of Solvation and Molecular Recognition of a Lipid Bilayer under Dynamical Phase Transition" by **P. Singh** and S. K. Pal,

was presented in the conference named ***International Conference On Complex and Functional Materials (ICCFM-2018)*** held at Biswa Bangla convention Center, Kolkata during December 13-16, 2018.

8. Poster entitled as "Modulation of Kinetic Pathways of an Enzyme under Nano-confinement: Microfluidic Techniques and Ultrafast Spectroscopy Studies" by **P. Singh** and S. K. Pal, was presented in the conference named ***63rd Annual Meeting of the Biophysical society (BPS19)*** held at Baltimore Convention Centre, Maryland, USA during March 2-6, 2019.